Loughborough University

This item was submitted to Loughborough's Institutional Repository (https://dspace.lboro.ac.uk/) by the author and is made available under the following Creative Commons Licence conditions.

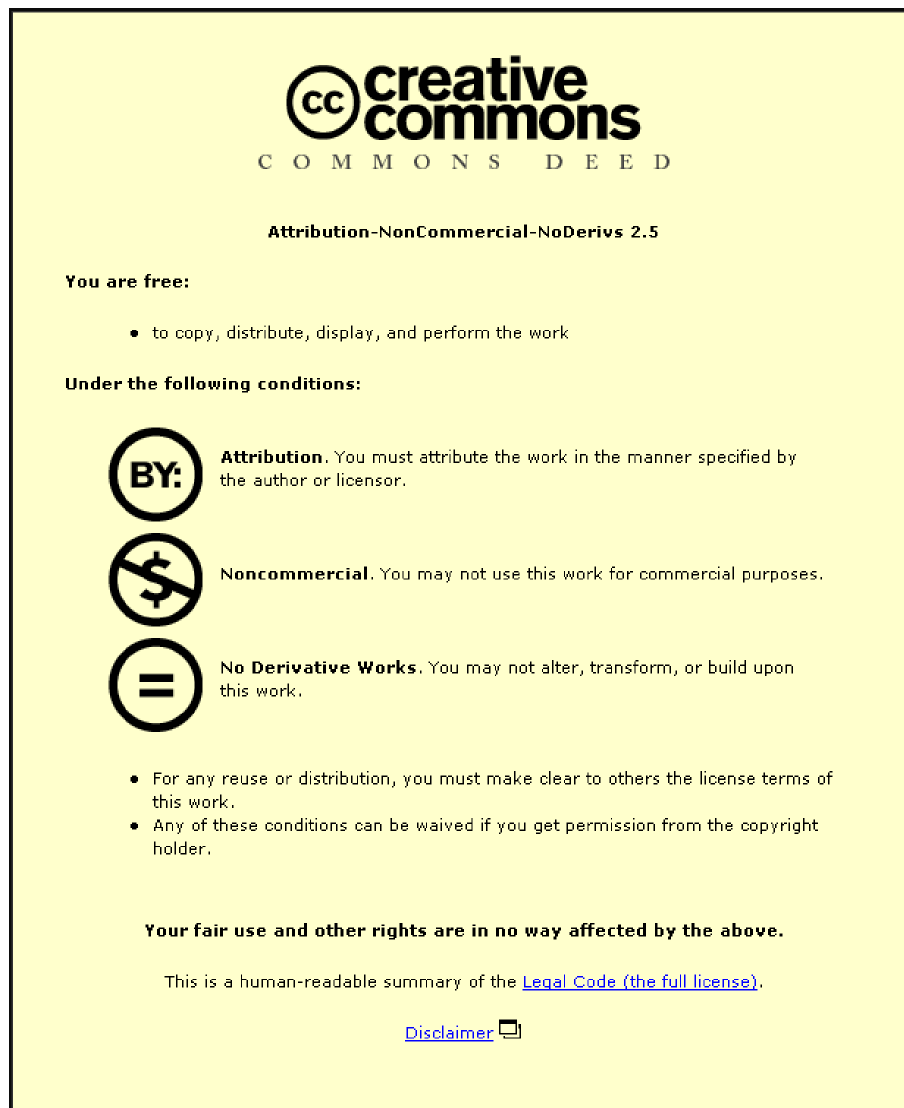

For the full text of this licence, please go to: http://creativecommons.org/licenses/by-nc-nd/2.5/

SIMULATION AND CHARACTERISATION OF ELECTROPLATED MICRO- COPPER COLUMNS FOR ELECTRONIC INTERCONNECTION

by

Jun Liu

A doctoral thesis

submitted in partial fulfilment of the requirements
for the award of Doctor of Philosophy of Loughborough University

January 2010

© by Jun Liu (2010)

DEDICATION

To my parents

Abstract

Growth mechanism of electroplated copper columns has been systematically studied by simulations and characterizations. A two-dimensional cross-sectional kinetic Monte Carlo (2DCS-KMC) model has been developed to simulate the electrodeposition of single crystal copper. The evolution of the microstructure has been visualized. The cluster density, average cluster size, variance of the cluster size and average aspect ratio were obtained from the simulations. The growth history of the deposition from the first atom to an equivalent of 100 monolayers was reconstructed. Following the single-lattice 2DCS-KMC model for a single crystal, a two-dimensional cross-sectional poly-lattice kinetic Monte Carlo (2DCSP-KMC) model has been developed for simulation of the electrodeposition of polycrystalline copper on both a copper and a gold substrate. With this model, the early-stage nucleation and the grain growth after impingement of nuclei can be simulated; as such the entire growth history is reconstructed in terms of the evolution of microstructure, grain statistics and grain boundary misorientation. The model is capable of capturing some key aspects of nucleation and growth mechanisms including the nucleation type (e.g. homogeneous or heterogeneous), texture development, the growth of grains and higher energetic state of grain boundaries. The model has also proven capable of capturing the effects of deposition parameters including applied electrode potential, concentration of cupric ions and temperature. Their effects are largely dependent on the substrates. The early-stage electrocrystallization of Cu on polycrystalline Au has been studied by ex-situ AFM observations. The evolution of surface morphology of the electrodeposited copper on a sputtered Au seed layer from 16ms to 1000s was observed and their formation mechanism discussed. The heterogeneous nucleation phenomenon, the competitive growth both longitudinally and laterally, and the dominant growth of some nuclei were experimentally observed, which are also visualized by the relevant KMC simulation results at a smaller size scale and a shorter time scale. A heuristic model is therefore proposed to describe the mechanism of the early-stage electrocrystallization of Cu on a polycrystalline Au seed layer. Electroplated copper columns plated for different times have been characterized in terms of the evolution of their external morphology, cross-sectional microstructure and crystal structure. The microstructure of electroplated

copper columns is characteristic of bi-modal or tri-modal grain size distribution. The results indicate that recrystallization has occurred during or after the plating, top-down and laterally. Slight changes of the crystal structure were observed by in-situ XRD and it was found that the changes of the (111) and (200) planes occurred at different stages of self-annealing. Finally, the results indicate the presence of organic additives is not essential for self-annealing of a copper column to occur.

Key words: electrodeposition, electroplating, Kinetic Monte Carlo simulation, copper column, electrocrystallization, nucleation, growth history, self-annealing

Acknowledgements

This PhD was funded by the UK Engineering and Physical Sciences Research Council (EPSRC) Innovative electronic Manufacturing Research Centre (IeMRC) at Loughborough.

It would not have been possible to write this doctoral thesis without the help and support of the kind people around me, to only some of whom it is possible to give particular mention here.

I am most grateful to my supervisors Dr Changqing Liu and Professor Paul P Conway. Without their support, patience and guidance throughout the course of my PhD, this thesis would not have been completed.

Generosity of Dr Changhai Wang and Professor Mark Mesmulliez is gratefully acknowledged for the access to their experimental facilities at Heriot-Watt University. I am also deeply indebted to Dr Jun Zeng and Dr David Flynn for their help with the sample preparation and the experiments I conducted there. I am grateful to Dr Geoff Wilcox for the free access to his lab at the Department of Materials at Loughborough University, and Dr Yi Zhang for his help with my early electroplating experiments there. I gratefully acknowledge Dr Geoff West's help with the FIB and EBSD analysis and his patience and many hours of training in FIB. Mr Hui Xu's help with the TEM analysis at NTU and useful discussion is very much appreciated. Generous help of the technicians from the EA Workshop and the Electronic Workshop with the fabrication of the wafer holder is gratefully acknowledged. I would also like to thank Mr Andy Sandavar for his help with the experimental work at Wolfson School.

I would like to thank the ICG group members Yingtao Tian, Tzeyang Hin, Dr Guangbin Dou, Dr Patric Webb, Dr Jicheng Gong etc, and many other friends who are not named here for their kind help and useful discussion during my PhD.

Above all, I would like to thank my wife Haixian Jia for her thoughtful personal support, infinite patience and understanding, at all times. My parents and sister have given me their unequivocal support as always, which has sustained me throughout the studying of my PhD. My mere expression of thanks does not suffice.

Table of Contents

ABSTRACT .... **I**

ACKNOWLEDGEMENTS .... **III**

TABLE OF CONTENTS .... **IV**

LIST OF FIGURES .... **VIII**

LIST OF TABLES .... **XIV**

ABBREVIATIONS .... **XV**

NOMENCLATURES AND UNITS .... **XVII**

PUBLICATIONS .... **XX**

CHAPTER 1 INTRODUCTION **1**

1.1 BACKGROUND 1
1.2 AIM AND SCOPE 3
1.3 ORGANIZATION OF THIS THESIS 3
1.4 SUMMARY OF CONTRIBUTIONS 4

CHAPTER 2 ELECTRODEPOSITION AND ELECTROCRYSTALLIZATION **6**

2.1 ELECTRODEPOSITION 6
2.1.1 Definition *6*
2.1.2 Cu Electrodeposition in Microelectronics *6*
2.2 SELF-ANNEALING OF ELECTRODEPOSITED CU 9
2.2.1 Resistance drop and stress relaxation *9*
2.2.2 Microstructural evolution *11*
2.2.3 Evolution of crystal structure *12*
2.2.4 Driving force *14*
2.2.5 Kinetics *15*
2.3 NANO-TWINNING IN ELECTRODEPOSITED CU 17
2.4 ELECTROCRYSTALLIZATION 20
2.4.1 Definition *20*
2.4.2 Basic processes *20*
2.4.3 Thermodynamic aspect *21*
2.4.4 Nucleation theories *24*
2.4.5 Experimental studies of Initial stages of electrocrystallization *24*
2.5 SUMMARY 29

CHAPTER 3 KINETIC MONTE CARLO SIMULATION OF ELECTROCRYSTALLIZATION OF SINGLE-CRYSTAL COPPER 30

3.1 INTRODUCTION ... 30
3.2 DESCRIPTION OF THE MODEL ... 32
3.2.1 Events ... 33
3.2.2 Parameters ... 35
3.2.3 KMC Algorithm ... 36
3.2.4 Post-processing ... 38
3.3 RESULTS AND DISCUSSION ... 39
3.3.1 Growth history ... 39
3.3.2 Effects of deposition parameters ... 42
3.4 CONCLUSIONS ... 46

CHAPTER 4 KINETIC MONTE CARLO SIMULATION OF ELECTRODEPOSITION OF POLYCRYSTALLINE COPPER 47

4.1 INTRODUCTION ... 47
4.2 SIMULATION METHODS ... 48
4.2.1 System ... 48
4.2.2 Data structure and Algorithm ... 49
4.2.3 Events ... 51
4.2.4 Parameters ... 52
4.2.5 Post-processing ... 53
4.3 RECONSTRUCTION OF THE GROWTH HISTORY ... 53
4.4 EFFECTS OF THE DEPOSITION PARAMETERS ... 59
4.4.1 Applied electrode potential ... 59
4.4.2 Concentration of cupric ions ... 69
4.4.3 Temperature ... 71
4.4.4 Combination of parameters ... 73
4.4.5 Dependence on substrate ... 74
4.5 EFFECTS OF THE JUMP FREQUENCY ... 76
4.6 CONCLUSIONS ... 80

CHAPTER 5 MATERIALS AND EXPERIMENTAL METHODS ... 82

5.1 FABRICATION OF MICRO- COPPER COLUMNS BY ELECTROPLATING AND MATERIALS ... 82
5.1.1 Si wafer ... 83
5.1.2 Metallization ... 83
5.1.3 Patterning ... 83
5.1.4 Electroplating ... 84

5.1.5 Etching ... *84*
5.2 ELECTROPLATING ... 84
5.3 CHARACTERISATION METHODS ... 86
CHAPTER 6 EARLY-STAGE ELECTROCRYSTALLIZATION OF CU ON POLYCRYSTALLINE AU ... 89
6.1 INTRODUCTION ... 89
6.2 AU SEED LAYER ... 89
6.3 EVOLUTION OF THE SURFACE MORPHOLOGY ... 91
6.4 MODEL FOR THE NUCLEATION AND GROWTH ... 96
6.5 SUMMARY ... 97
CHAPTER 7 GROWTH AND RECRYSTALLIZATION OF ELECTROPLATED COPPER COLUMNS ... 98
7.1 INTRODUCTION ... 98
7.2 OVERVIEW OF ELECTROPLATED COPPER COLUMNS ... 98
7.3 GROWTH HISTORY ... 101
7.3.1 Evolution of the external morphology ... *101*
7.3.2 Evolution of the cross-sectional microstructure ... *107*
7.3.3 Size effects ... *110*
7.3.4 Evolution of the crystal structure ... *115*
7.4 RECRYSTALLIZATION ... 117
7.5 DISCUSSION AND CONCLUSIONS ... 119
CHAPTER 8 GENERAL DISCUSSION ... 121
8.1 KMC SIMULATIONS ... 121
8.1.1 Single-lattice model ... *121*
8.1.2 Poly-lattice model ... *122*
8.1.3 Limitations ... *123*
8.2 EX-SITU EXPERIMENTAL OBSERVATIONS AND COMPARISION WITH SIMULATIONS ... 124
8.3 RECONSIDERATION OF THE DEFINITION OF ELECTRO-CRYSTALLIZATION ... 126
CHAPTER 9 CONCLUSIONS ... 127
9.1 KMC SIMULATIONS ... 127
9.2 CHARACTERISATION ... 128
9.3 SUMMARY ... 129
CHAPTER 10 RECOMMENDATIONS OF FUTURE WORK ... 130
REFERENCES ... 131
APPENDICES ... 144
APPENDIX I. DESIGN OF THE PHOTOMASK ... 144

APPENDIX II. ASSEMBLY DRAWING OF THE WAFER HOLDER ... 145
APPENDIX III. PART DRAWINGS OF THE WAFER HOLDER ... 146
APPENDIX IV. SIMULATION CODES FOR THE 2DCS-KMC MODEL ... 150
APPENDIX V. POSTPROCESSING CODES FOR THE 2DCS-KMC MODEL ... 163
APPENDIX VI. SIMULATION CODES FOR THE 2DCSP-KMC MODEL ... 167
APPENDIX VII. POSTPROCESSING CODES FOR THE 2DCSP-KMC MODEL ... 197

List of Figures

Fig. 1-1 Single crystal copper gold wire produced by electrodeposition in pores of polymer ion-track membranes [7-8]. 2

Fig. 2-1 A schematic of an electrolytic cell for plating metal "Me" from a solution of the metal salt "MeA". 7

Fig. 2-2 An array of reflowed C4s fabricated by electrodeposition [25] (Reproduced by permission of The Electrochemical Society).......... 8

Fig. 2-3 IBM's six-level copper interconnect technology [29](Figure reprinted with permission from IEEE © 1999 IEEE).......... 9

Fig. 2-4 Sheet resistance (top) and stress (bottom) of the electroplated Cu layers as a function of time after deposition for four and three values of the layer thickness, respectively.[32] 10

Fig. 2-5 The evolution of (a) deposit stress thickness and (b) average film stress as a function of pulse deposition time. [33] 11

Fig. 2-6 Series of TEM micrographs for a 0.3 mm thick electroplated Cu film transforming at room temperature (a) t=11 min, (b)t=1 h, (c) t=2.5 h, (d) t=8 h, (e) t=23.5 h, (f) t=80 h. After t=80 h, no further transformation took place. [35] 13

Fig. 2-7 X-ray diffraction showing the Cu (111) peak for a 970 nm thick electroplated film. The time during which the film was stored at room temperature is indicated. [30] 14

Fig. 2-8 Transient time vs film thickness showing data point from Gignac et al. [39] and the function $\tau - t_0 = k / (d - d_0)$ with τ=2.5, t_0 = 5.5h, and d_0 = 0.23. [31] 16

Fig. 2-9 Schematic of twin crystals and twin boundary 18

Fig. 2-10 (a) A bright-field TEM image and the electron diffraction pattern (inset) show roughly equiaxed sub-micrometer-sized grains with random orientations separated by high-angle grain boundaries. (b) A typical tensile stress-strain curve for the as-deposited Cu sample with nano-twins in comparison with that for a coarse-grained polycrystalline Cu sample and a nano-crystalline Cu sample (mean grain size ~30 nm). (c) Resistivity of nano-twinned copper compared to coarse-grained and nano-crystalline copper. [4] 19

Fig. 2-11 Steps involved in the process of electrocrystallization. The cathodic reaction $Cu^{2+} + 2e \rightarrow Cu$ is schematically considered. 21

Fig. 2-12 Schematics of different growth modes for metal (Me) deposition on foreign substrate (S) depending on the binding energy ψ and on the crystallographic misfit characterized by the interatomic distances d_0 . (a) "Volmer-Weber" growth mode (3D island formation) for $\Psi_{Me_{ads}\text{-}S} \ll \Psi_{Me_{ads}\text{-}Me}$ independent of the ratio $(d_{0,Me} - d_{0,S})/d_{0,S}$. (b) "Frank-van der Merwe" growth mode (Me layer-by-layer) formation for $\Psi_{Me_{ads}\text{-}S} \gg \Psi_{Me_{ads}\text{-}Me}$ and ratio $(d_{0,Me} - d_{0,S})/d_{0,S} \approx 0$. (c) "Stranski-Krastanov" growth mode (3D Me island formation on top of pre-deposited 2D Meads overlayers on S for $\Psi_{Me_{ads}\text{-}S} \gg \Psi_{Me_{ads}\text{-}Me}$ and $(d_{0,Me} - d_{0,S})/d_{0,S} < 0$ (negative misfit). [56] 23
Fig. 2-13 a) Cyclic current-potential curve for the UPD of Cu on Au (111) in 0.05M H_2SO_4 + 1mM $CuSO_4$. Scanning rate: 1mV/s. b) STM image of Au (111) at 150mV versus Cu/Cu^{2+} in 0.1M H_2SO_4 + 1mM $CuSO_4$. [87] 25
Fig. 2-14 a) STM images of Au(111) in 5mM H_2SO_4 + 0.05mM $CuSO_4$ at +0.1 V and -0.185 V versus Cu/Cu^{2+}. Nucleation and growth occurs almost exclusively at step edges. b) Au (111) in 0.1 M H_2SO_4 + 1mM $CuSO_4$ at 0.15 and ±0.3 V, respectively. At higher overpotential nucleation and growth sets in also on terraces. [56, 75, 87] 26
Fig. 2-15 An in-situ STM image of bulk copper deposition on a gold film at -200 mV (vs. Cu/Cu^{2+}) in 0.1M H_2SO_4 + 1mM $CuSO_4$, [77] 28
Fig. 2-16 In-situ STM image of Cu-deposition on a gold film from 0.1M H_2SO_4 + 1mM $CuSO_4$ + 10 mg/l BT-B. [77] 28
Fig. 2-17 In-situ AFM images of Cu-deposition on a conductive polypyrrole from 0.1M H_2SO_4 + 1mM $CuSO_4$ (a) without additive and (b) with 10 mg/l BT-B. [77] 29
Fig. 3-1 Schematic of the idealized electrodeposition system 33
Fig. 3-2 the flow chart of the KMC algorithm 38
Fig. 3-3 the dependence of (a) the cluster density, (b) the average cluster size, (c) the variance of the cluster size and (d) the average aspect ratio of the cluster on the deposition amount by EML. 40
Fig. 3-4 the snapshots of the microstructure on deposition of a series of amounts of deposit: (a) the enlarged of the area indicated by a rectangle box in (b), (b) 1EML, (c) 5 EML, (d) 10 EML, (e) 20 EML, (f) 40 EML, (g) 72 EML and (h) 100 EML. 41

Fig. 3-5 the microstructure history map showing the evolution of the microstructure from the beginning until 100 EML. 42

Fig. 3-6 the snapshots of the microstructure after 30 EML under different conditions: (a) the concentration of Cu^{2+} of solution, c = 0.1 mol, the temperature T=298 K and potential ρ= -0.11 V; (b) c=0.32 mol, T=298K, ρ= -0.11 V (c) c=0.66 mol, T= 298 K, ρ= -0.11 V and (d) c=0.32 mol, T=313 K, ρ= -0.11 V (e) c=0.32 mol, T=298 K, ρ= -0.13 V 43

Fig. 3-7 the dependence of (a) cluster density and (b) the variance of cluster size on the KMC time under different deposition conditions. 45

Fig. 4-1 Schematics of the idealized system for electrodeposition of polycrystalline copper 49

Fig. 4-2 Schematic of the simulation cell and the data structure 50

Fig. 4-3 the snapshots of simulated microstructure on deposition of from 0.5 EML to 50 EML Cu atoms on a Cu substrate 54

Fig. 4-4 the snapshots of simulated microstructure on deposition of from 0.5 EML to 50 EML Cu atoms on a Au substrate 55

Fig. 4-5 Illustration of the three unit shapes that constitutes various grain shapes 56

Fig. 4-6 the statistics on grain growth including the dependence of the grain density (a), the average effective grain size (b) and variance of the effective grain size (c) on deposition time. 57

Fig. 4-7 Distribution and evolution of grain boundary misorientation for copper deposition on a Cu substrate 58

Fig. 4-8 Distribution and evolution of grain boundary misorientation for copper deposition on a Au substrate 58

Fig. 4-9 Snapshots of the simulated microstructure on deposition of 50 EML Cu on a Cu substrate using different deposition parameters. 60

Fig. 4-10 Simulated grain density as a function of deposition time for the deposition of Cu on a Cu substrate using different deposition parameters. 61

Fig. 4-11 Simulated average effective grain size as a function of deposition time for the deposition of Cu on a Cu substrate using different deposition parameters. 63

Fig. 4-12 Simulated variance of the grain size as a function of deposition time for the deposition of Cu on a Cu substrate using different deposition parameters. 63

Fig. 4-13 The evolution and the distribution of the grain boundary misorientation for deposition on a Cu substrate at a potential of -0.20V. 64
Fig. 4-14 The evolution and the distribution of the grain boundary misorientation for deposition on a Cu substrate at a potential of -0.11V. 64
Fig. 4-15 Snapshots the simulated microstructure on deposition of 50 EML Cu on a Au substrate using different deposition parameters 65
Fig. 4-16 Simulated grain density as a function of deposition time for the deposition of Cu on a Au substrate using different deposition parameters. 67
Fig. 4-17 Simulated average grain size as a function of deposition time for the deposition of Cu on a Au substrate using different deposition parameters. 67
Fig. 4-18 Variance of the grain size as a function of deposition time for the deposition of Cu on a Au substrate using different deposition parameters. 68
Fig. 4-19 The evolution and the distribution of the grain boundary misorientation for deposition on a Au substrate at -0.20V 68
Fig. 4-20 The evolution and the distribution of the grain boundary misorientation for deposition on a Au substrate at -0.11V 69
Fig. 4-21 The evolution and the distribution of the grain boundary misorientation for deposition on a Cu substrate at a lower concentration of Cu^{2+} ions of 0.1mol. 70
Fig. 4-22 The evolution and the distribution of the grain boundary misorientation for deposition on a Au substrate at a lower concentration of Cu^{2+} ions of 0.1mol. 71
Fig. 4-23 The evolution and the distribution of the grain boundary misorientation for deposition on a Cu substrate at a higher temperature of 313K. 72
Fig. 4-24 The evolution and the distribution of the grain boundary misorientation for deposition on a Au substrate at a higher temperature of 313K. 73
Fig. 4-25 Dependences of the difference between the deposition rates on substrate and on a pre-deposited Cu, Δr, on the deposition parameters. The colors show difference of the deposition rates. 76
Fig. 4-26 Snapshots of the simulated microstructure for deposition on Cu or Au substrate using different values of jump frequency w 77
Fig. 4-27 Grain density as a function of time for deposition on a Cu or a Au substrate at different values of jump frequency. 78

Fig. 4-28 Average effective grain size as a function of time for deposition on a Cu or a Au substrate at different values of jump frequency......79
Fig. 4-29 Variance of grain size as a function of time for deposition on a Cu or a Au substrate at different values of jump frequency......79
Fig. 5-1 Process flow for fabrication of micro- copper column by electroplating......82
Fig. 5-2 A picture of the plating system......85
Fig. 5-3 A picture of wafer holder......86
Fig. 5-4 Illustration of FIB cross-sectioning process a) the secondary electron (SE) image of a complete copper column, b) part way through cutting c) SE image of cross-section on completion d) ion bean induced SE image showing the microstructure .87
Fig. 6-1 an AFM image of the as-sputtered Au seed layer......90
Fig. 6-2 XRD spectrum of a metallized test wafer before deposition......91
Fig. 6-3 AFM image of the copper deposits for a series of period of time: a) before deposition, b) 16ms, c) 100ms, d) 10s, e) 100s, f) 1000s. 92
Fig. 6-4 The overpotential-time transient curves of galvanostatic electrodeposition of copper for 16ms. 93
Fig. 6-5 AFM images of a) the marked area in Fig. 6-3b and b) the as-sputtered gold seed layer. 93
Fig. 6-6 HRTEM image of the interface between a Cu deposit and the Au seed layer......94
Fig. 6-7 AFM image of the copper deposit after 100s of deposition. 95
Fig. 6-8 Dependence of the roughness and surface areas of the copper deposits on deposition time......96
Fig. 6-9 Schematic of a heuristic model for nucleation and growth of Cu on polycrystalline Au 97
Fig. 7-1 SEM images of copper columns of 15μm in diameter plated for one hour (a) Top view (b) stereoscopic view. 99
Fig. 7-2 SEM images of copper columns of 15μm in diameter plated for 3 hours (a) Top view (b) stereoscopic view. 100
Fig. 7-3 Distribution of the large grains (a) frequency counts of the grains in each column (b) Percentage of the large grains which are on the edge of each column. 101
Fig. 7-4 The SEM image of a copper column plated for half an hour (a) top view, (b) stereoscopic view 103

Fig. 7-5 An ion-beam-induced secondary electron image of the top surface of the column plated for half an hour showing the grain boundaries. 103
Fig. 7-6 The SEM image of a copper column plated for 1 hour (a) top view, (b) stereoscopic view 104
Fig. 7-7 The SEM image of a copper column plated for 2 hours (a) top view, (b) stereoscopic view 105
Fig. 7-8 The SEM image of a copper column plated for 2 hours (a) top view, (b) stereoscopic view 106
Fig. 7-9 FIB image of the cross-sectional microstructure of the copper column plated for a) 0.5 hour, b) 1 hour, c) 2 hours and d) 3 hours. 109
Fig. 7-10 the morphology and microstructure of the copper column of 10μm in diameter plated for one hour (a) the top view (b) the stereoscopic view and (c) the cross-section 112
Fig. 7-11 the morphology and microstructure of the copper column of 10μm in diameter plated for 2 hours (a) the top surface (b) the stereoscopic view and (c) the cross-section 113
Fig. 7-12 the morphology and microstructure of the copper column of 10μm in diameter plated for 3 hours (a) the top surface (b) the stereoscopic view and (c) the cross-section 115
Fig. 7-13 XRD line profiles of (a) bare Si wafer, (b) Si with sputtered Au, (c) plated for 0.5 hour, (d) 1 hour, (e) 2 hours and (f) 3 hours 117
Fig. 7-14 XRD line profiles at different time after deposition of a sample plated for one hour for the a) 111 and b) 200 texture..118

List of Tables

Table 2-1 Overview of the estimated driving force ΔG for microstructural evolution related to different sources of stored energy in the as-deposited film. [30] 15

Table 3-1 Values of the parameters used in the simulation 36

Table 4-1 Values of the parameters different from Chapter 3 53

Table 4-2 Description of the combination of the deposition parameters for the simulations 59

Table 4-3 Values of some statistical data of the grain growth history for deposition on a Cu substrate and a Au substrate. 62

Table 5-1 Characterisation methods 87

Abbreviations

1D	one dimensional
2D	two dimensional
2DCS	two-dimensional cross-section
2DCSP	two-dimensional cross-section poly-lattice
3D	three dimensional
AFM	Atomic Force Microscopy
bcc	body centred cubic
C	Concentration of Cu^{2+} ions in the electrolyte
C4	Controlled Collapse Chip Connection
CTT	Current Time Transient
DI	deionised
EBSD	Electron Back Scattered Diffraction
EML	Equivalent MonoLayer
fcc	face centred cubic
FD	Finite Difference
FEG-SEM	Field Emission Gun Scanning Electron Microscopy
FIB	Foucsed Ion Beam
HRTEM	High Resolution Transmission Electron Microscopy
KMC	kinetic Monte Carlo
OPD	Over Potential Deposition

P	Applied electrode potential
S	Substrate
SCE	Saturated Calomel Electrode
SEM	Scanning Electron Microscopy
SPM	Scanning Probe Microscopy
STM	Scanning Tunnelling Microscopy
T	Deposition temperature
TEM	Transmission Electron Microscopy
TSV	Through Silicon Via
UPD	Under Potential Deposition
XRD	X-Ray Diffraction

Nomenclatures and Units

SYMBOL	NAME	UNIT
$a_{0,Me_{ads}}$	activity of Me_{ads} at $E = E_{Me/Me^{n+}}$	
a_{Me}	activity of the Me	
$a_{Me_{ads}}$	activity of Me_{ads} at $E \neq E_{Me/Me^{n+}}$	
$a_{Me^{n+}}$	activity of the solvated Me^{n+} ions in the electrolyte	
B	The structure matrix of the simulation cell for the 2DCSP-KMC model	
$C_{Cu^{2+}}$	concentration of the Cu^{2+} ions at the electrode surface	mol/m^3
d_{inh}	inhibiting distance	
E	electrode potential	V
E_{act}	activation energy for surface diffusion	J
E_{barr}	energy barrier of an atom	J
E_f	the energy of the system after diffusion	J
E_{mig}	migration energy	J
$E_{Me/Me^{n+}}$	Nernst equilibrium potential of the Me/Me^{n+} electrode	V
$E^0_{Me/Me^{n+}}$	standard electrode potential of Me/Me^{n+}	V
F	Faraday constant	C mol^{-1}
k_{Cu-Au}	rate constant for deposition of species of Cu^2 on Au	m^3·mol^{-1}·s^{-1}
k_{Cu-Cu}	rate constant for deposition of species of Cu^2 on pre-deposited Cu	m^3·mol^{-1}·s^{-1}
K_0	a temperature-dependent grain growth rate	m/s
m	a material-dependent growth exponent	

SYMBOL	NAME	UNIT
M_{occp}	lattice matrix	
Me	an atom of the metal	
$\mathrm{Me^{n+}}$	an n-valent cation of Me	
n	electron number	
N	the number of atoms in an individual grain	
N_A	Avogadro constant	
N_{cord}	coordinate number of an atom, i.e. the number of the nearest neighbouring Cu atoms.	
N_{cord}^{str}	strange coordination number	
r_0	initial grain size	m
$r_{d_{Cu-Au}}$	deposition rate on Au	s^{-1}
$r_{d_{Cu-Cu}}$	deposition rate on Cu	s^{-1}
$r_{dif_{Cu-Au}}$	diffusion rate on Au	s^{-1}
$r_{dif_{Cu-Cu}}$	diffusion rate on Cu	s^{-1}
$r_{s_{Cu-Au}}$	surface diffusion rate on Au	s^{-1}
$r_{s_{Cu-Cu}}$	surface diffusion rate on Cu	s^{-1}
R	ideal gas constant	$J \cdot mol^{-1} \cdot K^{-1}$
V_m	the molar volume of the solid phase	m^3/mol
w_{Cu-Au}	jump frequency for diffusion on Au	
w_{Cu-Cu}	jump frequency for diffusion on Cu	
α	charge transfer coefficient for the deposition of Cu^{2+}	
ΔE	the difference between the energy of the system after	J

SYMBOL	NAME	UNIT
	and before the diffusion	
η_c	overpotential	V
λ	correction coefficient	
υ_{Cu-Au}	jump frequency for surface diffusion on Au	s^{-1}
υ_{Cu-Cu}	jump frequency for surface diffusion on Cu	s^{-1}
ξ	random number	
ρ	applied potential	V
$\rho_{0_{Cu^{2+}/Au}}$	equilibrium potential for Cu^{2+}/Au	V
$\rho_{0_{Cu^{2+}/Cu}}$	equilibrium potential for Cu^{2+}/Cu	V
τ	KMC time increment	s
$\Psi_{Me_{ads}-Me}$	binding energy between a Me adatom and a deposited Me atom	J
$\Psi_{Me_{ads}-S}$	Binding energy between a Me adatom and a substrate atom	J

Publications

1. J. Liu, C. Liu and P.P. Conway, Kinetic Monte Carlo simulation of electrodeposition of polycrystalline Cu. Electrochemistry Communications, 2009. 11(11): p. 2207-2211.
2. J. Liu, C. Liu and P.P. Conway, Kinetic Monte Carlo simulation of kinetically limited copper electrocrystallization on an atomically even surface. Electrochimica Acta, 2009. 54(27): p. 6941-6948.
3. J. Liu, C. Liu, P.P. Conway, J. Zeng and C. Wang. Growth and recrystallization of electroplated copper columns. in Electronic Packaging Technology & High Density Packaging, ICEPT-HDP '09 International Conference. 2009. Beijing
4. J. Liu, C. Liu and P.P. Conway, Growth mechanism of copper column by electrodeposition for electronic interconnections. in 2nd Electronics System-Integration Technology Conference, ESTC 2008. 2008. Greenwich, London.
5. J. Liu, C. Liu and P.P. Conway, Crystallographic features of copper column growth by reversible pulse current electrodeposition. in Electronic Components and Technology Conference, 2007. ECTC '07. Proceedings. 57th. 2007.

Chapter 1 Introduction

1.1 Background

Miniaturization of electronic devices has been one of the main driving forces behind the rapid development of electronics for many years. Meanwhile, it poses increasing challenges to electronic packaging technology, which has become a major concern in both cost and performance of electronic products. Nowadays, electronic devices have been miniaturized to a scale where the size of an interconnect joint is comparable with the microstructure feature size of the materials in the joint. It has been reported that there are only a very small number of grains in a microelectronic solder joint, implying a multi-crystalline rather than polycrystalline structure [1-3]. This has become a concern in the predictability of reliability of a package due to the indeterminate anisotropic behaviour of such multi-crystalline joint systems. Therefore, solutions to interconnect materials and manufacturing are required to meet such challenges. Two possible approaches are proposed here. One is to reduce the feature size of interconnect materials, e.g. using nano-crystal interconnects. A micro-scale joint with nano-crystalline microstructure is still polycrystalline. Nano-crystalline joints are anticipated to have other attractive properties such as high tensile strength, superplasticity and good conductivity [4-5]. For example, a copper deposit produced by pulse plating containing a high density of nano-twins produces ten times higher tensile strength than pure copper and comparable electrical conductivity, which are usually unavailable by conventional strengthening methods [4]. Alternatively, another solution is to use a single crystal for interconnects i.e. one crystal is one joint. Without grain boundaries, single crystals exhibit numerous attractive characteristics in terms of mechanical, electrical and thermal performance. The elongation percentage of continuous-cast-single-crystal copper is 80%-270% greater than polycrystalline copper; contraction of cross-section area 4%-395% greater; resistivity 4.25%-15.75% lower[6]. Single crystal copper wires have been widely applied in electronic communication, audio and video and super high-frequency signal transmission and ultra fine connector wires in semiconductor connectors. It is indicative that single crystals can perform multiple functions that are required for electronic interconnect: structural integrity, electrical and thermal conductivity, and possibly optical signal transmission.

Either the nano-crystal or the single-crystal solution is promising to solve the problem if it can be produced in a way that is compatible with electronic manufacturing processes. Electrochemical deposition, or electrodeposition, also known as electroplating, has been widely used in the fabrication of micro- or nano- components in electronic devices e.g. copper interconnect, Through Silicon Via (TSV) for 3D electronic packaging, micro-copper columns, flip-chip bumps, nano-wires etc. Deposits of a wide variety of microstructures ranging from single-crystal [7-13] to nano-crystal [14] have been obtained by electrodeposition using different deposition parameters and assisting techniques. For example, template-assisted electrodeposition has been employed to produce single-crystal copper and gold wires of approximately 5μm in diameter on a polycrystalline gold seed layer [7-8] as shown in Fig. 1-1, as well as nano-wires of Sn, Bi, Ag and Au [9, 15-18].

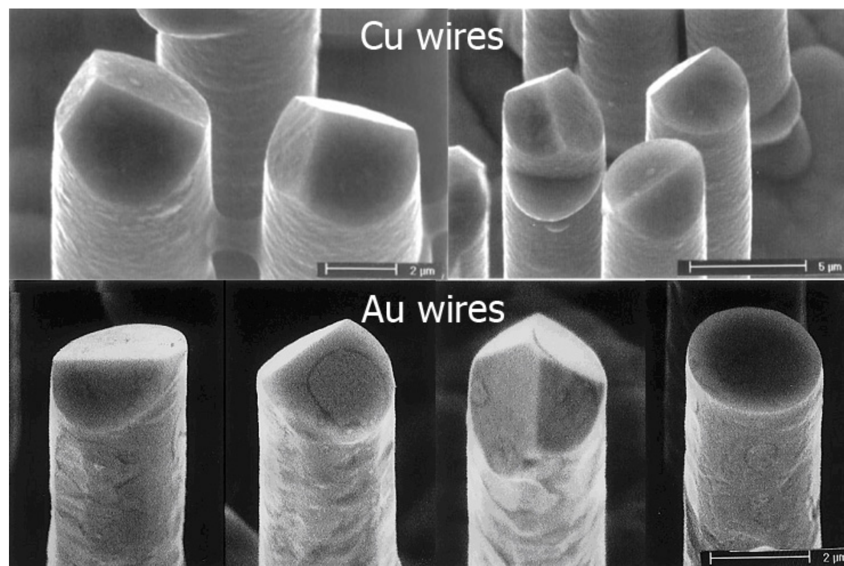

Fig. 1-1 Single crystal copper gold wire produced by electrodeposition in pores of polymer ion-track membranes [7-8].[i]

Micro- copper columns have advantages over lead-free solder joints as the next-generation IC package interconnect in terms of electrical performance, mechanical properties, thermal and electro-migration resistance [19]. The copper column is also a

i Reprinted from Electrochimica Acta, 45 (19), D. Dobrev, J. Vetter, N. Angert, R. Neumann, Periodic reverse current electrodeposition of gold in an ultrasonic field using ion-track membranes as templates: growth of gold single-crystals p. 3117-3125., Copyright (2000), with permission from Elsevier, and with kind permission from Springer Science+Business Media: Applied Physics A, 69, 1999, p.233-237, Dobrev, D., et al, Figure 2.

feature of Intel's 45nm processor packaging solution [20]. Finally, electrodeposition of copper columns is identified here. It promises a practical approach to obtain single-crystal or nano-crystal bumps for application in the subsequent assembly operations. Fabrication of copper columns using electrodeposition has been previously reported [19], but little attention has been given to the resultant microstructure of such copper columns.

The formation mechanism behind various microstructures of electrodeposits is still unclear to large degree. It has been found that electroplated copper tends to recrystallize at room temperature after plating [21-22], which adds a further complexity. It is imperative to understand the growth mechanism of an electrodeposit in order to tailor a specific microstructure for various applications in electronic packaging.

1.2 Aim and scope

The aim of this PhD is to enhance the understanding of the growth mechanism of electroplated copper columns and to provide guidance for microstructure-tailoring. To achieve this, kinetic Monte Carlo (KMC) simulations of copper electro-crystallization have been conducted. A single-lattice KMC model was developed for simulations of single-crystal electrocrystallization and an advanced poly-lattice KMC model to treat growth of a polycrystalline deposit. Experimentally, the early-stage nucleation and growth were studied by characterizing the evolution of the surface morphology of copper electrodeposit by Atomic Force Microscope (AFM). Finally, growth and recrystallization of electroplated copper columns were examined by characterizing the external morphology, microstructure and crystal structure of copper columns plated for a series of periods of time.

1.3 Organization of this thesis

This thesis consists of ten chapters. Chapter 1 serves as a general overview of the background information, problem description and proposed methodology, aim and scope, the organization of this thesis and finally a summary of contributions arising from this PhD research. Chapter 2 is a literature review on electrocrystallization and copper electrodeposition including fundamentals on electrocrystallization, experimental studies on copper electrocrystallization at initial stages and two relevant aspects in the field of

copper electrodeposition: self-annealing and nano-twinning. The purpose of this chapter is twofold. One is to provide readers with a quick review of fundamentals on electrodeposition and electrocrystallization that is necessary for them to understand this thesis. The other serves as an expansion of the introduction of the background knowledge and information with respect to this PhD research. Chapter 3 presents a single-lattice KMC model for simulation of single-crystal copper electrocrystallization. A more advanced poly-lattice KMC model for simulations of polycrystalline deposit is presented in Chapter 4. The following three chapters present results from experimental studies. Materials and methods for the experiments and characterization are described in Chapter 5. Chapter 6 presents an experimental study of the early-stage nucleation and growth of copper deposit. The results are compared with the KMC simulation results and a heuristic model is proposed to describe the nucleation and growth mechanism. Chapter 7 deals with the later-stage growth and recrystallization of copper columns. Chapter 8 discusses reconstruction of the growth history of electroplated copper column to understand the growth mechanism by both simulation and experimental study. The conclusions of the thesis are summarized in Chapter 9. Finally, future work is recommended in Chapter 10.

1.4 Summary of contributions

This PhD mainly makes the following contributions:

- The growth history of electroplated micro- copper columns is incompletely reconstructed both computationally and experimentally, which partly uncover their complex growth mechanism.
- A single-lattice two-dimensional cross-sectional KMC model was developed for simulation of electrocrystallization of single crystal copper, which enables a reconstruction of the growth history of not only the early stages but also the crystal growth process at later stages, while most of the reported 3D and/or multi-scale models focused only on the early-stage nucleation processes.
- An advanced poly-lattice KMC model was developed for simulation of polycrystalline copper electrodeposition on a copper or gold substrate. This work is the first attempt of using a poly-lattice KMC model to simulate the

electrodeposition process. This also leads to several advancements over other reported multi-lattice KMC models which have been developed for other thermal deposition processes, as explained in detail in Section 8.1.2.

- These models have proved capable of capturing the effects of the deposition parameters on electrocrystallization, deposit microstructure and the grain growth history. They promise to develop into a simulation tool for an optimum selection of deposition parameters for generation of a desirable microstructure e.g. a single-crystal or nano-crystal one.
- A heuristic model is proposed to describe the mechanism of the early-stage electrocrystallization of Cu on a polycrystalline Au seed layer. The heterogeneous nucleation phenomenon, the competitive growth both longitudinally and laterally, and the dominant growth of some nuclei were experimentally observed, which also validates the relevant KMC simulation results.
- A detailed characterization of electroplated micro- copper columns in terms of their external morphology, cross-sectional microstructure and crystal structure has been carried out. It was found that the recrystallization accompanying growth and the spontaneous self-annealing after plating played important roles in the formation of the final microstructure of a bi-modal or tri-modal grain size distribution. A size effect on the microstructure of copper columns was observed and attributed to its effect on the recrystallization during and/or after plating.

Chapter 2 Electrodeposition and Electrocrystallization

This chapter presents a literature review on the fundamental issues and experimental studies relating to electrodeposition and electrocrystallization that are relevant to the scope of this thesis. The purpose of this chapter is twofold. 1) It provides readers with a generic review of fundamentals on electrodeposition and electrocrystallization which are necessary to understand this thesis. 2) it serves as an expansion of the introduction of the background knowledge and scientific context of this PhD research.

2.1 Electrodeposition

2.1.1 Definition

Electrodeposition was invented by an Italian chemist, Luigi Brugnatell, who applied the electrodeposition process to plate gold for the first time in 1805 [23]. Electrodeposition is a process of producing a coating, usually metallic, on a conductive surface by the action of electric current. Fig. 2-1 shows a schematic of a basic electroplating cell for plating metal 'Me' from a solution of the metal salt 'MeA'. The deposition of Me onto a substrate (the cathode) is achieved by reducing the Me^{n+} ions to metallic form. The reaction was sustained by a continuous supply of electrons and M^{n+} ions at the electrode by a power supply. Me^{n+} ions are transported to the electrode by diffusion, convection of electrolyte and electro-migration.

Electrodeposition is exceptionally versatile, and valuable applications keep being invented. There has been an upsurge of interests in electrodeposition since the growth of the microelectronic industry.

2.1.2 Cu Electrodeposition in Microelectronics

Electrodeposition technology has been widely applied in electronic industry to fabricate a variety of coatings such as conductive, solderable, information carrier, electromagnetic shielding, electronic functional coatings, PCB plating, protection of electronic components, and decorative coating of electronic products.

Three main attributes of electrodeposition make it well suited for nano- and micro-technologies [24]. Firstly, it can be used to grow functional material through complex 3D masks. Secondly, it can be performed near room temperature from a water-based electrolyte. Finally, it can be scaled down to the deposition of a few atoms up to macroscopic dimensions. Electrodeposited flip-chip solder C4 (Controlled Collapse Chip Connection) connections were introduced in 1995 as the first application of electrodeposition on a semiconductor chip [24-25]. Fig. 2-2 shows a SEM image of electrochemically fabricated flip-chip interconnects. This technology offers significant cost, reliability and performance advantages over the previously used evaporation technology. Electrodeposition has also been used to produce various micro-bumps of e.g. Au, Ni, Cu etc [19, 26]. The packaging technology for Intel's forthcoming 45 nanometre (nm) high-k metal gate family of processors uses an electroplated copper column bump and a Sn-Ag-Cu solder alloy to replace the previously used Sn-Pb solder alloy to attach a silicon die to a package substrate [20].

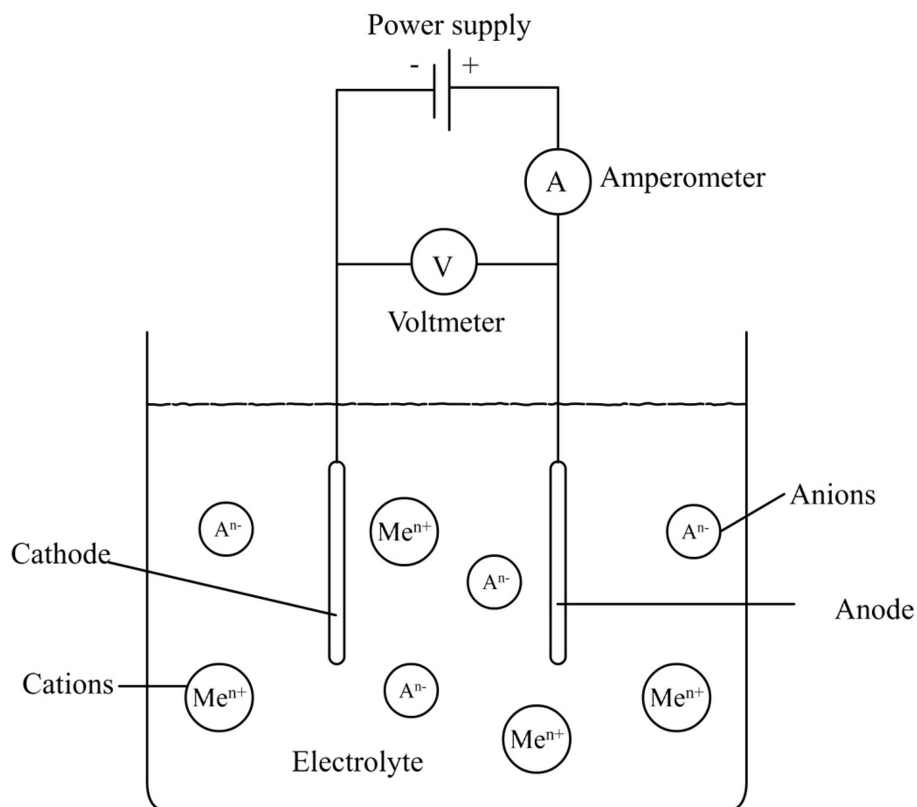

Fig. 2-1 A schematic of an electrolytic cell for plating metal "Me" from a solution of the metal salt "MeA".

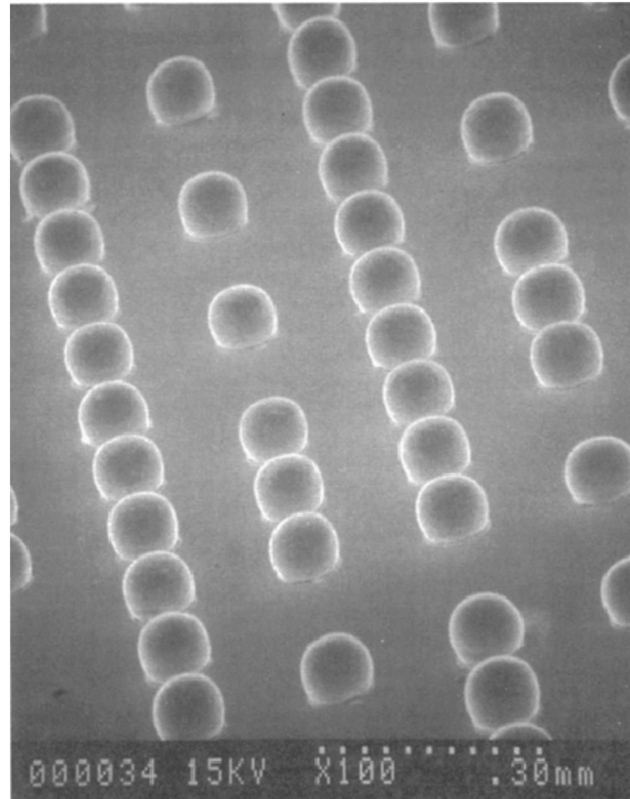

Fig. 2-2 An array of reflowed C4s fabricated by electrodeposition [25] (Reproduced by permission of The Electrochemical Society)

In 1997, copper interconnect technology was introduced in semiconductor manufacturing to replace aluminium for creating circuitry on silicon wafers [27]. Today, copper metallization is being used in every major semiconductor fabrication facility in the world. The implementation of Cu wiring resulted in a 40-50% drop in resistance, a 20-30% anticipated boost in chip performance, a substantial improvement in electromigration resistance and a 10-15% lower chip cost. Fig. 2-3 shows an SEM image of IBM's six-level copper interconnect technology.

3D packaging is the one of the hottest topics in the community of electronic packaging. 3D chip integration using TSV is considered to be one of the most advanced and promising technologies for next-generation packaging solutions [14, 28]. Electrodeposition of Cu can fill high-aspect-ratio features without defects, such as seams and voids, which makes electrodeposition of copper one of main approaches for filling TSVs.

Electrodeposition is also emerging as a uniquely capable method for nano-fabrication. It is anticipated to play important roles in future nano-electronic fabrication.

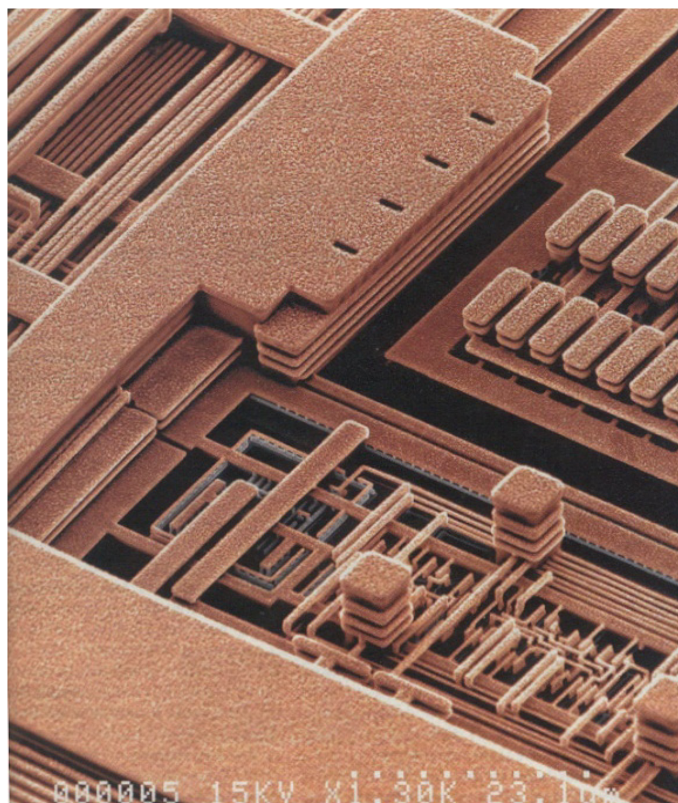

Fig. 2-3 IBM's six-level copper interconnect technology [29](Figure reprinted with permission from IEEE © 1999 IEEE)

2.2 Self-annealing of electrodeposited Cu

In the last decade, recrystallization of electroplated copper film during storage at room temperature, also termed self-annealing, has drawn increasing concern [4-11]. It is often accompanied by four typical phenomena, namely resistance drop, stress relaxation, microstructural evolution and evolution of crystal structure.

2.2.1 Resistance drop and stress relaxation

This typically causes up to a 20% decrease of deposit resistance and considerable stress relaxation within hours, or days, depending on the thickness of the deposit and deposition parameters, as illustrated in Fig. 2-4 as one of the many examples [21-22, 30-32].

Xu et al. [33] performed in-situ measurement of the stress during high-frequency pulse plating of copper and found periodical stress increases and drops during the pulse-on

and pulse-off time, respectively. Fig. 2-5 shows the stress thickness and the average film stress as a function of the deposition time. The stress thickness evolves in sync with the pulse current cycles. It was found that the stress was generated during the pulse-on periods and partially relaxed during the pulse-off periods and the stress relaxation of each off cycle is a miniature version of the overall stress response, i.e. high tensile stress followed by partial relaxation. It was proposed that the stress relaxation during the pulse-off periods is a consequence of nano-twin formation during pulse electrodeposition.

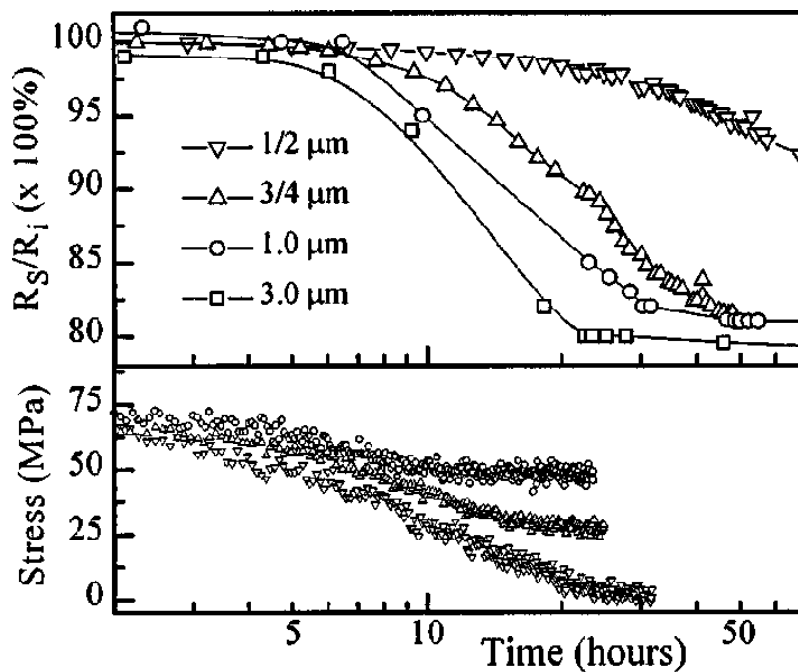

Fig. 2-4 Sheet resistance (top) and stress (bottom) of the electroplated Cu layers as a function of time after deposition for four and three values of the layer thickness, respectively.[32][ii]

[ii] Reprinted with permission from Brongersma, S.H., et al., Two-step room temperature grain growth in electroplated copper. Journal of Applied Physics, 1999. 86(7): p. 3642-3645.Copyright [1999], American Institute of Physics.

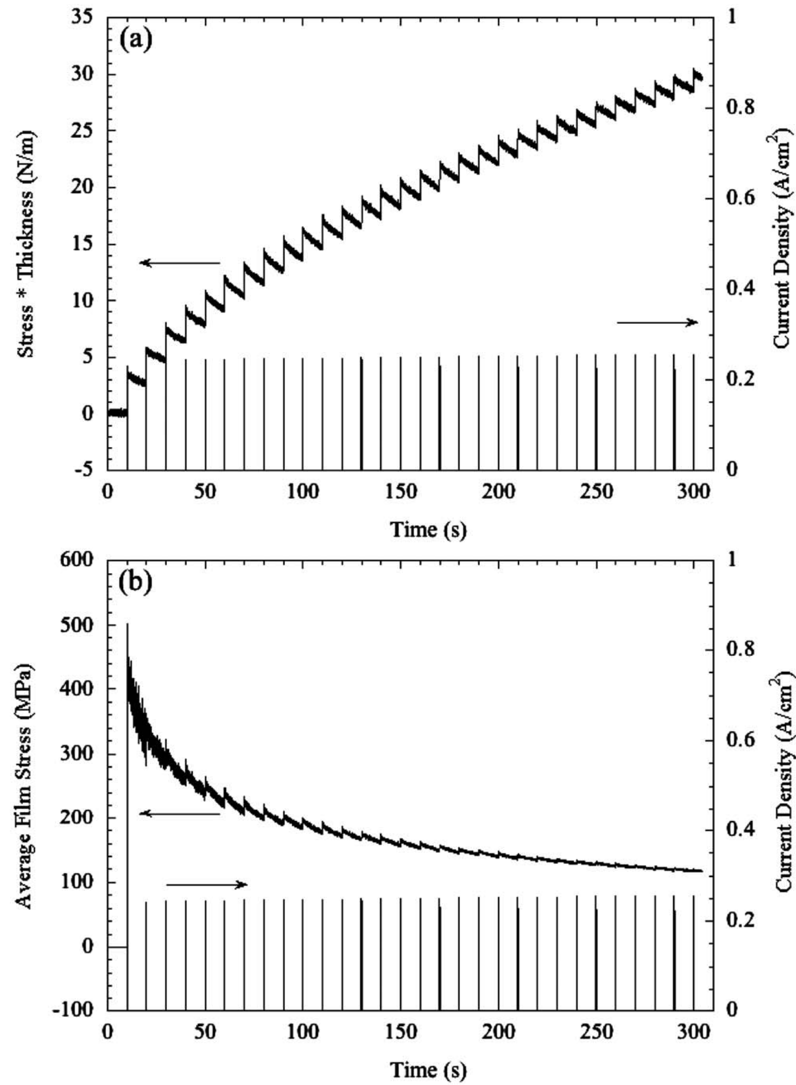

Fig. 2-5 The evolution of (a) deposit stress thickness and (b) average film stress as a function of pulse deposition time. [33][iii]

2.2.2 Microstructural evolution

One of the typical features of microstructural evolution is the secondary grain growth, that is, growth of large grains in the matrix of small grains which usually results in bi-modal grain size distribution in the case of an incomplete transformation. Brongersma et al. [32] proposed a two-step grain growth mechanism based on experimental observations on the FIB cross-sectional microstructure of plated copper. Two steps refer to a very rapid crystallization that occurs from the top surface down, immediately after

[iii] Reprinted with permission from Journal of Applied Physics, 105(2), Xu, D., et al., In situ measurements of stress evolution for nanotwin formation during pulse electrodeposition of copper. 2009. p. 023521-6. Copyright [2009], American Institute of Physics.

deposition, followed by a slower lateral recrystallization resulting in large secondary grains. Yin et al.'s finding [34], however, was the opposite, in that the microstructure transformation started and nucleated from the bottom of the deposit near the deposit/substrate interface and then propagated towards free surfaces. Hau-Riege et al. [35] performed in situ TEM observation of the grain growth in free-standing electroplated copper films at room temperature, starting minutes after the plating process. The results, as shown in Fig. 2-6, seem to suggest that the observed twins (see also section 2.3) are attributed to recrystallization.

2.2.3 Evolution of crystal structure

Crystal structure also evolves due to self-annealing. Detavernier et al. [30] reported that Cu(111) peaks became much narrower and underwent a splitting into CuKα1 and CuKα2 components during storage, as illustrated in Fig. 2-7. The authors ascribed the phenomena to the decrease of defect density of the plated film. Pantleon et al. [36] found the similar phenomenon of peak splitting in both Cu (111) and Cu (200) peaks. Additionally, they performed detailed and quantitative analyses of the grain size, the grain orientation and the grain boundary characters of self-annealed copper films of different thickness using in-situ XRD and EBSD [36-38]. One of the major conclusions was that the crystallographic texture of electrodeposits changes as a result of multiple twinning during self-annealing and more pronounced twinning occurred for thicker film.

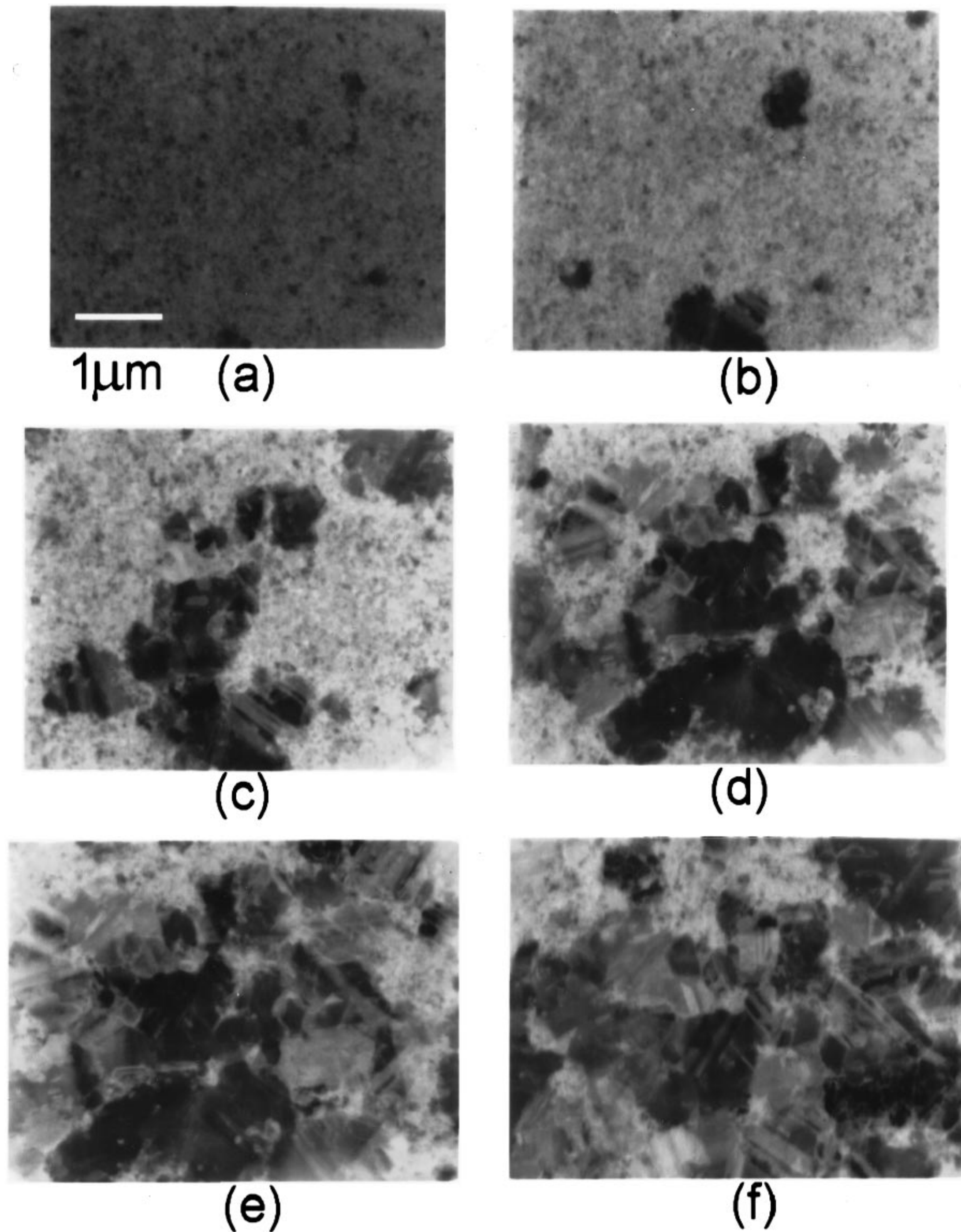

Fig. 2-6 Series of TEM micrographs for a 0.3 mm thick electroplated Cu film transforming at room temperature (a) t=11 min, (b)t=1 h, (c) t=2.5 h, (d) t=8 h, (e) t=23.5 h, (f) t=80 h. After t=80 h, no further transformation took place. [35][iv]

[iv] Reprinted with permission from [Hau-Riege, S.P. and C.V. Thompson, In situ transmission electron microscope studies of the kinetics of abnormal grain growth in electroplated copper films. Applied Physics Letters, 2000. 76(3): p. 309-311]. Copyright [2000], American Institute of Physics.

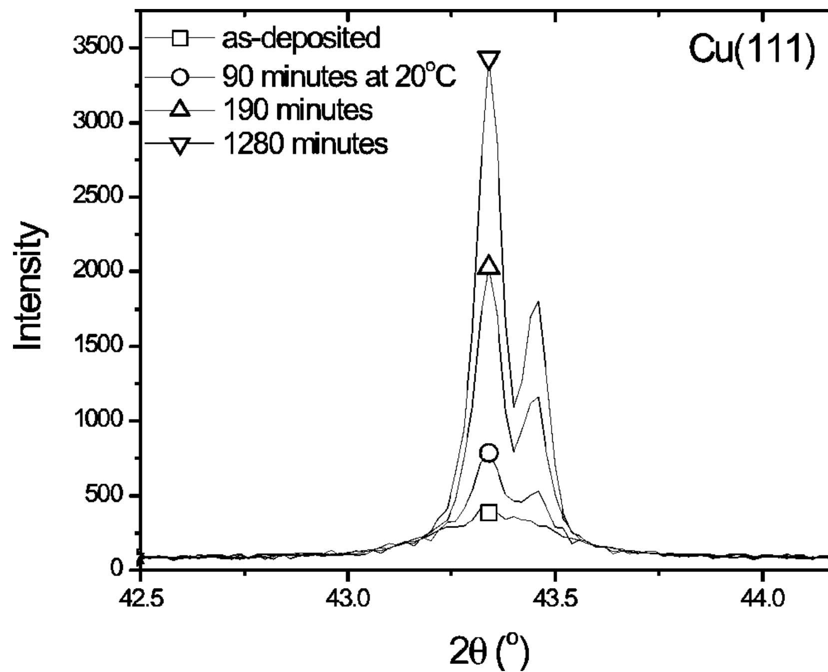

Fig. 2-7 X-ray diffraction showing the Cu (111) peak for a 970 nm thick electroplated film. The time during which the film was stored at room temperature is indicated. [30] [v]

2.2.4 Driving force

What is the driving force behind these intriguing phenomena? Harper et al. [31] proposed that grain boundary energy in fine-grained as-deposited films was the driving force for self-annealing. They observed a period of incubation time before recrystallization and attributed it to Ostwald ripening of the pinning species along grain boundaries. The subsequent unpinning of certain grain boundaries led to rapid secondary grain growth. Detavemier et al. [30] studied the thermodynamics and kinetics of microstructural evolution in copper films by estimating the magnitude of possible driving forces including grain boundaries, stacking faults, dislocations, surface energy, elastic strain and Zener pinning, as summarized in Table 2-1 . They concluded that a high density of dislocations and/or stacking faults is the primary driving force for self-annealing while Zener pinning by impurities from the plating bath is not crucial, although it may strongly influence the kinetics (e.g. the incubation time). Hau-Riege et al. [35], however, proposed that impurities play important roles in self-annealing of electroplated copper films. First, the normal growth of grains in an untransformed

[v] Reprinted with permission from [Detavernier, C., et al., Thermodynamics and kinetics of room-temperature microstructural evolution in copper films. Journal of Applied Physics, 2003. 94(5): p. 2874-2881]. Copyright [2003], American Institute of Physics.

matrix is impaired by solute drag due to the impurities. The resulting stabilized small grain size contributes to a high driving force for self-annealing. Second, impurity rejection contributes to the energy which drives the transformation to a large-grained structure. Third, accumulation of rejected impurities at the perimeters of growing grains can slow down the rate of transformation. Pantleon et al. [36-38] believed that their EBSD results, together with in-situ XRD analysis, had confirmed multiple twinning in copper electrodeposits as a mechanism for microstructural evolution at room temperature.

Table 2-1 Overview of the estimated driving force ΔG for microstructural evolution related to different sources of stored energy in the as-deposited film. [30] [vi]

Mechanism	Equation	Assumption	ΔG in J/cm^3
Grain boundaries	$E_{\mathrm{GB}} = \frac{3\gamma}{2R}$	$R = 50$ nm; $\gamma = 0.625$ J/m^2	≈20
Stacking faults	$E_{\mathrm{SF}} = \frac{\gamma_{SF}}{nd_{111}}$	$n = 3 - 20$; $\gamma_{SF} = 0.078$ J/m^2	≈150 -20
Dislocations	$E_{\mathrm{disl}} = 1/2\rho G b^2$	$\rho = 10^{12} - 10^{13}/cm^2$	≈15-140
Surface energy	$E_{\mathrm{surf}} = -2\Delta\gamma/h$	$h = 500$ nm	≈0.05
Elastic strain	$E_{\mathrm{strain}} = \epsilon^2(F(111) - F(100))$	$\epsilon = 0.2\%$	≈2
Zener pinning	$E_{\mathrm{Zener}} = \frac{3\gamma\rho_p}{2r}$	$\rho_p = 0.2\%; r = 0.1$ nm	≈-20

2.2.5 Kinetics

An incubation time of a few hours was observed before the onset of self-annealing [31, 34]. Once it begins, the rate of microstructural transformation remains nearly constant until the end of the process [34]. A number of factors have been found to have effects on the kinetics of self-annealing.

[vi] Reprinted with permission from [Detavernier, C., et al., Thermodynamics and kinetics of room-temperature microstructural evolution in copper films. Journal of Applied Physics, 2003. 94(5): p. 2874-2881]. Copyright [2003], American Institute of Physics.

It has been widely accepted that deposit thickness strongly influences the kinetics of the self-annealing of a film [21, 30-32, 36]. Generally, the thicker the deposit, the faster the self-annealing; when it is less than a critical value, e.g. 250 nm [30] no self-annealing can be observed at all. Harper et al. [31] proposed a simple model to describe the inverse dependence of transformation time on deposit thickness: $\tau - t_0 = k/(d - d_0)$, where τ is the transient time (the time for half of the resistivity decrease of the deposits to occur), d thickness, t_0 incubation time and d_0 minimum thickness. The model was used to estimate the incubation time and critical minimum thickness. The function is shown as a solid line in Fig. 2-8 with an estimate of incubation time (t_0=5.5h) and minimum thickness (d_0=0.23 μm) for the data presented by Gignac et al. [39].

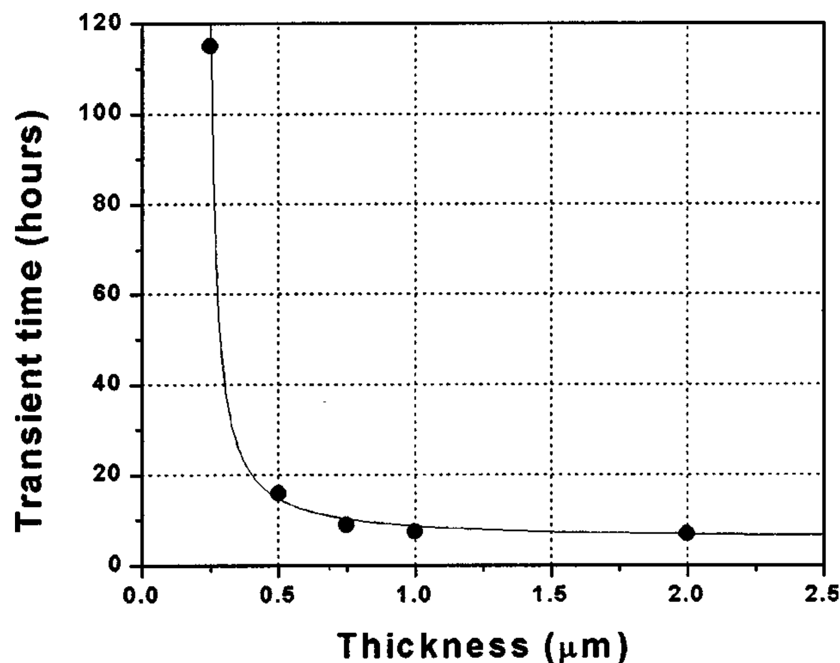

Fig. 2-8 Transient time vs film thickness showing data point from Gignac et al. [39] and the function τ - t_0 = k / (d - d_0) with τ=2.5, t_0 = 5.5h, and d_0 = 0.23. [31][vii]

Yin et al. [34] described the transformed fraction as a function of self-annealing time using the Avrami equation and obtained the Avrami constants, from which it was inferred that 3D growth and nucleation saturation has occurred.

[vii] Reprinted with permission from [Harper, J.M.E., et al., Mechanisms for microstructure evolution in electroplated copper thin films near room temperature. Journal of Applied Physics, 1999. 86(5): p. 2516-2525]. Copyright [1999], American Institute of Physics.

Deposition parameters e.g. current density, also have effects on the self-annealing kinetics. It was found [40] that the microstructures of self-annealed Cu deposits obtained at different current density looked similar while the transformation rate for the high current density (32 mA/cm^2) sample was much higher than at the lower current density (8 mA/cm^2).

Plating bath additives are critical to the self-annealing kinetics. Brongersma's group [21, 32] concluded that organic additives in a plating bath were necessary for self-annealing to occur, but slowed down the process for higher concentration. Vas'ko et al. [41] reported that self-annealing occurred only if both the two organic additives the 3-N,N-dimethylaminodithiocarbamoyl-1-propanesulphonic acid (DPS) and polyethylene glycol (PEG) were present in the plating bath. It is worth noting that all the above-reviewed work in which self-annealing phenomena were experimentally observed, used commercial copper plating bath or lab-made solutions which normally contain organic additives.

The kinetics of self-annealing of electroplated Cu damascene trenches were studied and it was found that the topography, or geometry, of the trench, e.g. trench width and spacing, has an influence on the recrystallization [22].

To sum up, the driving force behind the self-annealing of electroplated copper remains controversial. Whether it occurs during plating has not been confirmed. Most of the above-reviewed work concerned electroplated copper films. Since the microstructural transformation is direction-selective, the shape of plated samples is anticipated to affect the self-annealing process. The growth and recrystallization with respect to cylindrical interconnects such as copper columns and through-wafer interconnects has not been reported.

2.3 Nano-twinning in electrodeposited Cu

Crystal twinning occurs when two seperate crystals share some lattice points in a symmetric manner. Such crystals are referred to as twin crystals and they are separated by a twin boundary, as illustrated in Fig. 2-9. The growth of twins is often observed in electrodeposited copper because of the low stacking fault energy in copper[42-43].

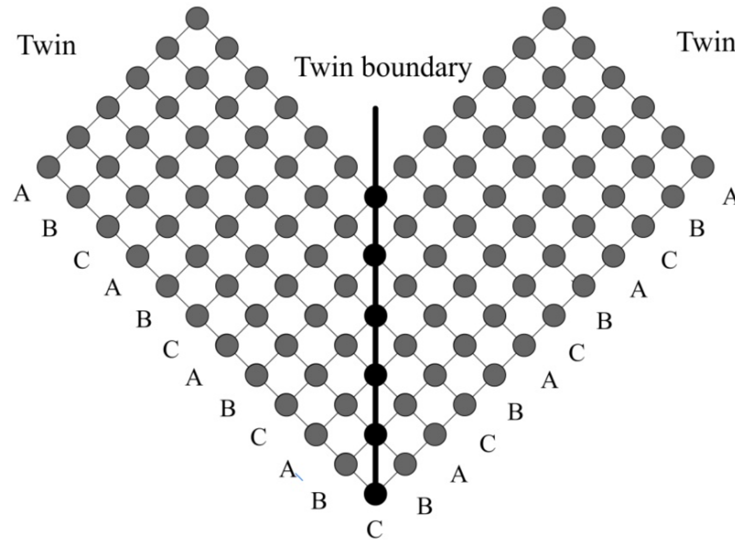

Fig. 2-9 Schematic of twin crystals and twin boundary

Over the last decade, nano-twinned copper synthesized by electrodeposition has attracted considerable attention [4-5, 14, 33, 44-49]. Fig. 2-10a shows a TEM image of typical nano-twins in a copper film produced by pulse plating. Such copper films with a high density of nano-twins present very attractive mechanical and electrical properties e.g. ultrahigh tensile strength [4-5, 50] (Fig. 2-10b), comparable electric conductivity (Fig. 2-10c) [4, 14] and excellent plasticity (>13% plastic strain) [5, 44]. In deformed nano-twinned copper samples, many dislocations were observed at twin boundaries and grain boundaries. It indicates that the ultrahigh strength originates from effective blockage of dislocation motion by numerous coherent twin boundaries [4-5]. It was found that nano-twinned copper had better thermal stability and did not undergo much self-annealing, compared to copper films without twins [48]. Chen et al [51] observed electromigration-induced atomic diffusion in the twin-modified grain boundaries using in situ ultra-high-vacuum and high-resolution transmission electron microscopy. The triple point where a twin boundary meets a grain boundary was found to slow down grain-boundary and surface electromigration by one order of magnitude. It indicates nano-twinned copper has good resistance to electromigration. A combination of high strength, good resistance to electromigration, excellent plasticity and comparable conductivity makes nano-twinned electroplated copper a great choice for electronic interconnection. L. Xu et al [14] fabricated high aspect ratio and ultrafine pitch through-wafer copper interconnection columns by pulse electroplating. Ultrafine copper grains with nanoscale

twins (twin lamellar width <20 nm) were obtained in the copper columns. The average resistance of one individual copper column ranged from 0.005 to 0.12 Ω, which is two orders lower than the interconnect of wire bonding (1 Ω/via).

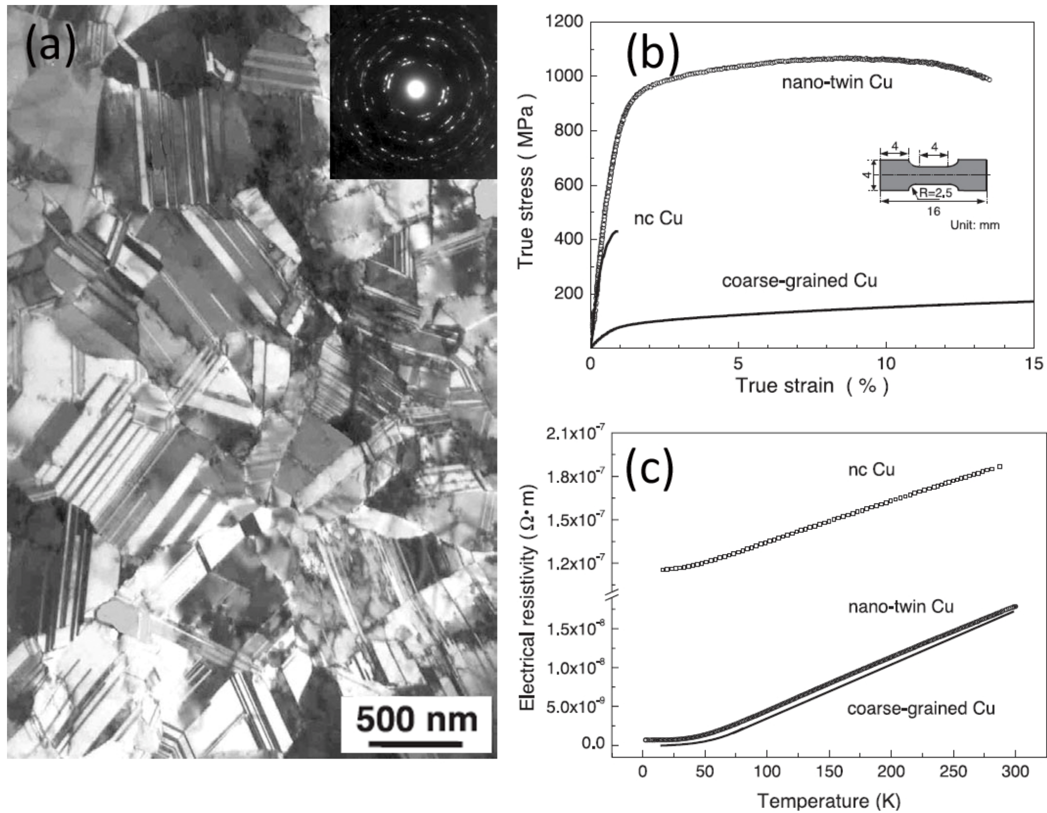

Fig. 2-10 (a) A bright-field TEM image and the electron diffraction pattern (inset) show roughly equiaxed sub-micrometer-sized grains with random orientations separated by high-angle grain boundaries. (b) A typical tensile stress-strain curve for the as-deposited Cu sample with nano-twins in comparison with that for a coarse-grained polycrystalline Cu sample and a nano-crystalline Cu sample (mean grain size ~30 nm). (c) Resistivity of nano-twinned copper compared to coarse-grained and nano-crystalline copper. [4] [viii]

D. Xu et al [33, 46-47]proposed that nano-twins can be formed during Cu film deposition if the deposition introduces a large strain/stress in the film, followed by a relaxation of strain/stress. Pulse electrodeposition can provide such strain/stress evolution during deposition. During the pulse-on time period, the growth of copper grains introduces an increasing tensile stress. During the pulse-off time period, Cu grains have a period of time to undergo structure rearrangement such as recrystallization and grain growth, in

[viii] From [Lu, L., et al., Ultrahigh Strength and High Electrical Conductivity in Copper. Science, 2004. 304(5669): p. 422-426]. Reprinted with permission from AAAS.

order to stay in a lower energy status. Total energies of fcc Cu and periodic nano-twinned Cu were estimated using first-principle total energy calculations. It was found that the strain-relaxed nano-twinned Cu is energetically more stable than the strained fcc Cu. In-situ stress measurement of a copper film during pulse plating was performed and an abrupt increase of the tensile force was detected for each potential pulse, followed by a relaxation of the force during the pulse-off time [33].

2.4 Electrocrystallization

2.4.1 Definition

The term 'electrocrystallization' was coined by Fischer[52] in the 1940s to describe a crystallization process in which mass transfer is accompanied by charge transfer. It has also been described as a 'phenomenological field of electrochemistry' [53] or a particular case of a first order phase transition or electrochemical kinetics [54-55]. Electrocrystallization is an interdisciplinary subject involving Electrochemistry, Nucleation and Crystal Growth. From this point of view, it is better defined as nucleation and crystal growth in electrochemical systems under the influence of an electric field [54-63].

2.4.2 Basic processes

Electrocrystallization of metal takes place at an interface between an electronic conductor (metal electrode) and an electrolyte. Fig. 2-11 illustrates the steps involved in the process of electrocrystallization, taking Cu as an example. The steps are described as follows [60]:

- The solvated cupric ions from the bulk electrolyte are transported to the cathode/electrolyte interface via convective diffusion through the diffusion layer;
- The cupric ions then lose their hydration molecules and are adsorbed to the cathode surface and become ad-ions;
- Cu atoms are deposited onto the electrode surface by electron transfer and become adatoms;
- Cu adatoms diffuse across the surface to more stable sites;
- Nucleation, cluster growth and grain growth.

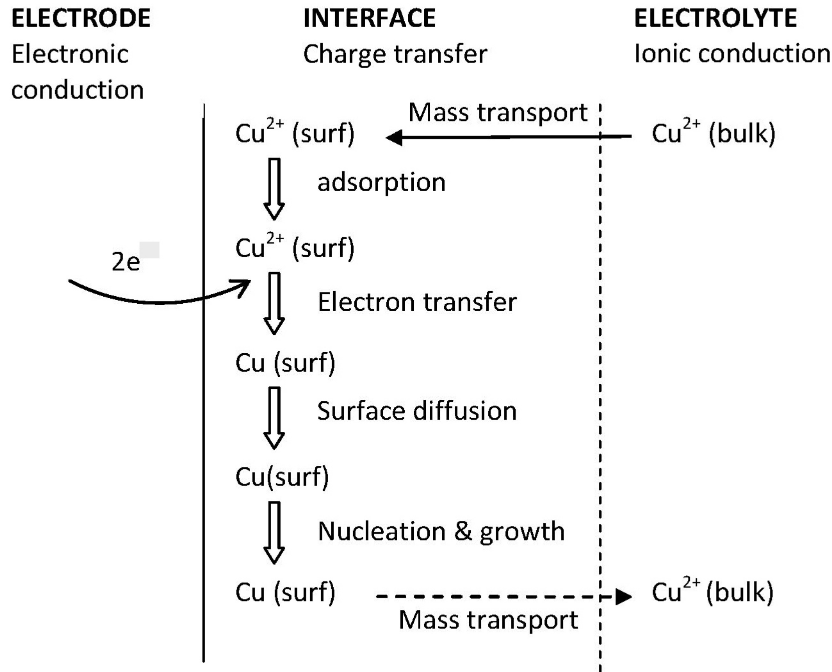

Fig. 2-11 Steps involved in the process of electrocrystallization. The cathodic reaction Cu^{2+} + 2e→ Cu is schematically considered.

2.4.3 Thermodynamic aspect

The thermodynamic equilibrium of a $\mathrm{Me/Me^{n+}}$system can be described by Nernst equation [55-56, 64]given by:

$$E_{Me/Me^{n+}} = E^{0}_{Me/Me^{n+}} - \frac{RT}{nF}\ln\left[\frac{a_{Me^{n+}}}{a_{Me}}\right] \tag{2.1}$$

$E_{Me/Me^{n+}}$ is the Nernst equilibrium potential of the Me/Me^{n+} electrode; $E^{0}_{Me/Me^{n+}}$ denotes the standard electrode potential of Me/Me^{n+}, and $a_{Me^{n+}}$ is the activity of the solvated Me^{n+} ions in the electrolyte. For pure bulk Me phase, a_{Me} is equal to unity.

The driving force for Me electrocrystallization is the overpotential, η_c, of the Me/Me^{n+} electrode, which was defined by Vetter [58] :

$$\eta_c = E - E_{Me/Me^{n+}} = -\frac{RT}{nF}\ln\left[\frac{a_{Me_{ads}}}{a_{0,Me_{ads}}}\right] \tag{2.2}$$

where $a_{Me_{ads}}$ and $a_{0,Me_{ads}}$ stand for the activities of Me_{ads} at $E \neq E_{Me/Me^{n+}}$ and $E = E_{Me/Me^{n+}}$, respectively. Metal Me deposition occurs at a cathodic

overpotential, $\eta_c < 0$, while Me dissolution takes place at an anodic overpotential, $\eta_c > 0$. In the case of deposition of Me on a foreign substrate S, under certain conditions, the Me deposition can occur at underpotential, i.e. $\eta_c < 0$. Underpotential deposition (UDP) and overpotential deposition (OPD) of Me on S are associated with the formation of 2D (monolayer) and 3D (cluster or bulk) Me phases, respectively. Usually, the interactions between the substrate S on deposit Me for OPD deposition becomes negligible after about twenty monolayers.

Electrodeposition of metal on a foreign substrate follows different growth modes depending on the Me-S binding energy and the crystallographic misfit between the substrate S and the 3D Me bulk deposit as schematically illustrated in Fig. 2-12 [57, 65-67]. When the binding energy between a Me adatom Me_{ads} and a substrate atom S $\Psi_{Me_{ads}-S}$ is lower than that between Me_{ads} and Me $\Psi_{Me_{ads}-Me}$, it follows the Volmer-Weber or 3D island growth mode independent of crystallographic misfit as shown in Fig. 2-12(a). When the binding energy $\Psi_{Me_{ads}-S}$ is higher than $\Psi_{Me_{ads}-Me}$, it could follow either the Frank-van de Merwe (or layer-by-layer) growth mode up to the disappearance of the strong Me-S attraction, followed by Me-on-Me growth, or the Stranski-Krastanov growth mode for negligible crystallographic Me-S misfit and significant misfit, respectively.

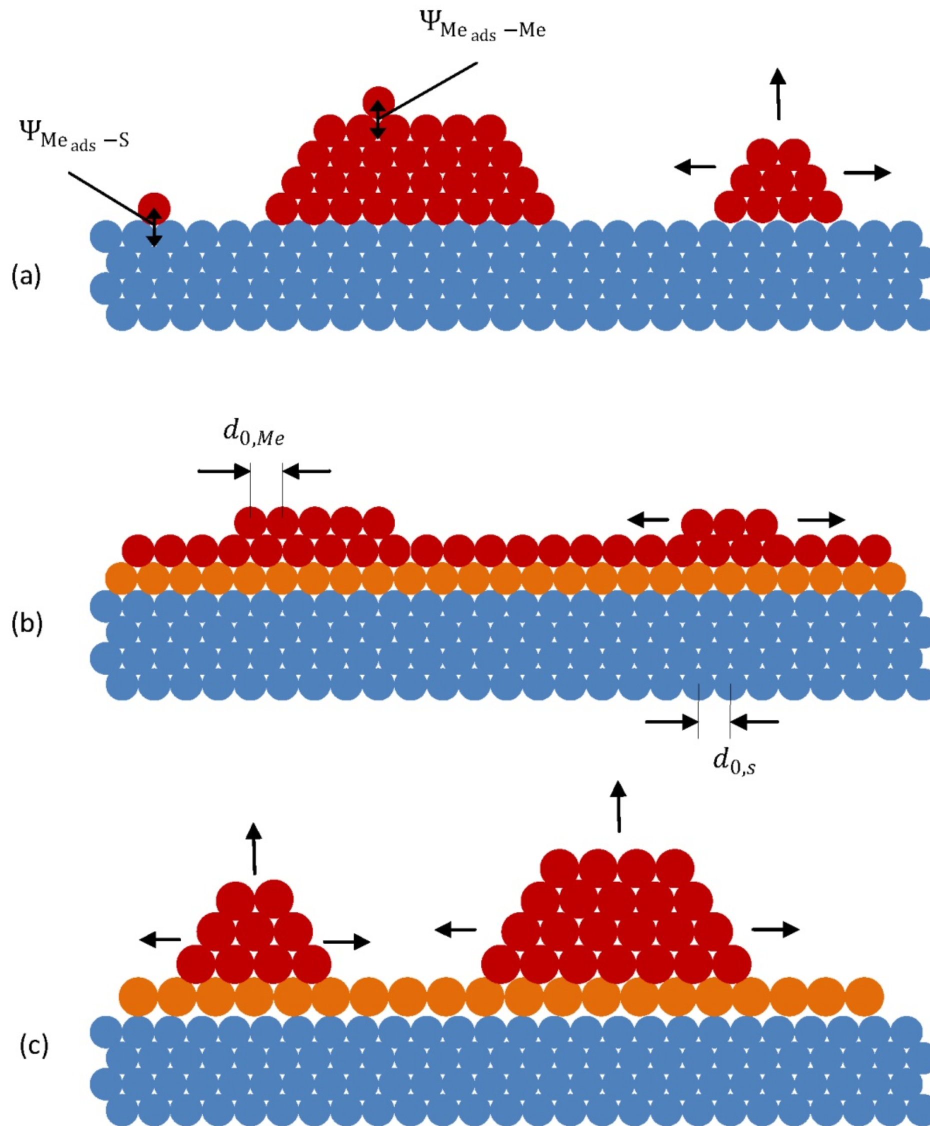

Fig. 2-12 Schematics of different growth modes for metal (Me) deposition on foreign substrate (S) depending on the binding energy ψ and on the crystallographic misfit characterized by the interatomic distances d_0 . (a) "Volmer-Weber" growth mode (3D island formation) for $\Psi_{Me_{ads}\text{-}S} \ll \Psi_{Me_{ads}\text{-}Me}$ independent of the ratio $(d_{0,Me} - d_{0,S})/ d_{0,S}$. (b) "Frank-van der Merwe" growth mode (Me layer-by-layer) formation for $\Psi_{Me_{ads}\text{-}S} \gg \Psi_{Me_{ads}\text{-}Me}$ and ratio $(d_{0,Me} - d_{0,S})/ d_{0,S} \approx 0$. (c) "Stranski-Krastanov" growth mode (3D Me island formation on top of pre-deposited 2D Meads overlayers on S for $\Psi_{Me_{ads}\text{-}S} \gg \Psi_{Me_{ads}\text{-}Me}$ and $(d_{0,Me} - d_{0,S})/ d_{0,S} < 0$ (negative misfit).[ix] [56]

[ix] E. Budevski: Electrochemical Phase Formation And Growth: An Introduction To The Initial Stages Of Metal Deposition. 410. 1996. Copyright Wiley-VCH Verlag GmbH & Co. KGaA. Reproduced with permission.

2.4.4 Nucleation theories

Theoretical expressions for stationary nucleation rate was firstly derived by Volmer and Weber [68], Farkas [69]and Kaischew and Stranski [70-72]. Becker and Döring [73], Zeldovich [74]and Frankel [75]did more rigorous treatments by a discrete and a continuous approach, respectively. Walton employed an atomistic approach deriving an explicit expression for the stationary nucleation rate valid for small critical nuclei to overcome the quantitative contradiction between the classical nucleation theory and the experimental results. Details about the kinetics of electrochemical nucleation can be found in a number of books [55-56] and review articles [54, 59, 61, 63]. F. Sagues et al [62]made a review on morphologies and corresponding growth dynamics observed in quasi-two-dimensional electrocrystallization. Simulations of electrocrystallization will be reviewed in the next two chapters.

2.4.5 Experimental studies of Initial stages of electrocrystallization

With the advent of Scanning Tunnelling Microscope (STM) and its application in electrochemistry, it is possible to observe the initial stage of metal deposition in situ. Copper deposition on Au (111)[76-78], Au (100) [79]and on polycrystalline Au [80]was among the first systems to be studied. The UPD of Cu on Au (111) is illustrated in Fig. 2-13, showing the cyclic voltammogram and an image of the gold electrode obtained at a potential between peak A and B. It was found that an ordered layer of Cu and co-adsorbed sulphate ions formed during the first step (peak A). The resultant $(\sqrt{3} \times \sqrt{3})R30°$ structure was observed by in-situ XRD[81], STM[82-84] and AFM[85]. This structure has now been widely employed as a standard in electrochemical STM. It should be noted that such structure was only observed in sulphate-containing electrolyte. During the second step (Peak B), a full monolayer of copper on gold is formed.

In the case of bulk copper deposition on Au (111), the deposition of a full monolayer of Cu at underpotential is followed by three-dimensional growth, which conforms to the Stranski-Krastanov mode. At a lower overpotential e.g. -185mV, nucleation takes place almost exclusively at atomic step edges as shown in Fig. 2-14a. This phenomenon has been found in a number of publications [76-77, 79, 86]. At a higher overpotential e.g. -

300mV, nucleation occurred on terraces as well as step edges and much larger and higher clusters were observed as shown in Fig. 2-14b [56, 87].

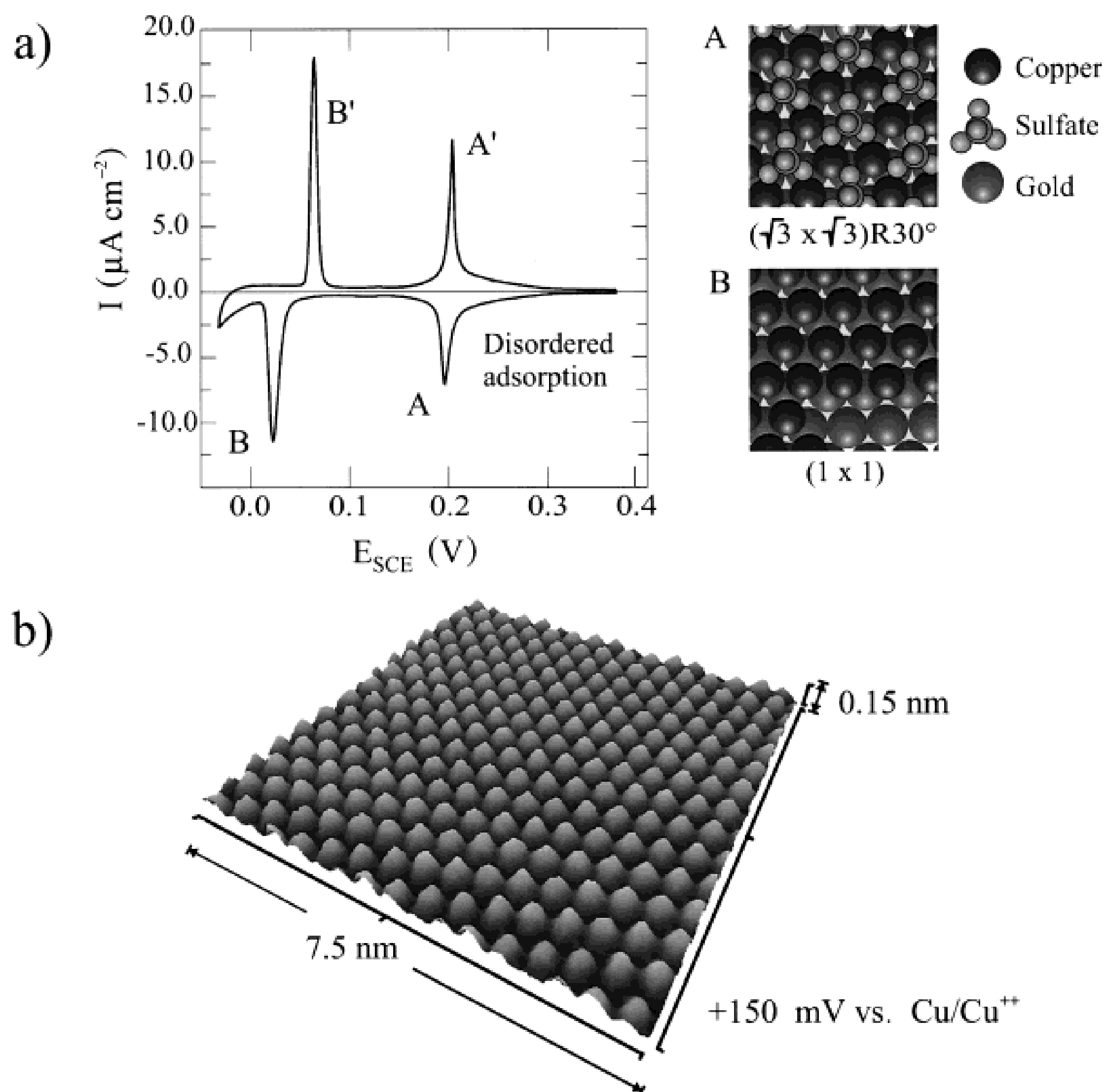

Fig. 2-13 a) Cyclic current-potential curve for the UPD of Cu on Au (111) in 0.05M H_2SO_4 + 1mM $CuSO_4$. Scanning rate: 1mV/s. b) STM image of Au (111) at 150mV versus Cu/Cu^{2+} in 0.1M H_2SO_4 + 1mM $CuSO_4$. [88][x]

[x] [Schneeweiss, M.A. and D.M. Kolb, The initial stages of copper deposition on bare and chemically modified gold electrodes. Physica Status Solidi a-Applied Research, 1999. 173(1): p. 51-71] Copyright Wiley-VCH Verlag GmbH & Co. KGaA. Reproduced with permission.

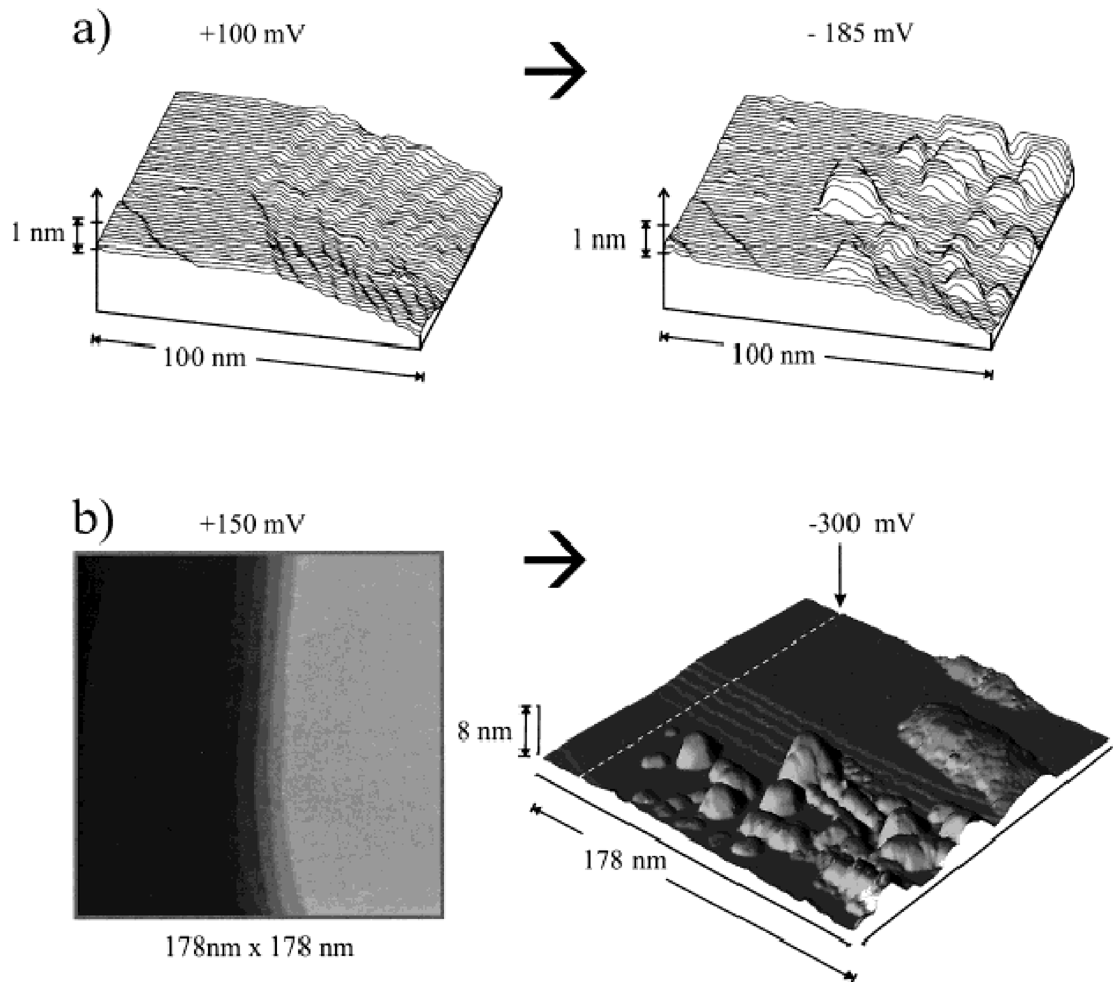

Fig. 2-14 a) STM images of Au(111) in 5mM H_2SO_4 + 0.05mM $CuSO_4$ at +0.1 V and -0.185 V versus Cu/Cu^{2+}. Nucleation and growth occurs almost exclusively at step edges. b) Au (111) in 0.1 M H_2SO_4 + 1mM $CuSO_4$ at 0.15 and ±0.3 V, respectively. At higher overpotential nucleation and growth sets in also on terraces. [56, 76, 88] [x]

Nichols et al [78]studied deposition of Cu on different substrates including gold, polypyrrole and gold which has been pre-covered with a multi-layer copper film using in-situ STM. The results indicate that substrates and organic additives have profound effects on the growth modes. Fig. 2-15 shows a STM image of a gold film at -200mV (versus Cu/Cu^{2+}) in an additive-free acidic copper sulphate solution. The growth morphology can be interpreted by the Stranski-krastanov growth mode. The Cu monolayers are formed at underpotential due to strong Cu-Au bonds and large lattice misfit. After that, 3D copper clusters, which generally nucleate at defect sites e.g. steps formed on top of the monolayers. With the presence of organic additives in the electrolyte, however, the growth morphology is quite different. Fig. 2-16 shows the STM

image of copper deposition on a gold film in an additive-containing solution. An ultra-thin copper film (typical multi-layers of 4-7 monolayers thick) is formed on top of the UPD monolayer. It grows laterally at a nearly constant height across the surface. It indicates that the organic additive inhibits the upward growth of the copper clusters in favour of their lateral growth. This supports the Frank-Van der Merwe growth mode. Not only organic additives can change the growth mode, but substrate orientations have significant influences on growth mechanism. For example, the bulk Cu deposition on Au (100) also follows the Frank-van der Merwe growth mode [89]. The copper follows the Au (100) structure up to several layers despite a large lattice mismatch of about 13%. The in-situ XRD measurements show the growing phase is body centred cubic (bcc) rather than face centred cubic (fcc) [88]. After ten layers, it begins to transit to fcc-like copper and a striped structure appears. Such behaviour were also observed for the analogous system of Cu on Ag (100) [90]. Volmer-Weber growth has been observed for Cu deposition on a polypyrrole substrate both in the presence or absence of organic additives, as shown in Fig. 2-17[78]. The interaction between the polypyrrole substrate and Cu is relatively weak, which favours the 3D island growth. In such a case, the effects of organic additives are not strong enough to promote a quasi-2D growth.

Grujicic and Pesic [91] studied the nucleation mechanism for copper deposition on a glassy carbon substrate using electrochemical techniques (cyclic voltammetry and chronoamperometry) and AFM. It was found that copper concentration, deposition potential, solution pH and the presence of a background electrolyte all had profound effects on the nucleation mechanisms of copper on the glassy carbon surface. An increase of pH and copper concentration results in nuclei with a coarser texture and lower population density. An increase of deposition potential and addition of background electrolyte had opposite effects.

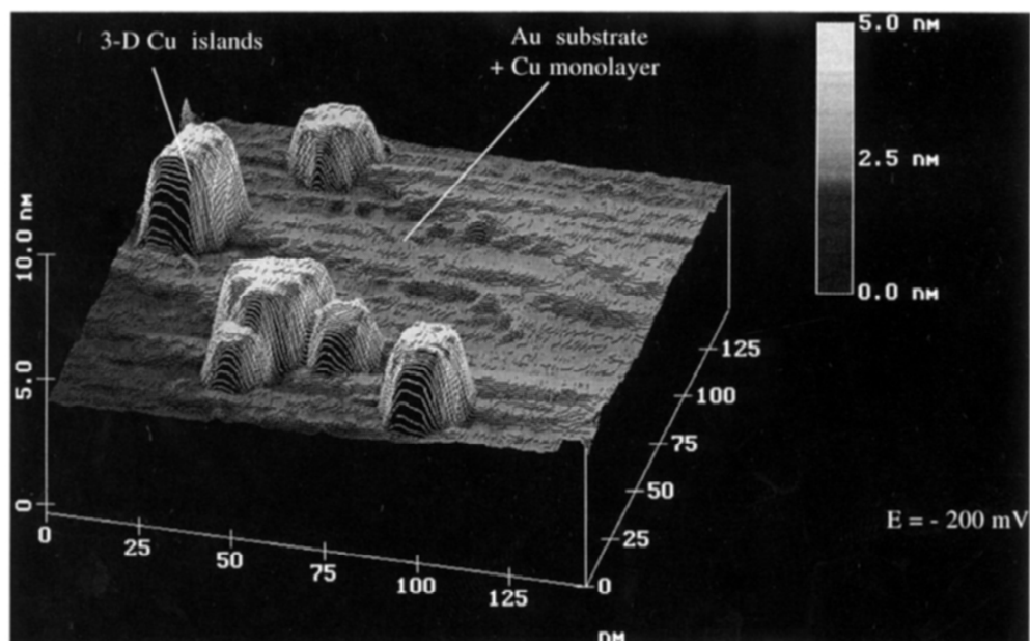

Fig. 2-15 An in-situ STM image of bulk copper deposition on a gold film at -200 mV (vs. Cu/Cu^{2+}) in 0.1M H_2SO_4 + 1mM $CuSO_4$, [78] [xi]

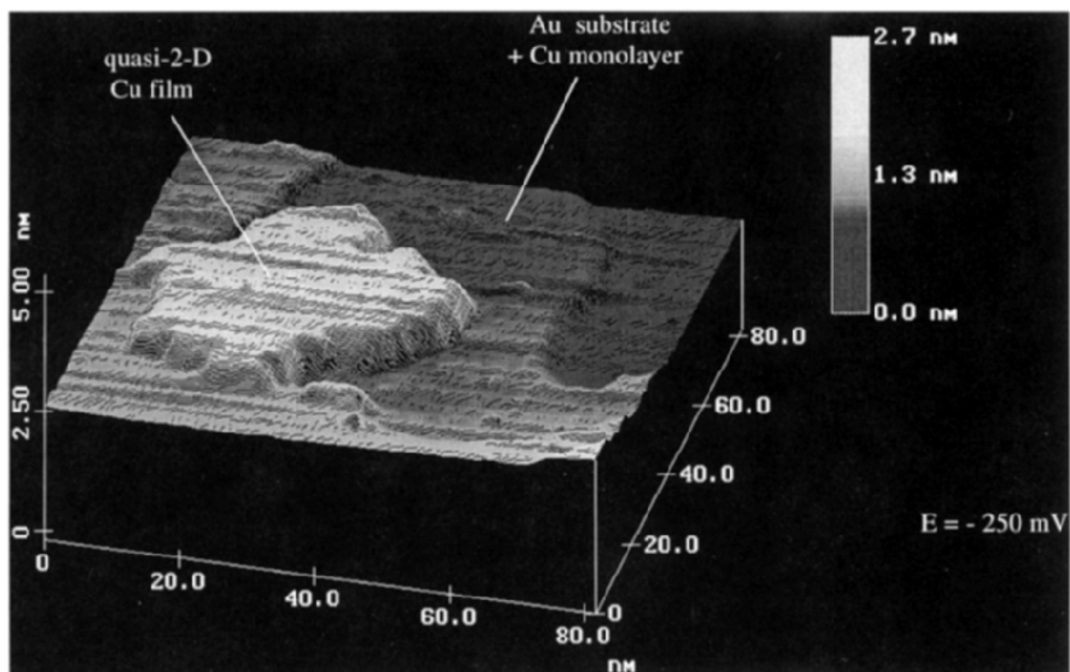

Fig. 2-16 In-situ STM image of Cu-deposition on a gold film from 0.1M H_2SO_4 + 1mM $CuSO_4$ + 10 mg/l BT-B. [78][xi]

[xi] Reprinted from Surface Science, 335, Nichols, R.J., et al., Classification of growth behaviour for copper on various substrates with in-situ scanning probe microscopy, p. 110-119, Copyright (1995) with permission from Elsevier.

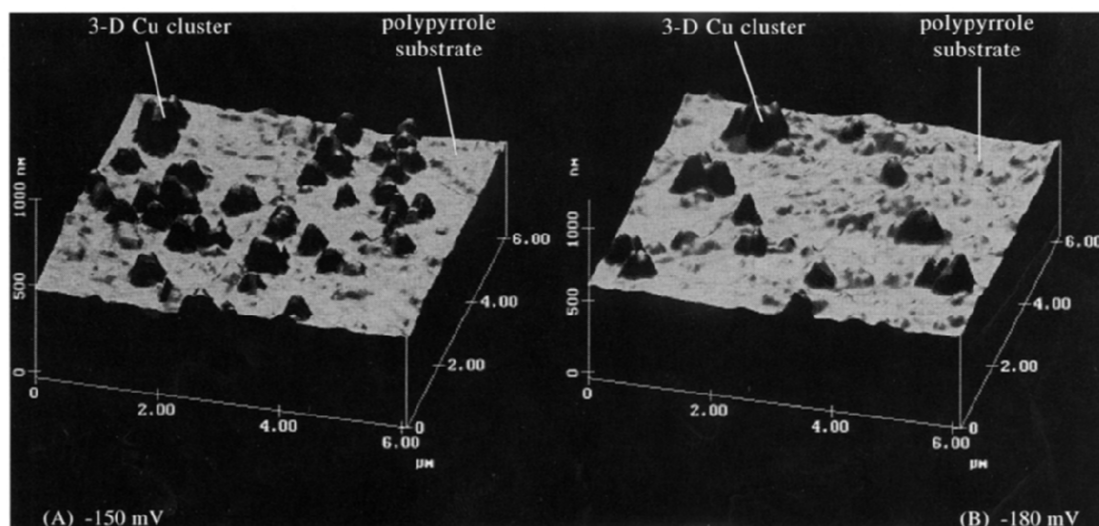

Fig. 2-17 In-situ AFM images of Cu-deposition on a conductive polypyrrole from 0.1M H_2SO_4 + 1mM $CuSO_4$ (a) without additive and (b) with 10 mg/l BT-B. [78][xi]

2.5 Summary

The fundamentals of electrodeposition and electrocrystallization have been briefly introduced, followed by a literature review focusing on application and experimental studies of copper electrodeposition and electrocrystallization. Self-annealing and nano-twinning of electrodeposited copper, which have drawn great attention during the last decade are also reviewed as two important issues related to the microstructure and crystal structure of electrodeposited copper.

Chapter 3 Kinetic Monte Carlo Simulation of Electrocrystallization of Single-crystal Copper

3.1 Introduction

Over the past few decades electrocrystallization has been studied extensively, mainly by experimental work [55-56] with review articles since published [54, 62, 92]. Since the 1980s the simulation of electrocrystallization has also become an effective tool to aid the understanding of the fundamentals. The models that have been developed can be broadly classified into two types. The first type is analytical models. Scharifker and Hills (SH) [93] proposed a model for multiple nucleation of diffusion-controlled growth by considering hemispherical diffusion to a hemispherical nucleus. Several modifications or improvements to the SH model were subsequently attempted by Scharifker and Mostanywere (SM) [94], Sluyters-Rehbach, Wijenberg, Bosco and Sluyterswere (SRWBS) [95], Mirkin and Nilov [96] and Heerman and Tarallo (HT) [97]. Abyanneh developed models for single-phase[98] and two-phase[99] electrocrystallization processes that are all charge transfer controlled and a model for diffusion-controlled processes[100]. These models derive the current time transient (CTT) based on a pre-assumption of the geometric shape of nuclei and related fundamental electrochemical laws. The CTT for the early stage of deposition is predicted, from which the nucleation rate can be extracted. However, all these models are incapable of simulating the evolution of the crystal structure. The crystal growth processes are generally too complex for a completely analytical description, except for much simplified models. When dealing with crystal growth [101], many possibilities are to be considered according to the stable or unstable nature of the growth process, to the growth mode (layer by layer, continuous, step flow, spiral, etc.), to the growth rate (linear versus non-linear in the disequilibrium), etc. It is sometimes possible to write a master equation whose solution is the set of probabilities for the possible surface configurations; even so, such an equation is in general too difficult to solve exactly and it is necessary to resort to other simulation methods.

The second type of model concerns stochastic techniques, mainly referring to kinetic Monte Carlo (KMC) models. KMC simulation is the only realistic approach at present for the simulation of crystal growth at a practical size and time scale, although molecular dynamics simulation can be useful at a much shorter time scale, down to nanoseconds or microseconds. These techniques have been successfully applied to the simulation of the thin film growth processes including electrodeposition, physical vapour deposition and chemical vapour deposition, amongst other areas of physics and chemistry.

Guo et al [102-103] have developed a KMC model in which ion transport in solution is modelled using Brownian dynamics for studying the nucleation and island growth during the bulk electrodeposition. The rate constants and nucleus density predicted by KMC have been compared to several analytic models. Their simulation results show good agreement with the SH model. The growth rate of the individual islands and the spatial distribution of the islands have also been reported. This, as one of many examples, demonstrates that the KMC method is generally more powerful than analytical methods.

In recent years, a research group from University of Illinois at Urbana-Champaign has been active in multi-scale KMC simulation of electrodeposition. For example, T.J. Pricer et al [104-105] developed a multi-scale model by linking a one-dimensional finite difference (1D FD) code dealing with the mass transfer within the diffusion layer to a 3D KMC code responsible for the surface growth. This model was used to simulate copper electrodeposition when bath additives were absent or present. The effects of the additives on the surface morphology were studied. Drews and co-workers [106-109] developed a multi-scale KMC model by linking a 2D continuum model to a (2+1)D solid-on-solid KMC model using a face-centred cubic lattice rather than the simple cubic lattice at both atomic and coarse-grained scale. The (2+1)D solid-on-solid KMC model alone has also been used to study the nucleation and growth at the early stage of the kinetically controlled electrodeposition [110]. By this approach, the lattice consists only of 2D “interface” sites on the surface; the roughness is accounted for in the “+1D” components. Only the atoms on the (2+1)D surface are tracked by the KMC codes; neither atoms buried in the deposit nor species in the solutions are tracked, which saves computational cost significantly compared to the real 3D models. More recently, Zheng

et al [111] have developed a hybrid multi-scale KMC model, which has accelerated the simulation by using the coarse-grained model without much loss of accuracy.

Saedi [112] from the Sharif University of Technology in Iran has developed a different method to couple a 2D KMC code to a 1D FD code for the simulations of various electrochemical processes. In his model, the KMC lattice is restricted to the deposited phase and moving atoms are limited to the first monolayer of the electrode surface, which reduces the processing time considerably when compared to Pricer's model. S. Harinipriya [113] recently developed a novel multistep continuum KMC model to evaluate the change of step-wise free energy in the process of copper electrodeposition.

To summarise, KMC method has become a powerful tool for the simulation of electrocrystallization. Nevertheless it is time-consuming and computationally costly, especially when a 3D model is used and a large number of particles or atoms are involved. Most of the research reviewed here has focused on the early stages of electrocrystallization, i.e. before most of the nuclei have impinged or merged. We have developed a 2D cross-sectional KMC model which, saving computational cost significantly when compared to 3D KMC models, enables the simulation of not only the nucleation processes at early stages but also the crystal growth processes at later stages e.g. merging of nuclei and faceting. The model has been used to simulate the growth history of single crystal copper on a gold seed layer from the beginning when the first atom is deposited until 100 equivalent monolayers have been deposited. It can be easily applied to other metal-substrate systems. The model has proven capable of capturing the effects of the deposition parameters on the growth history.

3.2 Description of the model

The current model represents the cross-section of an idealized electrodeposition system consisting of Cu^{2+} ions of a given concentration, the Cu atoms that have already been deposited and a gold substrate as illustrated in Fig. 3-1. In this kinetically-limited model, it is assumed that the deposition is kept slow and the solution is efficiently stirred so that the concentration of Cu^{2+} at the electrode surface do not differ appreciably from the given bulk values. In such a case, the mass-transfer effects are neglected and the deposition is kinetically limited. This can be a reasonable approximation when a low

overpotential is applied. In the present study, the applied electrode potentials are assumed to be offset by as low as -0.01V – -0.03V from the equilibrium potential for Cu^{2+}/Au system and -0.11V – -0.13V for Cu^{2+}/Cu system. Corresponding current density for a potentiostatic plating under such overpotential is about 4mA/cm^2 – 6mA/cm^2 as estimated based on a polarization curve measured using a Si wafer with sputtered Au seed layer as the cathode and a copper sheet as the anode in an additive-free acidic copper plating solution containing 0.66 mol/l Cu^{2+} at room temperature. It is worth noting that the low overpotential and hence a slow deposition, favours single crystal growth. Therefore, a kinetically-limited process is more likely to be successful for deposition of single crystals. All the Cu atoms are restricted to be on a lattice site in a face centred cubic (fcc) lattice of (111) orientation. The substrate is assumed to have the same lattice spacing as the deposit. Any Cu atom on the substrate has by default two neighbouring substrate atoms.

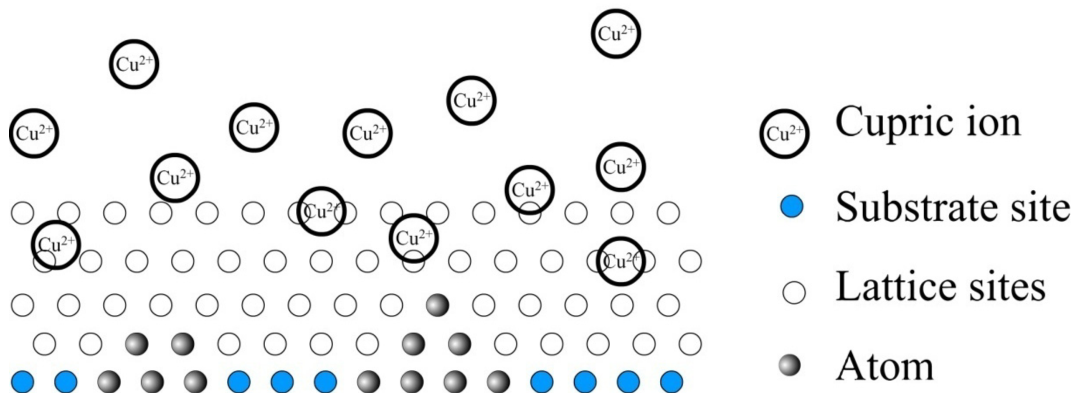

Fig. 3-1 Schematic of the idealized electrodeposition system

3.2.1 Events

Two types of events are presently included in this model: deposition and surface diffusion, although other events may be included in a later version for more complicated issues. For example, desorption can be considered for the simulation of the reversible pulsed electrodeposition; the diffusion inside grains or through grain boundaries may also be considered for recrystallization.

A Cu^{2+} ion is reduced and deposited on either the Au substrate or the pre-deposited Cu atoms. Deposition events are restricted to occur on a list of lattice sites which have at

least two neighbour atoms underneath considering that a site with fewer than two neighbour atoms is unstable [112]. The deposition rate on Au is determined [110] by

$$r_{d_{Cu-Au}} = k_{Cu-Au} C_{Cu^{2+}} e^{-\alpha_{Cu-Au} nF(\rho - \rho_{0_{Cu^{2+}/Au}})/RT} \tag{3.1}$$

and on pre-deposited Cu [110] by

$$r_{d_{Cu-Cu}} = k_{Cu-Cu} C_{Cu^{2+}} e^{-\alpha_{Cu-Cu} nF(\rho - \rho_{0_{Cu^{2+}/Cu}})/RT} \tag{3.2}$$

where k_{Cu-Au} and k_{Cu-Cu} are the rate constants, $C_{Cu^{2+}}$ the concentration of cupric ions, α_{Cu-Au} and α_{Cu-Cu} the charge transfer coefficient for the deposition of Cu^{2+}, n the electron number, F the Faraday constant, ρ the applied electrode potential, $\rho_{0_{Cu^{2+}/Au}}$ and $\rho_{0_{Cu^{2+}/Cu}}$ the equilibrium potential for Cu^{2+}/Au and Cu^{2+}/Cu respectively, R the ideal gas constant and T the deposition temperature.

A deposited atom is subject to surface diffusion to, if vacant, one of nearest neighbouring sites. Jumping up or down to a different layer is not allowed for simplicity. The surface diffusion rate on Au is computed [110] by:

$$r_{S_{Cu-Au}} = \nu_{Cu-Au} e^{(-E_{act_{Cu-Au}}/RT)} \tag{3.3}$$

and on pre-deposited Cu [110] by:

$$r_{S_{Cu-Cu}} = \nu_{Cu-Cu} e^{(-E_{act_{Cu-Cu}}/RT)} \tag{3.4}$$

where ν_{Cu-Au} and ν_{Cu-Cu} are the jump frequency for surface diffusion of Cu on Au and pre-deposited Cu respectively, the activation energy E_{act} is the energy barrier that a Cu atom must overcome in order to diffuse. The higher the energy barrier is, the less it is possible for an atom to diffuse. The energy barrier is assumed to be only determined by the coordinate number and the nature of the nearest neighbouring atoms. Such an assumption has been used in a wide variety of models in many systems e.g. [110, 112, 114-115]. Accordingly, the activation energy for a Cu atom on Au substrate and on deposited Cu atoms is computed by:

$$E_{act_{Cu-Au}} = 2E_{Cu-Au} + N_{cord}E_{Cu} \tag{3.5}$$

and

$$E_{act_{Cu-Cu}} = N_{cord}E_{Cu} \tag{3.6}$$

respectively, where E_{Cu-Au} is the binding energy between a Cu and a Au atom, E_{Cu} the cohesive energy of Cu. i.e. the binding energy between two Cu atoms, coordinate number N_{cord} only counts the nearest neighbouring Cu atoms.

3.2.2 Parameters

Values of the parameters used in this chapter are listed in Table 3-1. The rate constant for deposition on pre-deposited Cu k_{Cu-Cu} was determined from experiments [116]and the rate constant for deposition on Au k_{Cu-Au} was estimated [106] based on the experimental data in [116]. Charge transfer coefficients for deposition on Cu and Au are assumed to be the same value as in [106]. The values of the equilibrium potential for Cu deposition onto Cu and Au were taken from experimental data in [116]. The differences between equation (3.1) and (3.2) are in the values of the rate constants and the equilibrium potentials. The values of the energy barriers for a Cu-Cu bond $E_{Cu}$and a Cu-Au bond E_{Cu-Au} were sourced from [110]. Jump frequency for surface diffusion of a Cu atom on Au and on Cu was assumed to be the same value in this work. The difference between the equation (3.3) and (3.4) is in the value of the energy barriers for diffusion. The applied electrode potentials, concentration of Cu^{2+} ions and temperature have been varied to study the effects of these deposition parameters. In this model, the macroscopic dimensions with respect to a closely-packed plane of a fcc lattice is calculated by $l_w a/\sqrt{2}$ and $\sqrt{6}l_y a/4$ along the directions parallel and normal to the surface of a substrate respectively, where l_w is the lattice width, l_y the number of the layers of lattice sites or atoms and a the lattice constant. Accordingly, a lattice width of 1000 is equivalent to 255nm and 100 atomic layers 22.1nm. The simulated deposition time for depositing 100 equivalent monolayers vary from one to ten minutes depending on the combination of deposition parameters.

Table 3-1 Values of the parameters used in the simulation

Symbol	Parameter	Value
k_{Cu-Cu}	Rate constant for deposition on pre-deposited Cu	0.204 $m^3 \cdot mol \cdot s^{-1}$[116]
k_{Cu-Au}	Rate constant for deposition on Au	0.143 $m^3 \cdot mol \cdot s^{-1}$[106]
α_{Cu-Cu}	Charge transfer coefficient for deposition on Cu	0.5[106]
α_{Cu-Au}	Charge transfer coefficient for deposition on Au	0.5[106]
n	Electron number for Cu^{2+}	2
$\rho_{0\,Cu-Au}$	Equilibrium potential for Cu^{2+}/Au	-0.1 V[116]
$\rho_{0\,Cu-Cu}$	Equilibrium potential for Cu^{2+}/Cu	0 V[116]
ρ	Applied potential	-0.11, -0.13 V
E_{Cu}	Energy barrier for a Cu-Cu bond	0.13 eV[110]
E_{Cu-Au}	Energy barrier for a Cu-Au bond	0.35 eV[110]
v_{Cu-Cu}	Jump frequency for surface diffusion of a Cu atom on Au	3.9×10^5 s^{-1}
v_{Cu-Au}	Jump frequency for surface diffusion of a Cu atom on Cu	3.9×10^5 s^{-1}
$C_{Cu^{2+}}$	Concentration of Cu^{2+} ions at electrode surface	0.1, 0.32 or 0.66 mol/m^3
F	Faraday constant	96 485.3 $s\cdot A\cdot mol^{-1}$
R	Ideal gas constant	8.314 $J\cdot K^{-1}\cdot mol^{-1}$
a	Lattice constant for Cu	3.61×10^{-10} m

3.2.3 KMC Algorithm

A variety of KMC algorithms can be implemented for a simulation based on the theoretical foundation interpreted in [117]. A code has been developed that tries to balance computational efficiency against accuracy. Matrices were used to store and organize the data, which takes advantage of the discrete periodic nature of a crystal lattice. A $L \times J$ matrix M_{occp} was used to represent all the lattice sites, where L is the lattice width preset to be 1000 and J has an initial value of 1 and extends automatically when any site of a new layer is occupied. Changing the size of the matrices dynamically assures the minimum dimension of the matrix being used during the computing. This can save on memory usage and improve the efficiency of the computation. Each element of the matrix corresponds to a lattice site. If a site is occupied, the

corresponding element is evaluated with 1, otherwise 0. The deposition rates and surface diffusion rates were also organized in two matrices of same size respectively. The indices of the rate matrices correspond to the location of the sites as the M_{occp}. The algorithm is illustrated in the flow chart shown in Fig. 3-2 and the procedures are described as follows:

1. Define the initial rate matrices and the initial occupancy matrix M_{occp}.
2. Build a rate list $r_1, r_2, \dots, r_n$ consisting of all non-zero elements of the rate matrices and normalize it to form another list in which $R^N = \sum_{i=1}^{i} r_i / \sum_{i=1}^{n} r_i$.
3. Generate a random number ξ from a uniform distribution in the range (0, 1).
4. Select the first index w from the normalized rate list, which meets $R_w^N \geq \xi$.
5. Retrace the rate r_w in the rate matrices so as to determine which type of the event and where to occur.
6. Execute the move by updating the occupancy matrix accordingly.
7. Update the rate matrices. Only those elements corresponding to the location of the selected event and its nearest neighbours need updating. The periodic boundary condition is imposed in the x direction in step 6 and 7.
8. Update the KMC time with an increment of τ selected from an exponential distribution [117], i.e.,

$$\tau = \frac{1}{\sum_{i=1}^{n} r_i} \ln(\xi) \tag{3.7}$$

9. Steps 2-8 are repeated until the preset target has been reached.

Computations were implemented on either a 64-bit computer with a quad-core CPU of 3.6GHz and 8GB memories or a Bull Linux Cluster at the High Performance Computing Centre of the Loughborough University. The computing time was dependent on the combination of the simulation parameters ranging from half an hour to two hours. Three or more runs were done for each set of parameters to compute the average of the statistical data of clusters.

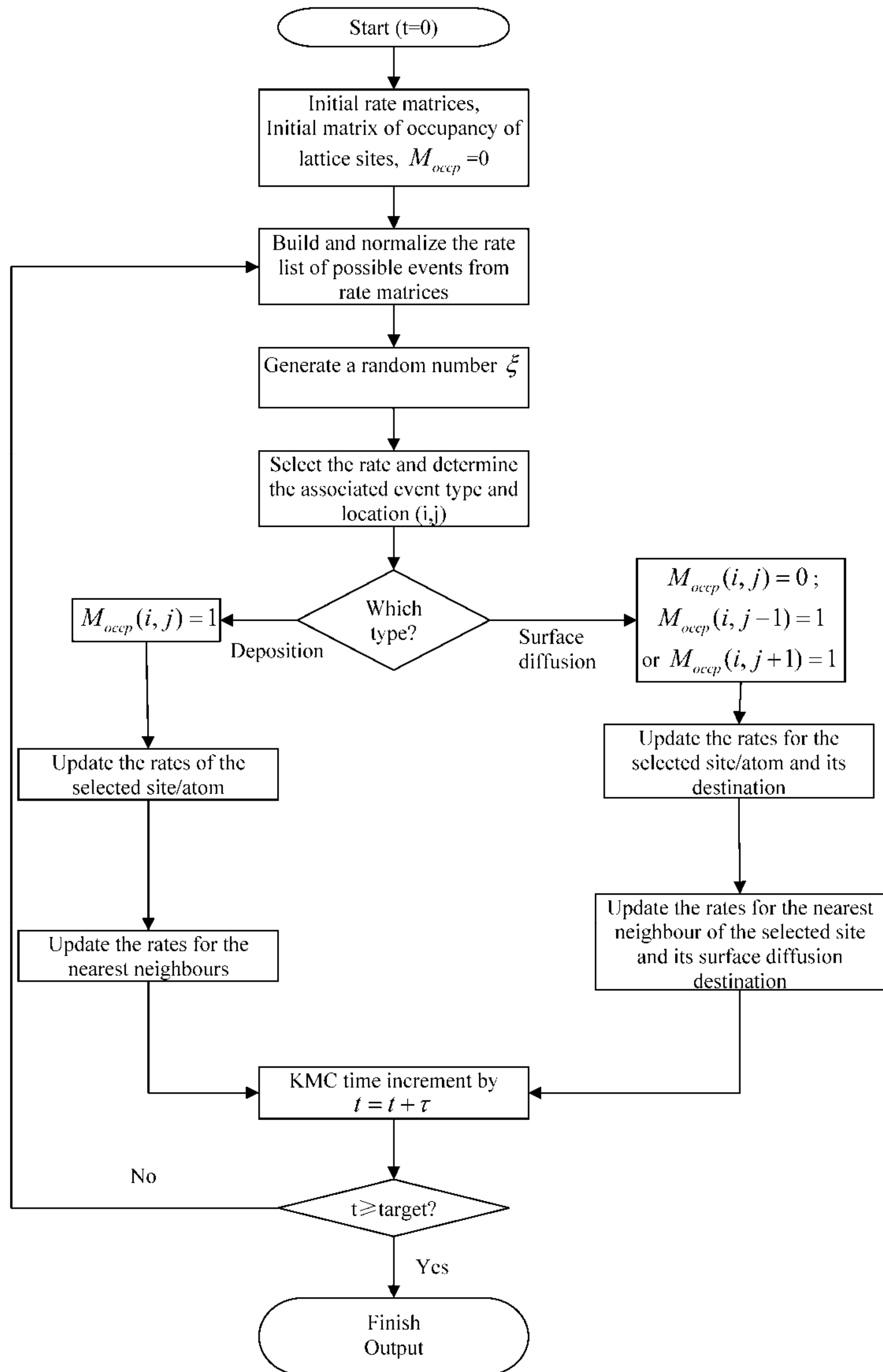

Fig. 3-2 the flow chart of the KMC algorithm

3.2.4 Post-processing

Post-processor codes (see Appendix V) were developed to visualize and analyze the simulation results. The sub-matrices representing an individual cluster were extracted

from the occupancy matrix and the cluster density, average size, variance of the size and the average aspect ratio analyzed statistically. A novel *microstructure history map*, which shows the correspondence of the microstructure to deposition amount, was invented in this work to visualize the evolution of the cross-sectional microstructure of the deposit from the beginning when the first atom is deposited until a given target of deposition amount is reached. The deposition amount is measured in the number of equivalent monolayers (EML) that have been deposited. The images from the simulation is coloured from dark blue to dark red according to the deposition amount, shown as a given colour bar. Snapshots were taken at certain EMLs to look at the microstructure separately.

3.3 Results and discussion

3.3.1 Growth history

Fig. 3-3 shows the dependence of the cluster density, average size, variance of the size and average aspect ratio on the deposition time. As can be seen in Fig. 3-3a the cluster density soars to a peak at 7.04×10^{8}/m within one EML and then goes down rapidly until 72 EML when all the clusters merge into one large crystal. In order to examine how the variation has been reflected in the microstructure, we took snapshots at a series of selected times. As can be seen in Fig. 3-4a and Fig. 3-4b, within one EML there have formed a large number of clusters (consisting of more than two atoms) and some adatoms (one single independent atom on the substrate). These adatoms tend to diffuse along the surface until they meet another adatom or cluster, since they are energetically unstable. Alternatively, they may take atoms from the solution and grow into a cluster. In the latter occasion one adatom is a nucleus. Then the cluster density falls by about 70% after 10 EML followed by a further 50% drop within the next 10 EML. After 72 EML, as shown in Fig. 3-4g, there remains only one large cluster, a single crystal.

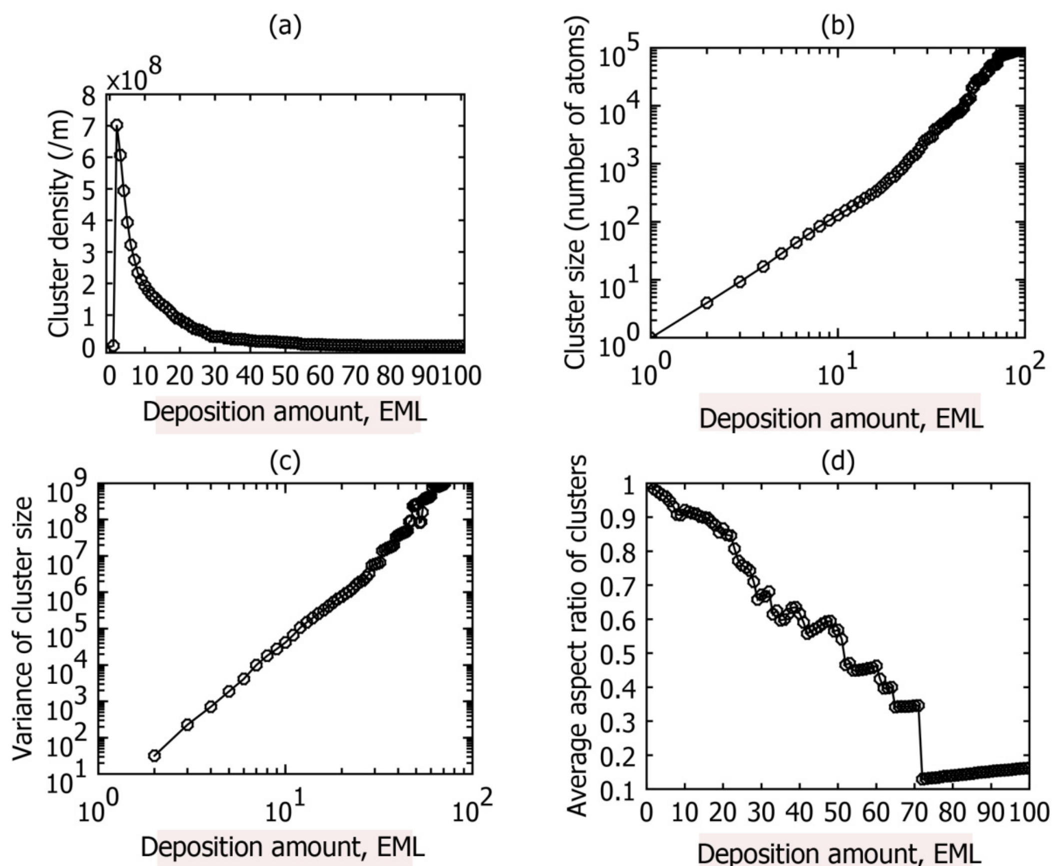

Fig. 3-3 the dependence of (a) the cluster density, (b) the average cluster size, (c) the variance of the cluster size and (d) the average aspect ratio of the cluster on the deposition amount by EML.

Before 1EML, most of the clusters are small and not significantly different in size. This is attributed to the assumption that the substrate surface is atomically flat and initially there is no particularly preferred nucleation site. Nevertheless, a few large clusters still stand out amongst many small ones as can be seen in Fig. 3-4a. Such stochastic *priority* for growth does not last long. After 5 EML, they are not prominent any more since many other clusters across the surface have reached a similar size, as shown in Fig. 3-4c. They then continue growing not only longitudinally, mainly by taking atoms directly from solution, but also laterally by merging with the adjacent clusters. Overall, the average cluster size and the variance of cluster sizes steadily increase as shown in Fig. 3-3b and Fig. 3-3c. A few steps that appear in the later part of these two curves are attributed to the merging of clusters when they have reached a critical size.

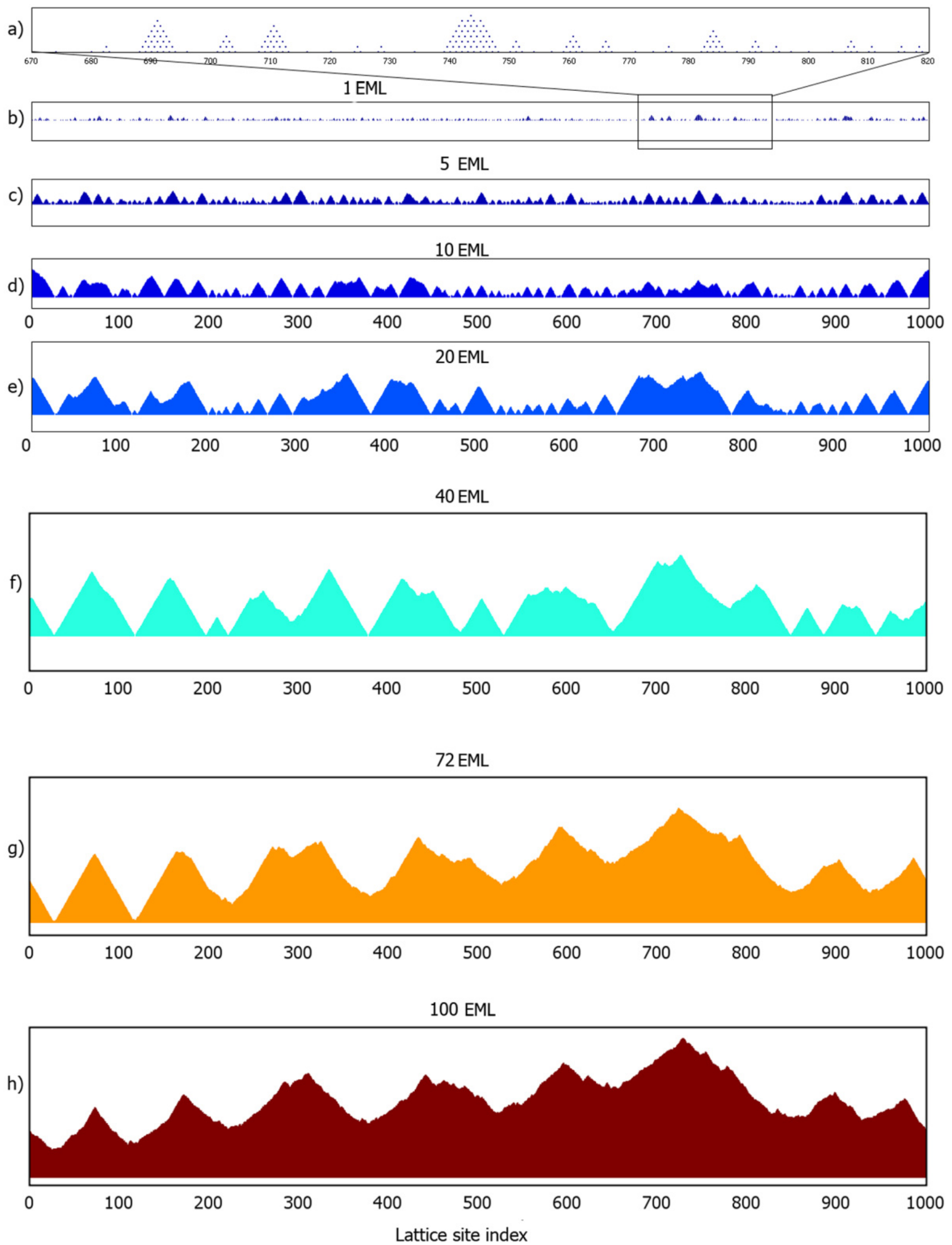

Fig. 3-4 the snapshots of the microstructure on deposition of a series of amounts of deposit: (a) the enlarged of the area indicated by a rectangle box in (b), (b) 1EML, (c) 5 EML, (d) 10 EML, (e) 20 EML, (f) 40 EML, (g) 72 EML and (h) 100 EML.

The cluster shape evolves during the growth. Overall, the average aspect ratio trends are down with intermittent fluctuations as shown in Fig. 3-3d, which indicates that the clusters become wider faster than higher. Before about 40 EML, the fluctuation is not

significant. The fluctuations can be accredited to the merging of the clusters. During early stages when clusters are relatively small, merging with a small cluster will not result in a significant change of the cluster shape. Most clusters grow wider and higher at a relatively even pace. Meanwhile, the facets of (11) orientation form and remain during the growth, as shown in Fig. 3-4c-f. The (11) facets start to fade after 40 EML. After this the aspect ratio fluctuates with larger amplitudes and longer intervals. This is due to the merging with the very large clusters. A plummet of aspect ratio appears at 72 EML when two remaining large clusters merge into a single crystal as shown in Fig. 3-4g.

The entire growth history has been visualized in a map from the beginning when the first atom is deposited until after 100 EML as shown in Fig. 3-5. The growth history of not only the deposit as a whole but also an individual cluster can be easily traced from this map. The phenomenon of cluster merging and faceting can be evidently seen. With the supplement of snapshots at particular times and the statistical analysis of the clusters, the growth history has been completely reconstructed.

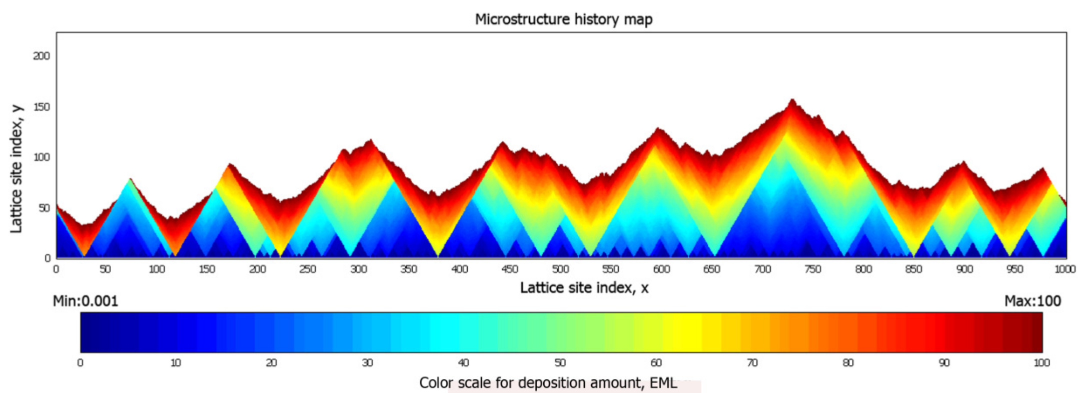

Fig. 3-5 the microstructure history map showing the evolution of the microstructure from the beginning until 100 EML.

3.3.2 Effects of deposition parameters

Fig. 3-6 shows snapshots of the microstructure obtained using different concentrations of Cu^{2+}, temperature and potential after 30 EML. By comparing Fig. 3-6a-c, the more concentrated a solution used, the larger the variance of the cluster size is observed. For the least concentrated solution with 0.1mol/l Cu^{2+}, the cluster height does not vary significantly across the surface, which indicates the upward growth is relatively uniform across all the clusters. For the most concentrated solution of 0.66mol/l Cu^{2+}, however,

several wide and large clusters are obvious amongst other much smaller pyramid ones. For the less concentrated solution of 0.32mol/l Cu^{2+} the cluster sizes are around the median. Fig. 3-6d shows the snapshot for deposition at 40°C. The cluster sizes varies to a lesser extent than at 25°C as can be seen by comparing Fig. 3-6d to Fig. 3-6b. For a more negative potential as shown in Fig. 3-6e, the cluster height varies less while cluster width varies more, as compared to Fig. 3-6b. It indicates that the lateral growth takes priority over the upward growth when a more negative potential is applied.

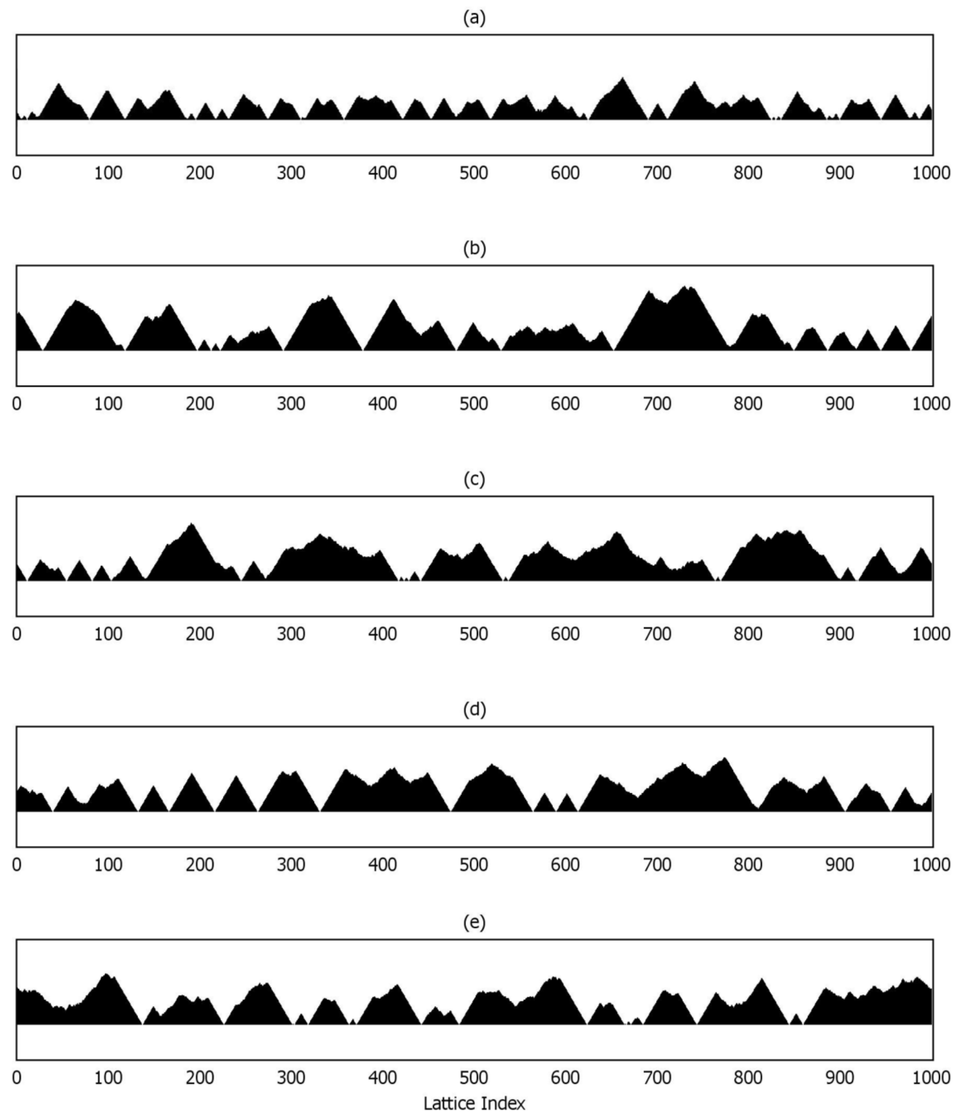

Fig. 3-6 the snapshots of the microstructure after 30 EML under different conditions: (a) the concentration of Cu^{2+} of solution, c = 0.1 mol, the temperature T=298 K and potential ρ= -0.11 V; (b) c=0.32 mol, T=298K, ρ= -0.11 V (c) c=0.66 mol, T= 298 K, ρ= -0.11 V and (d) c=0.32 mol, T=313 K, ρ= -0.11 V (e) c=0.32 mol, T=298 K, ρ= -0.13 V

According to the equation (3.1) and (3.2), the concentration, the temperature and the applied potential have all shown their effects on the deposition rate. The temperature has an effect on both the deposition rate and surface diffusion rate. These effects will be transferred to the increment of the KMC time τ, according to equation (3.7). For convenience the KMC time, instead of the equivalent monolayer, is used as the time axis for describing the growth history in such a case. Fig. 3-7 shows the dependence of cluster density and the variance of cluster size on the KMC time and the process parameters including the concentration of Cu^{2+}, the temperature and the potential. Interestingly, the temperature has shown no noticeable effects on the cluster density but slight changes in the variance of the cluster size between about 50s and 100s. By contrast, the concentration and the applied potential have significant effects on the cluster density and variance of the cluster size during the course of deposition. The cluster density has changed more rapidly when the more concentrated solution is used or the more negative potential applied. However, the temperature, concentration and potential all have little effect on the maximum cluster density as shown in Fig. 3-7a. Oscillations appearing near the end of the curves in Fig. 3-7b can be attributed to merging of very large clusters at these times and that there are deviations between different runs of a set of parameters due to the stochastic nature of KMC methods. In the present investigation, simulation data were collected and saved once per EML during the computation. These oscillations can probably be reduced by collecting data at finer steps as well as by doing more runs for computing the average at the expense of higher computational cost.

Finally, our simulation is ultimately aimed to guide the optimization of process parameters for the deposition towards growth of single crystals. Therefore, it is of great significance for our KMC model to be able to capture the effects of the deposition parameters on the growth history and the microstructure. This has proved to be able to capture the effects of some deposition parameters, including the concentration, temperature and potential. However, it should be noted that an accurate output of optimized deposition parameters are improbable at present, due to the unknown parameters (e.g. the jump frequency for surface diffusion) being used and limitations of the model. In the present model, once the values of all the parameters in equation (3.1)

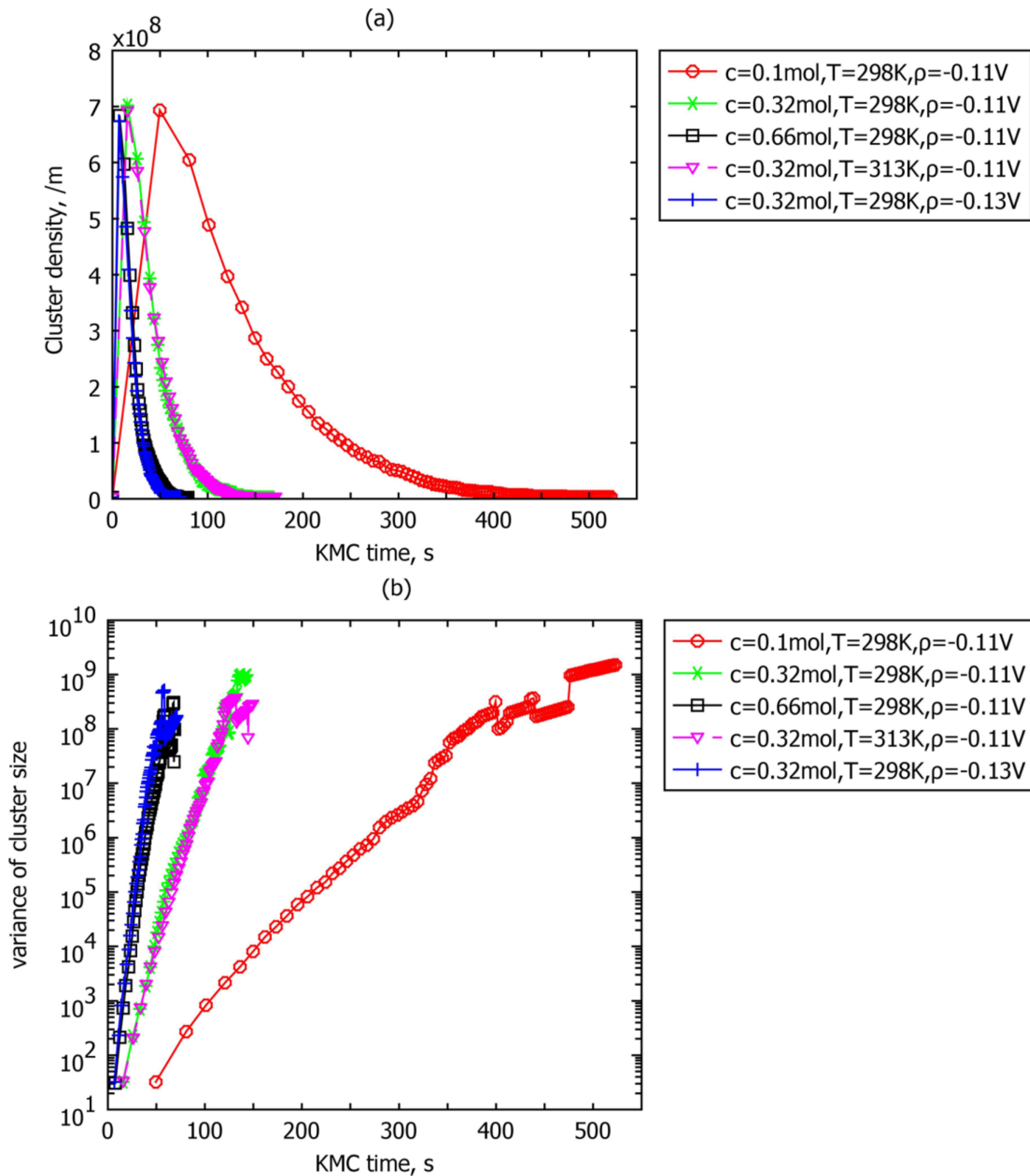

Fig. 3-7 the dependence of (a) cluster density and (b) the variance of cluster size on the KMC time under different deposition conditions.

and equation (3.2) are given, the deposition rates for Cu on Cu and Cu on Au will have a definite value respectively during the deposition. The surface diffusion rates determined by equation (3.3) and (3.4), however, vary during the deposition according to the coordinate number of the diffusing atom and the nature of its neighbour atoms. A deposition event or surface diffusion event is selected randomly at each KMC step with a probability proportional to its rate. The final structure of a deposit is the result of the competition between these two types of events at each step. The parameters have

effects on the simulation results by affecting the event rates. For a more accurate prediction, more work is needed to obtain the values of the unknown parameters and a more complicated model considering more events that may occur during the electrodeposition is necessary. In the future model, the microscopic reversibility [114] can be considered, and the embedded atom method (EAM) [112, 114] and Schowel-Ehrlich barriers [118-120]employed while determining the activation energy for the diffusion. Further to this single-lattice model, an advanced poly-lattice KMC model has been developed that enables the simulation of a polycrystalline deposit during electrodeposition as presented in the next chapter.

3.4 Conclusions

A 2DCS-KMC model has been developed for the simulation of electrodeposition of copper on a gold substrate. The entire growth history can be reconstructed at atomic scale. The cluster density, average size, variance of the size and average aspect ratio have been obtained from the simulations. They are found to vary with the deposition, which has been reflected in the evolution of the microstructure. A microstructure history map together with a series of separate snapshots has been used to visualize the evolution of the microstructure. It is possible to trace an individual cluster to find out the time and location of the occurrences of its formation, growth and its merging with others using the microstructure history map. The model has been proven to be able to capture the effects of the process parameters including the concentration of the solution, temperature and potential on the growth history. Using a concentrated solution tends to result in larger variance of the cluster size and accelerate the microstructure evolution. The cluster size varies to a lesser extent at higher temperatures. However the temperature has no notable effects on the rate of the change of cluster density and variance of cluster size. The cluster height varies less while cluster width varies more and the microstructure evolution is accelerated when a more negative potential is applied. All these parameters have little effect on the maximum cluster density.

Chapter 4 Kinetic Monte Carlo Simulation of Electrodeposition of Polycrystalline Copper

4.1 Introduction

Kinetic Monte Carlo (KMC) simulation has become a powerful tool for the study of electrocrystallization and is essentially the only feasible way of simulating the crystal growth at a practical size and time scale. It has been employed to simulate early-stage electrocrystallization [102-103, 110] at the both only the atomic scale or coupled to macroscopic models e.g. finite element or finite difference models for a multi-scale simulation of electrodeposition process [108-109, 111-112]. A detailed review of the KMC models for electrocrystallization can be found in Chapter 3. All those KMC models have one assumption in common: all atoms are forced to be deposited onto or jump to the sites of a single lattice. Strictly speaking, such single-lattice models are only suitable for simulation of single crystal electrocrystallization because the important features of a polycrystalline structure, including the texture development and grain boundary mis-orientation, cannot be captured in such models.

Although most electrodeposits of practical interests are polycrystalline, there have been few KMC models available for treating the electrodeposition of polycrystalline metals [121-122] and they simply associate a property representing several typical orientations with sites of a single lattice. This preliminary solution is also of interest in the simulation of polycrystalline Al [114] films, Cu [123], and Si[124] films by other thermal deposition processes. A major limitation of this approach is that the key aspects of grain boundaries, such as the high density of vacant sites and high energetic state, cannot be included. Bruschi et al [125] developed a 'real' poly-lattice KMC model that represents the first monolayer of a polycrystalline film at two dimensions. Obviously, this 2D model is restricted to the early-stage deposition, i.e. before the full coverage of the substrate is reached. Huang et al [126-127] developed a multi-lattice model by mapping a given number of lattices representing grains onto a single reference lattice for simulation of sputtering Al film. Rubio et al [115] broadly extended Bruschi's 2D model to three

dimensions, allowing atoms to diffuse across grain boundaries and change grain membership, but it gives a definite number of lattices such as Huang et al reported. However, the higher energetic state at a grain boundary is still not considered. And pre-setting a definite number of lattices renders these multi-lattice models incapable of dealing with the nucleation process.

In the last decade, KMC simulation for polycrystalline growth has attracted increasing attention in the area of multi-lattice KMC models that have encountered various limitations. Neither grain boundary mis-orientation nor poly- or even multi-lattice KMC models in simulation of electrodeposition have been considered. In this chapter, a 2D cross-sectional poly-lattice (2DCSP) KMC model to simulate electrodeposition of polycrystalline copper is developed, furthering the 2DCS-KMC model [128] for single-crystal electrocrystallization presented in Chapter 3. The evolution of microstructure, grain statistics and grain boundary mis-orientation distribution during the electrodeposition of copper on a copper or gold substrate have been considered through the simulation. The entire growth history of electrodeposits has been re-constructed based on the proposed growth mechanism.

4.2 Simulation methods

4.2.1 System

The current model represents the cross-section of an idealized electrodeposition system consisting of cupric ions Cu^{2+} of a given concentration, Cu atoms that have already been deposited, and a Cu or Au substrate as illustrated in Fig. 4-1. The substrate is assumed to be an atomically even surface. Any atom on the substrate or near the substrate (the distance to the substrate is less than the lattice space a has, by default, two neighbour substrate atoms. The type of substrate is defined by defining a list of available sites and corresponding deposition rate. For example, an amorphous substrate can be represented by sites with a random location and a same deposition rate; a single crystal substrate by sites located on a given lattice with same deposition rate; a polycrystalline substrate by sites with given location associated with the substrate grain structure and higher deposition rate at the grain boundaries of the substrate. In the present model, a

list of available sites randomly distributed across the substrate with fixed space a and a same deposition rate are defined.

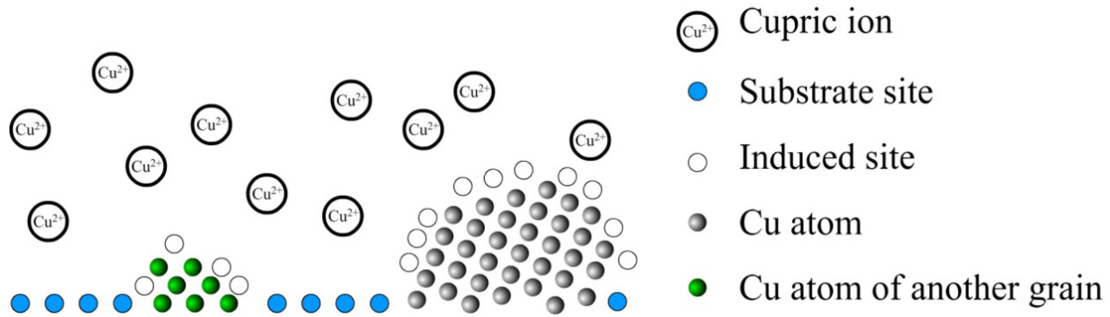

Fig. 4-1 Schematics of the idealized system for electrodeposition of polycrystalline copper

4.2.2 Data structure and Algorithm

The simulation cell is divided into a two-dimensional array of small boxes which are represented by a structure matrix B in the simulation code as illustrated in Fig. 4-2. The purpose of this treatment is to accelerate the investigation of the neighbourhood of the atom or the site of study by examining only the nearest neighbour boxes. Note that the time for this operation will not increase with the size of the simulation cell. Each box $B(i, j)$contains deposited atoms, induced sites and substrate sites each of which is represented by a sub-structure with appropriate fields storing its location, grain membership, orientation, normal coordination number, strange coordination number (see section 4.2.3 for its definition), deposition rate, diffusion destination sites and corresponding diffusion rates. Initially, the boxes in the first row are defined with substrate sites and empty fields of atoms and induced sites. The simulation cell expands dynamically in the y direction when a site is induced above the top box, which saves on the usage of memory and computation time. Only the first row of boxes is defined with a list of substrate sites and the fields of atoms and induced sites empty. The algorithm for event selection is similar to that described in the previous chapter.

When a Cu atom is deposited on a substrate site, a new 2D triangular lattice (i.e. a (111) plane of a face-centred cubic lattice) representing a grain is generated and a random orientation (defined by the tilt angle of the lattice against the surface normal direction) between 0 and 60 degree is assigned. The lattices of different orientation expand

dynamically with growth of the grains. A newly deposited atom induces up to six neighbour lattice sites which must meet the following criteria. First, it must have at least

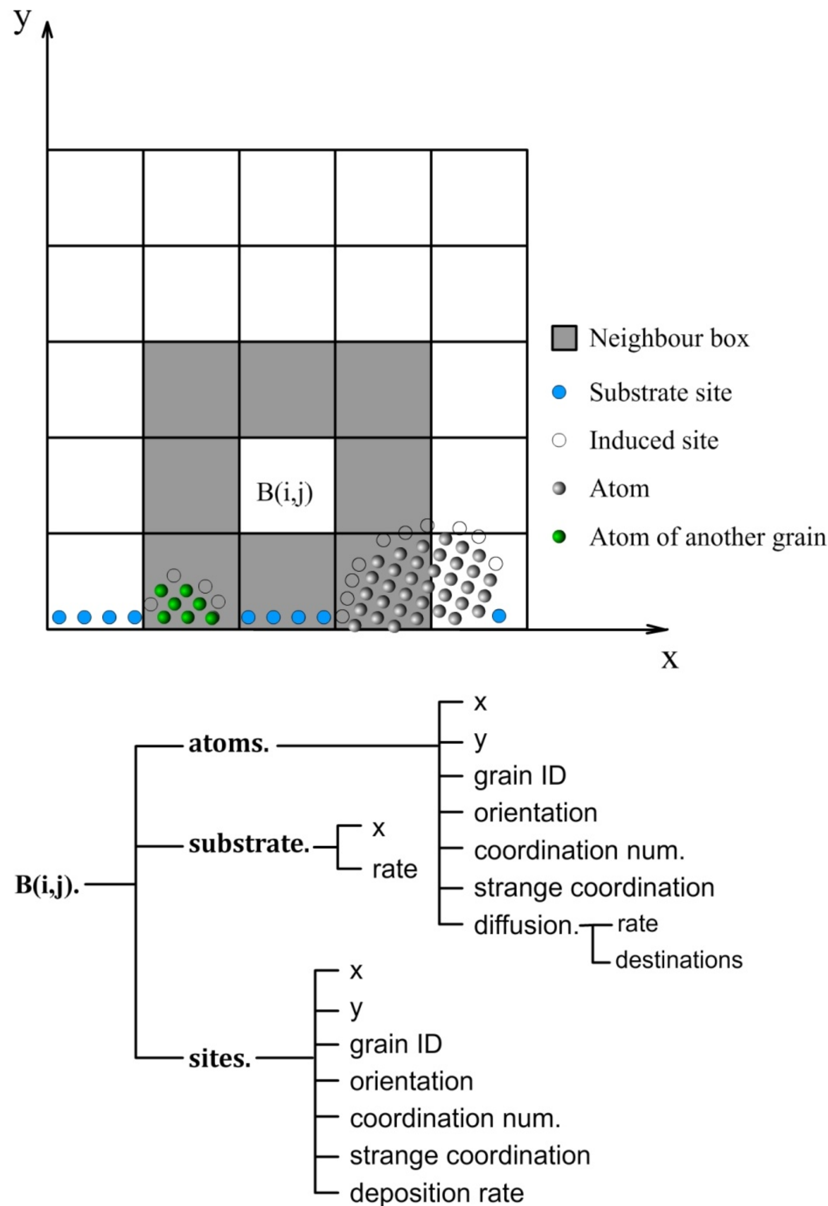

Fig. 4-2 Schematic of the simulation cell and the data structure

two neighbouring atoms, considering an atom with fewer than two neighbour atoms is unstable, except the sites on or near and above the substrate. Second, it is not inhibited by existing atoms. That is, if there is an atom within the inhibiting distance d_{inh}, the lattice site will not be induced taking into account the steep increase of repulsive strength arising when the interatomic distance is progressively reduced. Meanwhile, any neighbouring induced sites belonging to other grains or substrate sites within the range

of the inhibiting distance is annihilated. The possible diffusion destinations are searched and corresponding diffusion rates computed. The fields of the induced sites are computed and assigned. The affected neighbour sites and atoms are then updated. Only the fields of normal and/or strange coordination number, diffusion destination and corresponding diffusion rate require updating. When a Cu atom is deposited on a previously induced site, it replaces the site and inherits its coordinates, grain ID, orientation and normal and strange coordination number. Meanwhile, it induces up to six new sites and annihilates the sites within inhibiting distance. Then the induced sites are assigned and the affected neighbour sites and atoms are updated correspondingly. When a Cu atom diffuses to one of its possible destination sites, the atom and the site exchange the fields of coordinates, grain ID and orientation. Other fields are re-computed. The diffused atom will also induce new sites and annihilate the sites within the inhibiting distance. The affected neighbour sites and atoms of both the diffusing atom and the vacated site are then updated. Perodic boundary conditions are imposed in the x-axis direction.

4.2.3 Events

Two types of events are included in the present model: deposition events and diffusion events. A cupric ion Cu^{2+} is reduced and deposited on a substrate site or an induced site. The deposition rate on a substrate site or an induced site near the substrate is computed by

$$r_{d_{Cu-Au}} = k_{Cu-Au} C_{Cu^{2+}} e^{-\alpha_{Cu-Au} nF(\rho - \rho_{0_{Cu^{2+}/Au}})/RT} \quad (4.1)$$

and on other induced sites by

$$r_{d_{Cu-Cu}} = k_{Cu-Cu} C_{Cu^{2+}} e^{-\alpha_{Cu-Cu} nF(\rho - \rho_{0_{Cu^{2+}/Cu}})/RT} \quad (4.2)$$

Where k_{Cu-Au} and k_{Cu-Cu} are the rate constant, $C_{Cu^{2+}}$ the concentration of Cu^{2+}, α_{Cu-Au} and $\alpha_{Cu-Cu}$the charge transfer coefficient, n the electron number, F the Faraday constant, ρ the applied electrode potential, $\rho_{0_{Cu^{2+}/Au}}$ and $\rho_{0_{Cu^{2+}/Cu}}$ the equilibrium potential for Cu^{2+}/Au and Cu^{2+}/Cu systems respectively, R the ideal gas constant and T the temperature. The deposition on substrate or pre-deposited atoms is considered in terms of the rate constant, charge transfer coefficient and equilibrium potentials.

A deposited atom can diffuse to one of its nearest neighbour site within its own grain or to a site belonging to other grains within the range of a and change its grain membership. This enables the simulation of grain boundary dynamics at atomic scale. The diffusion rate on/near the substrate is computed by

$$r_{dif_{Cu-Au}} = w_{Cu-Au} \cdot e^{-(E_{mig}+\Delta E)/RT} \quad (4.3)$$

and on pre-deposited Cu atoms by

$$r_{dif_{Cu-Cu}} = w_{Cu-Cu} \cdot e^{-(E_{mig}+\Delta E)/RT} \quad (4.4)$$

where w_{Cu-Au} and $w_{Cu-Cu}$are the jump frequency for diffusion, $E_{mig}$is the migration energy dependent on the coordination. $\Delta E = E_f - E_{mig}$ is the difference between the energy of the system after and before the diffusion if the difference is positive and $\Delta E = 0$ if negative. E_{mig} and E_f are determined by $E_x = N_{cord}E_{barr} + N_{cord}^{str}(\lambda E_{barr})$, where E_x represents E_{mig} or E_f and N_{cord} is the coordination counting the nearest neighbour atoms within the same grain. Here we introduce a new concept 'strange' coordination N_{cord}^{str}, counting the number of nearest neighbours belonging to other grains within the range of a, and a correction coefficient λ to treat the higher energy of the grain boundary atoms.

4.2.4 Parameters

Table 4-1 lists the values of the new parameters introduced in this chapter and those parameters with a different value from that in Chapter 3. The inhibiting distance d_{inh} was assumed to be $0.8a$ based on the estimation for Al in [125]. The correction coefficient λ was assumed to be 0.5, considering the facts that a decrease of coordination number of an atom leads to a loss in its stability and a grain boundary atom is less stable. Jump frequency for diffusion of a Cu atom on Cu, w_{Cu-Cu} or on Au, w_{Cu-Au} was assumed to be the same value, and both varied in section 4.5 to study their effects. Deposition parameters including the applied electrode potentials, concentration of Cu^{2+} ions and temperature have been varied both separately and collectively as specified in Table 4-2 to study their effects on the grain growth.

Table 4-1 Values of the parameters different from Chapter 3

Symbol	Parameter	Value
d_{inh}	Inhibiting distance	$0.8a$
λ	Correction coefficient	0.5
w_{Cu-Au}	Jump frequency for diffusion of Cu on Au	1.5×10^6, 1.5×10^7 or 1.5×10^8 s^{-1}
w_{Cu-Cu}	Jump frequency for diffusion of Cu on pre-deposited Cu	1.5×10^6, 1.5×10^7 or 1.5×10^8 s^{-1}

4.2.5 Post-processing

Postprocessor codes (see Appendix VII) were developed to subtract grains from final structure array B by sorting all the atoms according to their grain ID into a grain structure array. Each element of the grain structure array represents a grain and stores the information including its atom members, grain orientation, grain ID and grain size. The grain boundary atoms are readily identified by the strange coordination number of atoms. Neighbour grains are identified by searching the grain boundary atoms in the neighbour boxes. This enables the study of grain boundary misorientation. The snapshot of the microstructure is obtained by plotting all the atoms and mapping their grain orientation to colours. Individual grains are tracked in the simulation and post-analyzed statistically. The grains consisting of fewer than 5 atoms are not counted in the statistics considering their negligible volume fraction. The simulation results were recorded at step of 0.1 EML before 5 EML and 0.5 EML after that.

4.3 Reconstruction of the growth history

The evolution of microstructure of Cu deposits on Cu and Au substrate is simulated using above-stated methods, and results are presented in Fig. 4-3 and Fig. 4-4. As can be seen in Fig. 4-3, a number of nuclei are evenly distributed across the Cu substrate on deposition of 0.5 equivalent monolayer (EML) Cu atoms, which indicates a homogeneous nucleation. On deposition of 5 EML these nuclei have grown into grains after impingement. These grains continue growing competitively both longitudinally and

laterally. As a result, some of the grains are suppressed by their neighbours growing over them on 20 EML. Consequently, the suppressed small grains remain while others proceed with upward and competitively lateral growth. Finally on 50 EML, the deposit shows fabric texture with some finer grains near the deposit/substrate interface. In sharp contrast, the microstructural evolution for deposition on Au substrate presents characteristics of heterogeneous nucleation and growth as illustrated in Fig. 4-4. A prominent grain stands out within 1 EML followed by another one in the next 4 EML, although initially no particularly preferred nucleation site on the substrate is preset in the present model. Before the saturation of the nucleation, the growth is basically dominated by a few grains which nucleate one after another at certain intervals. The resulting grains are, on average, much larger than on Cu substrate. Meanwhile, the grain growth after impingement follows the mechanism of competitive growth as on Cu substrate, as indicated by the suppressed grains.

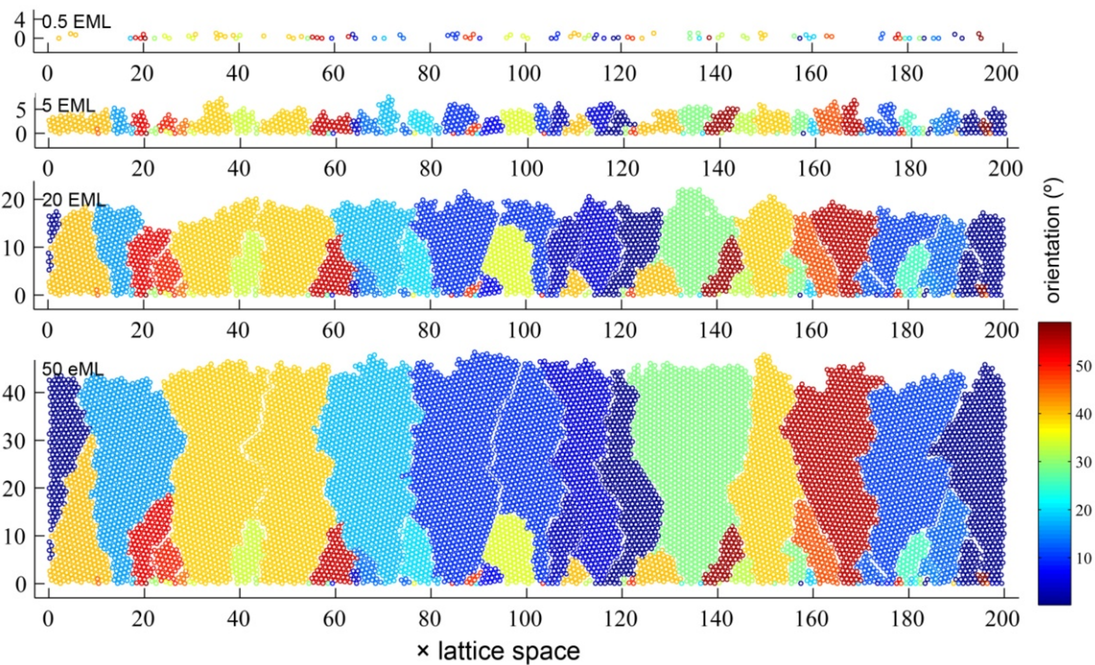

Fig. 4-3 the snapshots of simulated microstructure on deposition of from 0.5 EML to 50 EML Cu atoms on a Cu substrate

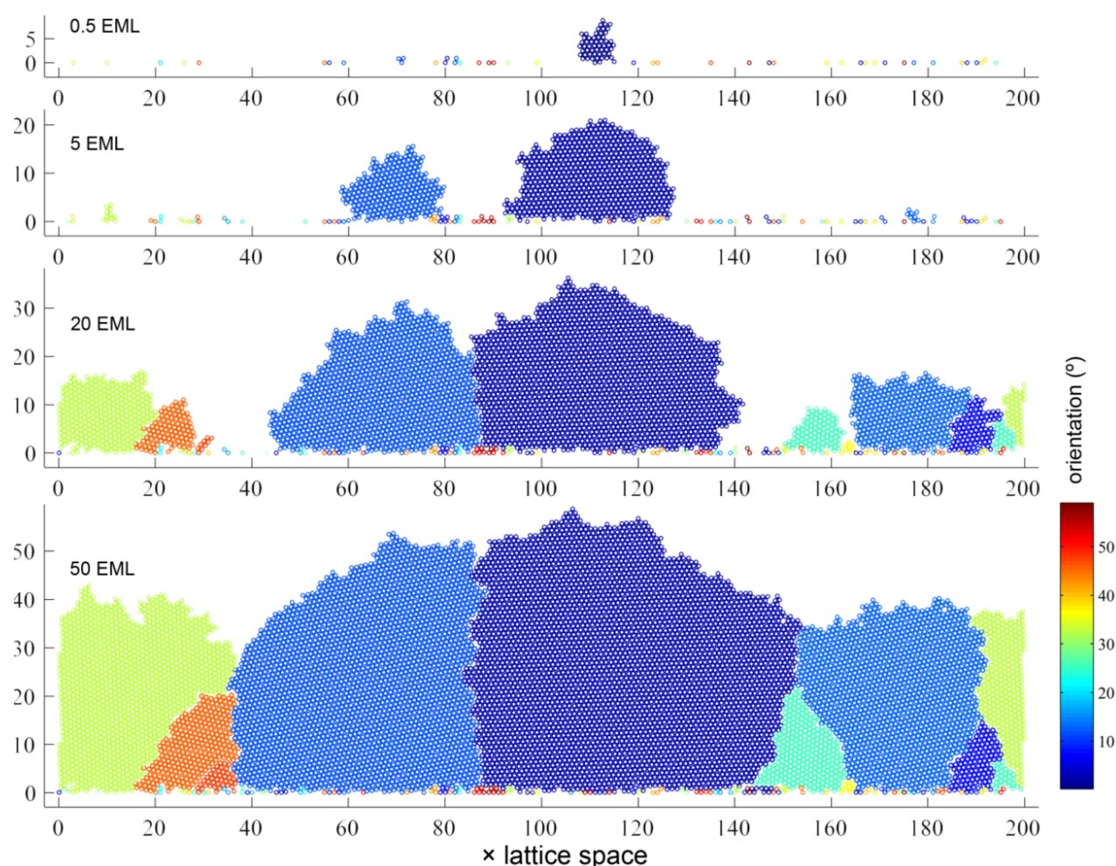

Fig. 4-4 the snapshots of simulated microstructure on deposition of from 0.5 EML to 50 EML Cu atoms on a Au substrate

The shape of individual grains also evolves during the growth and final grain shapes vary due to the competitive growth. In spite of their variety, the final grain shapes essentially consist of three unit shapes namely the funnel, pyramid and columnar shape as illustrated in Fig. 4-5. The competition between neighbouring grains ultimately determines the final grain shape. Each unit shape reflects one type of the status of the competitiveness of a grain for growth. The most competitive grains 'elbow' their way laterally and grow upwards at the same time and finally grow into a funnel-like shape. The less competitive grains can only hold their width during growing longitudinally. The resultant grains present a columnar shape. The least competitive grains are suppressed by their neighbours and eventually completely inhibited. Such suppressed grains usually present a pyramidal shape. Sometimes, a few small neighbouring grains are all suppressed by same grains that are more competitive and constitute together a pyramid shape. The variation of the competence of a grain at different stages of its growth history accounts for the final combined shape.

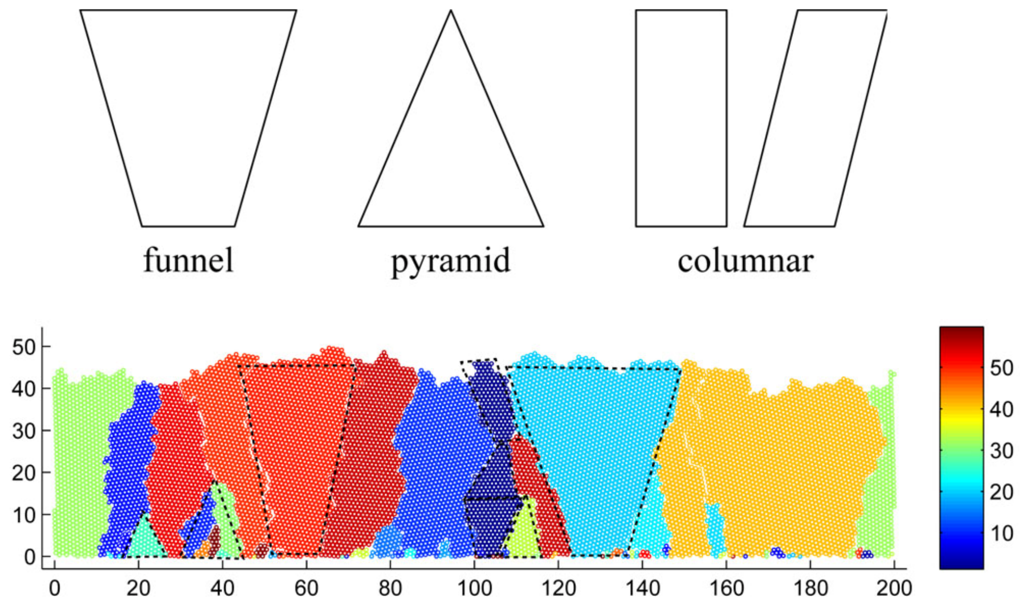

Fig. 4-5 Illustration of the three unit shapes that constitutes various grain shapes

The quantitative description of the grain growth history is presented in Fig. 4-6. The grain density soars to a saturation value at 8.1×10^{8}/m within about 0.4 s for the deposition on Cu substrate while for Au substrate it takes eight times as long to climb to a one-fourth saturated grain density as shown in Fig. 4-6a,. An effective grain size $d = \sqrt[3]{(6NV_m/N_A\pi)}$ is defined here, where N is the number of atoms in an individual grain,V_m the molar volume of the solid phase (0.71×10^{-6} m^3/mol for copper [103]) and $N_A$the Avogadro's constant. The average effective grain size as a function of time is plotted in Fig. 4-6b. The saw-toothed part of the curve for Cu substrate corresponding to the stepped one for Au substrate is due to the intermittent nucleation events and subsequent dominant growth of the large grains as described above. Normal grain growth generally obeys the power law $r^m - r_0^m = K_0 t$ where r_0 is the initial grain size, m is a material-dependent growth exponent, K_0 a temperature-dependent grain growth rate [129]. Least-squares regression was performed based on the simulated data of the average grain size, through which it was found that $m = 2.53$, $K_0 = 4.66 \times 10^{-10}$ m/s for Cu substrate and $m = 2.53$, $K_0 = 8.75 \times 10^{-10}$ m/s for Au substrate. The variance of grain size also increases with the growth of grains as shown in Fig. 4-6c. It can be seen that the curve of the variance of grain size versus time fits very well with the power law with an exponent of 1.265, exactly half the value of m , which further verifies the effectiveness of the regression analysis on the average grain size. The grain boundary

misorientation is also explored by simulation. As can be seen in Fig. 4-7 and Fig. 4-8, overall, there are more low-angle boundaries (0-12°) for both substrates although the orientation of a grain is assigned completely stochastically on deposition of its first atom.

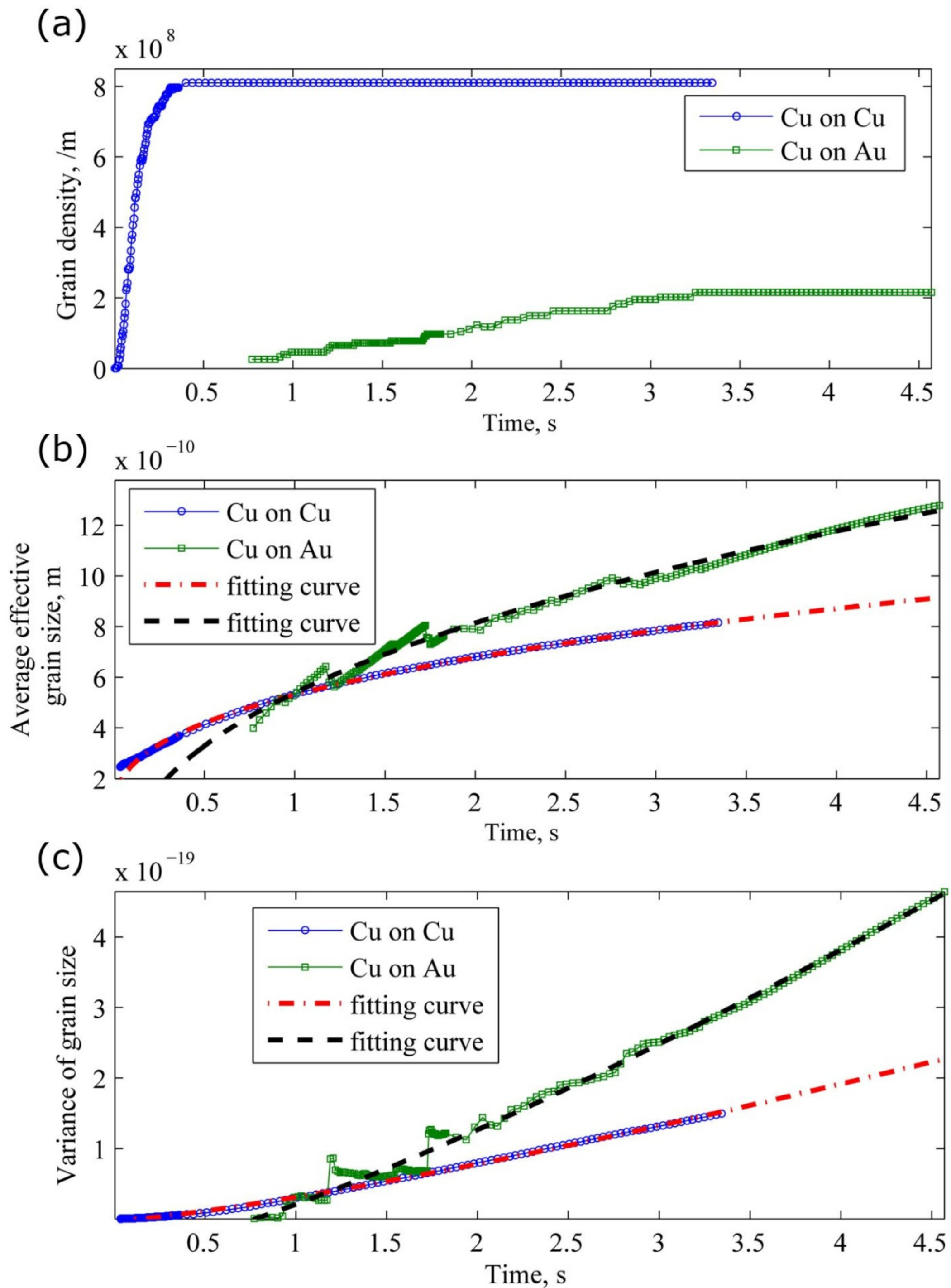

Fig. 4-6 the statistics on grain growth including the dependence of the grain density (a), the average effective grain size (b) and variance of the effective grain size (c) on deposition time.

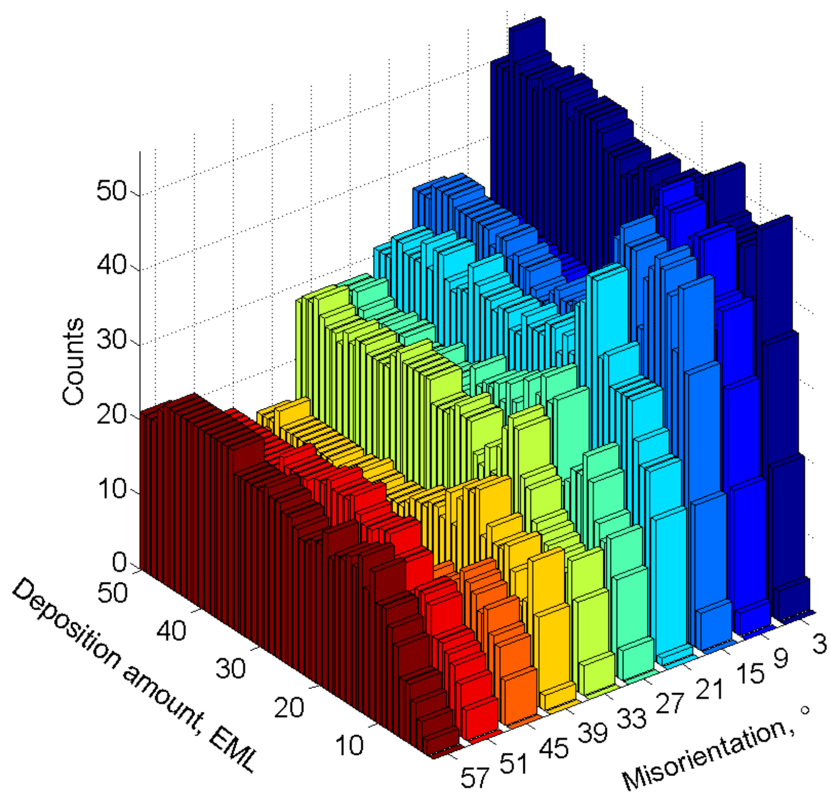

Fig. 4-7 Distribution and evolution of grain boundary misorientation for copper deposition on a Cu substrate

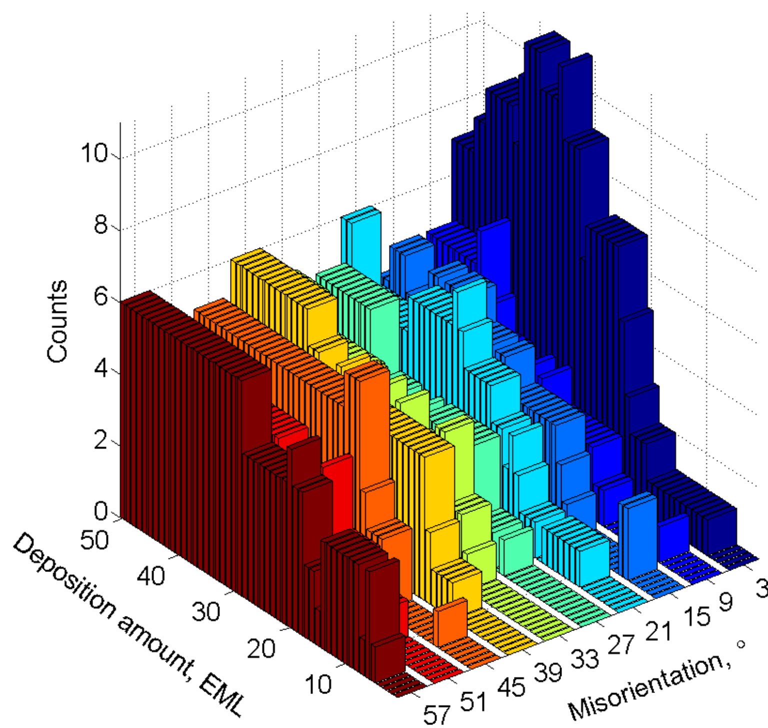

Fig. 4-8 Distribution and evolution of grain boundary misorientation for copper deposition on a Au substrate

The preference on low-angle boundaries is probably attributed to their lower energy as compared to high-angle boundaries. In terms of the distribution over time, the number of grain boundaries of a certain range of misorientation increases before about 20 EML for deposition on Cu and 30 EML for Au respectively and basically stabilizes afterwards.

4.4 Effects of the deposition parameters

Deposition parameters including applied electrode potential (P), concentration of Cu^{2+} ions in the electrolyte (C) and deposition temperature (T) were varied to study their effects on microstructures and grain growth history of deposits. Each deposition parameter was altered separately and collectively to look at the combined effects. The details about the variations are described in Table 4-2.

Table 4-2 Description of the combination of the deposition parameters for the simulations

Para. Set No.	P (V)	C (mol)	T (K)	Remark
1	-0.13	0.5	298	Reference parameters
2	-0.11	0.5	298	Low potential
3	-0.20	0.5	298	High Potential
4	-0.13	0.1	298	Low concentration
5	-0.13	0.5	313	High temperature
6	-0.11	0.1	313	Combination of low potential, low concentration and high temperature

4.4.1 Applied electrode potential

Fig. 4-9 presents a comparison of the simulated microstructures of Cu deposit on deposition of 50 EML on a Cu substrate using different sets of deposition parameters. In general, they all present the similar morphological features – fabric morphology and suppressed small grains near the deposit/substrate interface – as described earlier in this chapter. In comparison, the more negative the applied electrode potential, the finer the grain structure. At a lower potential of -0.11V, in Fig. 4-9, a few funnel-like grains as marked by a capital 'F' are distinctively larger than the rest of the columnar grains. Between them are other types of grains whose shapes and tilting direction are apparently dominated by their funnel-like neighbours. It indicates the dominance of the funnel- like grains during the grain growth. At higher potentials, the funnel-like grains seem to be less dominating.

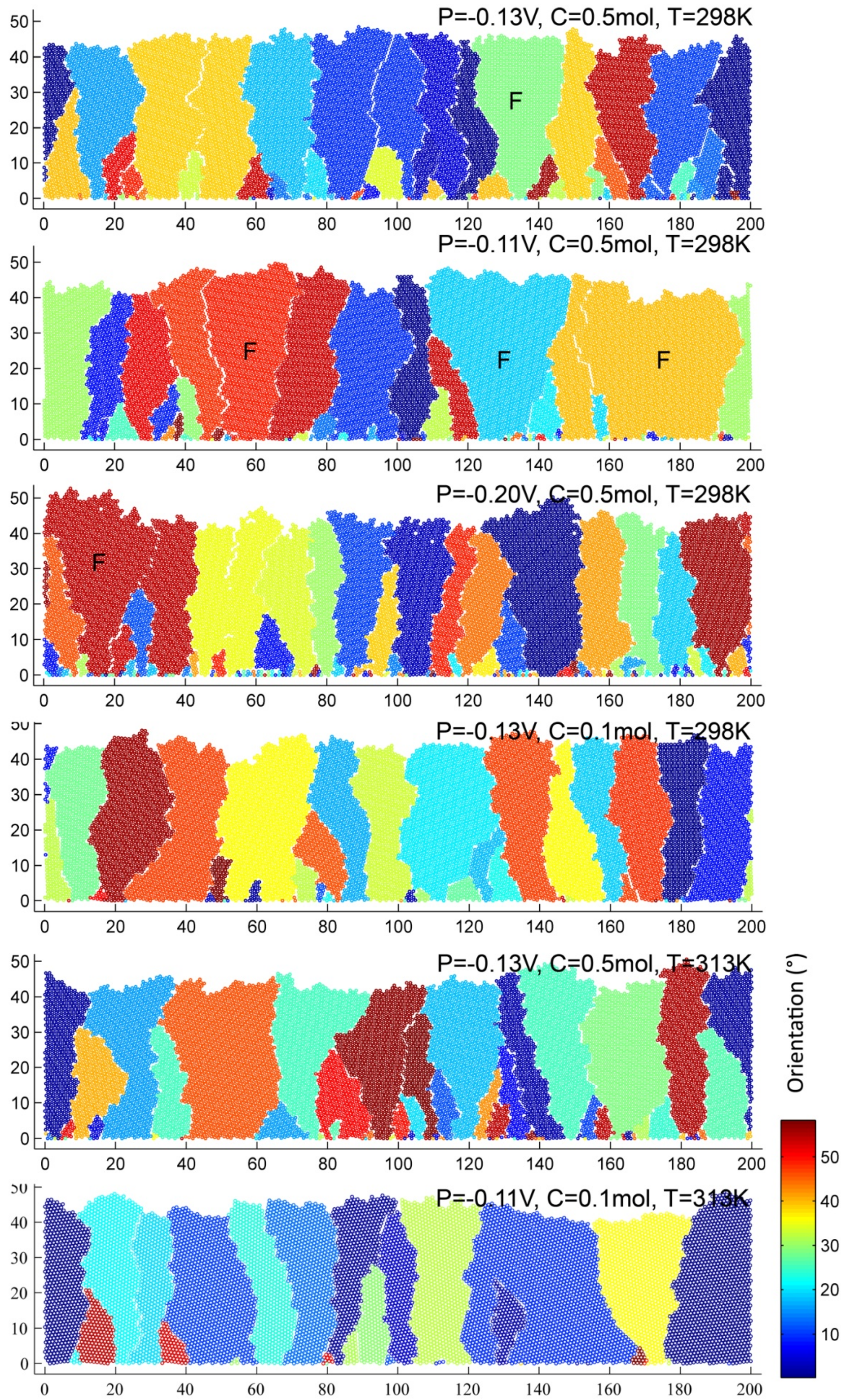

Fig. 4-9 Snapshots of the simulated microstructure on deposition of 50 EML Cu on a Cu substrate using different deposition parameters.

Fig. 4-10 shows the evolution of the grain density over growth of 50 EML Cu on a Cu substrate using different sets of deposition parameters. Generally, grain density soars to a saturation value and plateaus afterwards. It indicates a progressive nucleation process reaching the saturation when the nucleation saturates. The tangent slope of the grain density curves reflects the nucleation rate. Deposition parameters have various effects on the nucleation rate, growth rate, final grain density, average grain size and variance of the grain size. The values of some important statistical data reflecting grain growth history for deposition on both substrates are summarized and compared in Table 4-3.

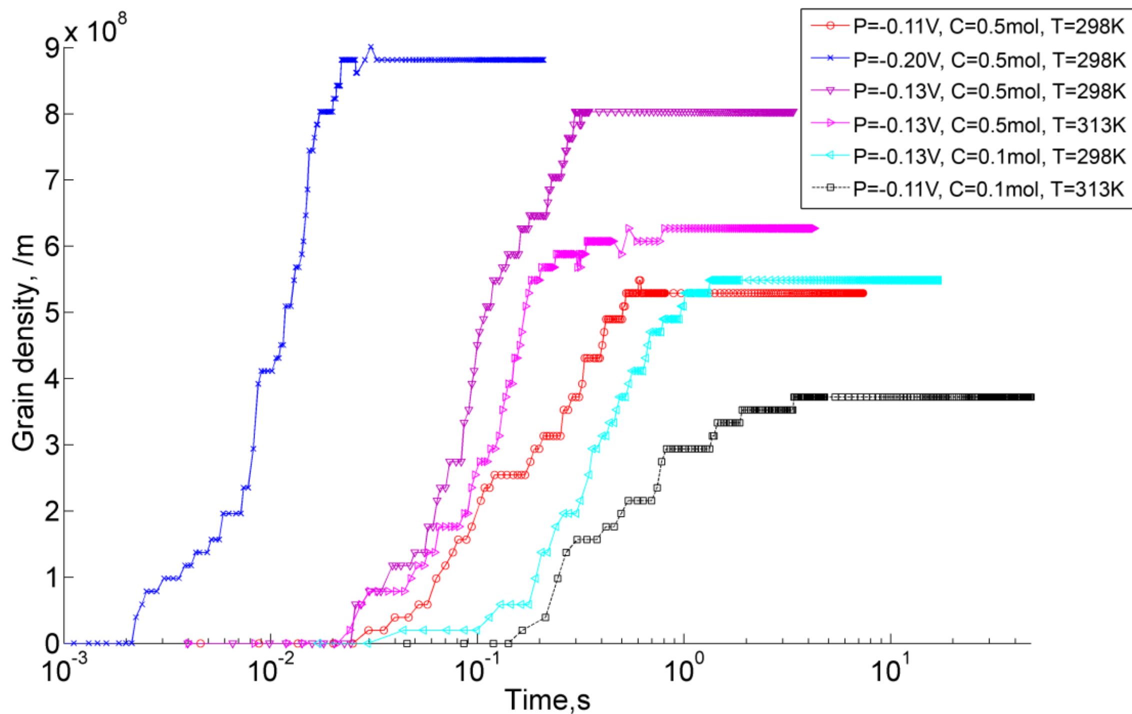

Fig. 4-10 Simulated grain density as a function of deposition time for the deposition of Cu on a Cu substrate using different deposition parameters.

It can be seen that a 15% (-0.02V) decrease of the applied electrode potential leads to more than twice longer deposition time; a 54% (-0.07V) increase shortens the deposition time by 16 times. At a lower potential of -0.11V, the grain density plateaus at 5.289×10^{8}/m, which is 35% less than that at -0.13V, within 0.526s, which is about 76% longer than that at -0.13V. At -0.2V, the time for reaching the saturation grain density has been reduced by ten times while the saturation value just rises by 9% in comparison with that at -0.13V. In conclusion, the more negative the applied electrode potential, the faster the nucleation and the higher the grain density. But the effects of potential on the

saturation grain density in the range between -0.11V and -0.13V are much more significant in comparison with the more negative range between -0.13V and -0.20V.

Table 4-3 Values of some statistical data of the grain growth history for deposition on a Cu substrate and a Au substrate.

Para. Set No.*	Deposition time, s		Saturation grain density, $\times 10^8$/m		Time reaching the saturation, s		Average grain size, $\times 10^{-10}$m		Variance of grain size, $\times 10^{-19}$	
	Cu	Au	Cu	Au	Cu	Au	Cu	Au	Cu	Au
1	3.387	4.244	8.031	1.959	0.298	2.709	8.163	13.06	1.307	4.476
2	7.358	12.42	5.289	2.742	0.526	8.051	9.384	11.65	1.817	2.705
3	0.209	0.267	8.814	1.959	0.022	0.168	7.9	13.06	1.288	4.476
4	17.09	26.93	5.484	2.938	1.335	17.01	9.291	11.4	1.509	3.015
5	4.281	6.065	6.628	3.33	0.805	3.303	8.875	10.93	1.322	2.104
6	47.64	57.94	3.722	1.567	3.408	34.92	10.58	14.06	1.695	3.607

* Refer to Table 4-2 for the detail of the deposition parameters

Fig. 4-11 and Fig. 4-12 show the evolution of the average grain size and the variance of the grain size over deposition of 50 EML Cu on a Cu substrate using different deposition parameters, respectively. From these, the more negative the applied electrode potential, the faster the growth, the smaller the average grain size and the less the variance. At -0.2V, in spite of a 54% increase of the applied electrode potential, the final average grain size and the variance of the grain size are just slightly smaller than at -0.13V while, at -0.11V, only a 15% decrease leads to a more significant increase of the grain size and the variance.

The distribution of the grain boundary misorientations over deposition of 50 EML Cu on a Cu substrate at -0.2V and -0.11V are presented in Fig. 4-13 and Fig. 4-14 respectively. Generally, both deposits show preferences in grain boundaries with a smaller misorientation. At -0.2V the preference steadily decreases with the misorientation while at -0.11V the smallest range of misorientations (0 - 6°) are distinctively favoured. Comparing them to Fig. 4-7, the distribution of the misorientation at -0.13V, it can be concluded that the less negative the potential, the stronger the preference.

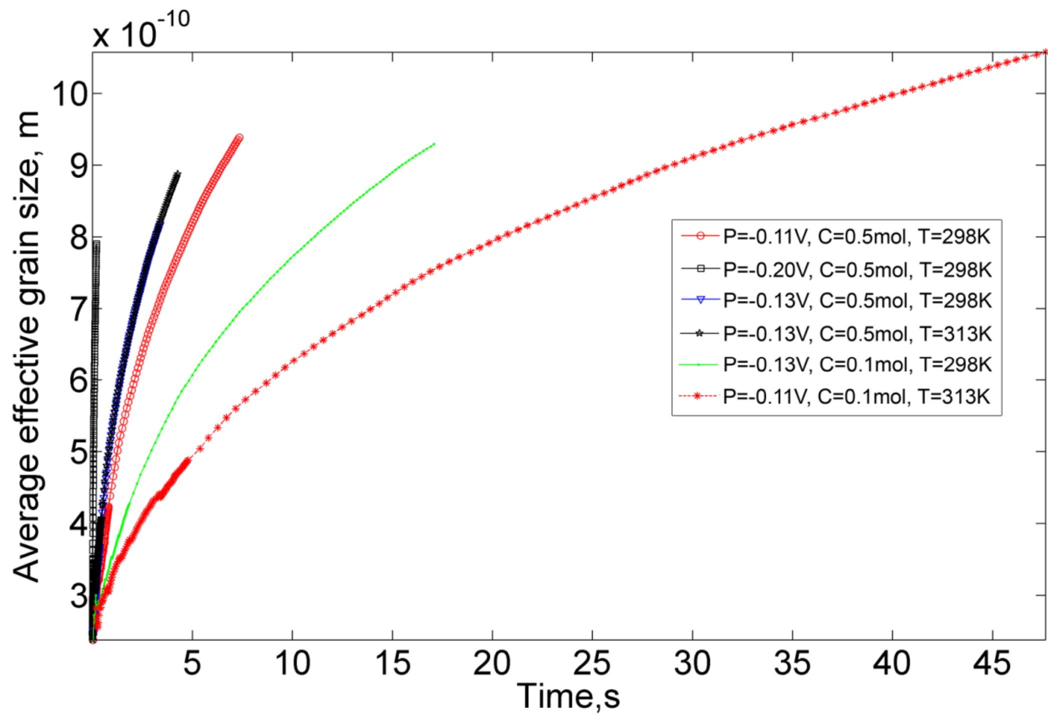

Fig. 4-11 Simulated average effective grain size as a function of deposition time for the deposition of Cu on a Cu substrate using different deposition parameters.

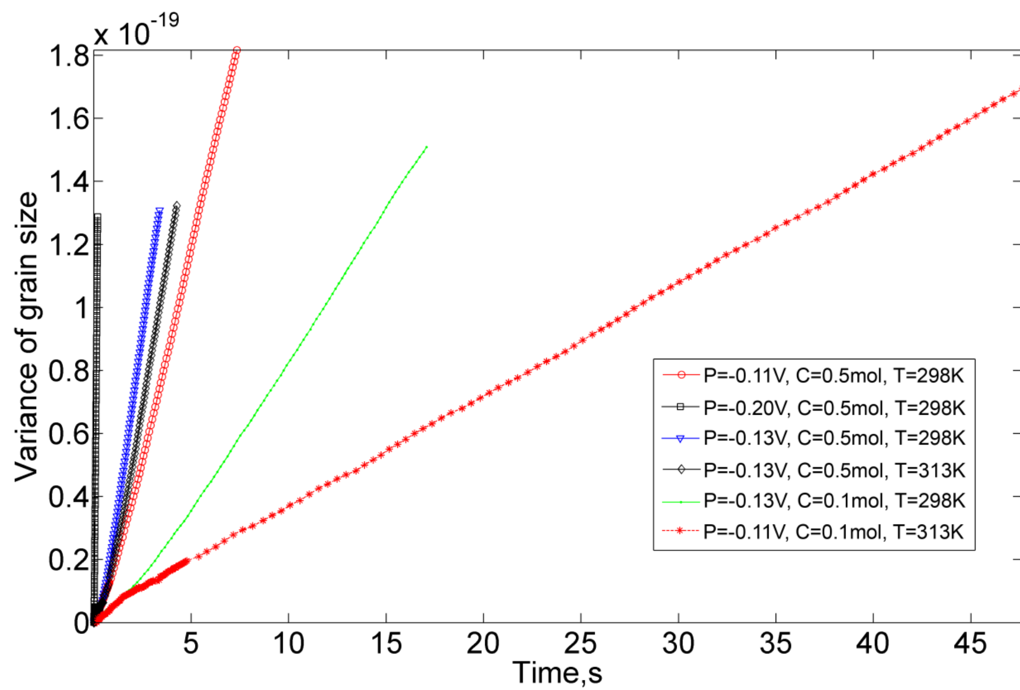

Fig. 4-12 Simulated variance of the grain size as a function of deposition time for the deposition of Cu on a Cu substrate using different deposition parameters.

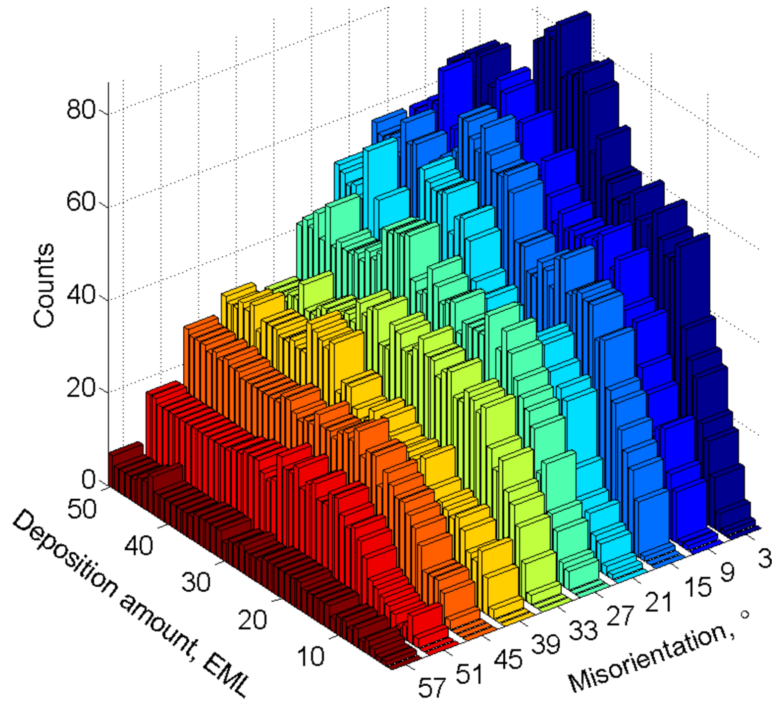

Fig. 4-13 The evolution and the distribution of the grain boundary misorientation for deposition on a Cu substrate at a potential of -0.20V.

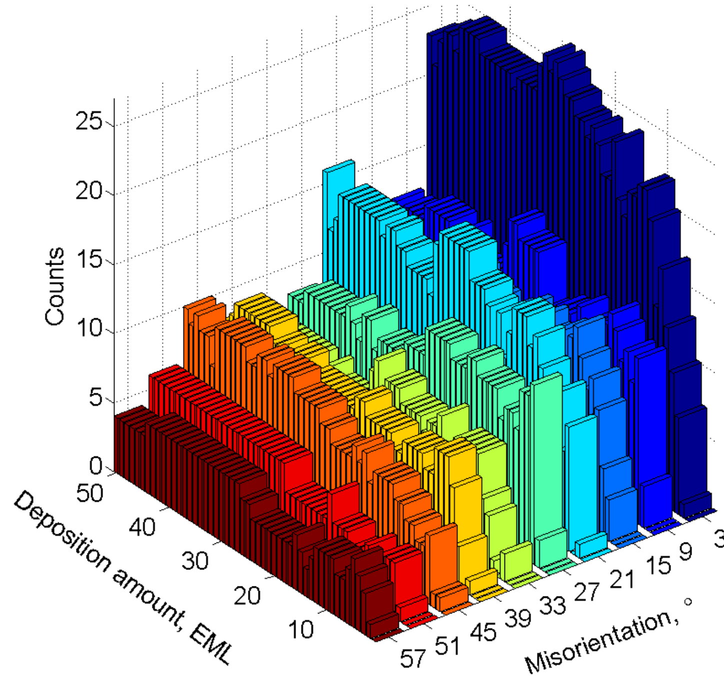

Fig. 4-14 The evolution and the distribution of the grain boundary misorientation for deposition on a Cu substrate at a potential of -0.11V.

Fig. 4-15 shows the snapshots of the simulated microstructures on deposition of 50 EML Cu on a Au substrate using different sets of parameters. By contrast with the deposition

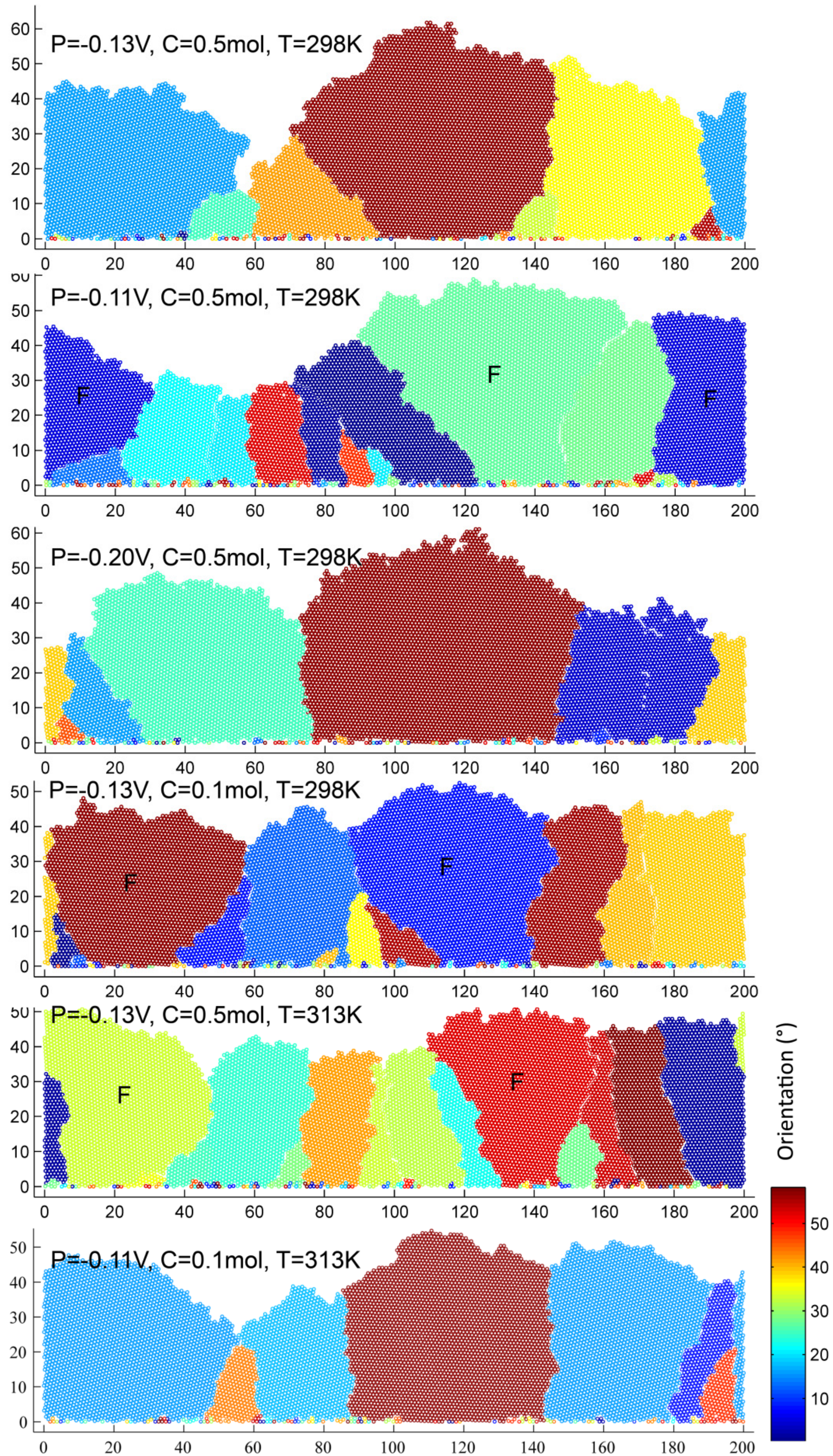

Fig. 4-15 Snapshots the simulated microstructure on deposition of 50 EML Cu on a Au substrate using different deposition parameters

on a Cu substrate, the effects of the applied electrode potential on the microstructure are seemingly inconclusive. The microstructure at -0.2V looks broadly similar to that at -0.13V and the average grain size and the variance of the grain size are exactly the same as shown in Table 4-3. At -0.11V, a few columnar and pyramidal grains are formed between two large funnel-like grains marked with 'F'. It is obvious that growth direction and the final shape of the former are dominated by the latter. Such phenomenon was also observed for the deposition on a Cu substrate at -0.11V. It is interesting that a smooth surface profile is formed as a result. And this phenomenon is repeatable. From the thermodynamic point of view, a smoother surface is more stable having lower surface energy. Such lower-energy surface profiles must be formed and maintained through diffusion since deposition events are insensitive to the energetic states of atoms.

The effects of the deposition parameters on the grain growth history for deposition on a Au substrate in terms of the evolution of the grain density, the average grain size and the variance of the grain size are quantitatively evaluated in Fig. 4-16, Fig. 4-17 and Fig. 4-18 respectively. Similar to Cu substrate, the more negative the applied electrode potential, the faster the nucleation and the growth. The steps and sawteeth of the curves are due to the dominant growth of some grains as explained earlier. The distribution and evolution of the misorientation for deposition on a Au substrate at -0.2V and -0.11V are illustrated in Fig. 4-19 and Fig. 4-20 respectively. Accordingly, there are slightly more low-angle grain boundaries. At -0.2V, the number of the misorientations of 0-6° is larger than the rest over which the misorientations are evenly distributed. At -0.11V, however, the distribution of the misorientations is more or less inconclusive, which is probably owing to the small sample space for the statistical analysis. Therefore, a larger simulation cell may be beneficial for a better statistic analysis for the simulation of the deposition on a Au substrate.

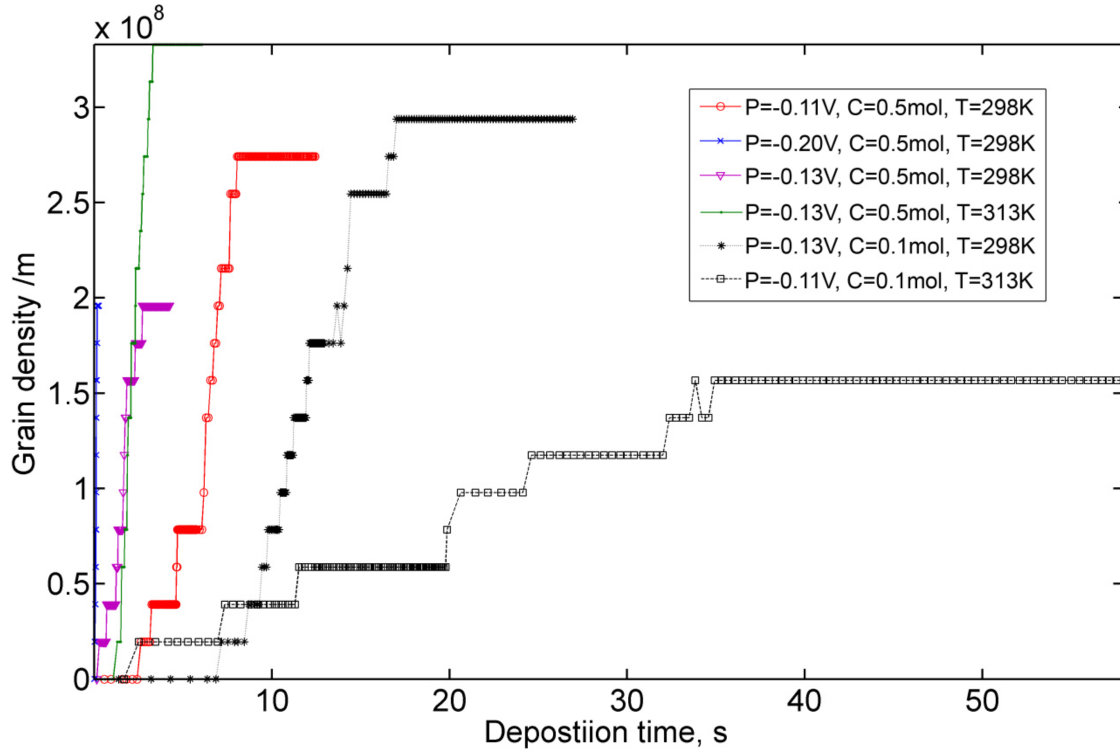

Fig. 4-16 Simulated grain density as a function of deposition time for the deposition of Cu on a Au substrate using different deposition parameters.

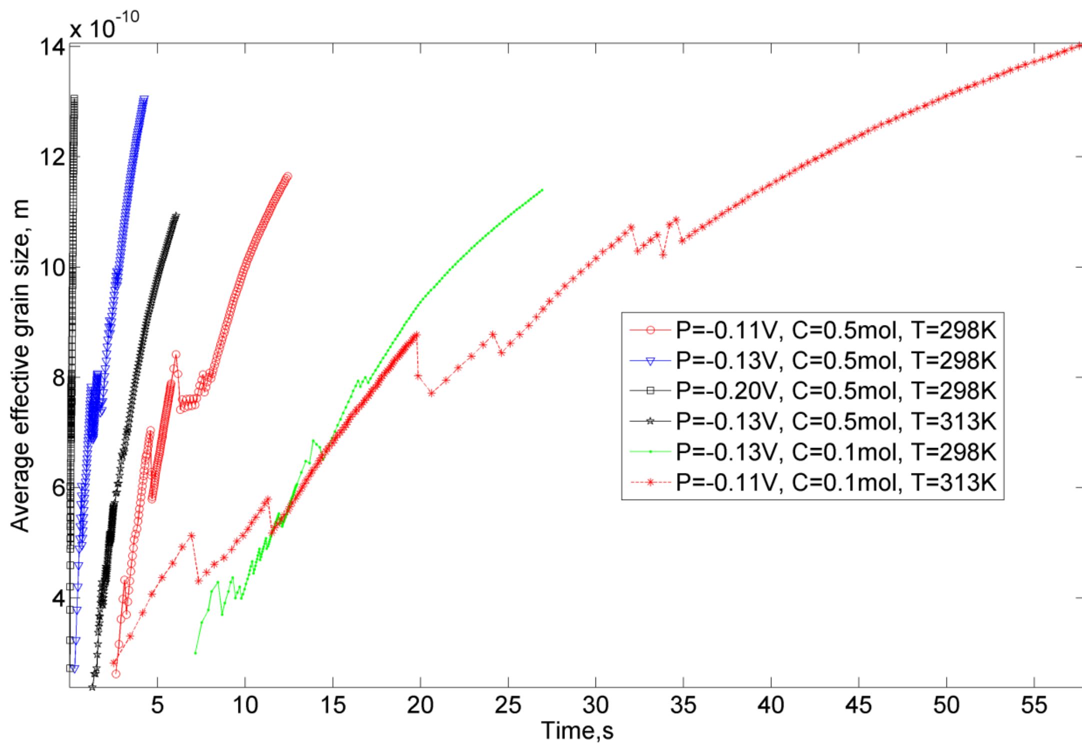

Fig. 4-17 Simulated average grain size as a function of deposition time for the deposition of Cu on a Au substrate using different deposition parameters.

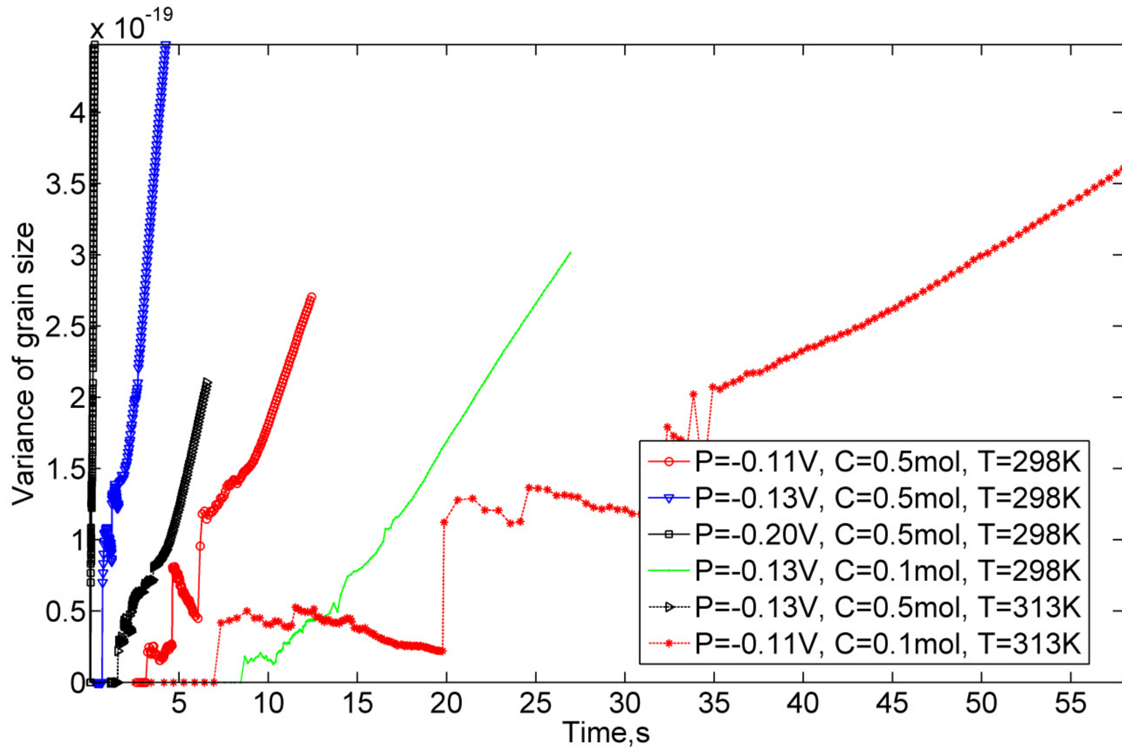

Fig. 4-18 Variance of the grain size as a function of deposition time for the deposition of Cu on a Au substrate using different deposition parameters.

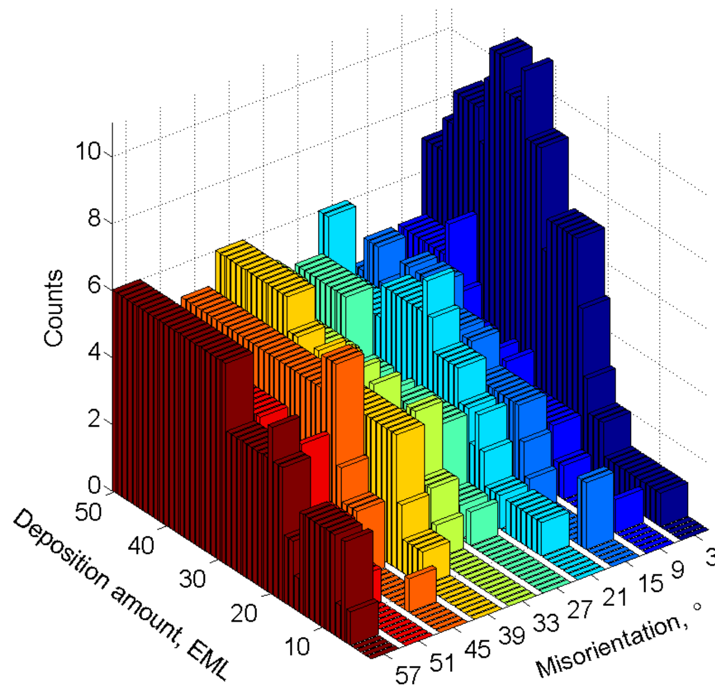

Fig. 4-19 The evolution and the distribution of the grain boundary misorientation for deposition on a Au substrate at -0.20V

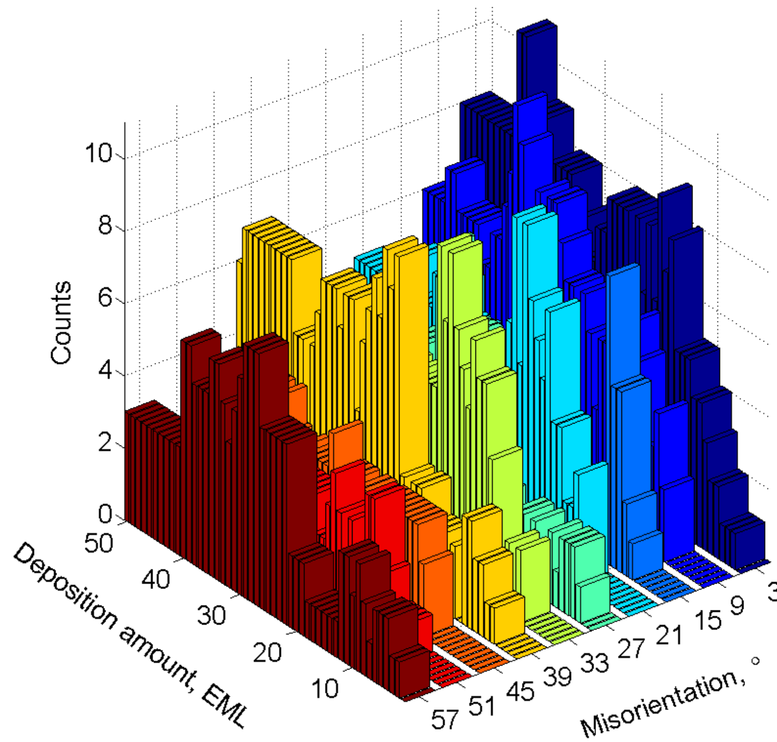

Fig. 4-20 The evolution and the distribution of the grain boundary misorientation for deposition on a Au substrate at -0.11V

4.4.2 Concentration of cupric ions

Concentration of cupric ions in the electrolyte was also varied. For deposition on a Cu substrate, at a concentration of 0.1mol the deposit morphology looks similar to that at 0.5mol as shown in Fig. 4-9. However, most of the grains present an irregular shape consisting of a number of unit shapes, which suggests a more competitive growth owing to the reduced concentration of Cu^{2+} ions. The average grain size is increased by about 14% and the variance is increased by 15.5% as illustrated in Table 4-3. Diluting the electrolyte has a dramatic effect on the growth kinetics. At 0.1mol, the time for reaching the saturation grain density and the total deposition time are five times as long as using a five times more concentrated electrolyte, which means the nucleation and growth rate increases linearly with concentration of the cupric ions. The evolution of the distribution of grain boundary misorientation for deposition on a Cu substrate at 0.1mol is presented in Fig. 4-21. We can clearly see the preference of grain boundaries on smaller misorientations. In comparison with Fig. 4-7, there is a bigger difference between the number of the grain boundaries of misorientations of 36-60° and the rest. It indicates that it is more difficult for high-angle grain boundaries to form at low concentration.

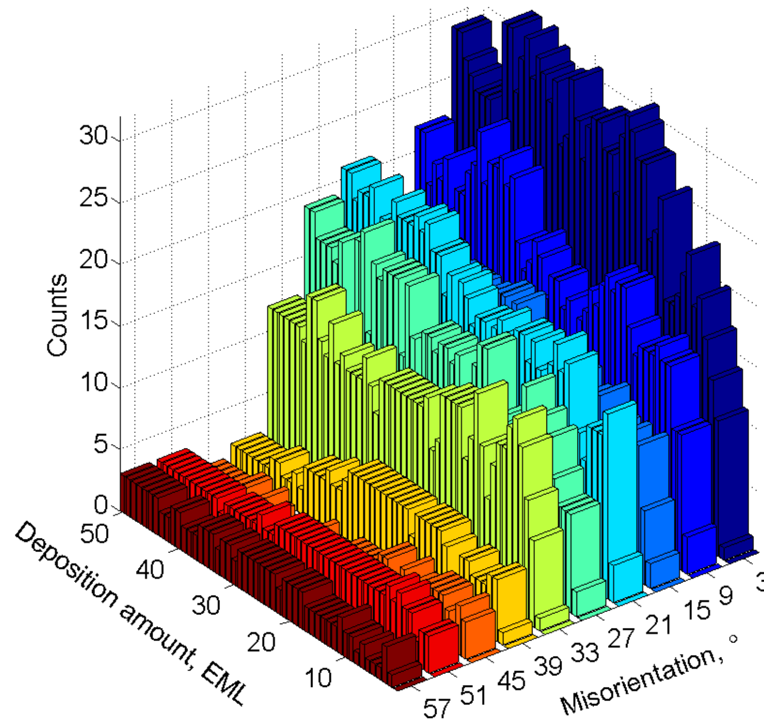

Fig. 4-21 The evolution and the distribution of the grain boundary misorientation for deposition on a Cu substrate at a lower concentration of Cu^{2+} ions of 0.1mol.

For the deposition on a Au substrate, the effects of the dilution are significant as shown in Fig. 4-15. The deposit surface is smoother than at 0.5mol. The average grain size and the variance are both reduced. The nucleation and growth at 0.1mol on a Au substrate slowed down by more than 6 times. The saturation value of the final grain density is increased by 50%. These effects are significant compared to those on a Cu substrate. Fig. 4-22 shows the evolution and distribution of misorientation for deposition on a Au substrate at 0.1 mol. It is distinctive that after about 20 EML and 40 EML, the number of the high-angle boundaries of 54-60° and 48-54°, respectively, are comparable with the number of lower-angle boundaries in the range of 0-12°. There is basically no significant preference on the smaller misorientations throughout the growth history.

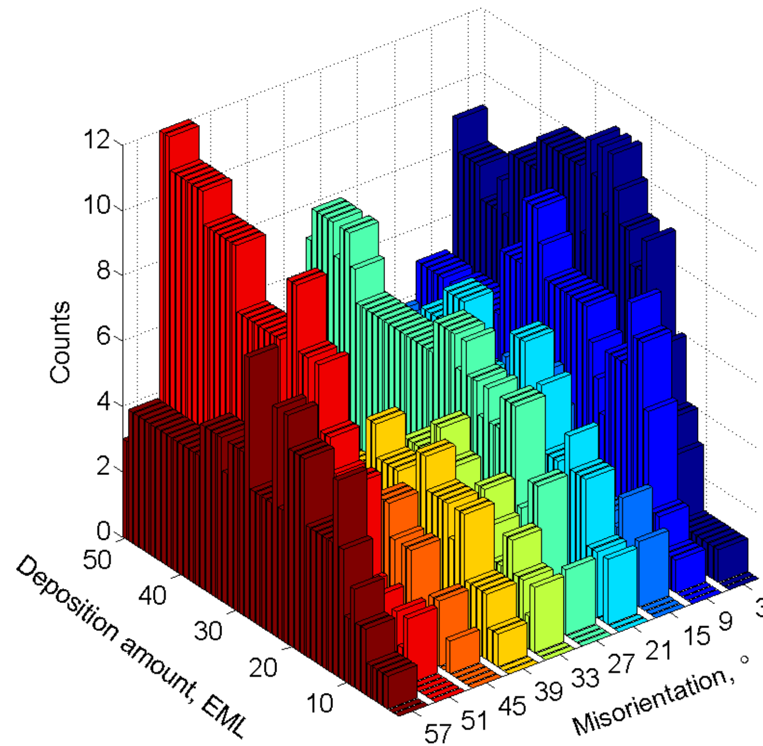

Fig. 4-22 The evolution and the distribution of the grain boundary misorientation for deposition on a Au substrate at a lower concentration of Cu^{2+} ions of 0.1mol.

4.4.3 Temperature

Increasing the deposition temperature by 15K has an effect on the deposit microstructure as shown in Fig. 4-9. The average grain size is increased by about 9% and the variance of the grain size is slightly increased. The effects on the evolution of the grain statistics are distinct from the other deposition parameters. The time for reaching the saturation grain density is increased by about 170%. The grain growth rate after the saturation is similar to that at 298K according to the almost overlapped curves while the variance of the grain size evolves more slowly as illustrated in Fig. 4-12. The distribution of misorientation for the deposition on a Cu substrate at 313K is shown in Fig. 4-23. The number of the grain boundaries decreases steadily with the misorientation. In terms of the distribution over deposition amount, it increases with deposition amount before 10-15 EML and basically stabilizes after that. In comparison with Fig. 4-7, the high-angle boundaries of the misorientation in the range of 48-60° are significantly less than the low-angle ones as observed at 313K.

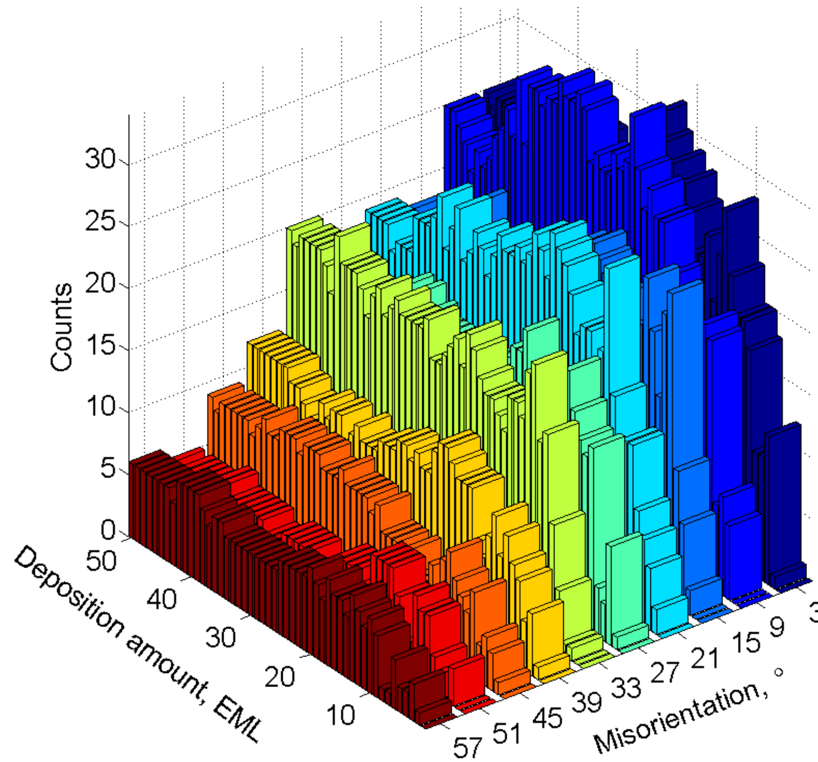

Fig. 4-23 The evolution and the distribution of the grain boundary misorientation for deposition on a Cu substrate at a higher temperature of 313K.

For deposition on a Au substrate, increasing the temperature by 15K has a significant effect on the microstructure and grain growth history. The grain density is significantly increased as shown in Fig. 4-16, on account of which, the average grain size is greatly reduced. The variance of the grain size is dramatically reduced as well as shown in Fig. 4-18. The curve corresponding to the evolution of grain density for deposition on a Au substrate before saturation roughly overlaps with the one at 298K, which indicates the insignificant effects on the nucleation rate in spite of an increased final grain density. However, it shows negative effects on the growth rate as shown in Fig. 4-17 and Fig. 4-18, respectively. Fig. 4-24 presents the distribution of the grain boundary misorientation for deposition on a Au substrate at 313K.

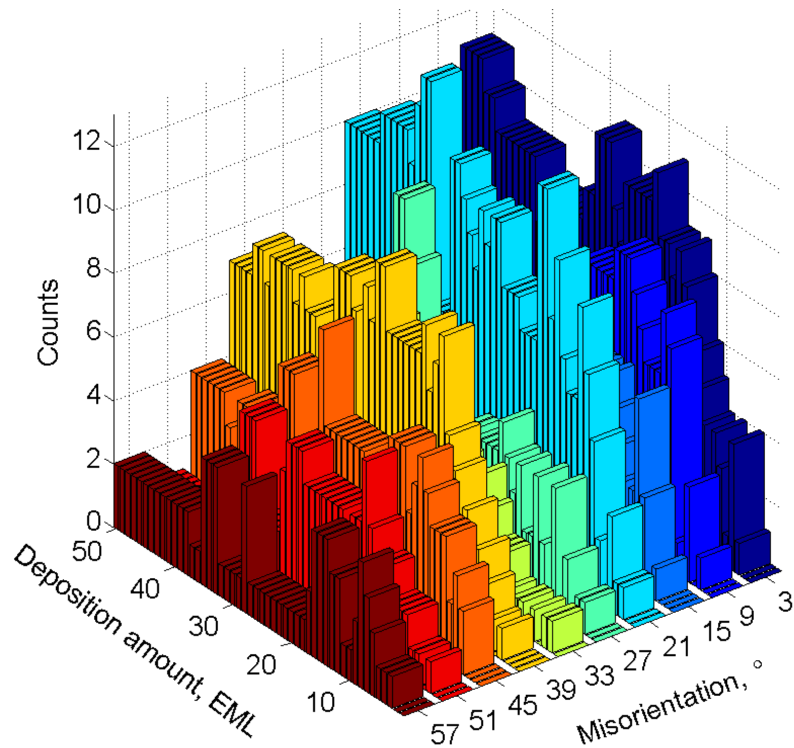

Fig. 4-24 The evolution and the distribution of the grain boundary misorientation for deposition on a Au substrate at a higher temperature of 313K.

It is worth noting that the temperature was changed in a relatively small range: 298-313K, based on the specific application of this project as has been explained in the Introduction. Electrodeposition in the field of electronic manufacturing is usually applied at room temperature, at approximately 25°C. It is on account of the pre-designed photoresist template used for our bumping process, which can be considerably damaged above 40°C. From the literature, varying temperature even in a seemingly small range, e.g. 25°C -45°C [130], can lead to obvious changes on the structure of a copper deposit.

4.4.4 Combination of parameters

These deposition parameters were also varied collectively to look at the combined effects. A set of parameters including a lower potential at -0.11V, a lower concentration cupric ions at 0.1mol and a higher temperature at 313K was selected as an example to show the combined effects of these deposition parameters.

For deposition on a Cu substrate, at the above-stated conditions the grain density is greatly reduced and the average grain size is increased in comparison with that at any of the reference parameters, the low potential at -0.11V or the high temperature at 313K,

as can be seen in Fig. 4-10, Table 4-3, and Fig. 4-11; the variance of the grain size is larger than that at the reference parameters, the high temperature at 313K as well as the low concentration at 0.1mol but smaller than that at the low potential at -0.11V as shown in Table 4-3 and Fig. 4-12. It was found earlier that lowering the applied electrode potential, diluting the electrolyte or increasing the temperature separately reduced the average grain size by approximately 14.9%, 13.8% and 8.7, respectively. The collective effects are more significant. The grain size under the combined parameters is increased by 32.9%, which is slightly less than the sum of decreases caused by varying them separately. Reducing the applied electrode potential led to an increase of variance of the grain size by 39.0%, while diluting the concentration and increasing the temperature resulted in a drop of the variance of the grain size by 15.5% and 1.2%, respectively. Collectively, the variance is increased by 29.7%, which is about 7% less than the algebraic summation of the variation rate of the variance.

In contrast, for deposition on a Au substrate, the combined effects are more complicated. Varying the deposition parameters separately led to an increase of the grain density, a decrease of the grain size and a significant reduction of the variance of the grain size for deposition on a Au substrate. By changing them collectively, however, the effects on the grain density and grain size are quite contrary – i.e. a decrease of the grain density and an increase of the grain size. And the variance of the grain size is just slightly reduced in comparison with that at the reference parameters.

For both substrates, the deposition is dramatically slowed down at the combined conditions. The times for reaching a plateau and total deposition times are increased by more than 10 times.

4.4.5 Dependence on substrate

The effects of the deposition parameters on microstructure, average grain size and the variance of grain size, saturation grain density and the time of reaching the saturation are found to be largely dependent on substrates. At each KMC step, an event is stochastically selected at a probability proportional to its rate. For deposition on a Cu (native) substrate, the rate for deposition at any site is the same. The nucleation process at its initial stage, which largely determines the final microstructure, is governed by the

competitions between the events of deposition and diffusion. For deposition on a Au (foreign) substrate, however, the deposition rates on pre-deposited Cu or Au are different. The nucleation at the initial stage is influenced by the competition among the events of deposition on the Au, on the pre-deposited Cu, as well as the diffusion events. According to the equation (4.1) and (4.2), concentration of cupric ions and applied electrode potential have effects on the deposition rates but have no effect on the diffusion rates. Therefore, they effect the differences between the deposition rates on pre-deposited Cu and substrate, Δr, through which, their effects can be qualitatively predicted. Deposition temperature has effects on both deposition rates and diffusion rates. Therefore, it effects not only the Δr but also the difference between the depsition rates and diffusion rates. Fig. 4-25 shows the dependences of the deposition parameters on Δr whose values are mapped to colours indicated by the colour bar. Generally, the smaller the Δr, the more chance for the deposition event on the substrate i.e. nucleation to occur, which accounts for the larger grain density and smaller average grain size at the low potential of -0.11V, low concentration of 0.1mol and the high temperature of 313K for deposition on a Au substrate. Without considering the competition of the diffusion rate, at higher potentials and higher concentrations, growth of existing nuclei is more dominant and there is less chance for further nucleation. Consequently, the grain population is small and grains are large. At the combined parameters however, the combined effects are not only determined by Δr, but also the changes in the diffusion rates and the differences between the deposition rates and diffusion rates. The deposition rate reduces so significantly and diffusion rate increases at the same time as such diffusion events become dominating. Therefore, the final grain density is small and the average grain size is larger.

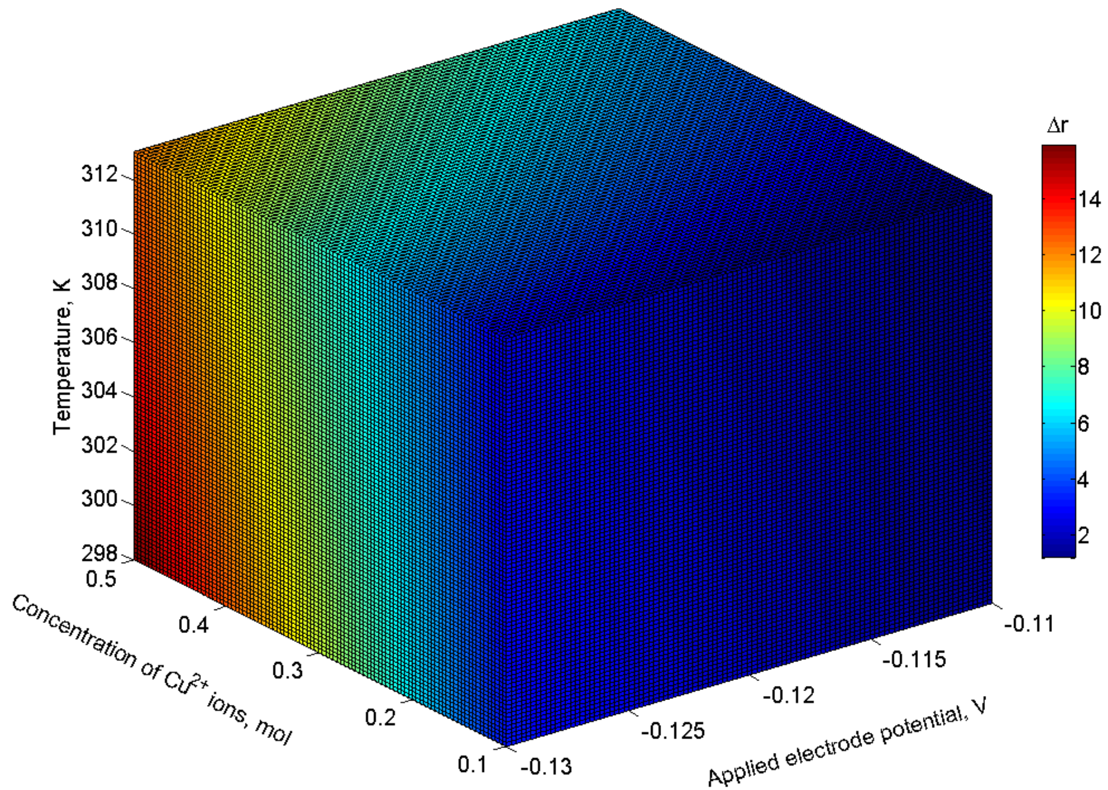

Fig. 4-25 Dependences of the difference between the deposition rates on substrate and on a pre-deposited Cu, Δr, on the deposition parameters. The colors show difference of the deposition rates.

4.5 Effects of the jump frequency

The value of the jump frequency was assumed to be 1.5×10^{6} s^{-1} in the simulations discussed above. Fig. 4-26 shows the snapshots of the simulated microstructure for deposition on a Cu or a Au substrate using the jump frequency of 1.5×10^{7} s^{-1} and 1.5×10^{8} s^{-1}. For deposition on both substrates, the simulated microstructures at different values of jump frequency look broadly similar to that at 1.5×10^{6} s^{-1} in spite of the slight differences in the grain population. It is discernible that at the higher jump frequency of 1.5×10^{8} s^{-1}, the free surfaces of grains are smoother at an atomic scale, which is attributed to the enhanced diffusion owing to the increased diffusion rate. Fig. 4-27, Fig. 4-28 and Fig. 4-29 show the evolution of the grain density, the average grain size and the variance of the grain for deposition on a Cu and a Au substrate, respectively.

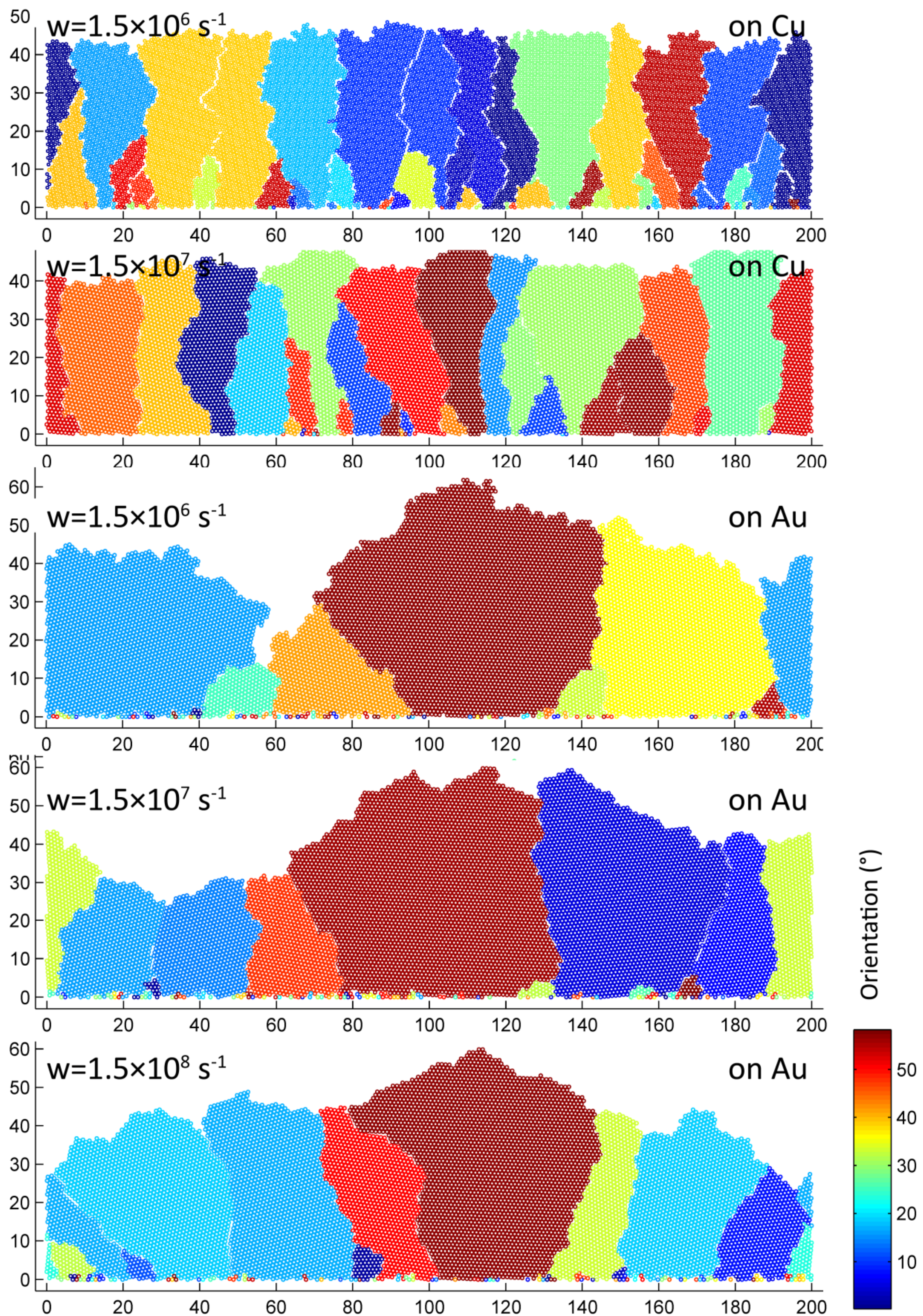

Fig. 4-26 Snapshots of the simulated microstructure for deposition on Cu or Au substrate using different values of jump frequency w

For deposition on a Cu substrate, the time to reach a plateau of the grain density is shorter, and the saturation grain density is much smaller at the higher jump frequency

while the total deposition time has not significantly changed. This can be ascribed to the fact that at a higher jump frequency, surface diffusion of adatoms is promoted, hence the nucleus density is reduced. The average grain size at the medium jump frequency is larger throughout the deposition and the difference increases steadily within about the first 1.5 seconds, and then remains nearly unchanged afterwards as shown in Fig. 4-28. The effects on the variance of the grain size are insignificant within the first 1.5 seconds. After that the variance is slightly smaller at the medium jump frequency as can be seen in Fig. 4-29.

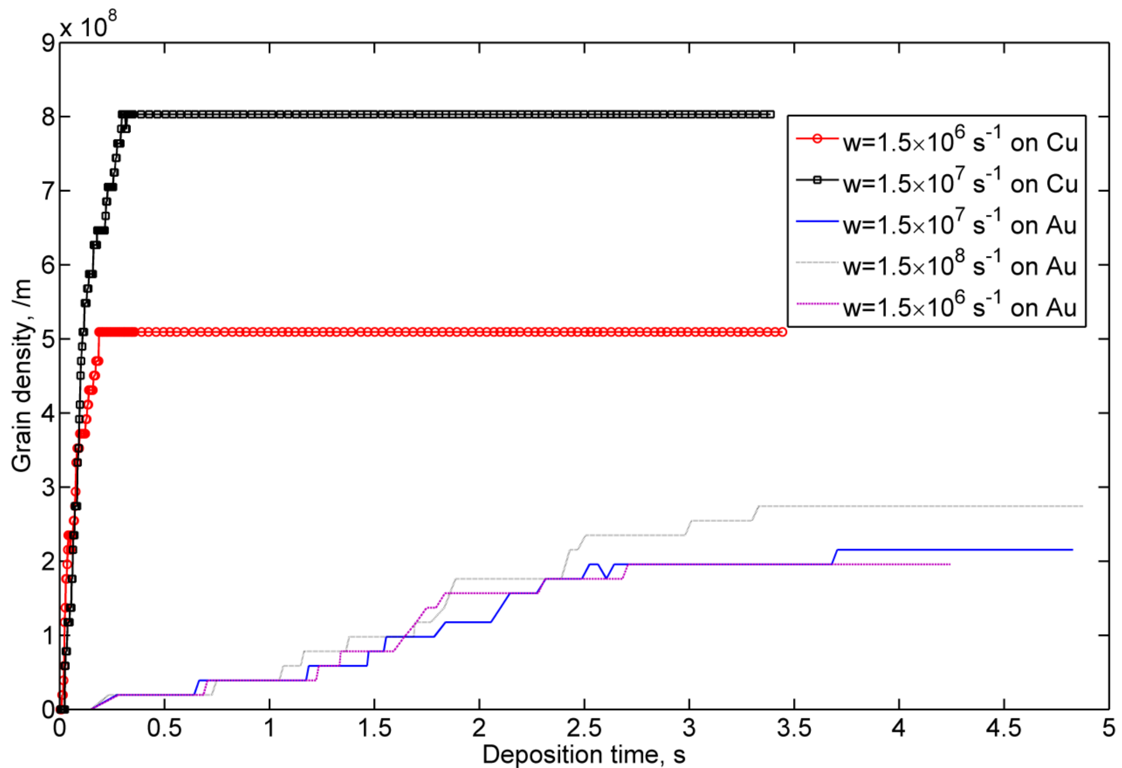

Fig. 4-27 Grain density as a function of time for deposition on a Cu or a Au substrate at different values of jump frequency.

For deposition on a Au substrate, the higher the jump frequency, the smaller the average grain size and the variance of the grain size, and the slightly slower the growth as can be seen in Fig. 4-26, Fig. 4-28 and Fig. 4-29. It has an insignificant effect on the nucleation rate at the medium jump frequency as shown in Fig. 4-27. At the high jump frequency, the time for reaching the saturation is longer and the saturation value of the grain density increased.

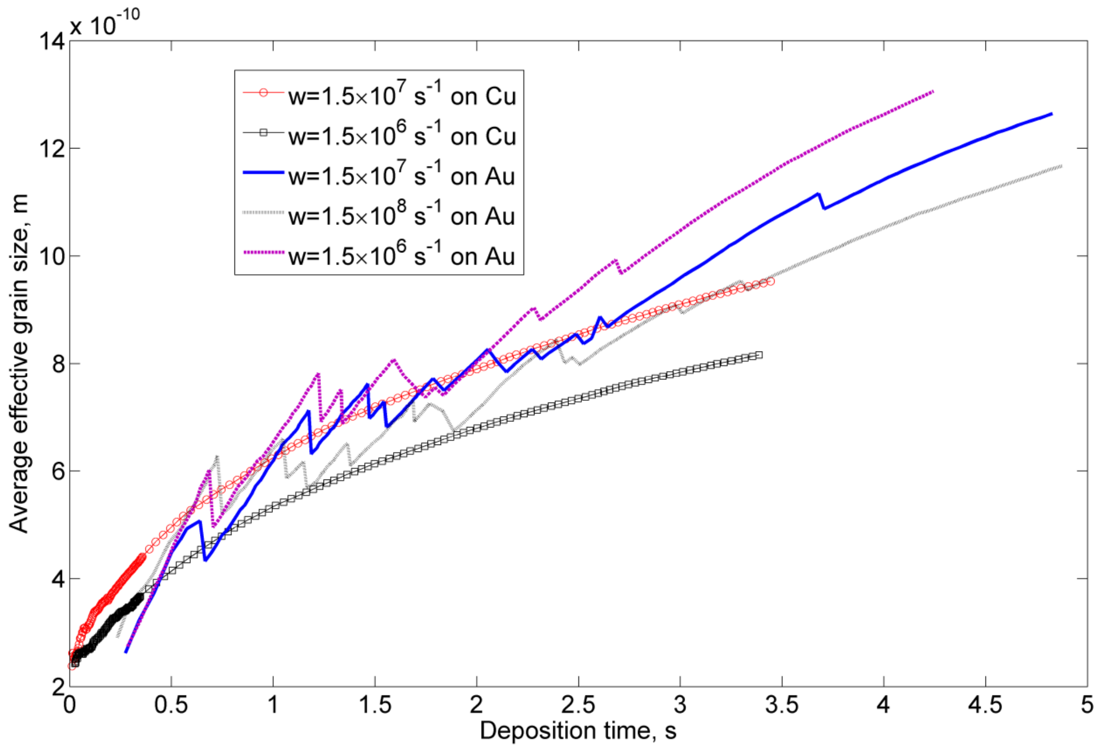

Fig. 4-28 Average effective grain size as a function of time for deposition on a Cu or a Au substrate at different values of jump frequency.

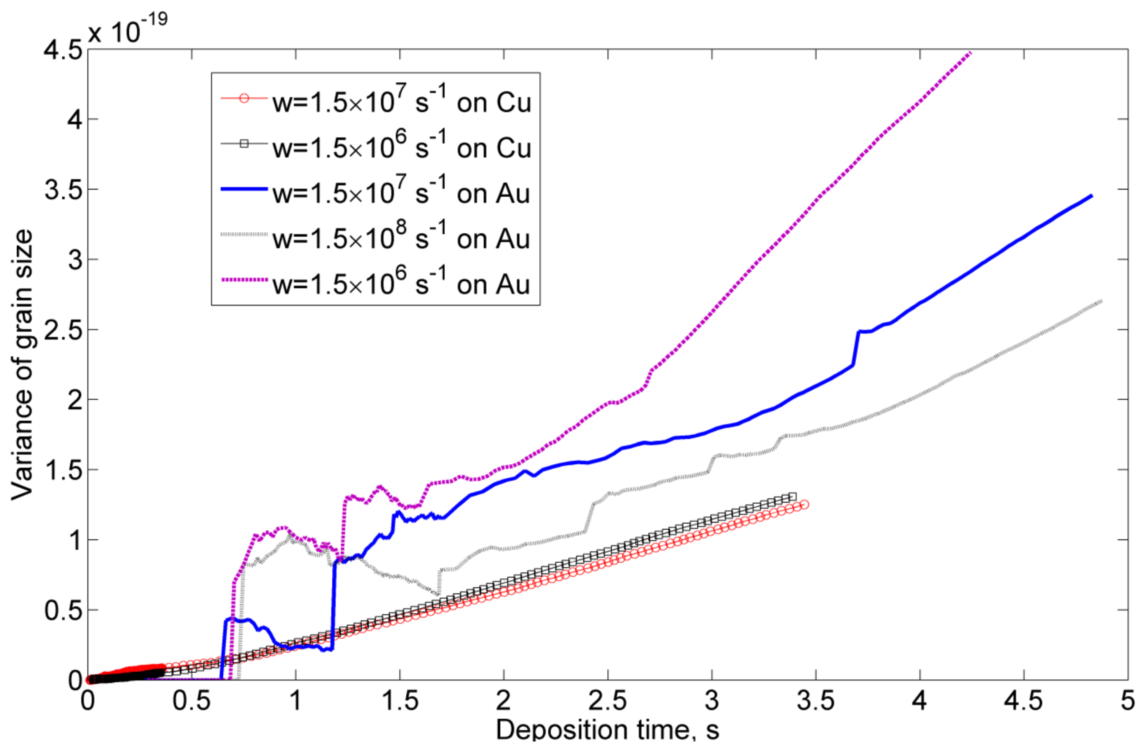

Fig. 4-29 Variance of grain size as a function of time for deposition on a Cu or a Au substrate at different values of jump frequency.

4.6 Conclusions

A 2DCSP-KMC model has been developed for the simulation of electrodeposition of polycrystalline copper on a copper or gold substrate. With this model, the early-stage nucleation and the grain growth after impingement of the nuclei can be studied as a whole process and the entire growth history reconstructed in terms of the evolution of microstructure, grain statistics and grain boundary misorientation. The growing-over growth mechanism is visualized by the simulation. The growth of the grains fits well with the power law. The simulated distribution of grain boundary misorientation shows preference for the most stable boundaries, which indicates that the energetic state of grain boundaries have been captured in the simulations by introducing the concepts of strange coordination number and correction coefficient. The model has also proved capable of capturing the various effects of the deposition parameters including applied electrode potential, the concentration of cupric ions and temperature. Their effects were found to be largely dependent on substrates. For deposition on a Cu substrate, generally, the more negative the applied electrode potential, the faster the nucleation, the higher the saturation grain density, the smaller the average grain size, the less the variance of the grain size and the less significant the preference on low-angle grain boundaries. Diluting the electrolyte leads to an increase of grain size and variance of the grain size, a decrease of the nucleation and growth rate and an increase of the preference on the low-angle boundaries. Increasing deposition temperature results in an increase of grain size and the variance of the grain size, accelerates the nucleation process but has an insignificant effect on the growth rate. Varying the related parameters collectively led to combined effects. For deposition on a Au substrate, the effects of the applied electrode potential on the microstructure and the misorientation are more or less inconclusive. Its effects on the nucleation and growth rates are same as on a Cu substrate. Diluting the electrolyte has a significant effect on the microstructure and misorientation but an opposite effect on average grain size, grain density, variance of the grain size nucleation rate and growth rate in comparison with a Cu substrate. Increasing deposition temperature reduces grain size and variance of the grain size, but has insignificant effects on nucleation rate and a negative effect on growth rate, different effects on misorientations as compared to a Cu substrate. Varying them

collectively increases grain size and decreases grain density, and has a less significant effect on grain size and similar effects on the growth and nucleation rate, in comparison with the effects on a Cu substrate. Increasing the value of the jump frequency promotes diffusions and thereby has some effects on the microstructure and the growth history.

Chapter 5 Materials and Experimental Methods

In this chapter, the materials and experimental methods of this thesis are described.

5.1 Fabrication of micro- copper columns by electroplating and materials

Fig. 5-1 illustrates the fabrication of micro- copper columns by electroplating, which generally includes four processes: metallization (Fig. 5-1a), patterning (Fig. 5-1b-d), electroplating (Fig. 5-1e) and etching (Fig. 5-1f). Each process and the materials involved are described in detail as follows.

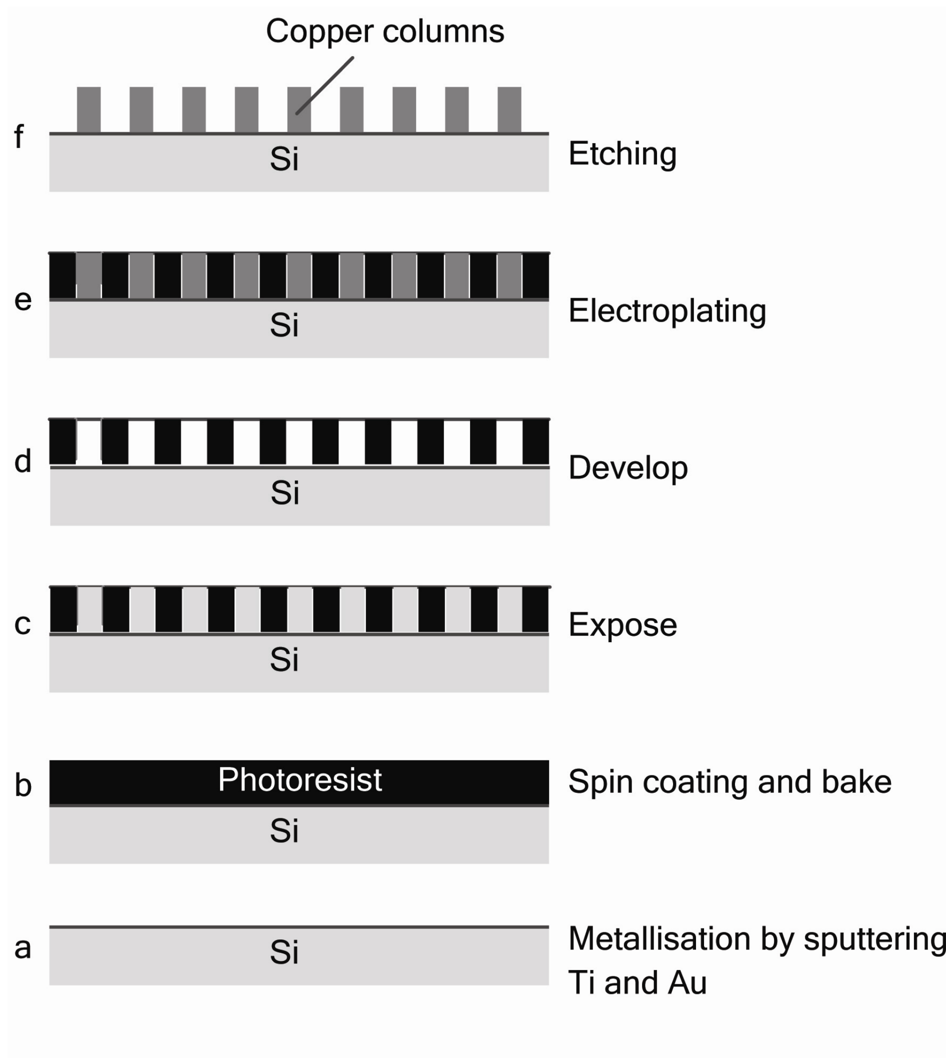

Fig. 5-1 Process flow for fabrication of micro- copper column by electroplating

5.1.1 Si wafer

Single-crystal silicon wafers made by Compart Technology Ltd in the UK were used as test wafers. Detailed specifications are described as follows:

Items	Descriptions
Growth method:	Czochralski
Grade:	Virgin Test
Diameter:	76.20 ± 0.30mm (3.00")
Orientation:	<100> ± 1°
Type/dopant:	p/Boron
Finish:	polished on one side/reverse etched

5.1.2 Metallization

The test wafers were metalized by sputtering 150nm of Ti followed by 100nm of Au to provide a conductive seed layer for subsequent electroplating. The Ti layer acts as an adhesion layer to guarantee a good adhesion between the seed layer and the Si substrate because Si and Au have relatively poor adhesion. Au was selected as the seed layer material because it combines good conductivity and excellent oxidation resistance. As no further chemical or mechanical pre-treatment is needed, the as-sputtered Au seed layer is the initial surface state where copper nucleation starts. The Au seed layer is very smooth with a roughness of 14.62nm. And it is a polycrystalline film with extremely fine grain size of 38.6nm and a strong (111) structure. More details about the seed layer can be found in Chapter 6.

5.1.3 Patterning

Photolithography was utilised to provide a template suitable for electroplating of copper columns. A layer of AZ-9260 (Clariant) photoresist of a nominal thickness of 24μm was deposited onto a pre-metallized test wafer by spinning coating. It was then baked at 80 °C for 2 minute followed by 100 °C for 4 minutes. The coated photoresist was then exposed to the UV light of 1000 mJ/cm^2 through a mask with pre-designed patterns for micro- copper columns. The exposed photoresist was subsequently developed using a commercial alkaline developer (AZ400, Clariant). Finally it was rinsed with deionised (DI)

water and then dried by compressed nitrogen. All the patterning processes were done in a clean room.

A positive photoresist AZ9260 photoresist is chosen because it is suitable for high-aspect-ratio structures [131]and easy to be stripped after plating. A customized glass photo mask with chrome films of pre-designed patterns was used for the UV exposure. The patterns include small circles of 10µm, 15µm, 20µm and 25µm in diameter and six contact pads evenly distributed around the rim of wafer for a good electrical connection and uniform current density distribution for plating. A drawing of the mask pattern is attached in Appendix I.

5.1.4 Electroplating

The patterned wafers were immersed into a plating bath in a pre-designed cell. Acting as a mask, the template only facilitates the copper deposition to occur at the pad openings. More details about the electroplating experiments are described in section 5.2.

5.1.5 Etching

The photoresist template is then stripped off after plating using acetone to expose the copper columns. After that, the sample was rinsed with DI water and dried by compressed air.

5.2 Electroplating

A plating system was set up as shown in Fig. 5-2. The plating cell comprises of a test sample as the working electrode (or cathode), a large copper disk as the counter electrode (or anode) and, if electrode potential needs to be controlled or measured, a saturated calomel electrode (SCE) as the reference electrode. The ratio of the anode area to cathode area was greater than 50:1. Before plating, the anode was chemically cleaned in a 20% dilute nitric acid solution and then rinsed with running DI water. A test wafer, after being installed in a wafer holder, was rinsed with DI water and immersed in the electrolyte. The electrolyte is contained in a rectangular glass tank with a capacity of 3 litres. Before plating, an ultrasonic pre-wetting was applied by placing the tank with the test wafer being immersed in into an ultrasonic bath for 10 seconds. This is to help the electrolyte get into the small apertures in the photoresist template and wet the pads. Plating experiments were usually carried out at room temperature. The electrolyte

is a homemade acidic additive-free electrolyte consisting of 166 g/l $CuSO_4 \cdot 5H_2O$, 200 g/l H_2SO_4 and DI water. A PARSTAT® 2273 galvano/potentiostat served as a power supply for constant current for plating.

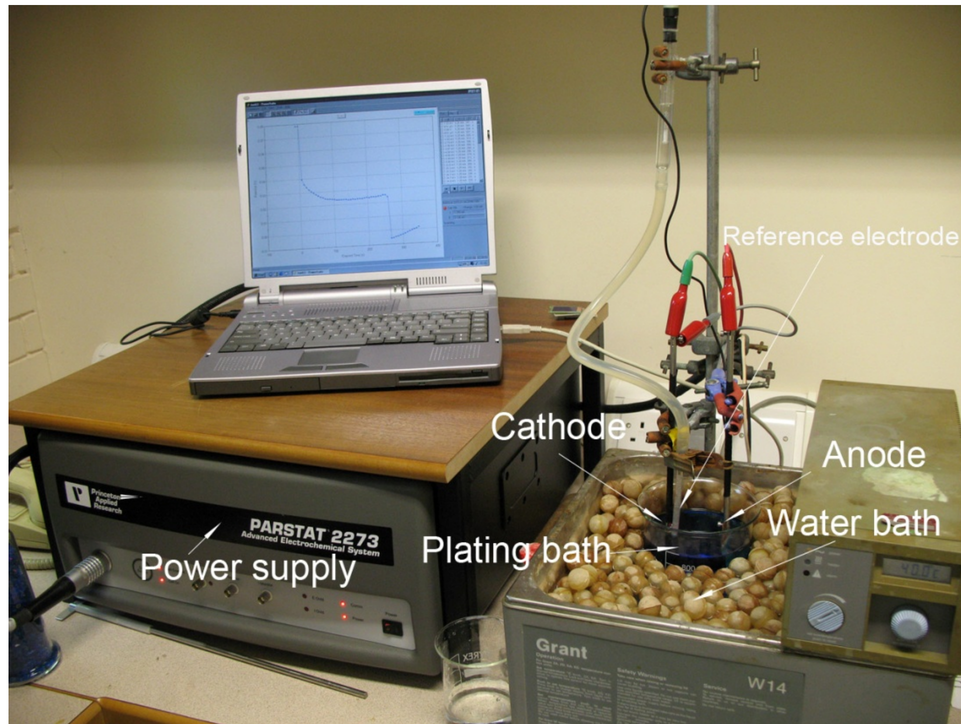

Fig. 5-2 A picture of the plating system

The test wafer was held by a wafer holder through which the sample was connected to the plating power supply. The holder was carefully designed to guarantee an excellent electrical connection between a sample and the power supply using multiple contact points. It consists of four main parts, namely a base, a racket, a copper ring and an outer ring as shown in Fig. 5-3. An assembly drawing and part drawings are attached in Appendix II and III respectively. Six spring-loaded contact probes with gold-plated rounded tips were soldered to the copper ring which was connected to the power supply through a wire. The copper ring is embedded into the racket and fixed by the outer ring which is also embedded into the racket. When the holder is closed, the six contact probes will be connected to the contact pads on the sample by contact under pressure. Using multiple contacts can significantly improve the current density distribution across the large wafer during plating.

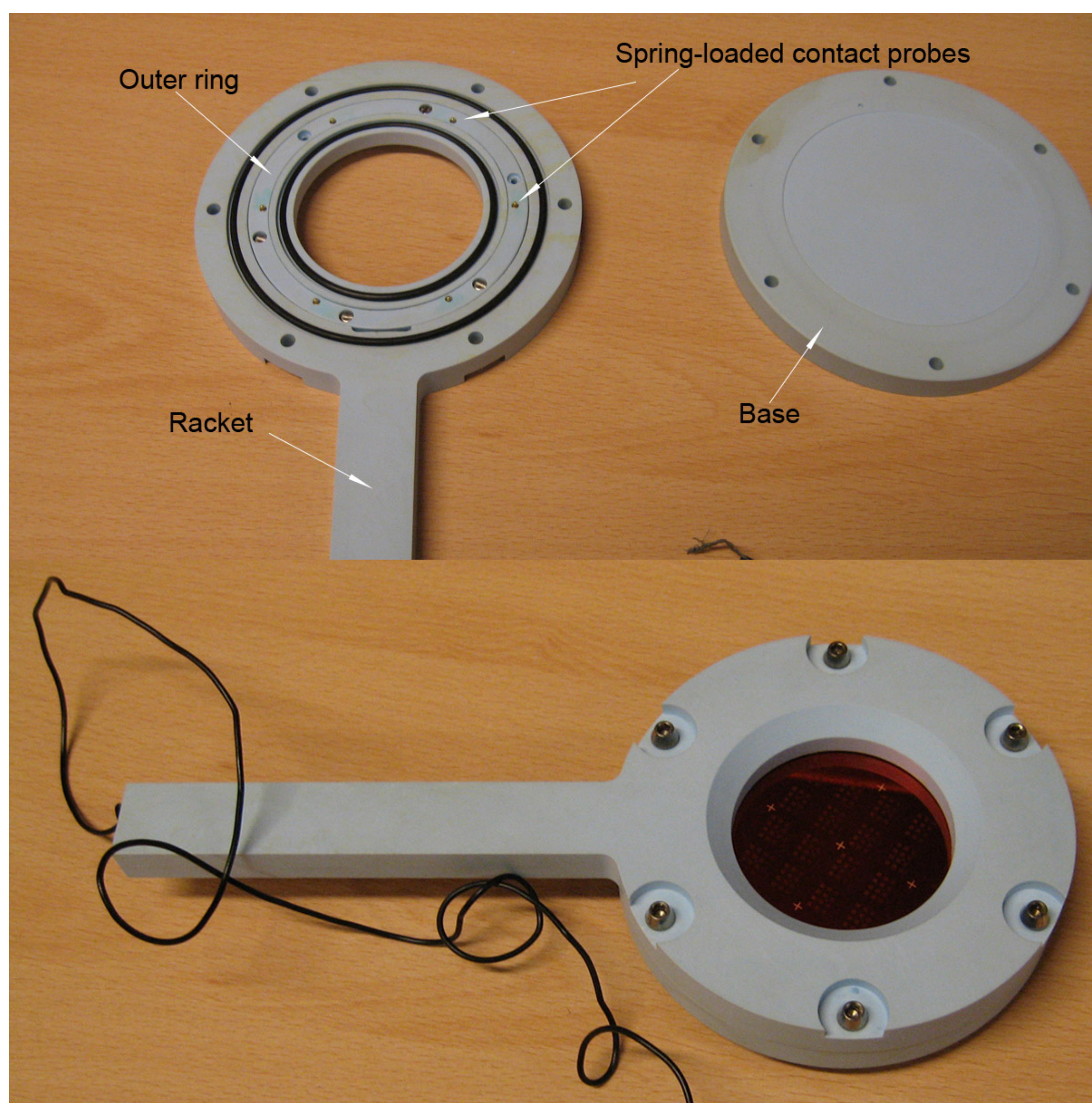

Fig. 5-3 A picture of wafer holder

5.3 Characterisation methods

A range of techniques have been employed to characterise the electroplated copper columns in terms of microstructure, surface morphology, crystal structure and the deposit/seed layer interface as summarized in Table 5-1.

A field emission gun scanning electron microscope (FEG-SEM) was used to obtain the stereoscopic images of the surface morphology. Atomic force microscope (AFM) was also used to characterise the surface of the copper deposit for studying the nucleation at the early stage of plating. AFM analysis provides not only the surface morphology at atomic scale but also a lot of useful information of the deposit e.g. roughness, actual

surface area and 3D surface plots. It has been widely used in surface characterisation of thin films.

A dual-beam focused ion beam (FIB) has been heavily used in this project to characterise the microstructure of copper columns. Firstly, it has been used to cross-section copper columns. Incorporating a focused ion beam and a FEG-SEM, it enables a local and precise cutting at a resolution of less than 200nm without damaging the rest of the samples. It has replaced the traditional mechanical cross-sectioning and polishing in the present case. The ion-beam-polished cross-section is of much higher quality than the mechanically polished cross-section. There is no need to chemically etch the cross-section to reveal the grain boundaries since the ion beam at a low beam current of about 30pA etches the cross-section in real time, inducing secondary electrons. Fig. 5-4 illustrates the cross-sectioning process by FIB.

Table 5-1 Characterisation methods

Techniques	Application M*	CS*	SM*	IF*	STM*	Type of results
FEG-SEM			●	●	●	Secondary electron (SE) images
FIB	●		●			Ion induced SE images revealing microstructure
XRD		●				XRD spectrum
HRTEM				●		High-resolution images
AFM			●			Surface image, surface profile, statistical results

* M represents microstructure, CS cross-section, SM surface morphology, IF interface and STM stereoscopic morphology.

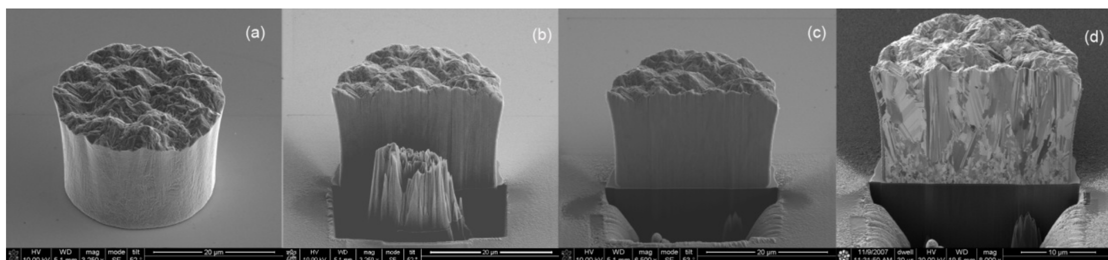

Fig. 5-4 Illustration of FIB cross-sectioning process a) the secondary electron (SE) image of a complete copper column, b) part way through cutting c) SE image of cross-section on completion d) ion bean induced SE image showing the microstructure

The FIB was also used to prepare TEM samples with the assistance of an Omini probe and gas injector depositing Pt for TEM sample lift-out. The FIB is equipped with an electron backscattered diffraction (EBSD) detector. A 3D-EBSD analysis can be done by the serial cutting with FIB and subsequent EBSD mapping followed by the 3D reconfiguration. This state-of-the-art 3D-EBSD technique is of great interests in the characterisation of grain orientations and grain boundaries, and other various information that is related to the crystal structure of the copper deposit.

Chapter 6 Early-stage Electrocrystallization of Cu on Polycrystalline Au

6.1 Introduction

Fundamentals of electrocrystallization have been extensively studied by experimental observations, theoretical calculations and numerical simulations, which have been reviewed in Chapter 2 and Chapter 3. Most of the earlier experimental studies were performed on single-crystal or glassy carbon substrates for simplicity. However, polycrystalline substrates are of more practical interests in industry. For example, in the electronic manufacturing industry, seed layers for electroplating of metals usually have a polycrystalline structure being produced by e.g. Phase Vapour Deposition (PVD). Nevertheless, there is little work on electrocrystallization based on polycrystalline substrates. As substrates can have significant effects on the nucleation at the initial stage and the final microstructure of a deposit, it is necessary to study the early-stage nucleation using an ordinary polycrystalline substrate for a complete reconstruction of growth history by experiments. It is challenging to observe nucleation processes since they occur at atomic scale. An ex-situ AFM observation of the evolution of the surface morphology of copper electrodeposited on a polycrystalline Au seed layer at early stages of the deposition was carried out in this study. An in-situ observation requires a special set-up of the plating cell and there is a concern that the scanning probes can disturb the nucleation process during the course of scanning. The present ex-situ method is straightforward without the need of a special set-up and dispels the concerns about the disturbance.

6.2 Au seed layer

The original substrate surface has significant effects on the early-stage nucleation and growth of copper deposit during electrodeposition. In this study, as-sputtered Au seed layer is the initial surface state where the nucleation begins since there is no further chemical or mechanical pre-treatment to the surface before electrodeposition. The seed layer was characterized by AFM and XRD to look at its surface morphology and crystal

structure. Fig. 6-1 shows an AFM image of the as-sputtered Au seed layer. It shows an extremely fine structure with a uniform distribution of grain size. The surface is smooth with a roughness of only 14.62 nm as measured by the AFM. Fig. 6-2 presents a XRD spectrum of an as-sputtered sample before deposition. The broadened Au peaks as shown in Fig. 6-2 , together with the AFM image as shown in Fig. 6-1 , indicate a polycrystalline seed layer. The grain size calculated from Scherrer Equation [132] is 38.6nm, which is in good agreement with the direct measurement from the AFM image.

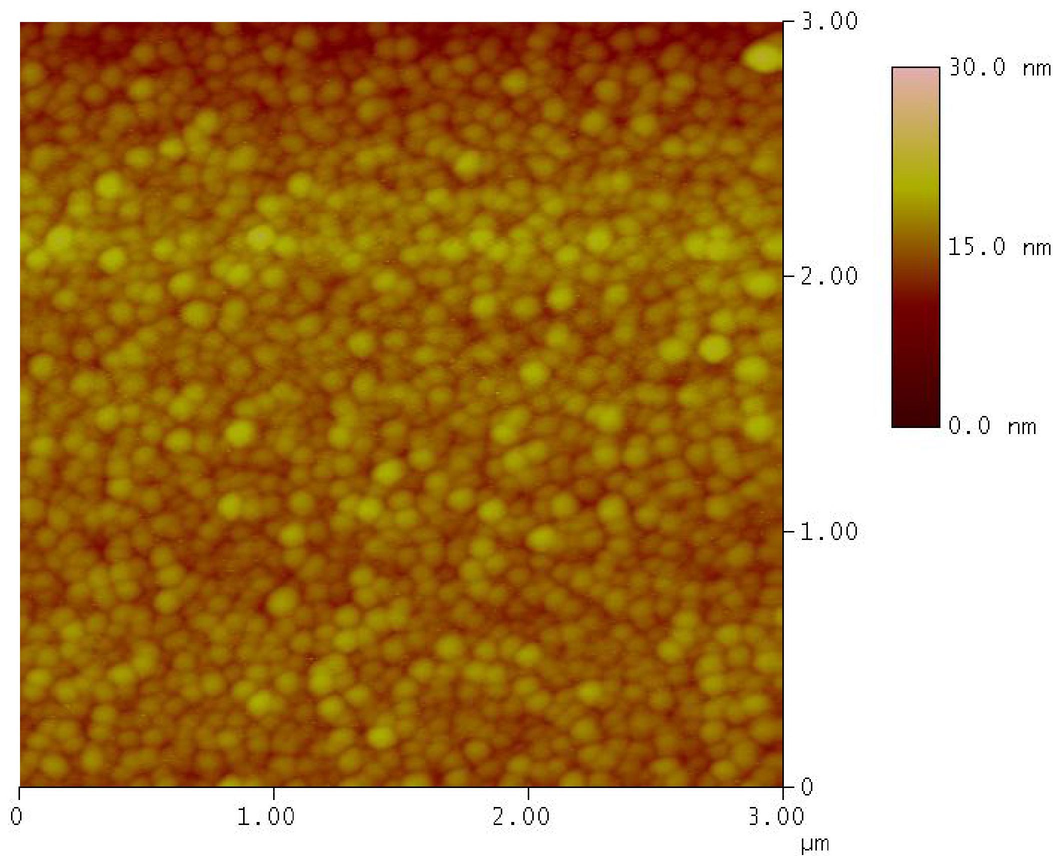

Fig. 6-1 an AFM image of the as-sputtered Au seed layer

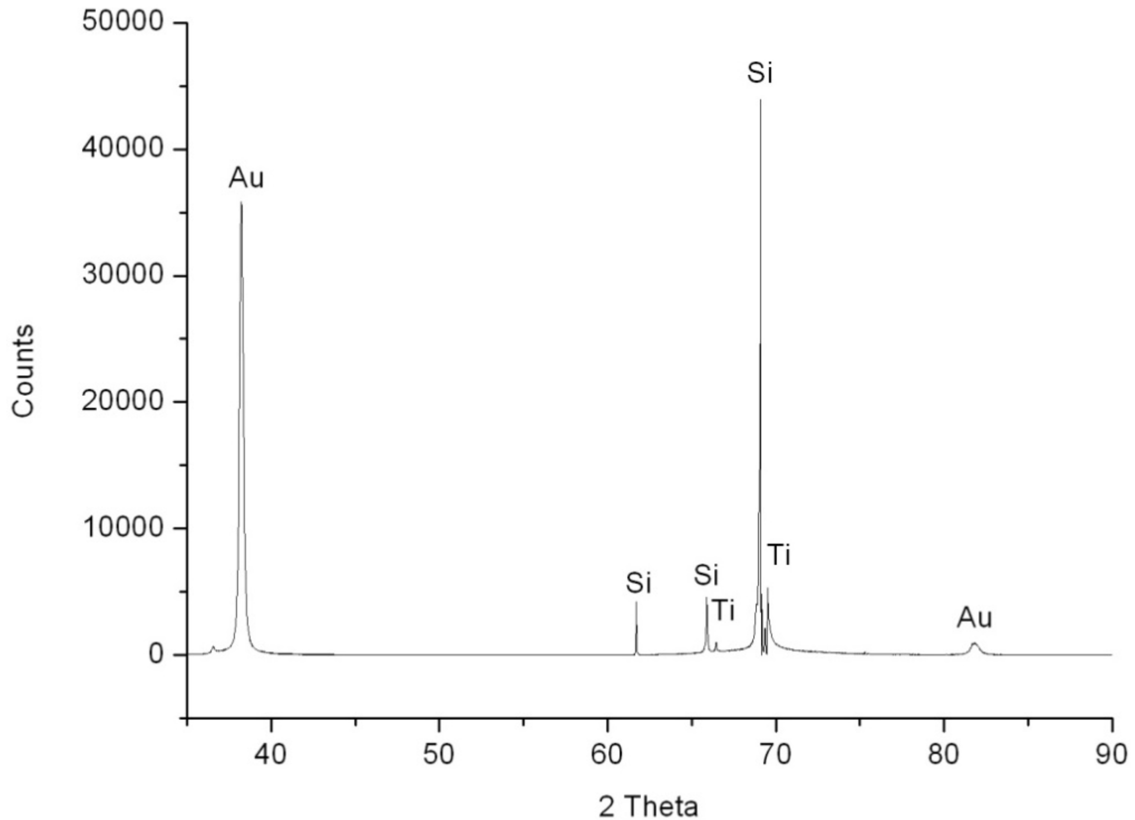

Fig. 6-2 XRD spectrum of a metallized test wafer before deposition

6.3 Evolution of the surface morphology

Fig. 6-3 presents the AFM images of surface morphology of an as-sputtered seed layer and a series of test wafers plated for different times. As can be seen in Fig. 6-3a, the as-sputtered Au surface is clean and very smooth with few noticeable defects. It indicates that there is hardly any preferred nucleation sites at the micro-scale. After only 16ms of deposition, a number of nuclei of various sizes and shapes are formed and unevenly distributed over the surface, as shown in Fig. 6-3b. The overpotential throughout the plating was measured. Fig. 6-4 shows the overpotential-time transient for a 16ms of plating of the sample. It can be seen that the overpotential reached a peak within 4ms, which is the minimum time step for the potentiostat to collect data, which indicates nucleation has already occurred within 4ms. The larger nuclei as shown in Fig. 6-3b are likely to be formed earlier and grow with priorities or at a higher growth rate while the smaller ones are probably formed instantly just before the deposition was terminated. The smooth area marked as a square in Fig. 6-3b was scanned at a higher magnification. In comparison to the as-sputtered Au seed layer as shown in Fig. 6-5, the plated sample

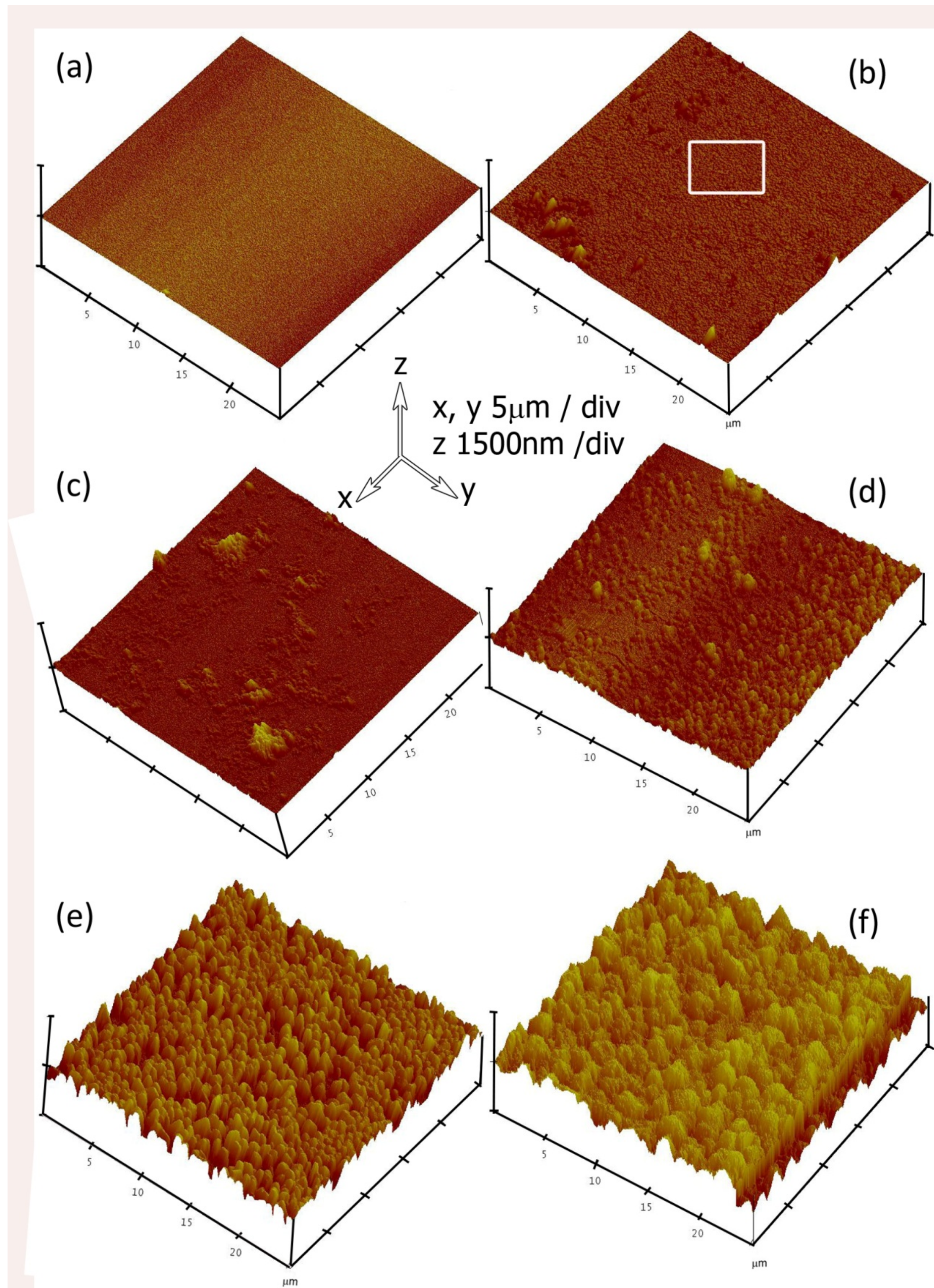

Fig. 6-3 AFM image of the copper deposits for a series of period of time: a) before deposition, b) 16ms, c) 100ms, d) 10s, e) 100s, f) 1000s.

has a finer structure. It indicates the sample surface has already been significantly modified within such a short time although no 3D nucleus is discernable in the smooth

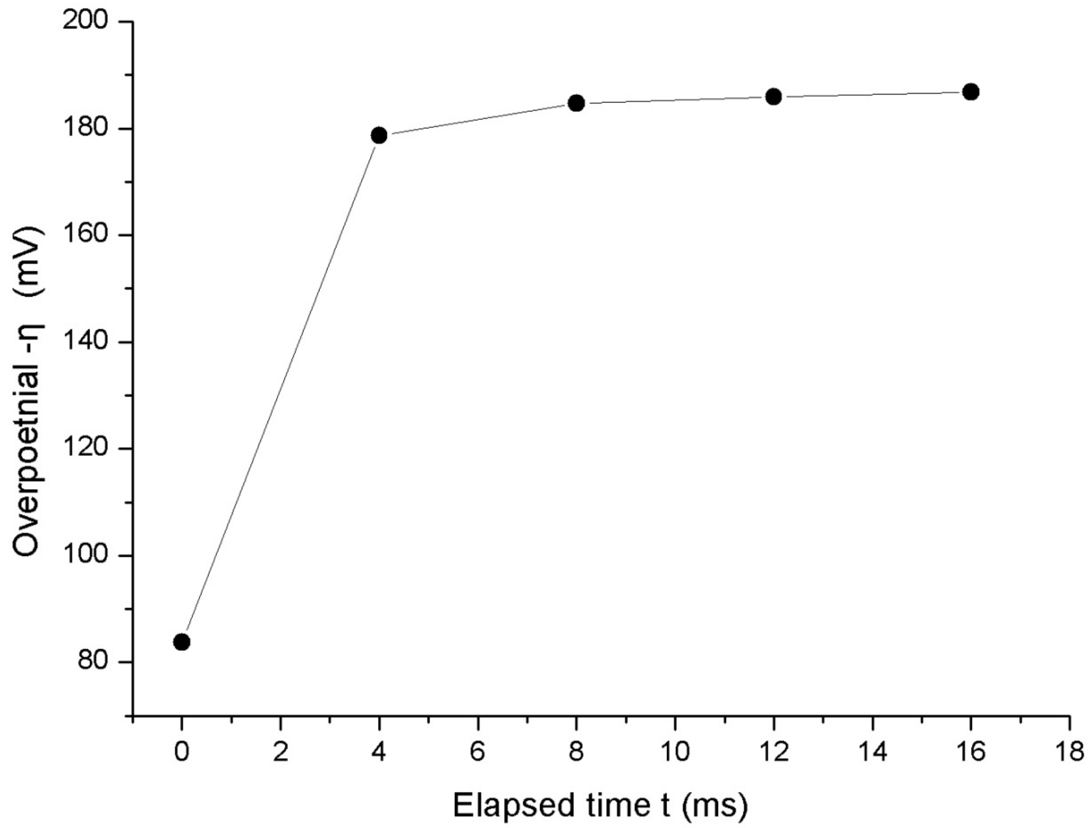

Fig. 6-4 The overpotential-time transient curves of galvanostatic electrodeposition of copper for 16ms.

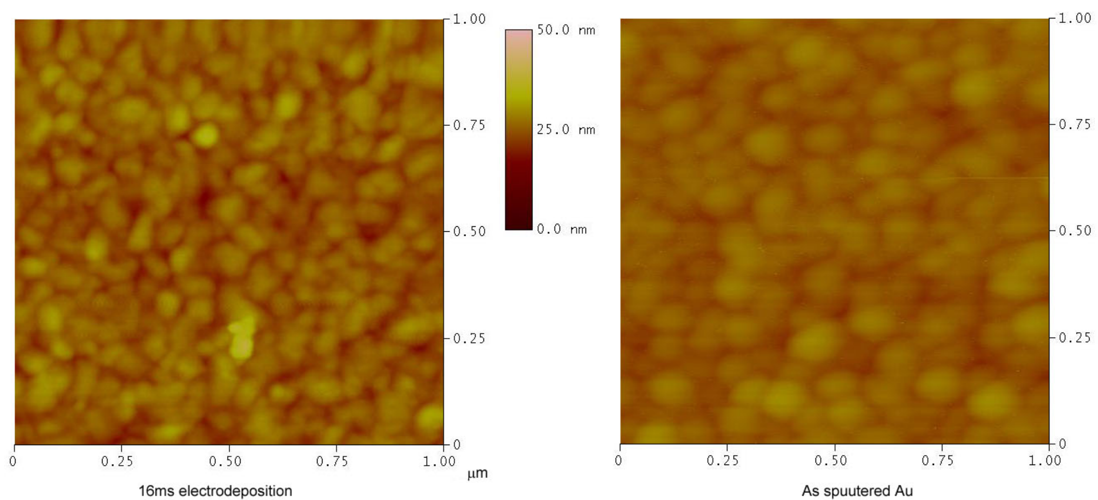

Fig. 6-5 AFM images of a) the marked area in Fig. 6-3b and b) the as-sputtered gold seed layer.

area. Such modification can be attributed to underpotential deposition (UPD) of a few copper monolayers of a distorted crystal structure. They are formed by copper atoms trying to follow the structure of the Au seed layer. After a few transitional atomic layers, when the interaction between the seed layer and Cu adatoms becomes weak, 3D nucleation starts. Fig. 6-6 presents a high-resolution TEM image of the interface between the Au seed layer and two Cu grains. There is an interfacial layer of around 10-20nm thick. Its contrast is close to the Cu grains, which indicates this interfacial layer is mainly of Cu rather than of a Au-Cu intermetallic compound. It is reasonable to infer this

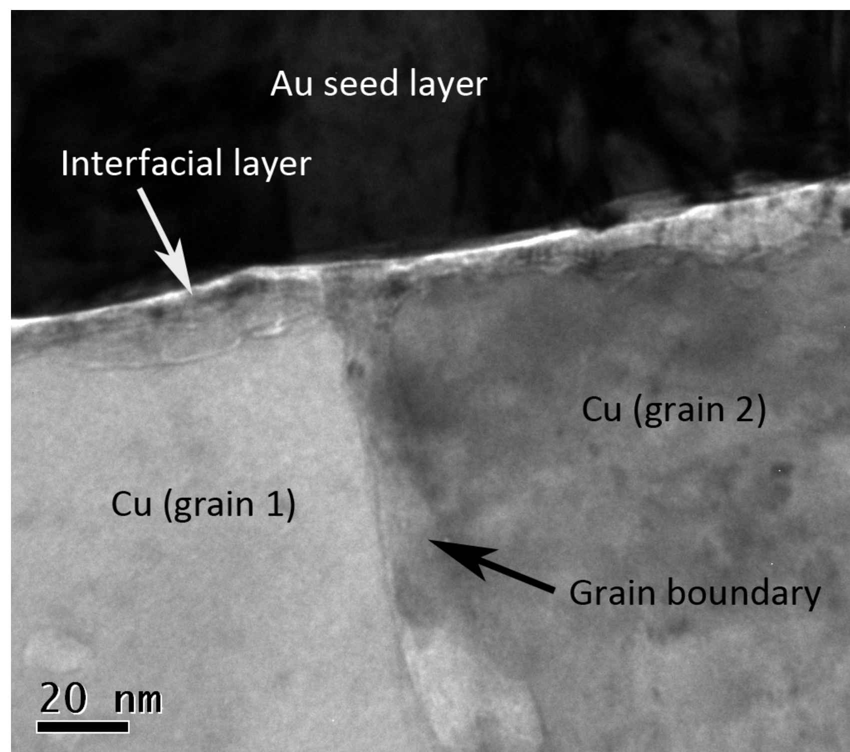

Fig. 6-6 HRTEM image of the interface between a Cu deposit and the Au seed layer

layer is due to the UPD of Cu initially. Fig. 6-3c shows the surface morphology of the sample plated for 100ms. In comparison to Fig. 6-3b, more nuclei are formed and the existing ones have grown larger. After 10s as shown in Fig. 6-3d, numerous nuclei have formed and the overall uniformity of the growing nuclei has been significantly improved where the growing nuclei have impinged. After 100s of deposition, as shown in Fig. 6-3e, most of the nuclei have impinged. Only a few small spots remain uncovered, as can be seen more clearly from the top view shown in Fig. 6-7. After 1000s of deposition, as shown in Fig. 6-3f, the sample surface has now been completely covered. And the

growing fronts have become larger as compared to Fig. 6-3e, which indicates that grains have also grown laterally apart from longitudinally. The longitudinal growth is expected since the deposition occurs from the bottom upwards. The lateral growth can be interpreted by a 'growing-over' mechanism visualized by KMC simulations as presented in Chapter 4.

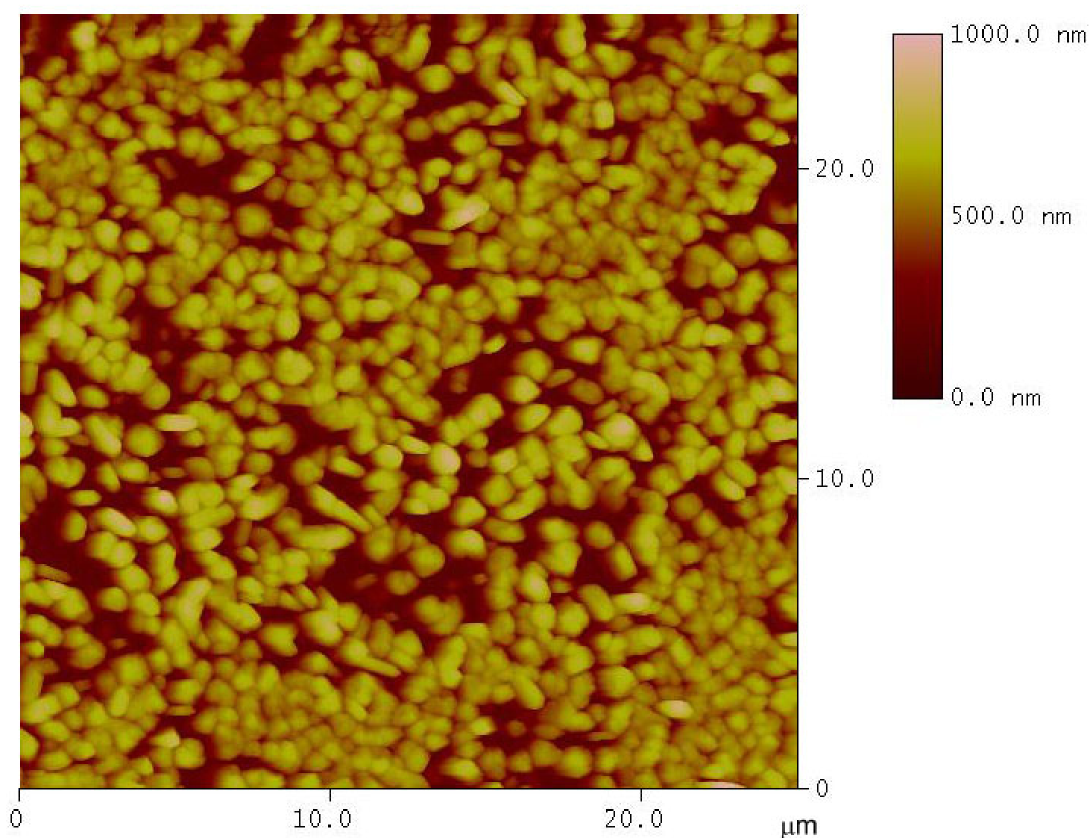

Fig. 6-7 AFM image of the copper deposit after 100s of deposition.

The roughness and surface area of the electrodeposits were measured by AFM based on 25×25µm scan size. These two variables as a function of plating time are illustrated in Fig. 6-8. The roughness of the surface increases rapidly during the initial stage of deposition, i.e. before 100s, when the surface has not been completely covered by electrodeposit, and nucleation and growth proceed simultaneously. However, the roughness of the electrodeposit increases slowly and steadily when the crystal growth dominates the plating process. The change of the surface area follows the similar trend before 100s. After crystal growth process has dominated the deposition, however, the surface area decreases with the growth fronts growing bigger.

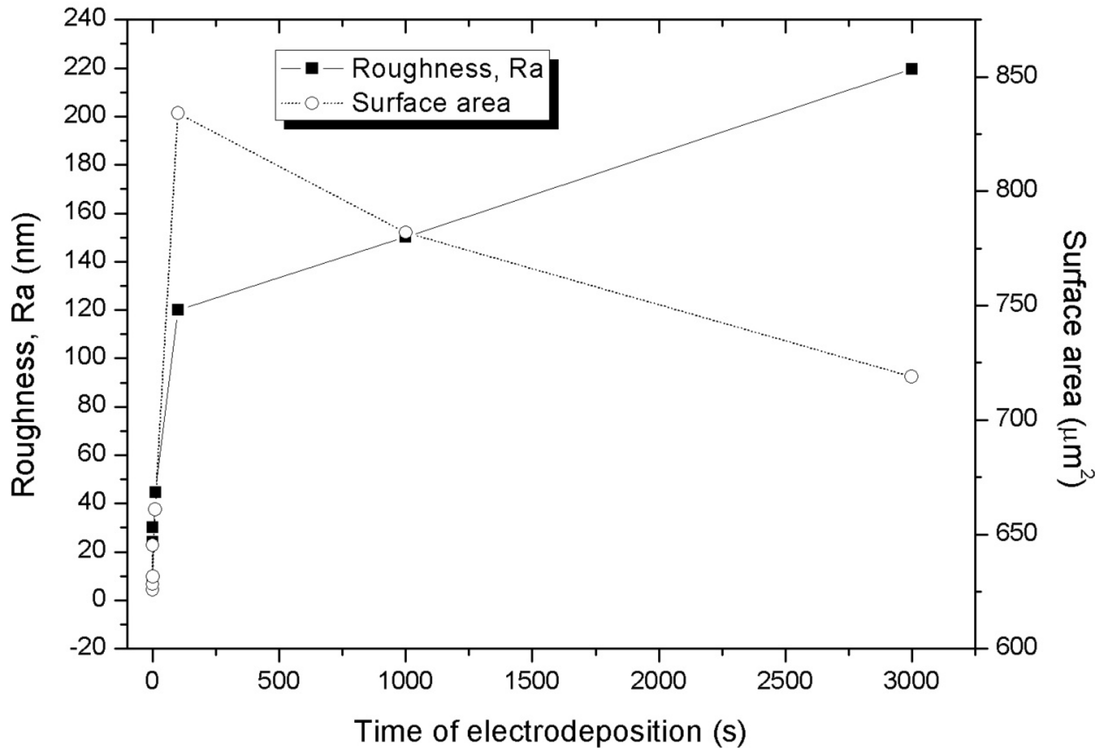

Fig. 6-8 Dependence of the roughness and surface areas of the copper deposits on deposition time

6.4 Model for the nucleation and growth

Based on the above results, together with the findings from the simulations as presented in Chapter 4, a heuristic model is proposed to describe the mechanism of the early-stage nucleation of Cu on a polycrystalline Au thin film. The binding energy between a copper adatom and a Au atom is greater than cohesive energy of Cu (i.e. binding energy between two copper atoms) [56]. And Cu and Au have a large lattice misfit. Therefore, nucleation of Cu on Au seed layer should follow the Stranski-Krastanov mode [56] as illustrated in Fig. 6-9a-b. In such case, copper adatoms tend to follow the structure of Au seed layer until, after a few layers, the attraction between the coming adatoms and the Au atoms is weak enough to free some Cu adatoms to form atomic clusters. As the nucleation continuously proceeds and growth of existing nuclei proceeds, the deposition reaches a stage where nucleation become less dominant (see Fig. 6-9d). Therefore, the continuous growth of existing nuclei dominates the deposition process. All the existing grains grow both longitudinally and laterally competitively. The more competitive grains grow over neighbouring grains and hence suppress their further growth (Fig. 6-9e). Recrystallization during deposition may also

occur by moving or rotation of small-angle grain boundaries, which increases the grain size and reduces the number of grains (Fig. 6-9f).

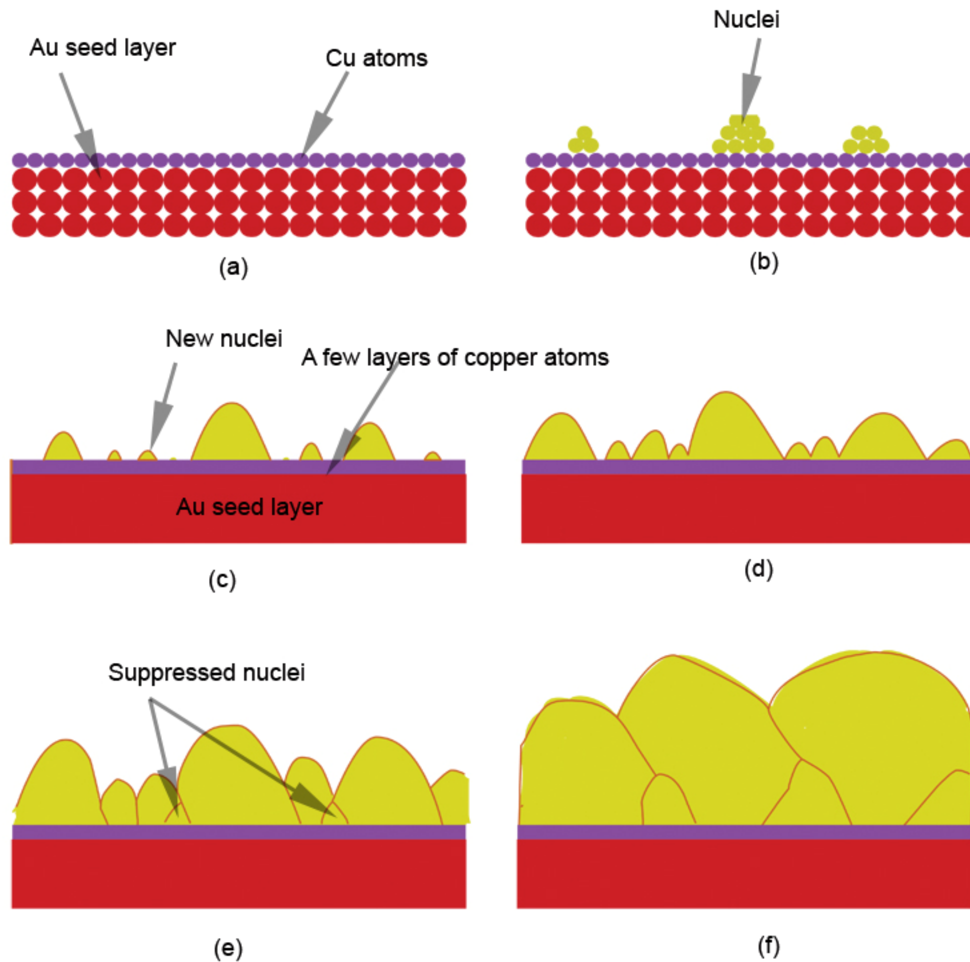

Fig. 6-9 Schematic of a heuristic model for nucleation and growth of Cu on polycrystalline Au

6.5 Summary

The evolution of the surface morphology of the electrodeposited copper on as-sputtered Au seed layer from 16ms to 1000s was observed and their formation mechanism discussed. It was found that the copper nucleation starts within 4ms. Then the nucleation parallels the growth of the existing nuclei until certain time after 100s, when the latter dominates the deposition process. After that, the surface morphology of copper deposit evolves following the mechanisms of growing-over and recrystallization. A heuristic model is finally proposed to describe the mechanism of the early-stage electrocrystallization of Cu on a polycrystalline Au seed layer based on the findings.

Chapter 7 Growth and Recrystallization of Electroplated Copper Columns

7.1 Introduction

The mechanisms of nucleation and grain growth of electroplated copper columns have not been well understood. The microstructural evolution at room temperature due to recrystallization observed in electroplated copper films further increases complexity. Recrystallization is believed to occur during plating [33, 133]. To study the growth history of copper columns experimentally, copper columns were plated on four test wafers by altering the deposition time while other plating parameters remain unchanged. The plated copper columns were characterized to study the evolution of their external morphology, cross-sectional microstructure and crystal structure. The size effects of diameters of the columns on their morphology and structure are studied and discussed. Finally, an in-situ XRD analysis of a plated sample was carried out at different times after plating to study the possible self-annealing after plating.

7.2 Overview of electroplated copper columns

Copper columns of 10µm, 15µm, 20µm and 25µm in diameter and 50µm in pitch have been electrodeposited by template-assisted galvanostatic electrodeposition at 4mA/cm^2. Fig. 7-1 and Fig. 7-2 show the SEM images of an array of the columns of 15µm in diameter plated for 1 hour and 3 hours respectively. Both have a prominent feature – many columns have extraordinarily large grains protruded from the finer matrix on the edge of the columns. Approximately, 150 columns were randomly selected from the sample after plating for 3 hours for statistical analysis on the number and position of the large grains, which are illustrated in Fig. 7-3. It can be seen most of the columns have two to four large grains on the top and most of them are on the edge of the columns. In addition, most of the columns plated for three hours have a well-formed facet parallel to the wafer surface while those plated for one hour show a pyramidal shape. In the following sections, detailed characterization of a few typical individual columns is presented.

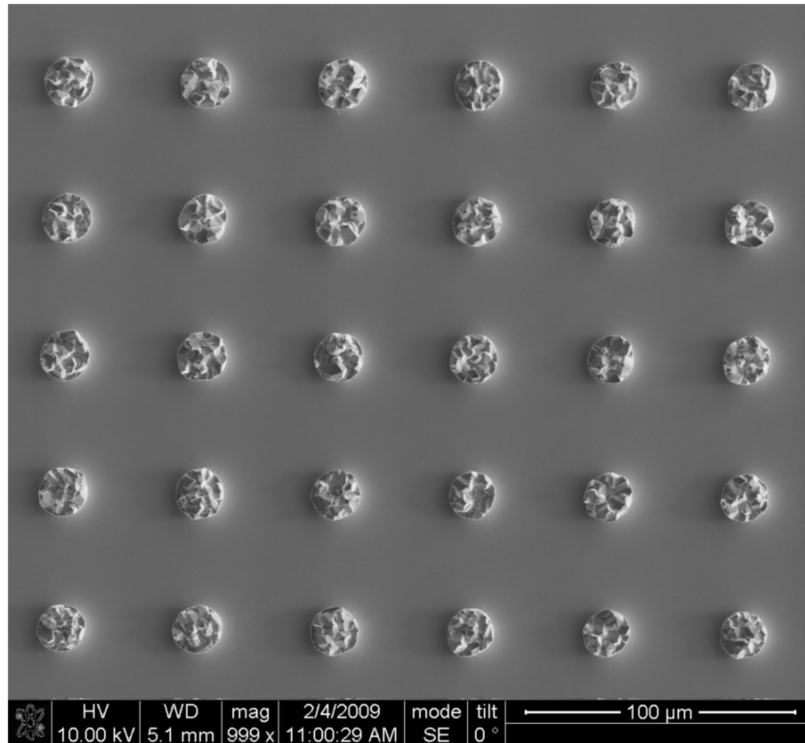

(a)

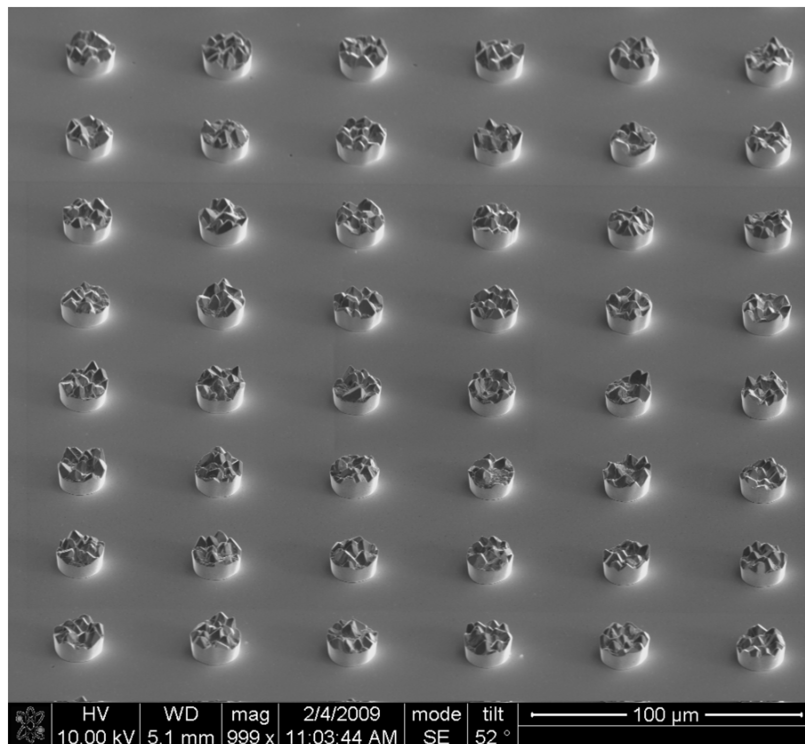

(b)

Fig. 7-1 SEM images of copper columns of 15μm in diameter plated for one hour (a) Top view (b) stereoscopic view.

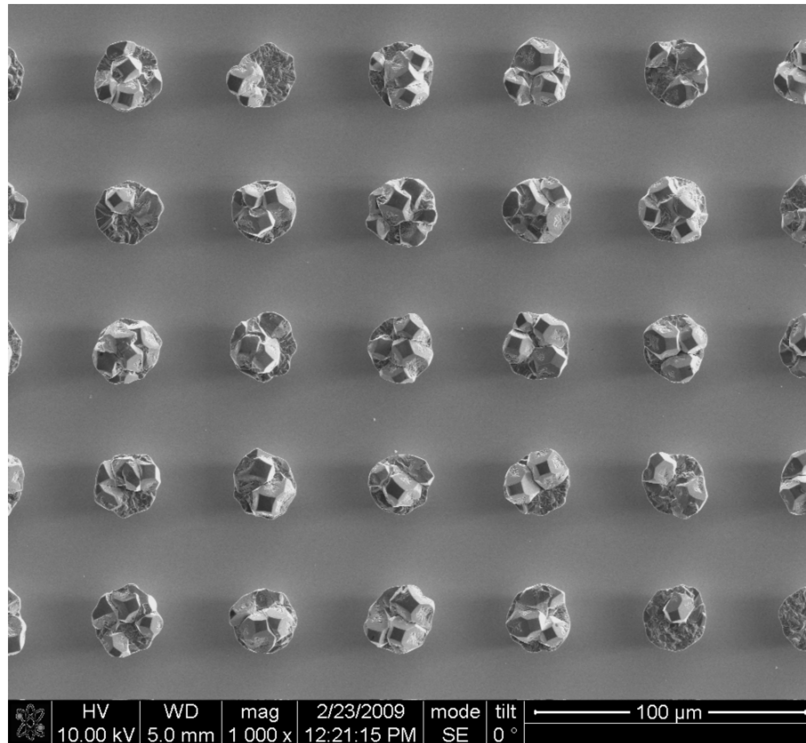

(a)

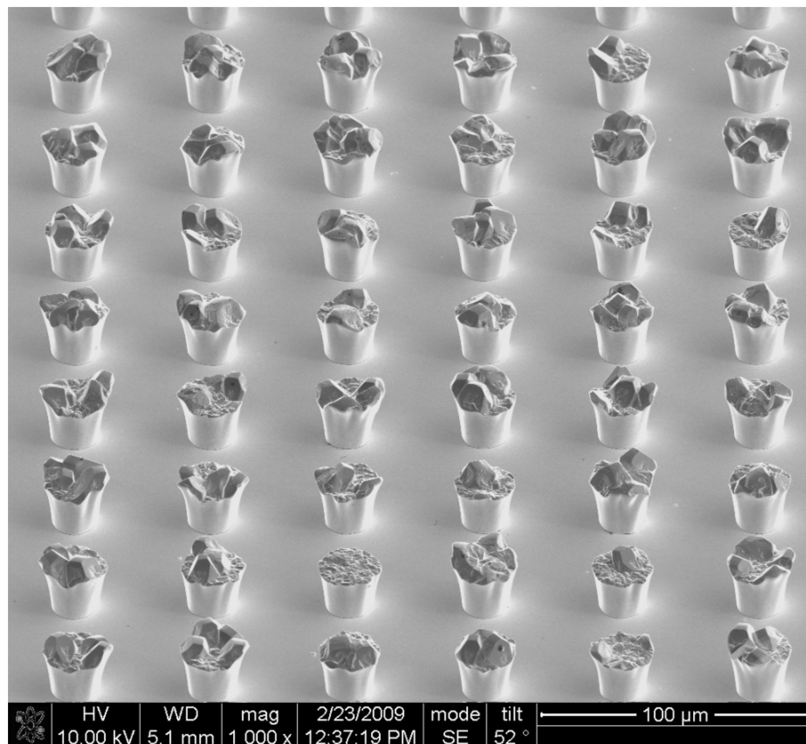

(b)

Fig. 7-2 SEM images of copper columns of 15µm in diameter plated for 3 hours (a) Top view (b) stereoscopic view.

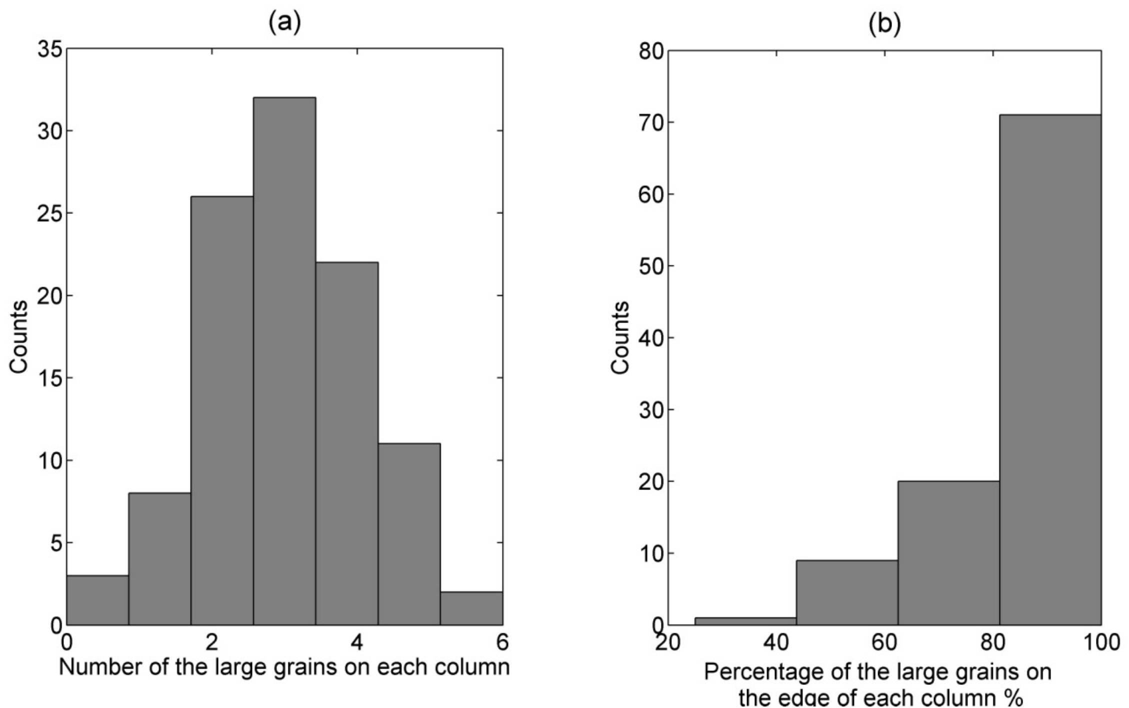

Fig. 7-3 Distribution of the large grains (a) frequency counts of the grains in each column (b) Percentage of the large grains which are on the edge of each column.

7.3 Growth history

7.3.1 Evolution of the external morphology

Surface morphology represents the growth front of a deposit. Its evolution reflects an important aspect of the growth history. Fig. 7-4 shows SEM images of the top view and stereoscopic view of a copper column of (ϕ15μm) obtained from a half-an-hour plating. Three large grains stand out from the finer matrix of the column. They all show morphology of a rectangular pyramid with a blunt tip and a rough surface. They are similar in size and are all on the edge of the column. Fig. 7-5 shows an ion-beam-induced secondary electron image of this column revealing the grain structures. It can be seen that the matrix is actually a mixture of many fine grains and some larger ones which are often known as secondary grains [134]. The formation mechanism of secondary grains will be discussed later in this chapter. Fig. 7-6 shows the top and stereoscopic view of a column plated for one hour. The number of the protrusions increases in comparison with that plated for half an hour. Some of them have already connected each other. The pyramid shape remains but the large grains are better faceted with smoother surfaces of the pyramids. Fig. 7-7 and Fig. 7-8 show the morphology of the copper columns plated for two hours and three hours respectively. The shapes of the protrusions have evolved

into a frustum of rectangular pyramid and they are much larger than those in the columns plated for one hour and half an hour. As can be seen in Fig. 7-8, the large grains have almost grown across the whole surface of the column after plating for three hours. Meanwhile, some triangular surfaces are formed at the base of the pyramid as marked by arrows in Fig. 7-7 and Fig. 7-8.

One can clearly see the grains growing larger with time and their shape evolving from rectangular pyramids into frustums of rectangular pyramids over three hours of plating. It should be noted that after plating of half an hour, three large grains were formed; if these large grains were formed by deposition, they would continue growing and evolving subsequently. After three hours, the column would be mainly consisted of these large grains. It is necessary to look at the cross-sectional microstructures to verify or rule out the above inference.

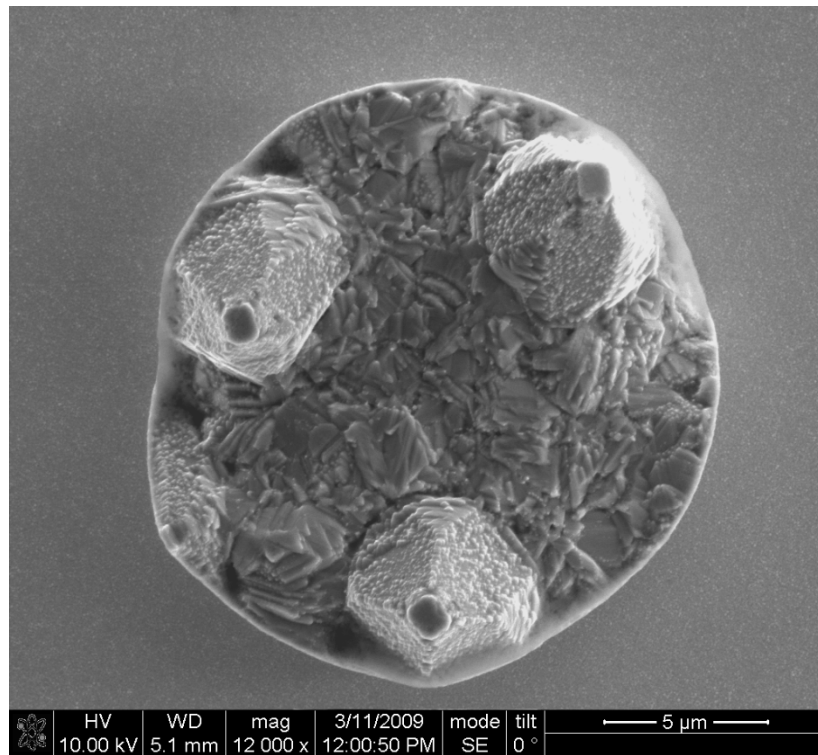

(a)

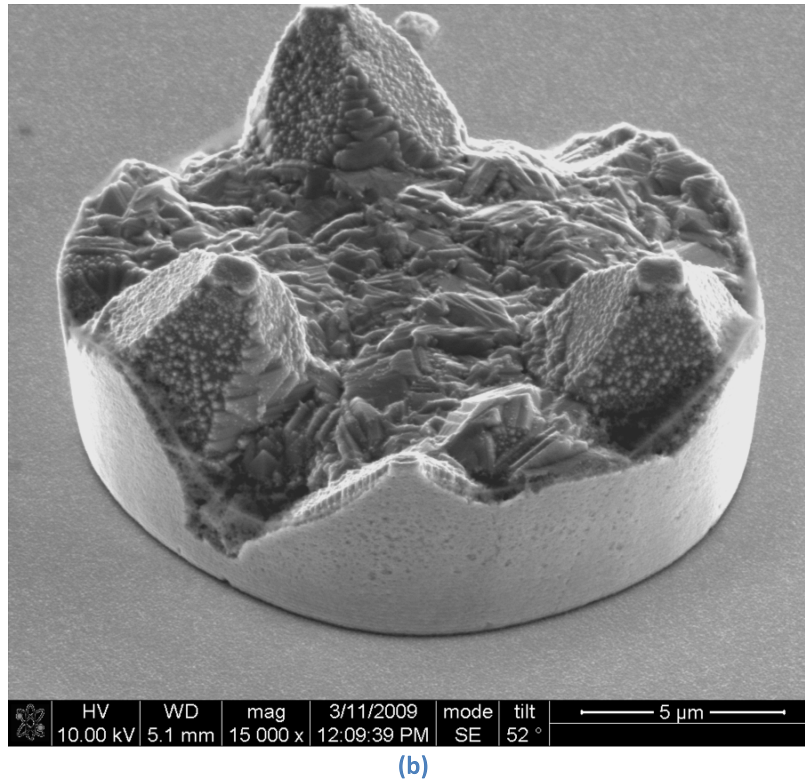

(b)

Fig. 7-4 The SEM image of a copper column plated for half an hour (a) top view, (b) stereoscopic view

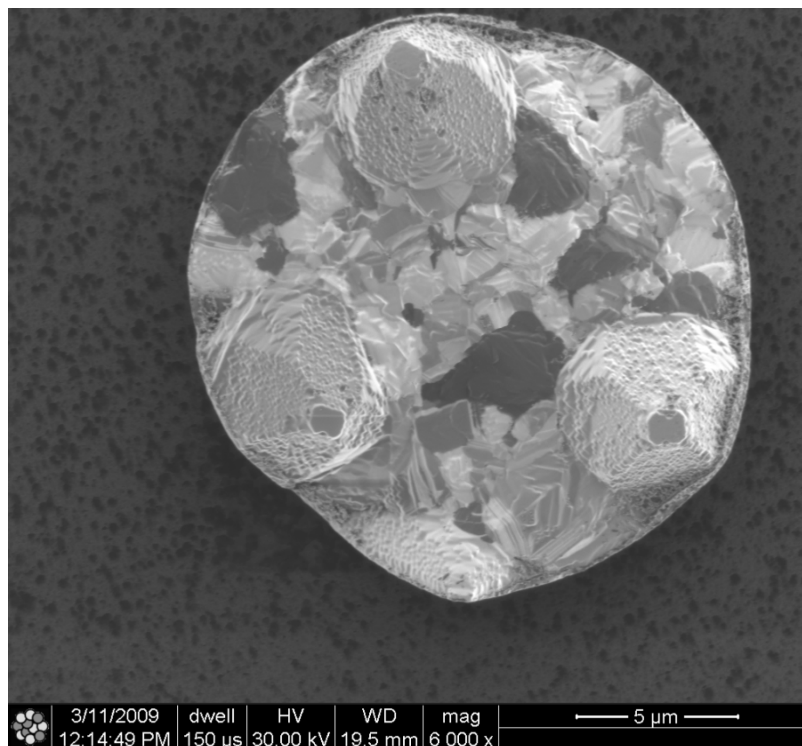

Fig. 7-5 An ion-beam-induced secondary electron image of the top surface of the column plated for half an hour showing the grain boundaries.

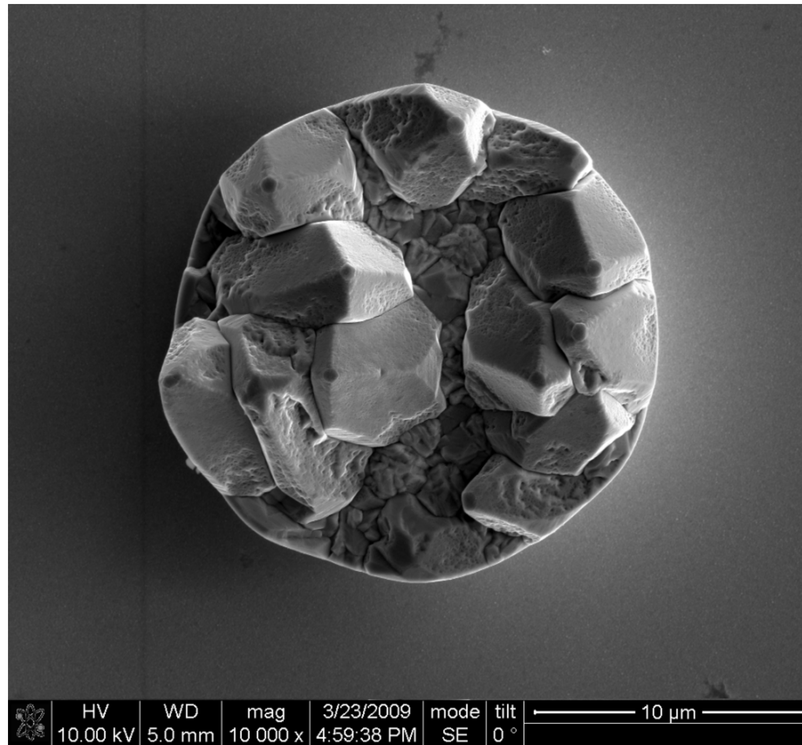

(a)

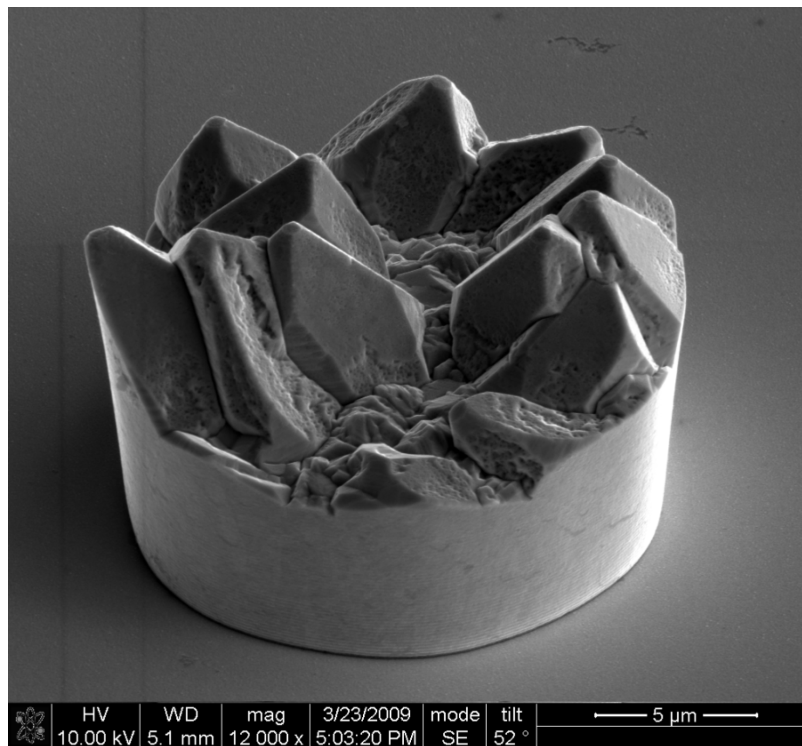

(b)

Fig. 7-6 The SEM image of a copper column plated for 1 hour (a) top view, (b) stereoscopic view

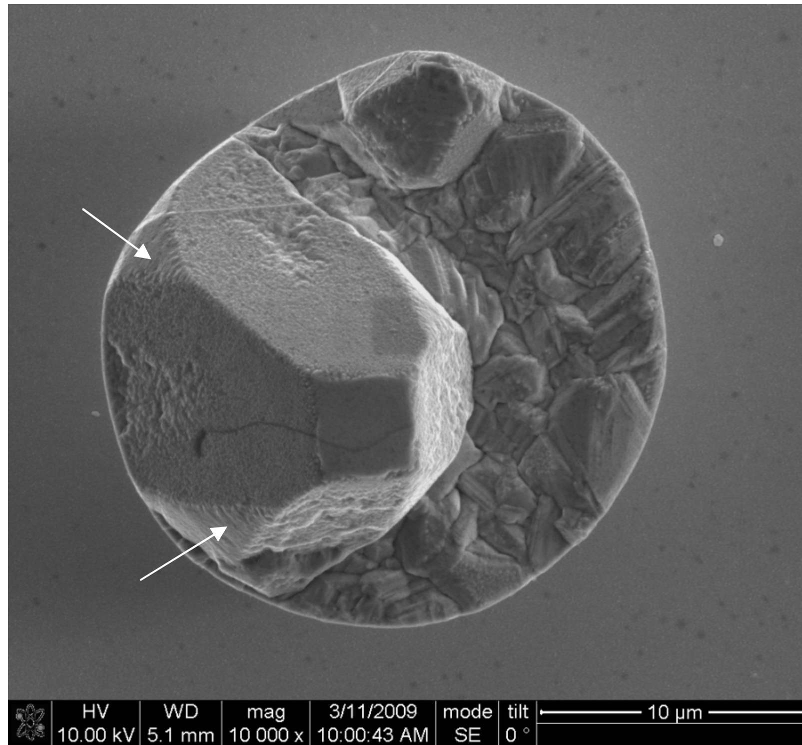

(a)

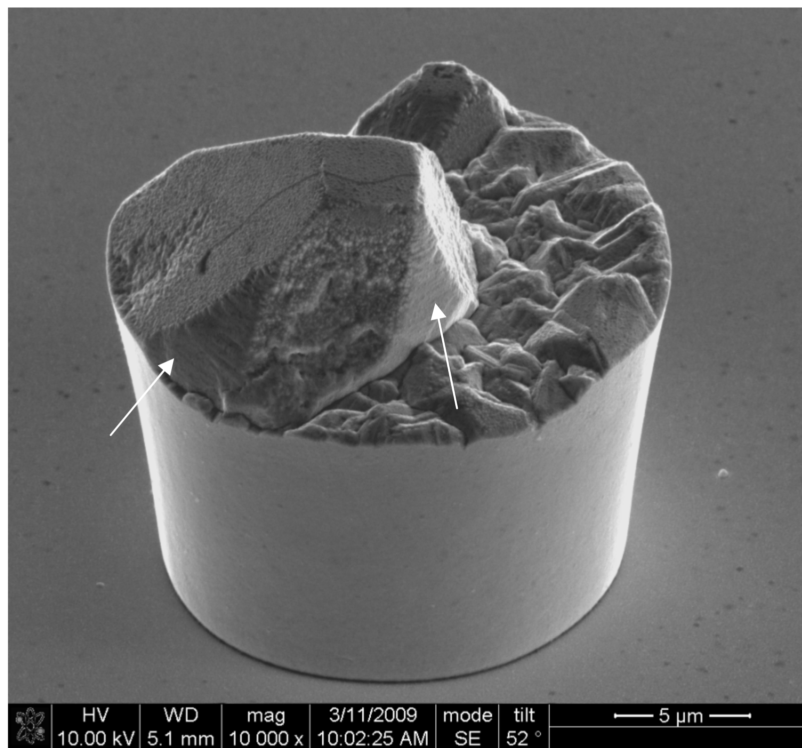

(b)

Fig. 7-7 The SEM image of a copper column plated for 2 hours (a) top view, (b) stereoscopic view

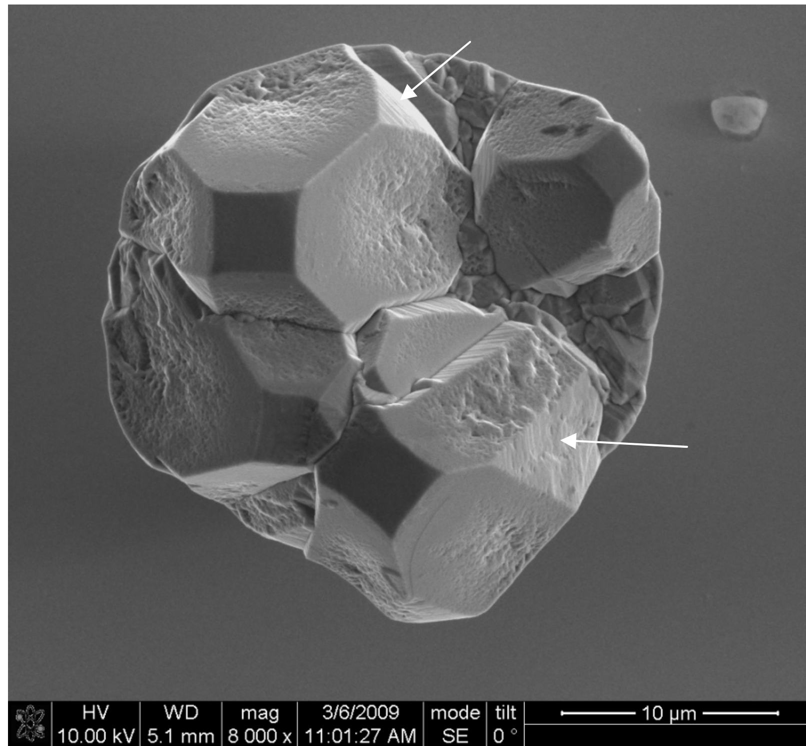

(a)

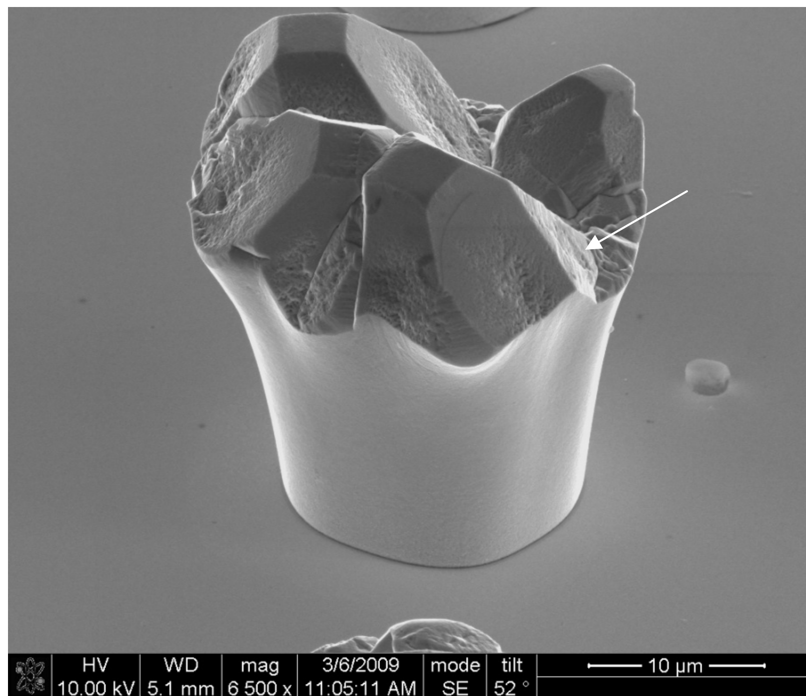

(b)

Fig. 7-8 The SEM image of a copper column plated for 2 hours (a) top view, (b) stereoscopic view

7.3.2 Evolution of the cross-sectional microstructure

The above four columns plated for different time were cross-sectioned using FIB to look at their microstructure. A precise cross-sectioning is available with FIB. The cutting positions were carefully chosen to involve as much of the large grains as well as the matrix. Fig. 7-9a-d show the ion beam induced images of the cross-sectional microstructure of the copper columns plated for half an hour, one hour, two hours and three hours, respectively. It can be seen that all these columns show bi-modal or tri-modal distribution of grain size. For succinct presentation, they are categorized into three regions in terms of their size distribution and morphological features. Region I: a few large grains on the top and/or the edge of columns. Region II: the ultra-fine grains near the deposit/substrate interface. Regions III: the grains characterized of a mixture of columnar grains of median size and twins. A column does not necessarily contain all these three types of grains. For example, Region III is missing from the columns plated for half an hour and two hours as shown in Fig. 7-9a and c respectively. The Region II grains of the column plated for one hour are generally finer than other columns. Note the methodology of this investigation is to use these columns plated for different periods of time to represent different points of time over the growth history of a column. Also note the growth direction is from the bottom up. Therefore, the microstructure of the column plated for half an hour should be similar to the bottom half of the one plated for one hour; the one-hour column to the bottom half of the two-hour one; and the like. On the contrary, covering the bottom one third of the column plated for three hours as shown in Fig. 7-9d, one can see its upper part looks broadly similar to the column plated for two hours as shown in Fig. 7-9c. In the same way, the column plated for half an hour as shown in Fig. 7-9a looks broadly similar to the upper half of the one plated for one hour as shown in Fig. 7-9b. This suggests that the growth of the Region I grains and probably some of the Region II grains occurred from the top surface down, i.e. by recrystallization. Furthermore, the Region I grains and the large Region II grains among the finer matrix have the features of secondary grains that are usually resulted from recrystallization. Therefore, one can conclude that it is the recrystallization, however during or after plating, that ultimately results in the bi-modal or tri-modal structure. The formation of the Region III grains is probably attributed to

the growing-over mechanism as proposed and verified by the simulations and the experimental observations presented in the earlier chapters.

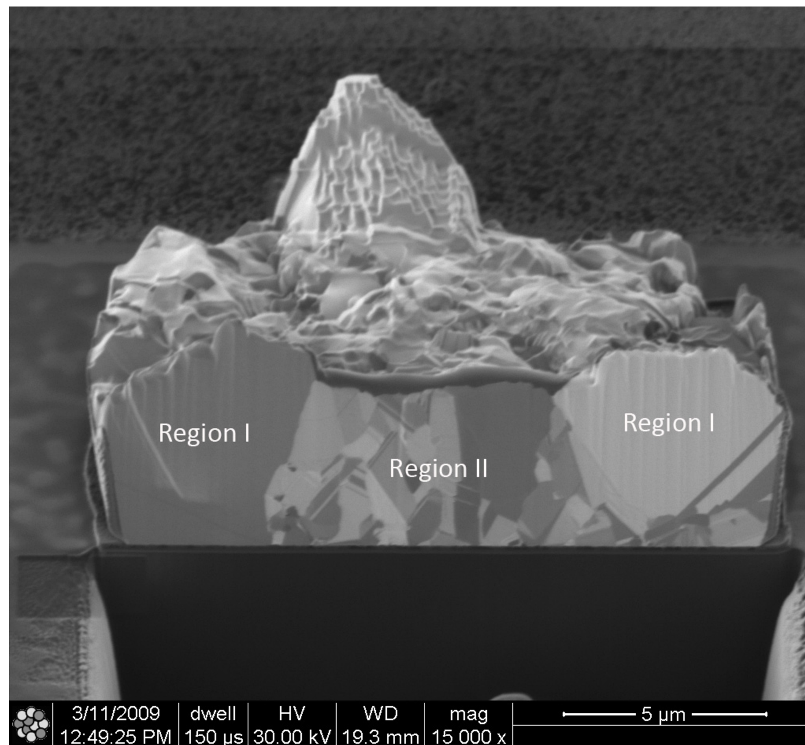

a)

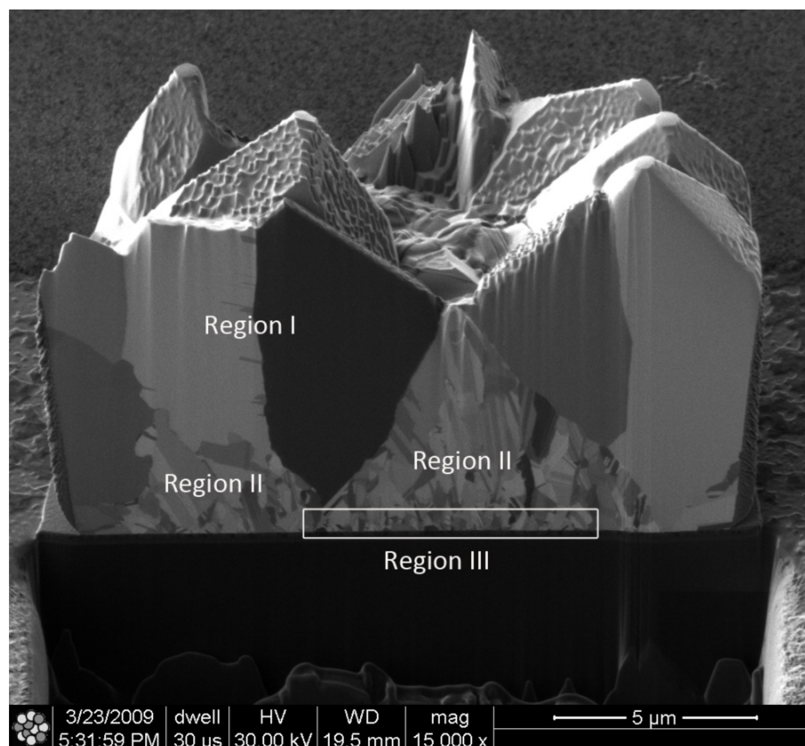

b)

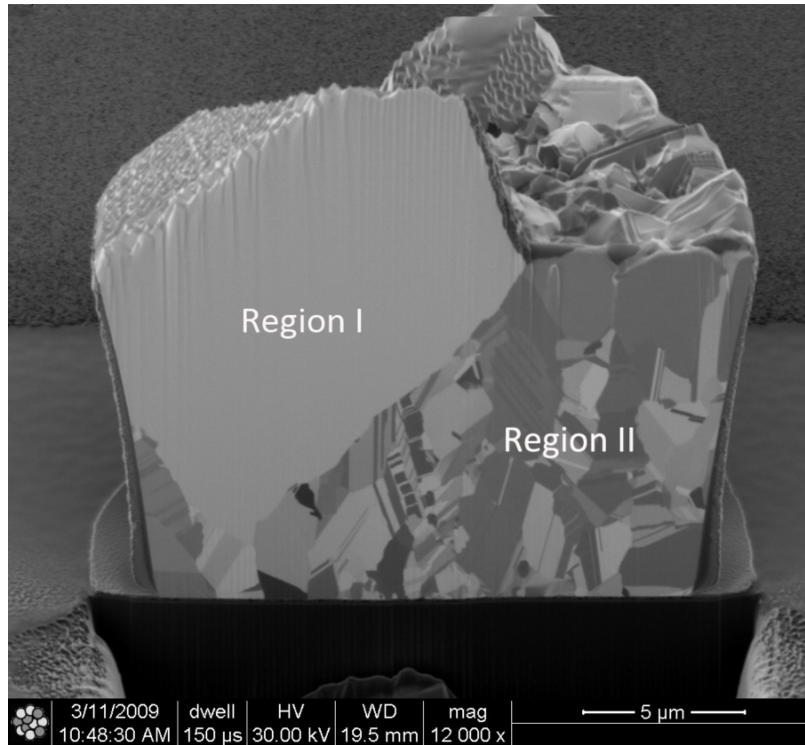

c)

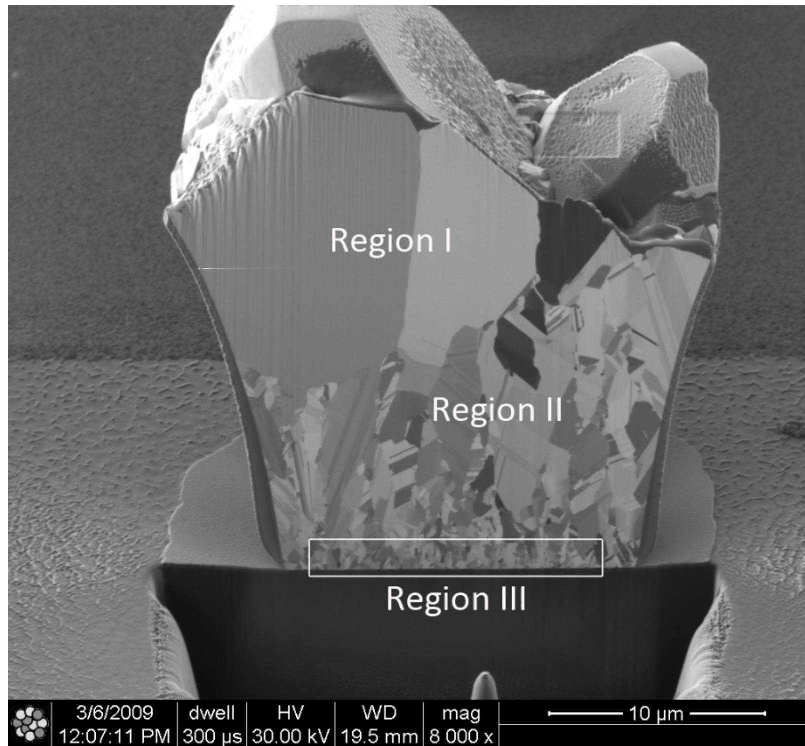

d)

Fig. 7-9 FIB image of the cross-sectional microstructure of the copper column plated for a) 0.5 hour, b) 1 hour, c) 2 hours and d) 3 hours.

7.3.3 Size effects

Fig. 7-10 to Fig. 7-12 show the morphology and microstructure of the columns of nominal diameter of 10μm plated for one hour, two hours and three hours respectively. Accordingly, the size of Region I grains become larger and comparable with the diameter of the column. Also their morphology has changed. As shown in Fig. 7-10, the column plated for one hour shows morphology of frustums of rectangular pyramid while such morphology was not observed until plated for two hours in the columns of 15μm in diameter. Fig. 7-11 and Fig. 7-12 presents the Region I grains in the 10μm columns plated for two hour and three hours, respectively. They have ridge-like morphology. Interestingly, the upper half of the column plated for three hours is a single crystal. This has demonstrated that the size of the columns caused the changes of the bump morphology and microstructure as the columns are sourced from the same samples. This size effect on the morphology and microstructure is likely due to recrystallization of the columns. Brongersma et al. [32] proposed that self-annealing in electroplated copper films follows a two-step growth mechanism i.e. a rapid primary top down recrystallization followed by a slower lateral one. The former is dominant owing to the lower energy barrier for recrystallization with respect to free surfaces. For copper columns, however, the cylinder surface is also regarded as free surface. This explains why the Region I grains tend to grow on the edge of the columns. It is hard to determine whether the top-down or the lateral recrystallization is primary based on present results. Nevertheless, the resultant microstructure as shown in Fig. 7-10c and Fig. 7-11c seems to suggest that lateral recrystallization is promoted when the column diameter decreases.

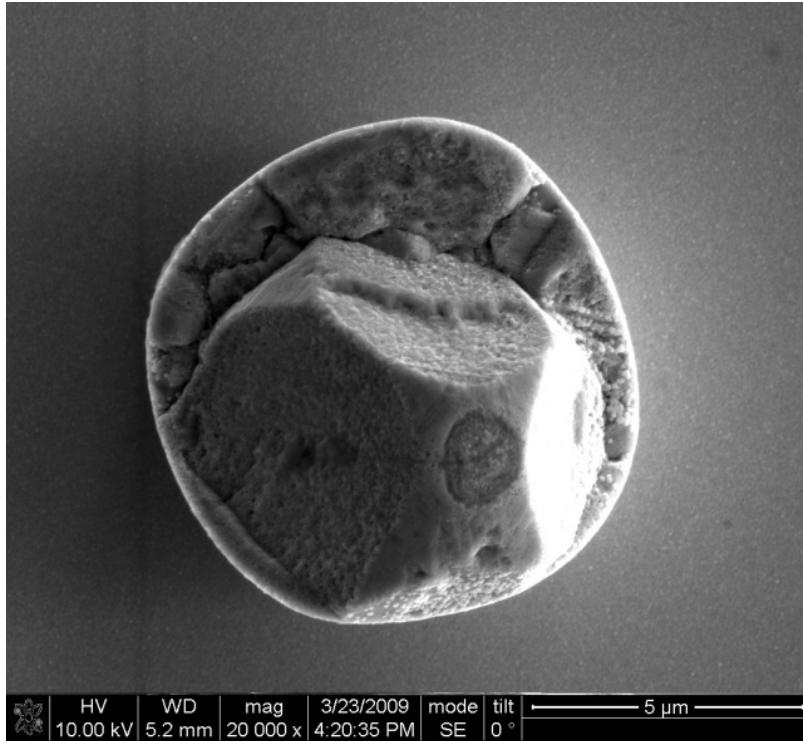

(a)

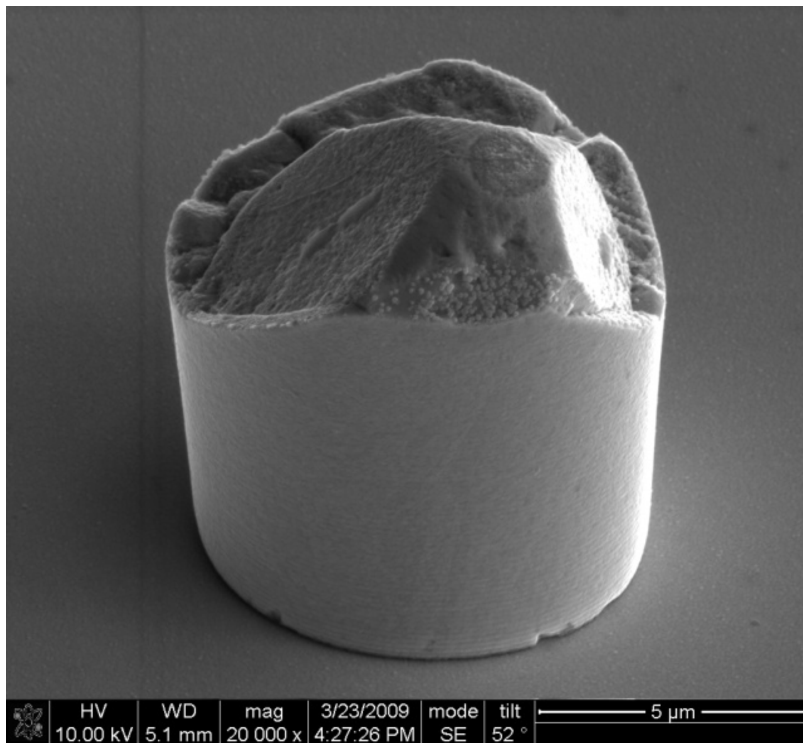

(b)

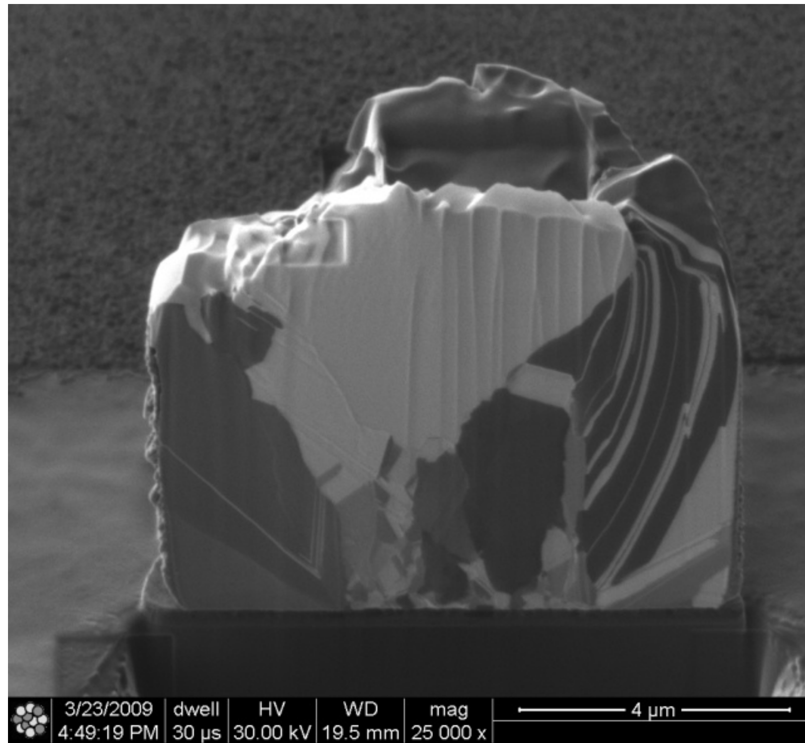

(c)

Fig. 7-10 the morphology and microstructure of the copper column of 10μm in diameter plated for one hour (a) the top view (b) the stereoscopic view and (c) the cross-section

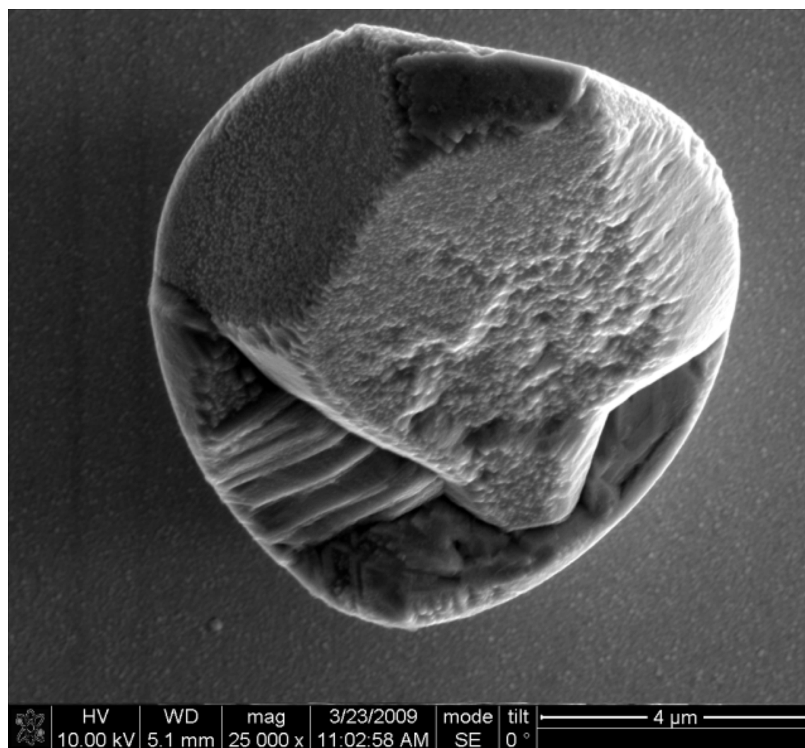

(a)

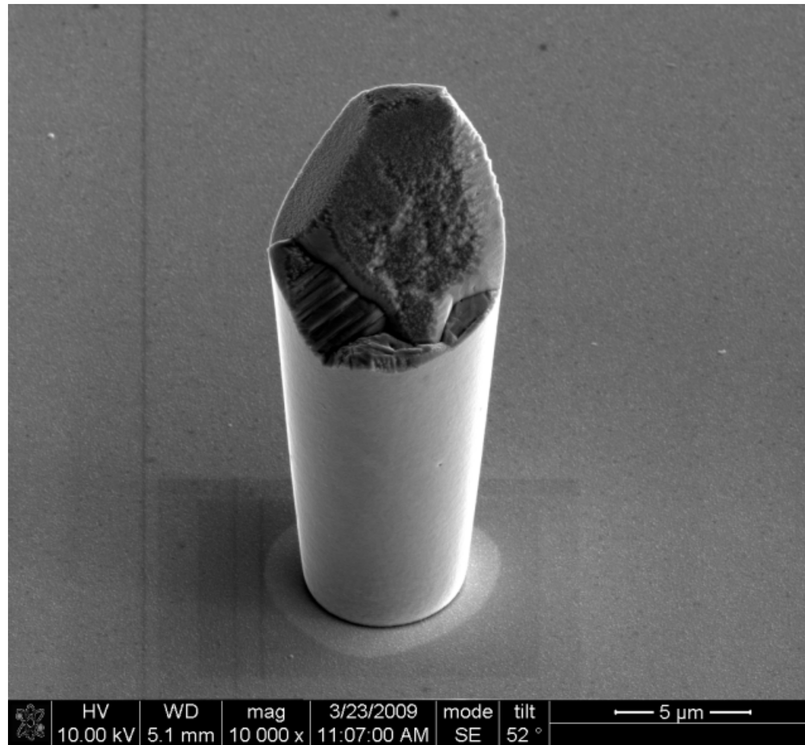

(b)

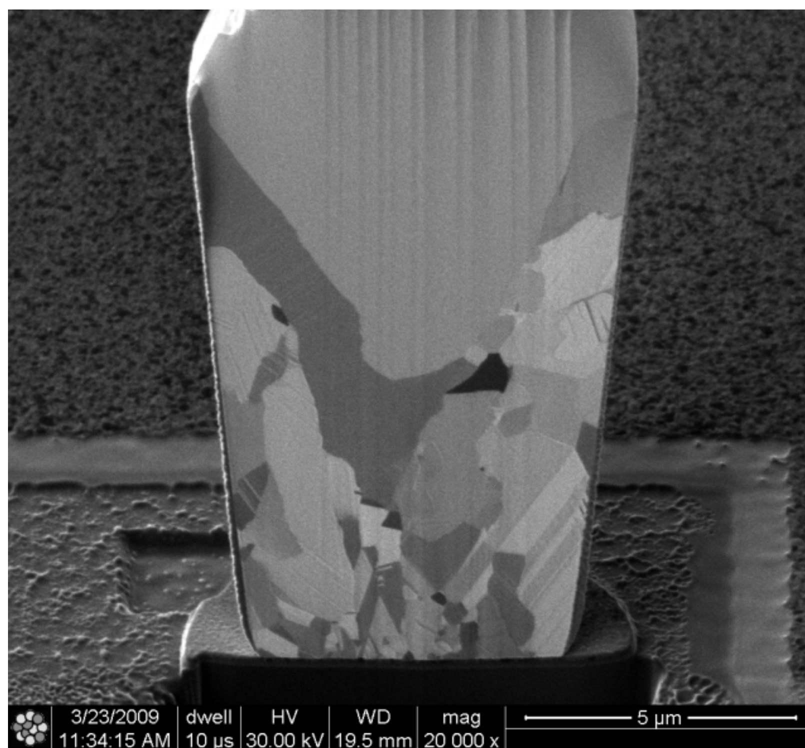

(c)

Fig. 7-11 the morphology and microstructure of the copper column of 10μm in diameter plated for 2 hours (a) the top surface (b) the stereoscopic view and (c) the cross-section

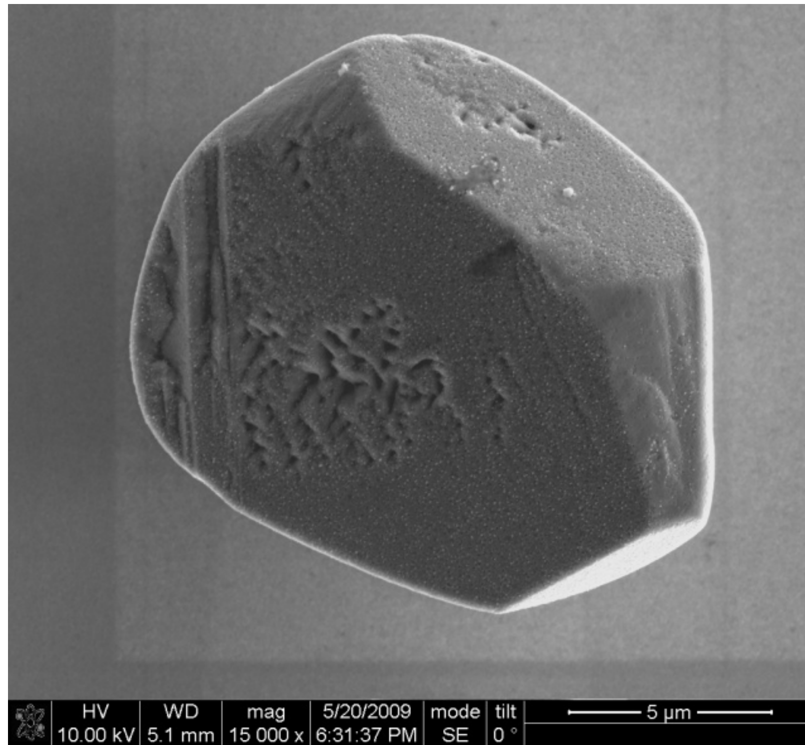

(a)

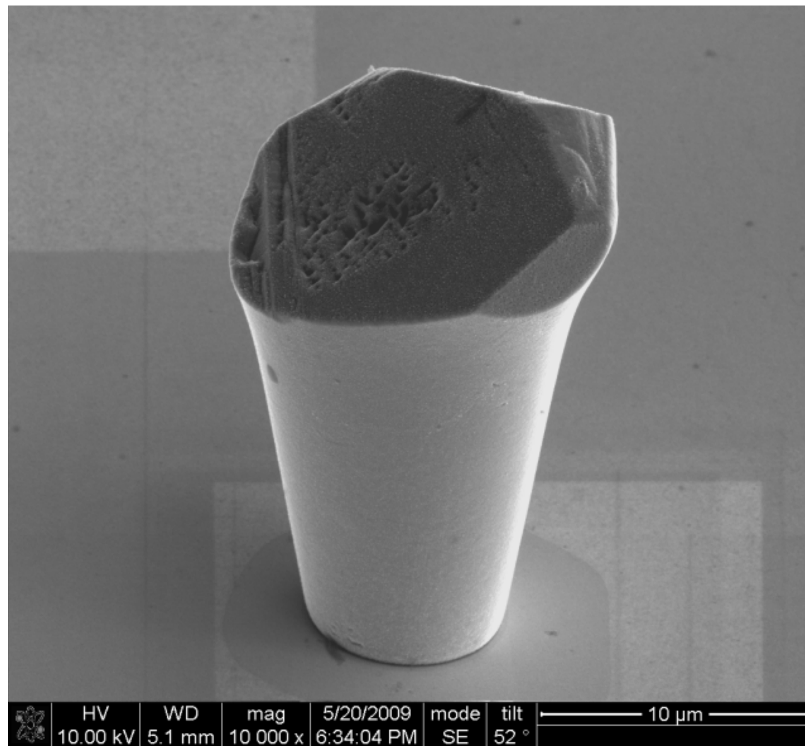

(b)

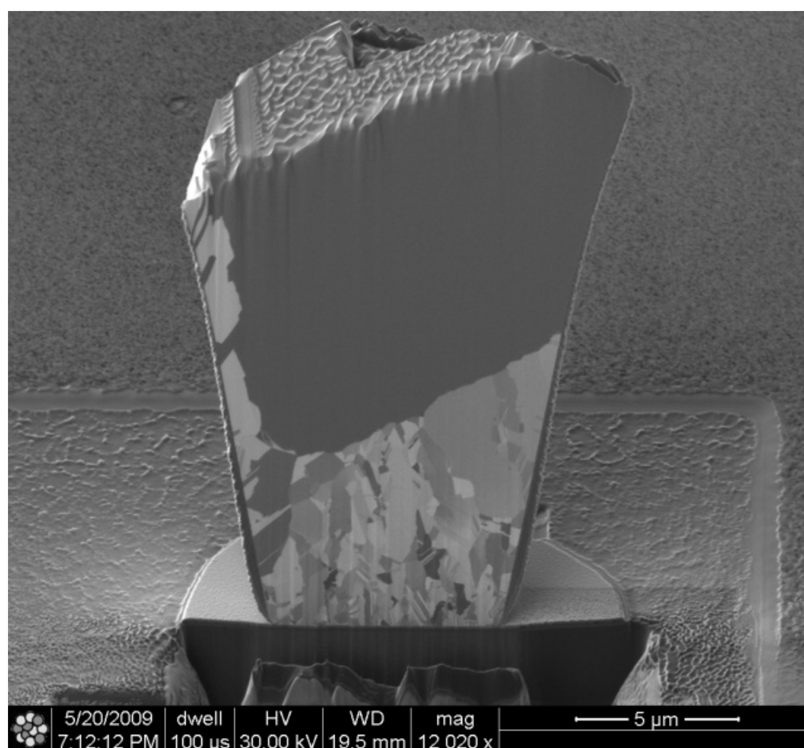

(c)

Fig. 7-12 the morphology and microstructure of the copper column of 10μm in diameter plated for 3 hours (a) the top surface (b) the stereoscopic view and (c) the cross-section

7.3.4 Evolution of the crystal structure

To examine the evolution of the crystal structure during electrodeposition of copper columns, a series of XRD analyses were carried out on the plated wafer samples as well as an as-sputtered wafer sample, and a bare Si wafer for comparison. The radiation area for the XRD beam was about 15mm×20mm which covered both copper columns and the Au seed layer. The amount of Cu scanned by the X-ray beam was very small compared to the Au and the single crystal Si substrate. Therefore, a detector with a high sensitivity and a smaller limit of intensity was used. Fig. 7-13 shows the XRD spectra of all the samples. The 2θ range corresponding to the main Si peak was skipped to avoid damaging the detector. For better comparison, only the XRD profiles in the range of 42°-91° was plotted focusing on Cu peaks. It can be seen that both the Cu (111) and the Cu (200) peaks are present in all the plated samples. The intensity of the Cu (200) peak of the sample plated for half an hour is about 5-6 times lower than other plated samples. The Cu (220) peaks are only present in the samples plated for three hours. And Cu (311) peaks, although very weak, are detected in the samples plated for two and three hours.

Evolution of grain orientation of a copper column can occur during plating and recrystallization. The final texture depends on which formation mechanisms and driving forces dominate. It has been found [135] that Cu (111) textures develop for surface-energy-driven growth, Cu(100) textures for strain-energy-driven growth in elastic regime and Cu (110) textures for the strain-energy-driven growth in plastic regime. If grain growth occurs during plating, it is likely to favour orientations which minimize surface and interface energy. If grain growth occurs during recrystallization, the stored strain energy will drive the texture development. Accordingly, the observed Cu (111) orientations must have developed by a surface energy minimizing growth during plating. The observed Cu (200) textures may be developed during recrystallization driven by strain energy at elastic regime. Stress accumulates with growth of a column and leads to strains at elastic regime or plastic regime. The strain energy minimizing process which can lead to preferred texture development can occur by recrystallization after or even during plating. There may have not been sufficient stress to lead to strain at plastic regime when plated for less than three hours, which can drive development of Cu (220) textures. That is probably why the weak Cu (220) texture is only observed in the columns plated for three hours. It is interesting to notice that the Au (311) peak, which is absent in the as-sputtered samples, appear in the plated samples. It indicates that plating and/or the post-plating recrystallization has changed the crystallographic texture of the Au seed layer at the mean time. This can be ascribed to diffusions of Cu atoms into the Au substrate and changes its structure.

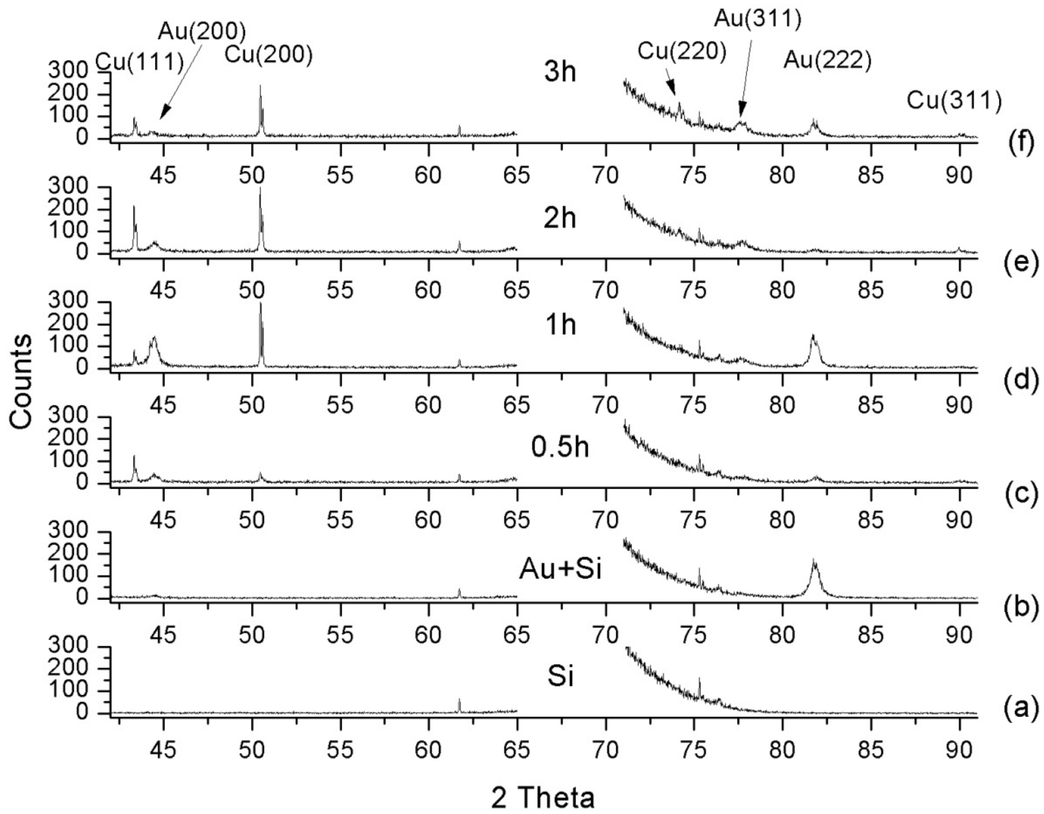

Fig. 7-13 XRD line profiles of (a) bare Si wafer, (b) Si with sputtered Au, (c) plated for 0.5 hour, (d) 1 hour, (e) 2 hours and (f) 3 hours

7.4 Recrystallization

Fig. 7-14 shows the selected XRD line profile for Cu (111) and (200) peaks from the in-situ analysis of one sample from a few minutes until 10 days after plating. The change of diffracting intensity of (111) planes was negligible until 10 days after plating. For (200) planes changes were observed within 100 minutes but remained nearly unchanged after that. This indicates that the self-annealing of plated copper columns may have preferences in different orientations during different stages. However, it should be noted the amplitude of the changes of the peak density is rather small and the phenomenon of peak-splitting due to self-annealing, which have been previously reported in literatures [30, 36], are not observed in this study. The Kα1 and Kα2 peaks already exist and no obvious broadening in as-deposited sample, for which the spectra was actually collected 32 minutes after plating. In such case, the deposit may have already undergone major recrystallization.

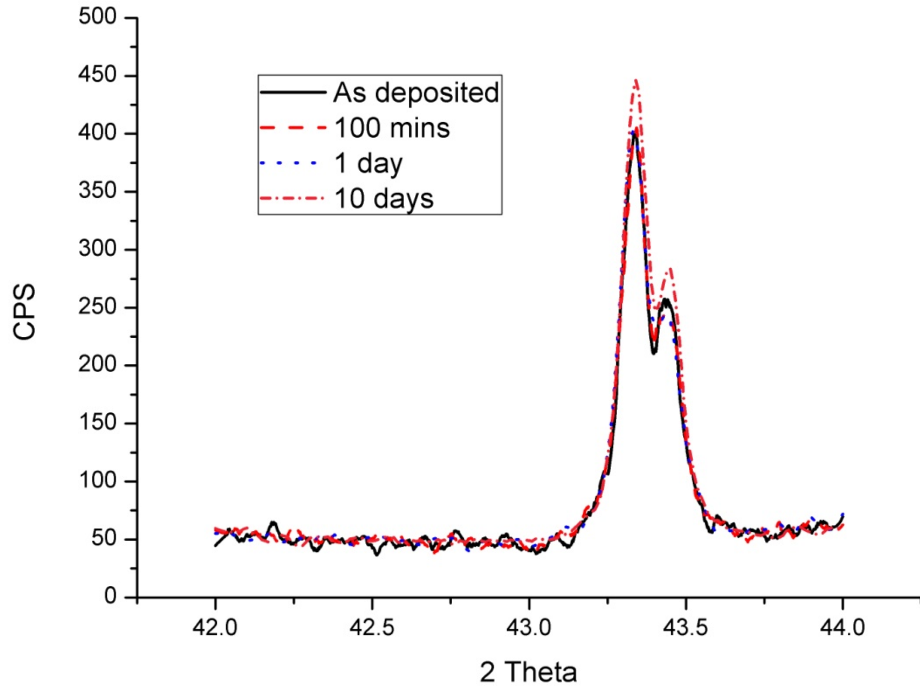

(a)

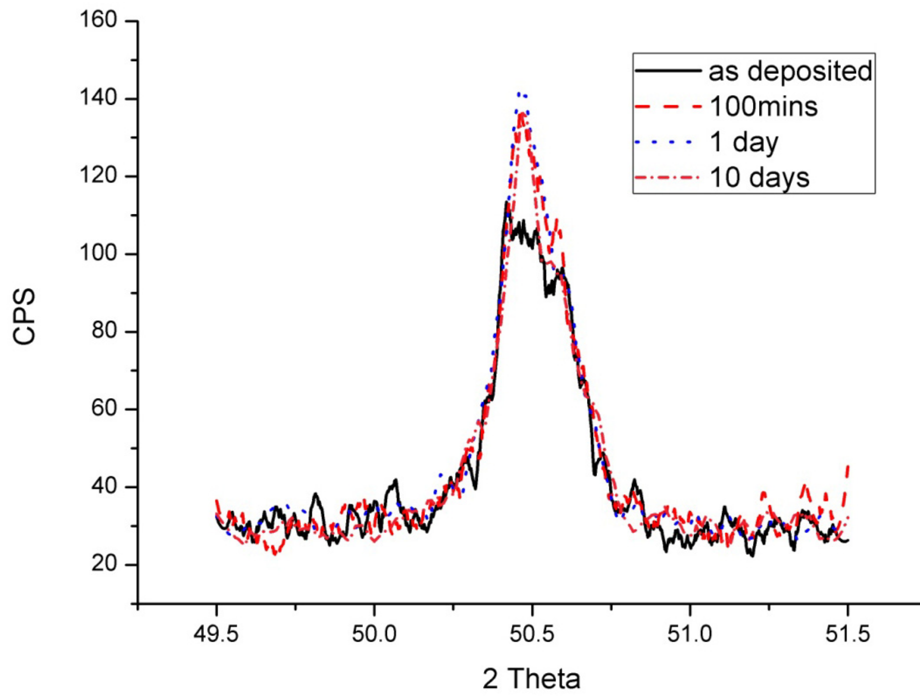

(b)

Fig. 7-14 XRD line profiles at different time after deposition of a sample plated for one hour for the a) 111 and b) 200 texture

As explained earlier, it was believed [32, 41] that the presence of organic additives is necessary for self-annealing of a copper film to occur. However, the present findings concerning the copper columns seem to disagree with the observations on thin films. Organic additives, which can be partially co-deposited with metal atoms, may retard the recrystallization during plating and save the energy for subsequent spontaneous self-annealing.

7.5 Discussion and conclusions

At room temperature, electro-crystallization is characterised as a non-equilibrium process. A high density of defects is therefore expected to be formed in a copper electrodeposit. The passage of electric current through the deposit may also influence the atomic diffusion process during plating as suggested by a recent paper [51]. For plating of electronic interconnects e.g. copper columns and through silicon vias, the shape and size of the deposit also effect crystal growth. These factors make the deposition process of electroplated copper columns very complex. A complete prediction of the final structure of a copper column requires consideration of not only the growth process during plating, which are governed by plating parameters and conditions, but also the simultaneous recrystallization accompanying the growth and spontaneous self-annealing after plating.

The ultrafine Region III grains are expected to contain the original as-plated grains; the Region II and Region I grains are predicted to be resulted from the original deposition, accompanying recryst[136]allization and self-annealing after plating. Based on the present results, it is hard to determine which process is dominant or mainly responsible for the final structure. In comparison with thin films (<5μm thick) that have been studied in the literature, the thicker deposit (about 5-25μm) in this work, the cylindrical shape of columns and the absence of organic additives in the plating solution have led to the faster kinetics of self-annealing and/or recrystallization during plating.

In summary, electroplated copper columns have been characterized in order to study the evolution of their external morphology, cross-sectional microstructure and crystal structure. The microstructure of electroplated copper columns is characteristic of bi-modal or tri-modal grain size distribution, i.e. large grains on the top and particularly the

edge (Region I), ultrafine grains near the deposit/seed layer interface (Region III) and mixture of columnar grains and twins (Region II). The size of the columns was also found to have significant effects on the microstructure of the columns when it is comparable with the size of the Region I grains. The results indicate that recrystallization have occurred during or after the plating in two ways, i.e. via the top surface down and laterally. And the lateral recrystallization seems to be more significant when the column diameter decreases. The copper columns plated for longer time show stronger Cu (200) peaks. The low intensity peaks including Cu (311) and Cu (220) were only found in XRD line profiles of the columns plated for longer than two hours. The Au (311) peaks, which are absent in as-sputtered Au, was found in plated samples and its intensity increased with deposition time. Slight changes of the crystal structure were observed by the in-situ XRD and it was found that the changes have preference in orientation in different stages of self-annealing. Finally, our results indicate the presence of organic additives is not essential for self-annealing of copper column to occur, which disagrees with the literature in the case of electroplated films.

Chapter 8 General Discussion

The aim of this project was to uncover the growth mechanism of electrodeposited copper columns. To achieve this, methodologies to reconstruct the growth history both computationally and experimentally have been adopted to elaborate the detailed fundamental mechanism.

8.1 KMC Simulations

8.1.1 Single-lattice model

A single-lattice 2DCS-KMC model to simulate the electro-crystallization of a copper single crystal was developed, thereby the microstructure history, incorporated with selected snapshots at any times of interest can be restored to visualize the processes of nucleation, merging of clusters and faceting. The statistics of the growth of clusters provided a quantitative description of the growth history. Finally, the entire growth history from the beginning of the first atom to 100 EML was reconstructed. The model is capable of capturing effects of the deposition parameters including applied electrode potential, temperature and concentration of the electrolyte on the growth history.

As a single-lattice model, it exactly represents a single crystal; as a 2D cross-sectional model, it saves on computational cost significantly when compared to 3D models. These features make it well suited for treating single crystal electrocrystallization and reconstructing the growth history of not only the early stages but also the crystal growth processes at later stages. Note most of the reported 3D and/or multi-scale models focused only on the early-stage nucleation processes. In Chapter 1, it is recognized that the electrodeposition of single crystal copper columns is one of the two solutions to eliminate the size effects. This study provides a simulation tool to aid the optimum selection of deposition parameters for the electrodeposition of a single crystal deposit. Nevertheless, the growth history was reconstructed in a rather idealized sense. Specifically, it is more likely for a single crystal to grow either from a seed crystal or by recrystallization from a polycrystalline structure [136-138], other than following the nucleation-growth-merging mechanism. Drew et al [139] introduced seed clusters in their single-lattice KMC model and simulated electrodeposition of a metal on a foreign

substrate. It was found that it was possible to obtain larger clusters with a smaller number of secondary nuclei at a lower applied potential. In the future, it may be useful to include a seed crystal in the present model to simulate the seeded electrodeposition of a single crystal. It is worth noting that single-crystal micro-wires [5-6] and nano-wires [9, 15-18]have been successfully obtained by electrodeposition without the presence of a seed crystal or undergoing an intended recrystallization. The formation mechanism of such single crystal electrodeposits is still unclear. Further improvements to the present single-lattice model require a firmer understanding to the growth mechanism, which may need aid of experiments. The improved KMC models will also be beneficial to the study of growth mechanisms.

8.1.2 Poly-lattice model

Further to the single-lattice KMC model for single-crystal electrocrystallization, a poly-lattice KMC model for simulation of polycrystalline copper electrodeposition on a copper or gold substrate was developed. The growth history was reconstructed by simulations of the evolution of the microstructures, the grain shapes and the grain statistics including the grain density, the grain size and the variance of grain size.

This work is the first attempt at using a poly-lattice KMC model to simulate the electrodeposition process. This leads to several advancements over other reported multi-lattice KMC models which have been developed for other thermal deposition processes in the following aspects: Firstly, the key feature of grain boundaries - the higher energetic state- is taken into account in this model by introducing two novel parameters, namely the strange coordination and the correction coefficient while determining the diffusion rate. Secondly, grains are generated on an ad hoc basis, as in real life; thereby no restriction is given to the number of lattices, which enable the model to treat the early-stage nucleation and grain growth at later stages as a whole process. In addition, the grain boundary misorientation can also be simulated. The model is capable of capturing the main aspects of the nucleation mechanism, grain growth, texture development and grain boundary misorientation distribution. The model is capable of capturing the effects of the deposition parameters on deposit microstructure and the grain growth history. In comparison with the single-lattice model, this poly-lattice model is more promising to develop into a simulation tool for an

optimum selection of deposition parameters for generation of a desirable microstructure.

In terms of the size scale, the simulation cell of 200×50 lattice spaces represents about 22×4nm in reality. The computing time spent based on a PC of 3.6GHz spanned from a few hours to about 100 hours and the simulated deposition time ranged from a few seconds to over 25 seconds depending on the deposition parameters as well as the physicochemical parameters. The computational cost of this model is slightly higher than the single-lattice one. In spite of this, it is still reasonable as an atomic-scale simulator. It is anticipated that the model may have great use and the potential in the simulation of the electrodeposition of polycrystalline nano-components to understand the growth mechanism without the need of coarse-grained approximation. Note the electrodeposition of nano-crystal copper columns was recognized as another solution to eliminate the size effects. This poly-lattice model is also identified as a major step towards the ultimate goal - to develop a simulation tool to guide the selection of optimum deposition parameters for various applications.

8.1.3 Limitations

The present 2DCS models save on computational costs significantly at the expense of less physical significance as well as the missing data of the third dimension. For example, the values of some physicochemical parameters that are originally defined and/or measured based on three dimensions need modification for their use in the 2DCS models. In the present work, assumptions were made about e.g. the values of unknown parameters such as jump frequency and it was varied to look at their effects on the simulations. However, if computational cost is not a major issue, then 3D models are better suited for a more complete reconstruction of the growth history, with more accurate prediction and a better comparison with the experimental observations. It is straightforward to extend the present 2DCS models to three dimensions; for instance, the present triangular lattice should be replaced by a 3D Bravis lattice (e.g. fcc for Cu) and the coordinate system extended to 3D. Another degree of freedom i.e. the rotation angle can also be introduced to define a grain orientation.

In the present models, the deposition parameters including applied electrode potential, the concentration of the Cu^{2+} ions and the temperature, once given, do not vary during a simulation. In reality, these parameters may change due to the change of the environment or the growth of the deposit. For example, the concentration of cupric ions at the electrode/electrolyte interface is usually less than the bulk value and varies during a diffusion-limited deposition process. The deposition temperature may also change with the ambient temperature or rise due to a strong and continuous stirring, for example, ultrasonic or mega-sonic agitations. The effects of the variation of these deposition parameters can be taken into account by coupling the present atomic-scale KMC models to a continuum or classical model which deals with these parameters. There have reported some multi-scale models coupling a single-lattice KMC model to a finite difference model as reviewed in Chapter 3. No multi-scale model coupling a poly-lattice KMC to a continuum model e.g. a finite element model has ever been reported.

8.2 Ex-situ experimental observations and comparision with simulations

To reconstruct the growth history experimentally, we carried out electrodeposition tests of a series of wafers for a series of deposition times respectively and then characterized them in terms of surface morphology, microstructure and crystal structures. At the early stages of electrodeposition, the nucleation process is dominant. Scanning probe microscopy (SPM) has proved to be a useful method to observe the nucleation at atomic scale experimentally. An ex-situ observation of the evolution of the surface morphology of Cu deposits on metallized but unpatterned wafers with AFM was performed. The heterogeneous nucleation phenomenon, the competitive growth both longitudinally and laterally and the dominant growth of some nuclei were observed and verified experimentally. These experimental observations were also visualized by the poly-lattice KMC simulation of deposition of Cu on a Au substrate at a smaller size scale and a shorter time scale as presented in Chapter 4. For a convincing validation of the model and the simulation results, however, either KMC simulations or experiments at comparable size and time scales are needed. For example, experimental observation at a size and time scale that is comparable with the present 2DCSP-KMC simulations may be achieved by in-situ SPM. For a more accurate prediction and a better comparison with

the experimental results, the present KMC models need significant improvements to overcome their limitations, some of which are stated above.

It should be noted that the patterned wafers are not suitable for this investigation because of the technical challenges of getting the probe into the apertures of high aspect ratio and performing scanning. Therefore, the experimental reconstruction of the growth history was divided into two stages, namely the nucleation-dominating early stage and later stages featuring growth and recrystallization. Patterned wafers were plated for the ex situ observation of the later stage growth of copper columns, which were then characterized in more detail in terms of the external morphology, cross-sectional microstructure and crystal structure. The results indicated that recrystallization, during or after plating or both, play important roles in the formation of the final bi-modal or tri-modal microstructure. This raised a methodological concern. Since the recrystallization can be critical, it may be more useful to reconstruct the history according to recrystallization time rather than deposition time, especially, when the time of characterization can be critical. The in-situ observation of the recrystallization after plating indicated that major recrystallization had already occurred during plating or very shortly after plating although there is still insignificant recrystallization going on afterwards. The results also suggested that the cylindrical shape of copper columns may promote the recrystallization laterally from outside inwards and accelerate the overall recrystallization process in comparison with the case of electroplated copper films. Therefore, the copper columns have already largely reached a stable state in terms of microstructure and crystal structure when being characterized, which means the methodology can still be applicable.

It is technically unrealistic at present to experimentally observe the growth and recrystallization process in situ in the course of deposition. For a more complete reconstruction of the growth history, simulations are required. The poly-lattice KMC model provides an approach to simulations of the nucleation, growth and recrystallization during and/or after plating as a whole process. However, at present, it is still too computationally costly to simulate the electrodeposition of copper columns at micro- scale over a long period of time up to hours. Coarse-grained methods can be considered to save computational costs at expense of accuracy.

8.3 Reconsideration of the definition of electro-crystallization

There has not been a unanimous definition of electrocrystallization. In this study, the best definition was “nucleation and crystal growth in electrochemical systems under the influence of an electric field”. Copper self-annealing has been observed in the last decades in electroplated copper and it is strongly influenced by plating parameters and compositions of plating baths. It was suggested by some earlier work [33, 133] and the present work that recrystallization may also occur during the course of electrodeposition. Accordingly, the formation of an electrodeposit can undergo nucleation, grain growth, accompanying recrystallization and post-deposition recrystallization. Therefore, a more general and up-to-date definition of electrocrystallization should include recrystallization during and after electrodeposition.

Chapter 9 Conclusions

9.1 KMC simulations

A 2DCS-KMC model has been developed for the simulation of electrodeposition of copper on a gold substrate. The entire growth history of the simulated timescale can be reconstructed at atomic scale. The cluster density, average size, variance of the size and average aspect ratio has been obtained from the simulations. They are found to vary with the deposition, which has been reflected in the evolution of the microstructure. A microstructure history map together with a series of separate snapshots has been used to visualize the evolution of the microstructure. The model has been proven to be able to capture the effects of the process parameters including the concentration of the solution, the temperature and the applied electrode potential on the growth history. Using a concentrated solution tends to result in larger variance of the cluster size and accelerate the microstructure evolution. The cluster size varies to a lesser extent at higher temperatures. However the temperature has no notable effects on the rate of the change of cluster density and variance of cluster size. The cluster height varies less while cluster width varies more and the microstructure evolution is accelerated when a more negative potential is applied. All these parameters have little effect on the maximum cluster density.

Further to the 2DCS-KMC model for single crystal electrocrystallization, an advanced 2DCSP-KMC model has been developed for simulation of the electrodeposition of polycrystalline copper on a copper or gold substrate. With this model, the early-stage nucleation and the grain growth after impingement of the nuclei can be simulated as a whole process and the entire growth history reconstructed in terms of the evolution of microstructure, grain statistics and grain boundary misorientation. The growing-over mechanism has been visualized by the simulation. And the simulated distribution of grain boundary misorientation shows preferences on the more stable low-angle boundaries. It is indicative of the fact that the energetic state of grain boundaries has been captured in the simulations. The model has also proved being capable of capturing the various effects of the deposition parameters including applied electrode potential, the concentration of cupric ions and temperature. They have effects on deposit

microstructure and various parameters describing the nucleation and growth history including the average of grain size, the variance of the grain size, saturation value of grain density, the time for reaching the saturation, the total deposition time and the distribution of misorientation, which were found to be significantly dependent on substrates. The unknown physicochemical parameter, the jump frequency was studied and it has been found that increased value of the jump frequency promotes diffusion and thereby has moderate effects on the microstructure and the growth history.

9.2 Characterisation

The evolution of the surface morphology of the electrodeposited copper on as-sputtered Au seed layer from 16ms to 1000s was observed and their formation mechanism discussed. It was found that the copper nucleation starts within as short as 4ms. Then the nucleation parallels the growth of the existing nuclei until certain time after 100s, when the latter dominates the deposition process. After that, the surface morphology of copper deposit evolves following the mechanism of growing-over and recrystallization. The heterogeneous nucleation phenomenon, the competitive growth both longitudinally and laterally and the dominant growth of some nuclei were observed and verified experimentally. These phenomena were also visualized by the poly-lattice KMC simulatios on a Au substrate at a smaller size scale and a shorter time scale. A heuristic model is finally proposed to describe the mechanism of the early-stage electrocrystallization of Cu on a polycrystalline Au seed layer based on the findings.

The microstructure of electroplated copper columns is characterized as bi-modal or tri-modal grain size distribution, i.e. large grains on the top and preferentially on the edge (Region I), ultrafine grains near the deposit/seed layer interface (Region III) and mixture of columnar grains and twins (Region II). The size of the columns was also found to have significant effects on the microstructure of the columns when it is comparable with the size of the Region I grains. The results indicate that recrystallization has occurred during and/or after the plating in two ways, i.e. from the top surface down and laterally. The lateral recrystallization also seems to be promoted when the column diameter decreases. The crystal structure of the electroplated columns also evolved during and/or after plating. Slight changes of the crystal structure were observed by the in-situ XRD

and it was found that the changes have preference in orientation in different stages of self-annealing.

9.3 Summary

To summarize, the growth history of electrodeposition of copper columns were incompletely reconstructed by KMC simulations and validated experimental observations.

Chapter 10 Recommendations of Future Work

Following future work is recommended to improve the present KMC models and/or extend their applications:

- The models can be used to simulate pulse plating with some minor modifications, i.e. closing the deposition event during the pulse-off time and activating it during the pulse-on time. The event of desorption needs to be considered for modelling reversible pulse plating.
- Defects e.g. twin boundaries, may also be taken into account by including lattices with staking faults, which makes it possible to simulate the interesting nano-twinning phenomenon that has attracted increasing attentions during the last decade as reviewed earlier in Chapter 2.
- The model can also be used to simulate the post-deposition recrystallization, e.g. copper self-annealing, being capable of capturing the grain boundary dynamics.
- We can see many future applications of the poly-lattice KMC model in multi-scale models for modelling multi-scale and multi-physics systems. For example, the effects of grain boundaries on the electrical and mechanical response of materials may be captured by such multi-scale models because the grain boundaries can be simulated by the poly-lattice KMC model.

References

1. D.W. Henderson, J.J. Woods, T.A. Gosselin, J. Bartelo, D.E. King, T.M. Korhonen, M.A. Korhonen, L.P. Lehman, S.K. Kang, P. Lauro, D.Y. Shih, C. Goldsmith, and K.J. Puttlitz, *The Microstructure of Sn in near-Eutectic Sn-Ag-Cu Alloy Solder Joints and Its Role in Thermomechanical Fatigue.* Journal of Materials Research, 2004. **19**(6): p. 1608-1612.
2. A. LaLonde, D. Emelander, J. Jeannette, C. Larson, W. Rietz, D. Swenson, and D.W. Henderson, *Quantitative Metallography of Beta-Sn Dendrites in Sn-3.8ag-0.7cu Ball Grid Array Solder Balls Via Electron Backscatter Diffraction and Polarized Light Microscopy.* Journal of Electronic Materials, 2004. **33**(12): p. 1545-1549.
3. A.U. Telang and T.R. Bieler, *Characterization of Microstructure and Crystal Orientation of the Tin Phase in Single Shear Lap Sn-3.5ag Solder Joint Specimens.* Scripta Materialia, 2005. **52**(10): p. 1027-1031.
4. L. Lu, Y. Shen, X. Chen, L. Qian, and K. Lu, *Ultrahigh Strength and High Electrical Conductivity in Copper.* Science, 2004. **304**(5669): p. 422-426.
5. Y.F. Shen, L. Lu, Q.H. Lu, Z.H. Jin, and K. Lu, *Tensile Properties of Copper with Nano-Scale Twins.* Scripta Materialia, 2005. **52**(10): p. 989-994.
6. Z. Xu, J. Li, J. Li, and H. Fu, *Mechanical Properties and Electrical Resistivity of Continuous Casting Single-Crystal Copper.* Zhongguo Youse Jinshu Xuebao/Chinese Journal of Nonferrous Metals, 1999. **9**(3): p. 577-581.
7. D. Dobrev, J. Vetter, N. Angert, and R. Neumann, *Electrochemical Growth of Copper Single Crystals in Pores of Polymer Ion-Track Membranes.* Applied Physics a-Materials Science & Processing, 1999. **69**(2): p. 233-237.
8. D. Dobrev, J. Vetter, N. Angert, and R. Neumann, *Periodic Reverse Current Electrodeposition of Gold in an Ultrasonic Field Using Ion-Track Membranes as Templates: Growth of Gold Single-Crystals.* Electrochimica Acta, 2000. **45**(19): p. 3117-3125.
9. S. Karim, M.E. Toimil-Molares, F. Maurer, G. Miehe, W. Ensinger, J. Liu, T.W. Cornelius, and R. Neumann, *Synthesis of Gold Nanowires with Controlled*

Crystallographic Characteristics. Applied Physics a-Materials Science & Processing, 2006. **84**(4): p. 403-407.

10. J.W. Shin, A. Standley, and E. Chason, *Epitaxial Electrodeposition of Freestanding Large Area Single Crystal Substrates.* Applied Physics Letters, 2007. **90**(26): p. 261909-3.
11. K.V. Singh, A.A. Martinez-Morales, G.T.S. Andavan, K.N. Bozhilov, and M. Ozkan, *A Simple Way of Synthesizing Single-Crystalline Semiconducting Copper Sulfide Nanorods by Using Ultrasonication During Template-Assisted Electrodeposition.* Chemistry of Materials, 2007. **19**(10): p. 2446-2454.
12. F. Xiao, B. Yoo, K.N. Bozhilov, K.H. Lee, and N.V. Myung, *Electrodeposition of Single-Crystal Cubes of Lead Telluride on Polycrystalline Gold Substrate.* Journal of Physical Chemistry C, 2007. **111**(30): p. 11397-11402.
13. F.Y. Yang, L. Kai, H. Kimin, D.H. Reich, and et al., *Large Magnetoresistance of Electrodeposited Single-Crystal Bismuth Thin Films.* Science, 1999. **284**(5418): p. 1335-1337.
14. L. Xu, P. Dixit, J. Miao, J.H.L. Pang, X. Zhang, K.N. Tu, and R. Preisser, *Through-Wafer Electroplated Copper Interconnect with Ultrafine Grains and High Density of Nanotwins.* Applied Physics Letters, 2007. **90**(3): p. 033111-3.
15. T.W. Cornelius, J. Brotz, N. Chtanko, D. Dobrev, G. Miehe, R. Neumann, and M.E.T. Mollares, *Controlled Fabrication of Poly- and Single-Crystalline Bismuth Nanowires.* Nanotechnology, 2005. **16**(5): p. S246-S249.
16. M. Tian, J. Wang, J. Snyder, J. Kurtz, Y. Liu, P. Schiffer, T.E. Mallouk, and M.H.W. Chan, *Synthesis and Characterization of Superconducting Single-Crystal Sn Nanowires.* Applied Physics Letters, 2003. **83**(8): p. 1620-1622.
17. M.L. Tian, J.U. Wang, J. Kurtz, T.E. Mallouk, and M.H.W. Chan, *Electrochemical Growth of Single-Crystal Metal Nanowires Via a Two-Dimensional Nucleation and Growth Mechanism.* Nano Letters, 2003. **3**(7): p. 919-923.
18. J. Zhang, X. Wang, X. Peng, and L. Zhang, *Fabrication, Morphology and Structural Characterization of Ordered Single-Crystal Ag Nanowires.* Applied Physics A: Materials Science & Processing, 2002. **75**(4): p. 485-488.
19. P.M.R. Rao R. Tummala, Ankur Aggarwal, Gaurav Mehrotra, Sau Wee Koh, Shubhra Bansal. *Copper Interconnections for High Performance and Fine Pitch*

Flipchip Digital Applications and Ultra-Miniaturized Rf Module Applications. in *2006 Electronic Components and Technology Conference*. 2006. San Diego.

20. *Intel Eliminates Use of Lead from Future Microprocessors*. [Online news] [cited 2009 17 February 2009]; Available from: http://www.intel.com/pressroom/kits/45nm/leadfree/index.htm.
21. S. Lagrange, S.H. Brongersma, M. Judelewicz, A. Saerens, I. Vervoort, E. Richard, R. Palmans, and K. Maex, *Self-Annealing Characterization of Electroplated Copper Films.* Microelectronic Engineering, 2000. **50**(1-4): p. 449-457.
22. C. Lingk and M.E. Gross, *Recrystallization Kinetics of Electroplated Cu in Damascene Trenches at Room Temperature.* Journal of Applied Physics, 1998. **84**(10): p. 5547-5553.
23. M. Schlesinger. *Electroplating*. 2002 [cited 2009 18 Septembper 2009]; Available from: http://electrochem.cwru.edu/encycl/art-e01-electroplat.htm.
24. W. SCHWARZACHER, *Electrodeposition : A Technology for the Future.* The Electrochemical Society interface 2006. **15**(1): p. 32-35.
25. M. Datta, R.V. Shenoy, C. Jahnes, P.C. Andricacos, J. Horkans, J.O. Dukovic, L.T. Romankiw, J. Roeder, H. Deligianni, H. Nye, B. Agarwala, H.M. Tong, and P. Totta, *Electrochemical Fabrication of Mechanically Robust Pbsn C4 Interconnections.* Journal of the Electrochemical Society, 1995. **142**(11): p. 3779-3785.
26. H. Honma, *Plating Technology for Electronics Packaging.* Electrochimica Acta, 2001. **47**: p. 75-84.
27. P.C. Andricacos, C. Uzoh, J.O. Dukovic, J. Horkans, and H. Deligianni, *Damascene Copper Electroplating for Chip Interconnections.* IBM J. Res. Dev., 1998. **42**(5): p. 567-574.
28. R. Beica, C. Sharbono, and T. Ritzdorf, *Copper Electrodeposition for 3d Integration*, in *Design, Test, Integration and Packaging of MEMS/MOEMS, 2008*. 2008, EDA Publishing Association: Nice, France. p. 127-131.
29. R.J. Gutmann, *Advanced Silicon Ic Interconnect Technology: Present Trends and Rf Wireless Implications.* IEEE Transactions on Microwave Theory and Techniques, 1999. **47**(6): p. 667-674.

30. C. Detavernier, S. Rossnagel, C. Noyan, S. Guha, J.C. Cabral, and C. Lavoie, *Thermodynamics and Kinetics of Room-Temperature Microstructural Evolution in Copper Films.* Journal of Applied Physics, 2003. **94**(5): p. 2874-2881.

31. J.M.E. Harper, J.C. Cabral, P.C. Andricacos, L. Gignac, I.C. Noyan, K.P. Rodbell, and C.K. Hu, *Mechanisms for Microstructure Evolution in Electroplated Copper Thin Films near Room Temperature.* Journal of Applied Physics, 1999. **86**(5): p. 2516-2525.

32. S.H. Brongersma, E. Richard, I. Vervoort, H. Bender, W. Vandervorst, S. Lagrange, G. Beyer, and K. Maex, *Two-Step Room Temperature Grain Growth in Electroplated Copper.* Journal of Applied Physics, 1999. **86**(7): p. 3642-3645.

33. D. Xu, V. Sriram, V. Ozolins, J.-M. Yang, K.N. Tu, G.R. Stafford, and C. Beauchamp, *In Situ Measurements of Stress Evolution for Nanotwin Formation During Pulse Electrodeposition of Copper.* Journal of Applied Physics, 2009. **105**(2): p. 023521-6.

34. K.B. Yin, Y.D. Xia, C.Y. Chan, W.Q. Zhang, Q.J. Wang, X.N. Zhao, A.D. Li, Z.G. Liu, M.W. Bayes, and K.W. Yee, *The Kinetics and Mechanism of Room-Temperature Microstructural Evolution in Electroplated Copper Foils.* Scripta Materialia, 2008. **58**(1): p. 65-68.

35. S.P. Hau-Riege and C.V. Thompson, *In Situ Transmission Electron Microscope Studies of the Kinetics of Abnormal Grain Growth in Electroplated Copper Films.* Applied Physics Letters, 2000. **76**(3): p. 309-311.

36. K. Pantleon and M.A.J. Somers, *In Situ Investigation of the Microstructure Evolution in Nanocrystalline Copper Electrodeposits at Room Temperature.* Journal of Applied Physics, 2006. **100**(11): p. 114319-7.

37. K. Pantleon, A. Gholinia, and M.A.J. Somers, *Quantitative Microstructure Characterization of Self-Annealed Copper Films with Electron Backscatter Diffraction.* physica status solidi (a), 2008. **205**(2): p. 275-281.

38. K. Pantleon and M.A.J. Somers, *X-Ray Diffraction Investigation of Self-Annealing in Nanocrystalline Copper Electrodeposits.* Scripta Materialia, 2006. **55**(4): p. 283-286.

39. L.M. Gignac, K.P. Rodbell, C. Cabral Jr., P.C. Andricacos, P.M. Rice, R.B. Beyers, P.S. Locke, and S.J. Klepeis, *Characterization of Plated Cu Thin Film*

Microstructures, in *Materials Research Society Symposium - Proceedings* 1999 Materials Research Society, Warrendale, PA, United States. p. 209-214

40. K.B. Yin, Y.D. Xia, W.Q. Zhang, Q.J. Wang, X.N. Zhao, A.D. Li, Z.G. Liu, X.P. Hao, L. Wei, C.Y. Chan, K.L. Cheung, M.W. Bayes, and K.W. Yee, *Room-Temperature Microstructural Evolution of Electroplated Cu Studied by Focused Ion Beam and Positron Annihilation Lifetime Spectroscopy.* Journal of Applied Physics, 2008. **103**(6): p. 066103-3.
41. V.A. Vas'ko, I. Tabakovic, S.C. Riemer, and M.T. Kief, *Effect of Organic Additives on Structure, Resistivity, and Room-Temperature Recrystallization of Electrodeposited Copper.* Microelectronic Engineering, 2004. **75**(1): p. 71-77.
42. A. Gangulee, *The Structure of Electroplated and Vapor-Deposited Copper Films.* Journal of Applied Physics, 1972. **43**(3): p. 867-873.
43. T.A. Tochitskii and L.V. Nemtsevich, *Twinning Mechanism in Electrolytic Films of Alloys Based on Cobalt with a Hexagonal Close-Packed Lattice.* Russian Journal of Electrochemistry, 2003. **39**(3): p. 301-304.
44. L. Lu, M.L. Sui, and K. Lu, *Superplastic Extensibility of Nanocrystalline Copper at Room Temperature.* Science, 2000. **287**(5457): p. 1463-1466.
45. D.X. Li, Q.H. Lu, and M.L. Sui, *Evolution of Twin Structure in Cold-Rolled Copper.* Microscopy and Microanalysis, 2003. **9**(Supplement S02): p. 596-597.
46. D. Xu, W.L. Kwan, K. Chen, X. Zhang, V. Ozolins, and K.N. Tu, *Nanotwin Formation in Copper Thin Films by Stress/Strain Relaxation in Pulse Electrodeposition.* Applied Physics Letters, 2007. **91**(25): p. 254105-3.
47. D. Xu, V. Sriram, V. Ozolins, J.-M. Yang, K.N. Tu, G.R. Stafford, C. Beauchamp, I. Zienert, H. Geisler, P. Hofmann, and E. Zschech, *Nanotwin Formation and Its Physical Properties and Effect on Reliability of Copper Interconnects.* Microelectronic Engineering, 2008. **85**(10): p. 2155-2158.
48. D. Xu, L. Xu, V. Sriram, K. Sun, J.-M. Yang, and K.-N. Tu. *Nanotwin-Modified Copper Interconnects and Its Effect on the Physical Properties of Copper*. in *59th ECTC*. 2009.
49. K. Lu, L. Lu, and S. Suresh, *Strengthening Materials by Engineering Coherent Internal Boundaries at the Nanoscale.* Science, 2009. **324**(5925): p. 349-352.

50. Y. Wang, M. Chen, F. Zhou, and E. Ma, *High Tensile Ductility in a Nanostructured Metal.* Nature, 2002. **419**(6910): p. 912-915.

51. K.-C. Chen, W.-W. Wu, C.-N. Liao, L.-J. Chen, and K.N. Tu, *Observation of Atomic Diffusion at Twin-Modified Grain Boundaries in Copper.* Science, 2008. **321**(5892): p. 1066-1069.

52. H. Fischer, Z. Electrochem., 1943. **49**: p. 343,376. in F.C. Walsh and M.E. Herron, Electrocrystallization and Electrochemical Control of Crystal Growth: Fundamental Considerations and Electrodeposition of Metals. Journal of Physics D: Applied Physics, 1991. 24(2): p. 217-225.

53. M. Nunez, *Metal Electrodeposition*. 2005, New York: Nova Science Publishers, Inc. . 212.

54. C. Donner, *Kinetics of Electrochemical Phase Formation in Two-Dimensional Systems.* Zeitschrift Fur Physikalische Chemie-International Journal of Research in Physical Chemistry & Chemical Physics, 2006. **220**(3): p. 265-304.

55. A. Milchev, *Electrocrystallization Fundamentals of Nucleation and Growth*. 1st ed. 2002, Boston, Mass.: Kluwer Academic Publishers. 280.

56. E. Budevski, G. Staikov, W.J. Lorenz, and I. Wiley, *Electrochemical Phase Formation and Growth an Introduction to the Initial Stages of Metal Deposition*. 1st ed. 1996, Weinheim; New York: VCH. 410.

57. G. Staikov and W.J. Lorenz, *Electrochemical Technology: Innovation and New Developments*, ed. N. Masuko, T. Osaka, and Y. Ito. 1996, Amsterdam: Kodansha, Tokyo and Gordon and Breach Publ. 440.

58. K.J. Vetter, *Theoretical Aspects, Section D*, in *Electrochemical Kinetics*. 1967, Academic Press: New York. p. 282.

59. E. Budevski, V. Bostanov, and G. Staikov, *Electrocrystallization.* Annual Review of Materials Science, 1980. **10**(1): p. 85-112.

60. F.C. Walsh and M.E. Herron, *Electrocrystallization and Electrochemical Control of Crystal Growth: Fundamental Considerations and Electrodeposition of Metals.* Journal of Physics D: Applied Physics, 1991. **24**(2): p. 217-225.

61. E. Budevski, G. Staikov, and W.J. Lorenz, *Electrocrystallization: Nucleation and Growth Phenomena.* Electrochimica Acta, 2000. **45**(15-16): p. 2559-2574.

62. F. Sagues, M.Q. Lopez-Salvans, and J. Claret, *Growth and Forms in Quasi-Two-Dimensional Electrocrystallization.* Physics Reports, 2000. **337**(1-2): p. 97-115.

63. A. Milchev and L. Heerman, *Electrochemical Nucleation and Growth of Nano- and Microparticles: Some Theoretical and Experimental Aspects.* Electrochimica Acta, 2003. **48**(20-22): p. 2903-2913.

64. A.J. Bard and L.R. Faulkner, *Electrochemical Methods and Applications*. 2000, New York; London: Wiley-Interscience.

65. I. Markov and R. Kaischew, *Influence of Supersaturation on the Mode of Crystallization on Crystalline Substrates.* Thin Solid Films, 1976. **32**(1): p. 163-167.

66. E. Bauer and J.H. van der Merwe, *Structure and Growth of Crystalline Superlattices: From Monolayer to Superlattice.* Physical Review B, 1986. **33**(Copyright (C) 2009 The American Physical Society): p. 3657-3671.

67. I. Markov and S. Stoyanov, *Mechanisms of Epitaxial Growth.* Contemporary Physics, 1987. **28**(3): p. 267 - 320.

68. M. Volmer and A. Weber, Z. Physik. Chem., 1926. **119**: p. 277 in A. Milchev, Electrocrystallization Fundamentals of Nucleation and Growth. 1st ed. 2002, Boston, Mass.: Kluwer Academic Publishers. p.89.

69. L. Farkas, Z. Phys. Chem., 1927. **125**: p. 236. in A. Milchev, Electrocrystallization Fundamentals of Nucleation and Growth. 1st ed. 2002, Boston, Mass.: Kluwer Academic Publishers. p.89.

70. I.N. Stranski and R. Kaischew, Z. Physik. Chem., 1934. **B26**: p. 317. in A. Milchev, Electrocrystallization Fundamentals of Nucleation and Growth. 1st ed. 2002, Boston, Mass.: Kluwer Academic Publishers. p.89.

71. I.N. Stranski and R. Kaischew, Z. Physik. Chem., 1934. **A170**: p. 295. in A. Milchev, Electrocrystallization Fundamentals of Nucleation and Growth. 1st ed. 2002, Boston, Mass.: Kluwer Academic Publishers. p.89.

72. I.N. Stranski and R. Kaischew, Phys. Z., 1935. **36**: p. 353. in A. Milchev, Electrocrystallization Fundamentals of Nucleation and Growth. 1st ed. 2002, Boston, Mass.: Kluwer Academic Publishers. p.89.

73. R. Becker and W. Döring, Ann. Phys., 1935. **24**: p. 719. in A. Milchev, Electrocrystallization Fundamentals of Nucleation and Growth. 1st ed. 2002, Boston, Mass.: Kluwer Academic Publishers. p.89.

74. Y.B. Zeldovich, Acta Physicochim. USSR, 1943. **18**: p. 1. in A. Milchev, Electrocrystallization Fundamentals of Nucleation and Growth. 1st ed. 2002, Boston, Mass.: Kluwer Academic Publishers. p.89.

75. Y.I. Frenkel, *Kinetic Theory of Liquids*. 2nd ed. 1955, Dover, New York: New York, Dover Publications. 488.

76. N. Batina, T. Will, and D.M. Kolb, *Study of the Initial Stages of Copper Deposition by in Situ Scanning Tunnelling Microscopy.* Faraday Discussions, 1992. **94**: p. 93-106.

77. R.J. Nichols, D.M. Kolb, and R.J. Behm, *Stm Observations of the Initial Stages of Copper Deposition on Gold Single-Crystal Electrodes.* Journal of Electroanalytical Chemistry, 1991. **313**(1-2): p. 109-119.

78. R.J. Nichols, E. Bunge, H. Meyer, and H. Baumgärtel, *Classification of Growth Behaviour for Copper on Various Substrates with in-Situ Scanning Probe Microscopy.* Surface Science, 1995. **335**: p. 110-119.

79. N. Batina, D.M. Kolb, and R.J. Nichols, *An in Situ Scanning Tunneling Microscopy Study of the Initial Stages of Bulk Copper Deposition on Gold(100): The Rim Effect.* Langmuir, 2002. **8**(10): p. 2572-2576.

80. J.E.T. Andersen and P. Moller, *Growth of a Copper-Gold Alloy Phase by Bulk Copper Electrodeposition on Gold Investigated by in Situ Stm.* Journal of The Electrochemical Society, 1995. **142**(7): p. 2225-2232.

81. M.F. Toney, J.N. Howard, J. Richer, G.L. Borges, J.G. Gordon, O.R. Melroy, D. Yee, and L.B. Sorensen, *Electrochemical Deposition of Copper on a Gold Electrode in Sulfuric Acid: Resolution of the Interfacial Structure.* Physical Review Letters, 1995. **75**(Copyright (C) 2009 The American Physical Society): p. 4472-4475.

82. T. Hachiya, H. Honbo, and K. Itaya, *Detailed Underpotential Deposition of Copper on Gold(Iii) in Aqueous Solutions.* Journal of Electroanalytical Chemistry, 1991. **315**(1-2): p. 275-291.

83. O.M. Magnussen, J. Hotlos, G. Beitel, D.M. Kolb, and R.J. Behm, *Atomic Structure of Ordered Copper Adlayers on Single-Crystalline Gold Electrodes.* Journal of Vacuum Science and Technology B, 1991. **9**(2): p. 969-975.

84. O.M. Magnussen, J. Hotlos, R.J. Nichols, D.M. Kolb, and R.J. Behm, *Atomic Structure of Cu Adlayers on Au(100) and Au(111) Electrodes Observed by in Situ*

Scanning Tunneling Microscopy. Physical Review Letters, 1990. **64**(Copyright (C) 2009 The American Physical Society): p. 2929-2932.

85. S.H. Manne, P. K.; Massie, J.; Elings, V. B.; Gewirth, A. A., *Atomic-Resolution Electrochemistry with the Atomic Force Microscope: Copper Deposition on Gold.* Science & Justice, 1991. **251**(4990): p. 183-186.
86. D.M. Kolb, R.J. Nichols, and R.J. Behm, *Electrified Interfaces in Physics, Chemistry and Biology*. Nato Asi Series. Series C, Mathematical and Physical Sciences, ed. Guidelli. Vol. C355. 1992, Dordrecht: Kluwer Academic Publ. ix, 606.
87. B.R. Scharifker, J. Mostany, M. Palomar-Pardave, and I. Gonzalez, *On the Theory of the Potentiostatic Current Transient for Diffusion-Controlled Three-Dimensional Electrocrystallization Processes.* Journal of the Electrochemical Society, 1999. **146**(3): p. 1005-1012.
88. M.A. Schneeweiss and D.M. Kolb, *The Initial Stages of Copper Deposition on Bare and Chemically Modified Gold Electrodes.* Physica Status Solidi a-Applied Research, 1999. **173**(1): p. 51-71.
89. D.M. Kolb, R.J. Randler, R.I. Wielgosz, and J.C. Ziegler, *Initial Stages of Metal Deposition on Metal and Semiconductor Electrodes Studied by in Situ Stm.* Mater. Res. Soc. Symp. Proc., 1997. **451**: p. 19-30.
90. M. Dietterle, T. Will, and D.M. Kolb, *The Initial Stages of Cu Electrodeposition on Ag(100): An in Situ Stm Study.* Surface Science, 1998. **396**(1-3): p. 189-197.
91. D. Grujicic and B. Pesic, *Electrodeposition of Copper: The Nucleation Mechanisms.* Electrochimica Acta, 2002. **47**(18): p. 2901-2912.
92. M.E. Hyde and R.G. Compton, *A Review of the Analysis of Multiple Nucleation with Diffusion Controlled Growth.* Journal of Electroanalytical Chemistry, 2003. **549**: p. 1-12.
93. B. Scharifker and G. Hills, *Theoretical and Experimental Studies of Multiple Nucleation.* Electrochimica Acta, 1983. **28**(7): p. 879-889.
94. B.R. Scharifker and J. Mostany, *Three-Dimensional Nucleation with Diffusion Controlled Growth : Part I. Number Density of Active Sites and Nucleation Rates Per Site.* Journal of Electroanalytical Chemistry, 1984. **177**(1-2): p. 13-23.
95. M. Sluyters-Rehbach, J.H.O.J. Wijenberg, E. Bosco, and J.H. Sluyters, *The Theory of Chronoamperometry for the Investigation of Electrocrystallization :*

Mathematical Description and Analysis in the Case of Diffusion-Controlled Growth. Journal of Electroanalytical Chemistry, 1987. **236**(1-2): p. 1-20.

96. M.V. Mirkin and A.P. Nilov, *Three-Dimensional Nucleation and Growth under Controlled Potential.* Journal of Electroanalytical Chemistry, 1990. **283**(1-2): p. 35-51.

97. L. Heerman and A. Tarallo, *Theory of the Chronoamperometric Transient for Electrochemical Nucleation with Diffusion-Controlled Growth.* Journal of Electroanalytical Chemistry, 1999. **470**(1): p. 70-76.

98. M.Y. Abyaneh, *Modeling of Single Phase Electrocrystallization Processes.* Journal of The Electrochemical Society, 2004. **151**(11): p. C737-C742.

99. M.Y. Abyaneh, *Kinetics of Two-Phase Electrocrystallization Processes.* Journal of The Electrochemical Society, 2003. **150**(8): p. C538-C543.

100. M.Y. Abyaneh, *Modelling Diffusion Controlled Electrocrystallisation Processes.* Journal of Electroanalytical Chemistry, 2006. **586**(2): p. 196-203.

101. A.C. Levi and M. Kotrla, *Theory and Simulation of Crystal Growth.* Journal of Physics: Condensed Matter, 1997. **9**(2): p. 299-344.

102. L. Guo, A. Radisic, and P.C. Searson, *Kinetic Monte Carlo Simulations of Nucleation and Growth in Electrodeposition.* Journal of Physical Chemistry B, 2005. **109**(50): p. 24008-24015.

103. L. Guo and P.C. Searson, *Simulations of Island Growth and Island Spatial Distribution During Electrodeposition.* Electrochemical and Solid-State Letters, 2007. **10**(7): p. D76-D78.

104. T.J. Pricer, M.J. Kushner, and R.C. Alkire, *Monte Carlo Simulation of the Electrodeposition of Copper - Ii. Acid Sulfate Solution with Blocking Additive.* Journal of the Electrochemical Society, 2002. **149**(8): p. C406-C412.

105. T.J. Pricer, M.J. Kushner, and R.C. Alkire, *Monte Carlo Simulation of the Electrodeposition of Copper - I. Additive-Free Acidic Sulfate Solution.* Journal of the Electrochemical Society, 2002. **149**(8): p. C396-C405.

106. T.O. Drews, *Multiscale Simulations of Nanofabricated Structures: Application to Copper Electrodeposition for Electronic Devices*, PhD thesis, University of Illinois at Urbana-Champaign. 2004.

107. T.O. Drews, R.D. Braatz, and R.C. Alkire, *Coarse-Grained Kinetic Monte Carlo Simulation of Copper Electrodeposition with Additives* International Journal for Multiscale Computational Engineering, 2004. **2**(2): p. 313-327.

108. T.O. Drews, E.G. Webb, D.L. Ma, J. Alameda, R.D. Braatz, and R.C. Alkire, *Coupled Mesoscale — Continuum Simulations of Copper Electrodeposition in a Trench.* AIChE Journal, 2004. **50**(1): p. 226-240.

109. T.O. Drews, S. Krishnan, J.C. Alameda, D. Gannon, R.D. Braatz, and R.C. Alkire, *Multiscale Simulations of Copper Electrodeposition onto a Resistive Substrate.* IBM Journal of Research and Development, 2005. **49**(1): p. 49-63.

110. T.O. Drews, A. Radisic, J. Erlebacher, R.D. Braatz, P.C. Searson, and R.C. Alkire, *Stochastic Simulation of the Early Stages of Kinetically Limited Electrodeposition.* Journal of the Electrochemical Society, 2006. **153**(6): p. C434-C441.

111. Z. Zheng, R.M. Stephens, R.D. Braatz, R.C. Alkire, and L.R. Petzold, *A Hybrid Multiscale Kinetic Monte Carlo Method for Simulation of Copper Electrodeposition.* Journal of Computational Physics, 2008. **227**(10): p. 5184-5199.

112. A. Saedi, *A Study on Mutual Interaction between Atomistic and Macroscopic Phenomena During Electrochemical Processes Using Coupled Finite Difference - Kinetic Monte Carlo Model: Application to Potential Step Test in Simple Copper Sulfate Bath.* Journal of Electroanalytical Chemistry, 2006. **588**(2): p. 267-284.

113. S. Harinipriya and V.R. Subramanian, *Monte Carlo Simulation of Electrodeposition of Copper: A Multistep Free Energy Calculation.* Journal of Physical Chemistry B 2008. **112**(13): p. 4036-4047.

114. H. Huang, G.H. Gilmer, and T.D. de la Rubia, *An Atomistic Simulator for Thin Film Deposition in Three Dimensions.* Journal of Applied Physics, 1998. **84**(7): p. 3636-3649.

115. J.E. Rubio, M. Jaraiz, I. Martin-Bragado, J.M. Hernandez-Mangas, J. Barbolla, and G.H. Gilmer, *Atomistic Monte Carlo Simulations of Three-Dimensional Polycrystalline Thin Films.* Journal of Applied Physics, 2003. **94**(1): p. 163-168.

116. A. Radisic, *Electrochemical Nucleation and Growth of Copper*, PhD thesis, Johns Hopkins University 2004.

117. K.A. Fichthorn and W.H. Weinberg, *Theoretical Foundations of Dynamic Monte-Carlo Simulations.* Journal of Chemical Physics, 1991. **95**(2): p. 1090-1096.

118. G. Ehrlich and F.G. Hudda, *Atomic View of Surface Self-Diffusion: Tungsten on Tungsten.* The Journal of Chemical Physics, 1966. **44**(3): p. 1039-1049.

119. M.G. Lagally and Z. Zhang, *Materials Science: Thin-Film Cliffhanger.* Nature, 2002. **417**(6892): p. 907-910.

120. R.L. Schwoebel and E.J. Shipsey, *Step Motion on Crystal Surfaces.* Journal of Applied Physics, 1966. **37**(10): p. 3682-3686.

121. Y.Y. Huang, Y.C. Zhou, and Y. Pan, *Simulation of Kinetically Limited Growth of Electrodeposited Polycrystalline Ni Films.* Physica E: Low-dimensional Systems and Nanostructures, In Press.

122. D.Y. Li and J.A. Szpunar, *A Monte Carlo Simulation Approach to the Texture Formation During Electrodeposition--I. The Simulation Model.* Electrochimica Acta, 1997. **42**(1): p. 37-45.

123. L. Wang and P. Clancy, *Kinetic Monte Carlo Simulation of the Growth of Polycrystalline Cu Films.* Surface Science, 2001. **473**(1-2): p. 25-38.

124. S.W. Levine and P. Clancy, *A Simple Model for the Growth of Polycrystalline Si Using the Kinetic Monte Carlo Simulation.* Modelling and Simulation in Materials Science and Engineering, 2000. **8**(5): p. 751-762.

125. P. Bruschi, A. Nannini, and F. Pieri, *Monte Carlo Simulation of Polycrystalline Thin Film Deposition.* Physical Review B, 2000. **63**(3): p. 035406-8.

126. H. Huang and G.H. Gilmer, *Multi-Lattice Monte Carlo Model of Thin Films.* Journal of Computer-Aided Materials Design, 1999. **6**(2): p. 117-127.

127. H. Huang and L.G. Zhou, *Atomistic Simulator of Polycrystalline Thin Film Deposition in Three Dimensions.* Journal of Computer-Aided Materials Design, 2004. **11**(1): p. 59-74.

128. J. Liu, C. Liu, and P.P. Conway, *Kinetic Monte Carlo Simulation of Kinetically Limited Copper Electrocrystallization on an Atomically Even Surface.* Electrochimica Acta, 2009. **54**(27): p. 6941-6948.

129. H.V. Atkinson, *Overview No. 65: Theories of Normal Grain Growth in Pure Single Phase Systems.* Acta Metallurgica, 1988. **36**(3): p. 469-491.

130. S.C. Barnes, G.G. Storey, and H.J. Pick, *The Structure of Electrodeposited Copper--Iii: The Effect of Current Density and Temperature on Growth Habit.* Electrochimica Acta, 1960. **2**(1-3): p. 195-204.
131. V. Conedera, B.L. Goff, and N. Fabre, *Potentialities of a New Positive Photoresist for the Realization of Thick Moulds.* Journal of Micromechanics and Microengineering, 1999. **9**(2): p. 173-175.
132. A.L. Patterson, *The Scherrer Formula for X-Ray Particle Size Determination.* Physical Review, 1939. **56**(10): p. 978-982.
133. X. Zhang, K.N. Tu, Z. Chen, Y.K. Tan, C.C. Wong, S.G. Mhaisalkar, X.M. Li, C.H. Tung, and C.K. Cheng, *Pulse Electroplating of Copper Film: A Study of Process and Microstructure.* Journal of Nanoscience and Nanotechnology, 2008. **8**: p. 2568-2574.
134. C.V. Thompson, *Secondary Grain Growth in Thin Films of Semiconductors: Theoretical Aspects.* Journal of Applied Physics, 1985. **58**(2): p. 763-772.
135. C.V. Thompson, *Texture Evolution During Grain Growth in Polycrystalline Films.* Scripta Metallurgica et Materialia, 1993. **28**(2): p. 167-172.
136. A. Mersmann, *Crystallization Technology Handbook*. 2nd ed. 2001, New York & Basel: Marcel Dekker, Inc. 832.
137. J.C. Brice, *Crystal Growth Processes*. 1st ed. 1986, New York: Glasgow : Blackie ; New York : Halsted Press. 298.
138. K. Byrappa and T. Ohachi, *Crystal Growth Technology*. Springer Series in Materials Processing ed. W. Michaeli, H. Warlimont, and E. Weber. 2003, Norwich, NY, USA: William Andrew Inc. XXII, . 309.
139. T.O. Drews, R.D. Braatz, and R.C. Alkire, *Monte Carlo Simulation of Kinetically Limited Electrodeposition on a Surface with Metal Seed Clusters.* Z. Phys. Chem., 2007. **221**(9-10): p. 1287-1305.

APPENDICES

Appendix I. DESIGN OF THE PHOTOMASK

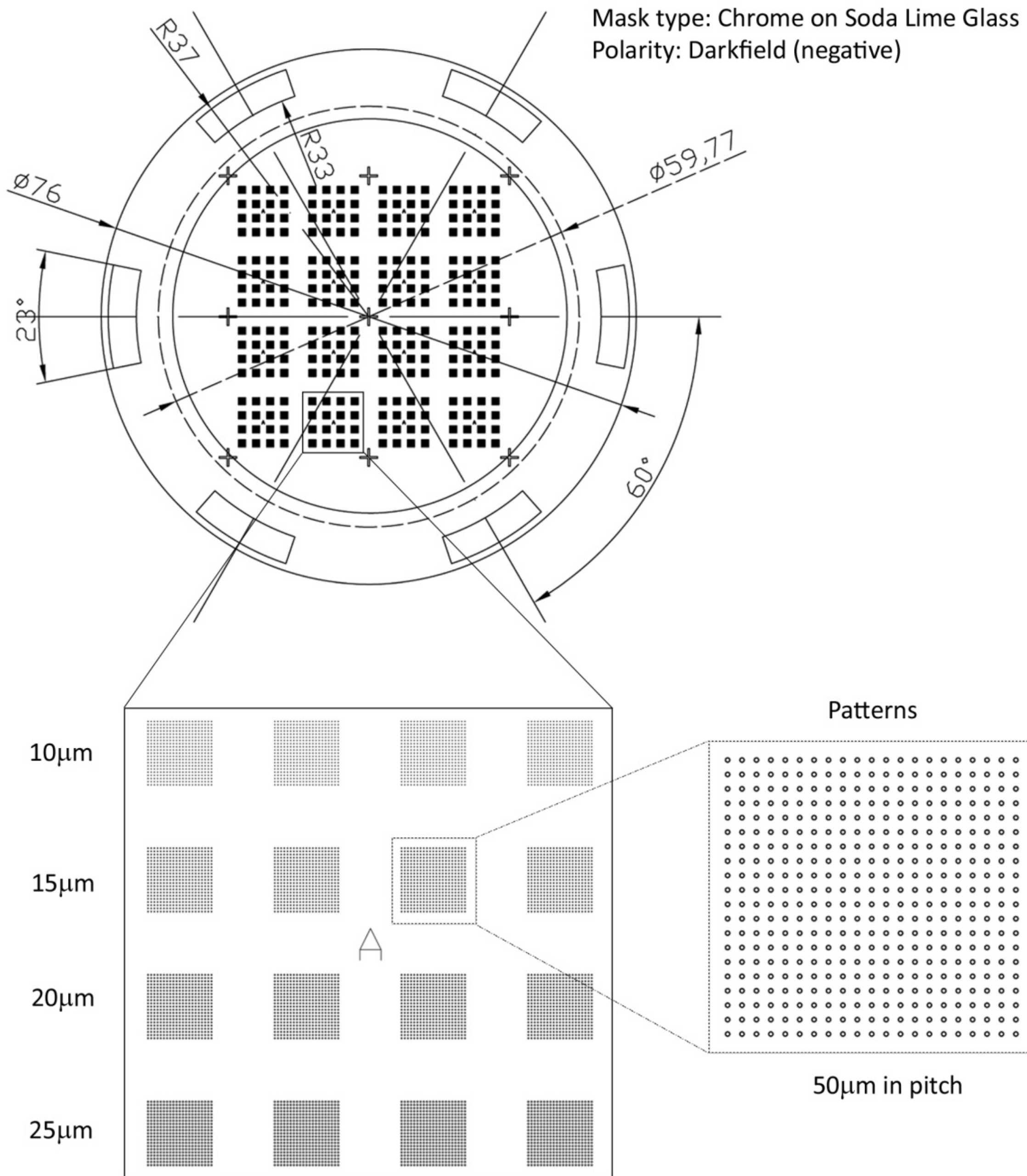

Appendix II. ASSEMBLY DRAWING OF THE WAFER HOLDER

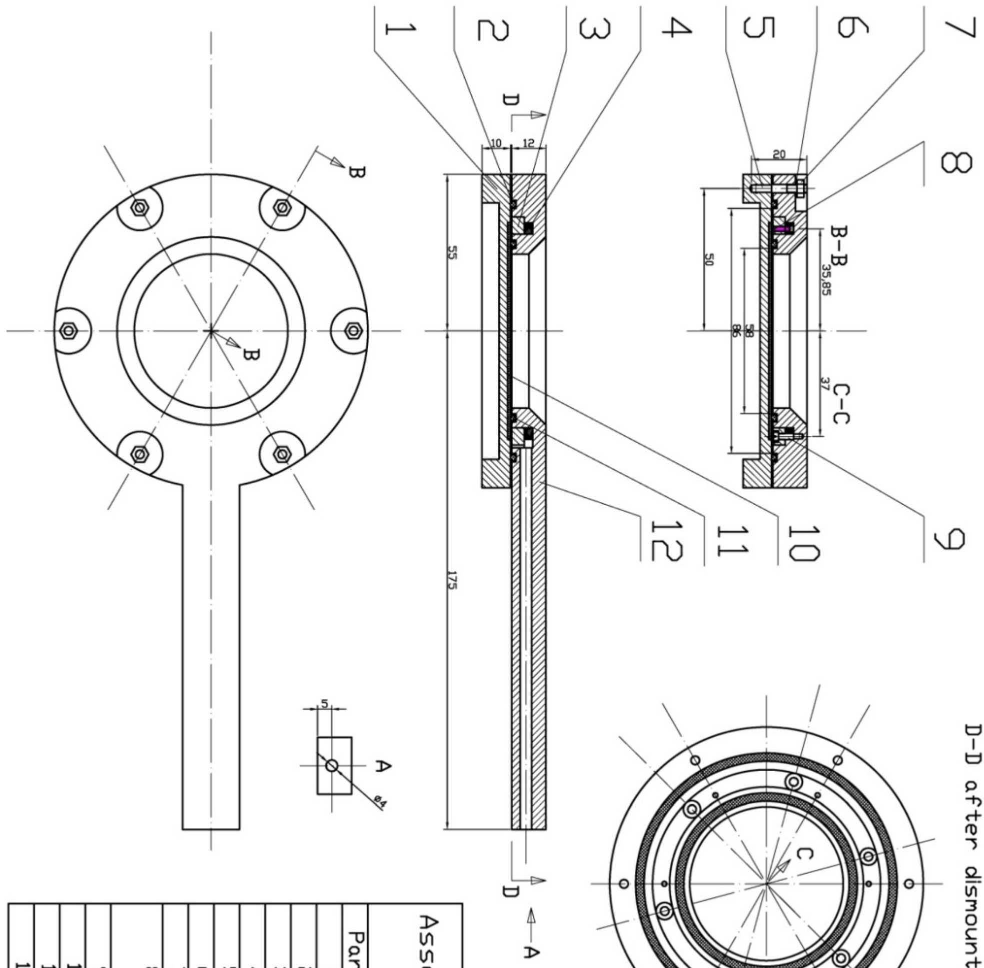

Technical Requirements

- Tolerance is 0.1mm unless otherwise states
- When the wafer holder is assembled and closed, it is required:
  1. All the spring laoded contact probes (part 8) must be compressed as equally as possible to make good contact with the wafer surface. The overall length of these probes are 8mm and maximum travel of the spring is 2mm.
  2. The o-rings are uniformly compressed to obtain safe seal.

Assembly Drawing of the Wafer Holder		No. of sheets	1
		Drawn by	Jun Liu
Part #	Name	Materials	Quantity
1	base	Tufset	1
2	outer o-ring	rubber/PTFE	1
3	embedded ring	Tufset	1
4	copper ring	Copper	1
5	double-ended bolt		6
6	washer		6
7	bolt cap		6
8	spring-loaded contact probe	gold plated brass	6
9	screw		6
10	Si wafer	Au-coated silicon	1
11	inner o-ring	rubber/PTFE	1
12	racket	Tufset	1

Appendix III. Part drawings of the wafer holder

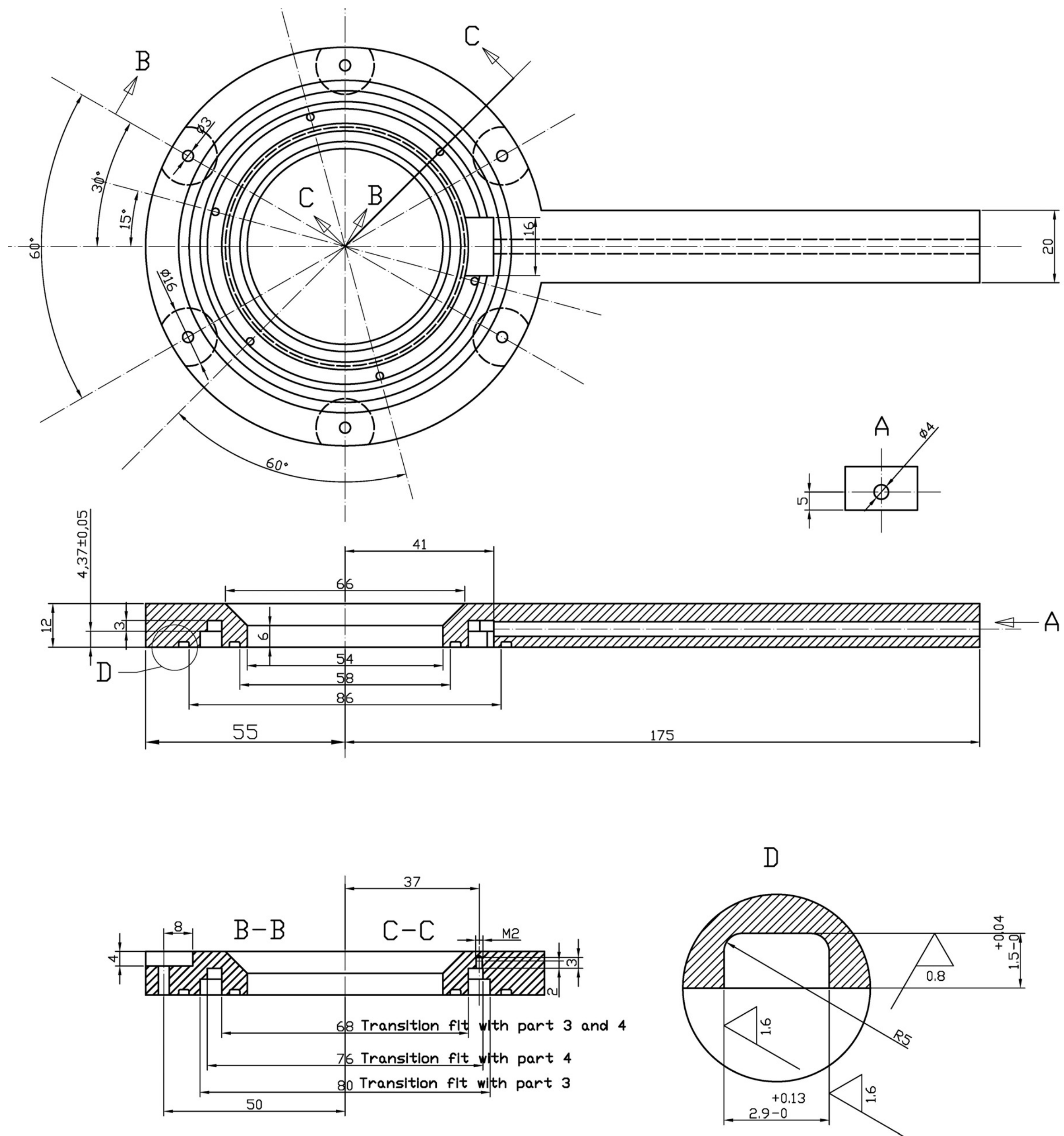

Part 12 Racket			
Drawn by:	Jun Liu	No. of sheets	1
Unit:	mm	Tolerance:	0.1mm unless otherwise states
Materials:	Tufset		

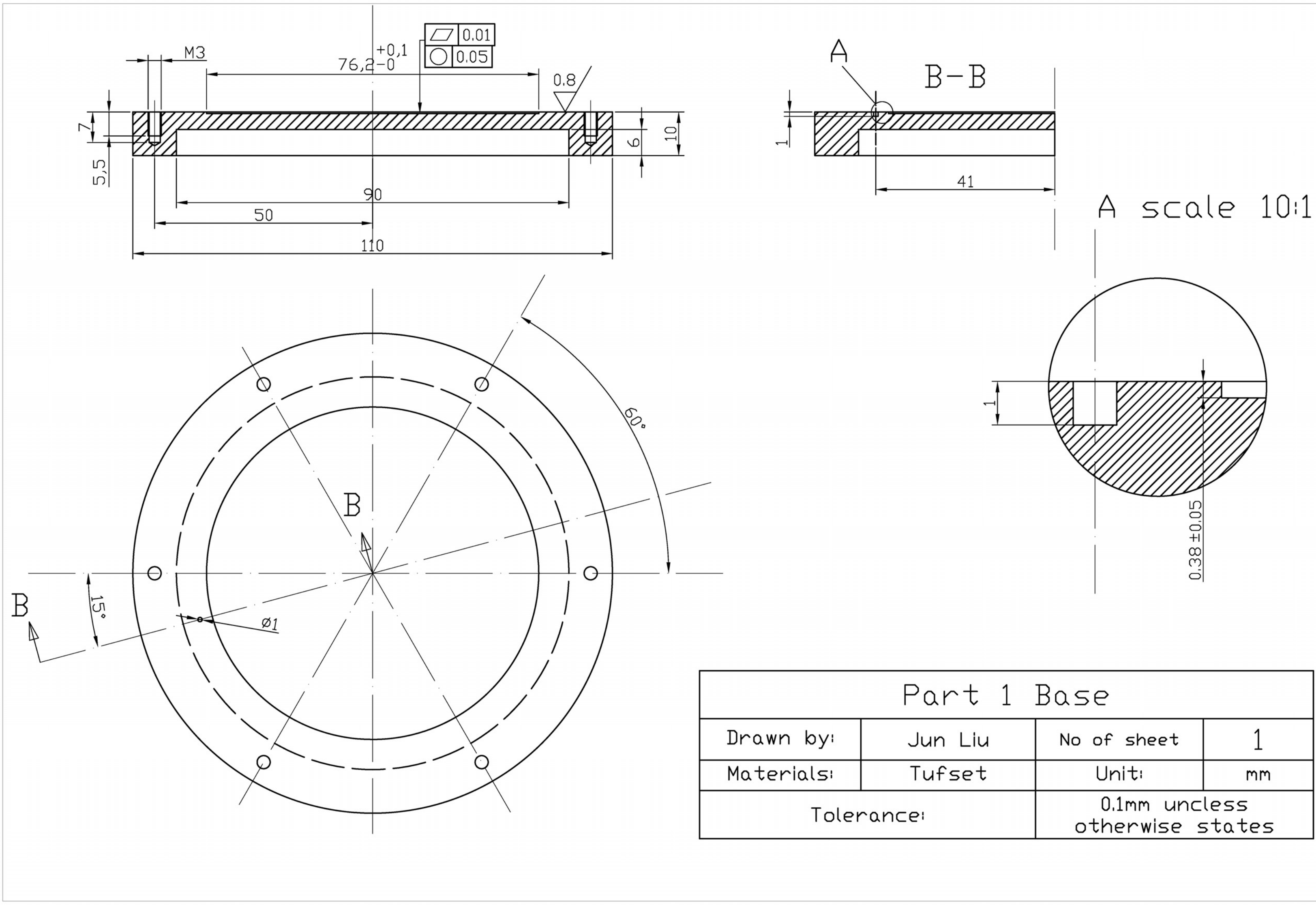

M3
76,2 +0,1 -0
0.01
0.05
0.8
7
5,5
6
10
90
50
110
A
B-B
1
41
A scale 10:1
1
0.38 ±0.05
60°
B
B
15°
ø1
Part 1 Base
Drawn by:
Jun Liu
No of sheet
1
Materials:
Tufset
Unit:
mm
Tolerance:
0.1mm uncless otherwise states

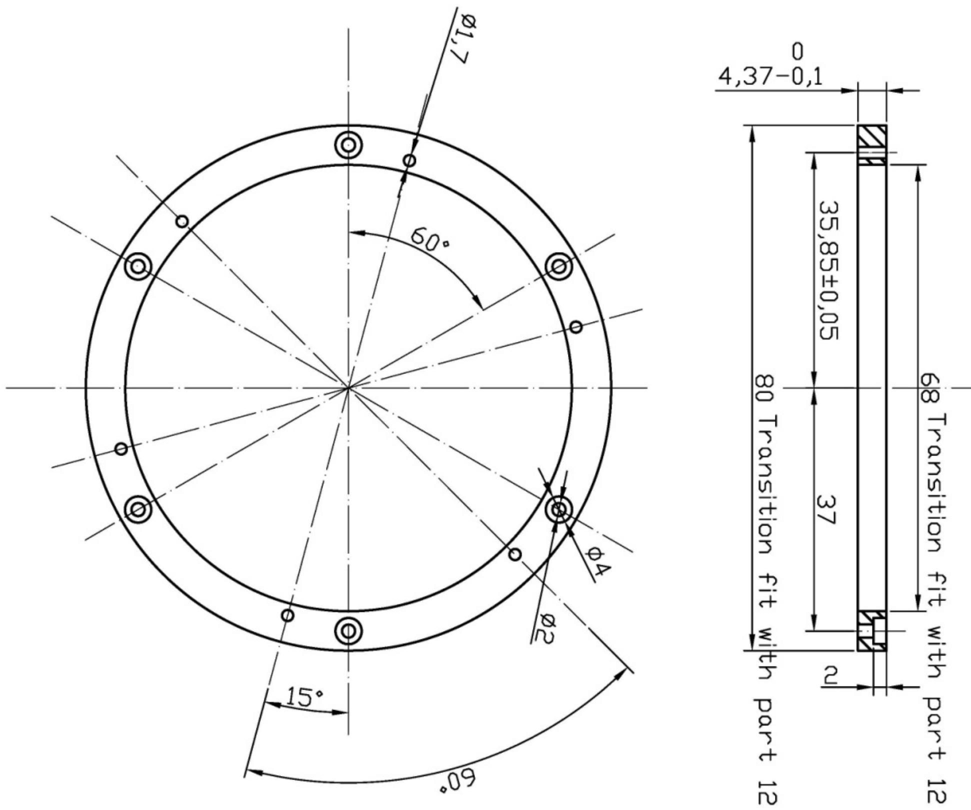

Part 3 Embedded Ring			
Drawn:	Jun Liu	No of sheets	1
Materials:	Tufset		
Tolerance:		0.1mm uncless otherwise states	

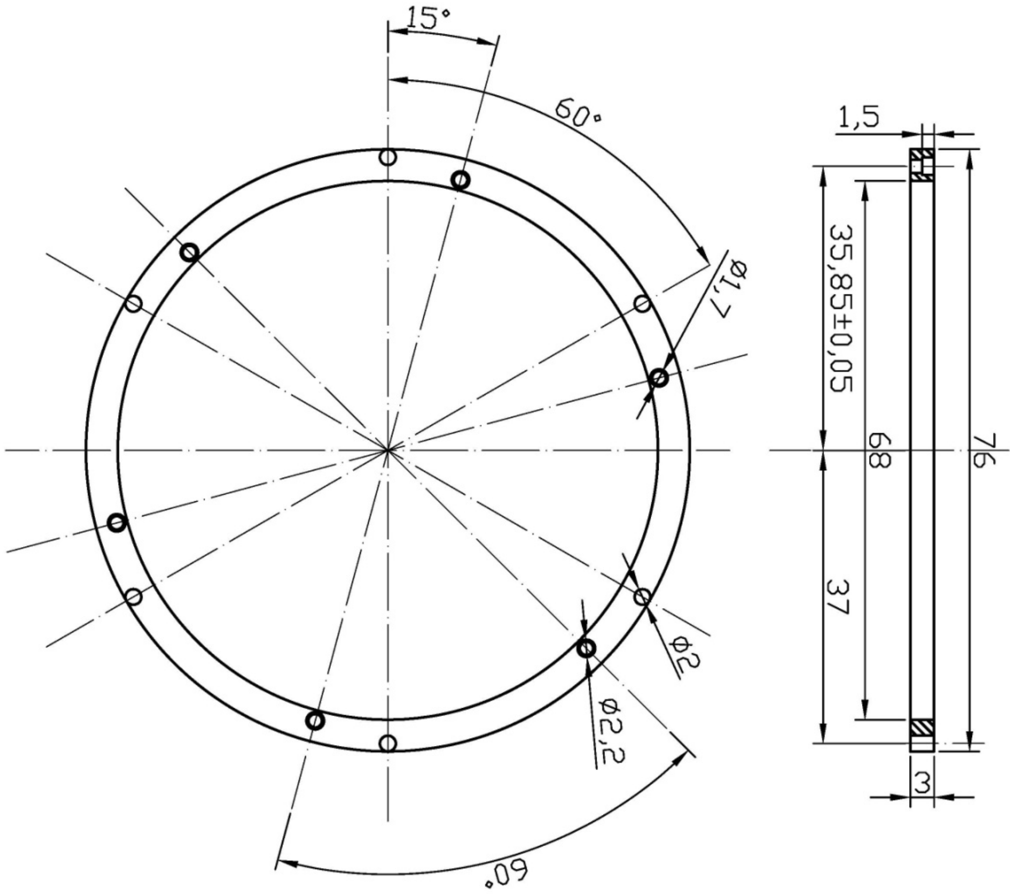

Part 4 Copper Ring			
Drawn:	Jun Liu	No. of sheets	1
Materials:	copper		
Tolerance:		0.1mm uncless otherwise states	

Appendix IV. SIMULATION CODES FOR THE 2DCS-KMC MODEL

MAIN SCRIPT

```
%********************************************
% The simulation code for the 2DCS-KMC model.
%********************************************
clear
% Define global variables
global wsub;
global wcu;
global R;
global T;
global ebsub;
global ebcu;
global kb;
global ls
global occp
global ii

% Constants and Parameters

Frd=96485.3415;    % Faraday constant (s.A / mol)
R=8.314472;        % Gas constant (J K-1 mol-1)
kb=8.617343;       % Boltzmann (eV.k-1)
nn=2;              % electron number, which is 2 for Cu ion
NA=6.02e23;        % Avagadro constant
kcu=0.143;         % Deposition rate constant for Cu on Cu (m^3/mol.s)
ksub=0.0143;       %  Deposition  rate  constant  for  Cu  on  substrate
(m^3/mol.s)
eeqcu=0;           % Equilibrium potential for Cu deposition on Cu (V)
aphcu=0.5;         % charge transfer coefficient for Cu deposition on Cu
eeqsub=-0.1;       % Equilibrium potential for Cu deposition on substrate
(V)
aphsub=0.5         %  charge  transfer  coeffiecient  for  Cu  deposition  on
substrate
wcu=1.5e1;         %  Jump  frequency  for  Cu  surface  diffusion  on  Cu,  (s^-
1)
ebcu=0.13;         % Energy barrier for breaking a Cu-Cu bond, (eV)
wsub=1.5e1;        % Jump frequency for Cu surface diffusion on substrate
(s^-1)
ebsub=0.35;        % Energy barrier for breaking a Cu-substrate bond (eV)
T=298;             % Temperature K
ap=-0.1;           % applied potential(V)
con=0.66;          % Cu ion concentration (mol)
ls=1000;           % Lattice size

% Deposition rate
rdcu=kcu*con*exp(-aphcu*nn*Frd*(ap-eeqcu)/(R*T));      %deposition   rate
on Cu
rdsub=ksub*con*exp(-aphsub*nn*Frd*(ap-eeqsub)/(R*T)); %Deposition   rate
on substrate

%Initial status

occp=zeros(2,ls);
% occp is a matrice in which stored the state of the occupancy of each
sites. occp(i,j)=1 if occupied, else 0. at the beginning it's a zero
matrice.
```

```
% At the beginning, a deposition event is allowed to occur on any site
of the first row of the lattice by rate rdsub.

rd=rdsub*ones(1,ls);      % Deposition rate on substrate initially
rd=sparse(rd);            % Convert it into sparse matrix
rsl=zeros(1,ls);          % Rate of surface diffusion to the left
rsl=sparse(rsl);
rsr=zeros(1,ls);          % Rate of surface diffusion to the right
rsr=sparse(rsr);

time=100;           %Specify the simulation time
kmctime=0;          %The timer reading is zero initially
evtind=[];
mcstep=1;           % counter of MC steps
m=1;
numdep=0;           % counter of deposition events
events={};          % A cell array to store every events including the
lattice site index and type of event
history={};         % A cell array to store the history of the
microstructur
timestep=linspace(0,time);
% set time steps at which the microstructure and events are stored in
'history'
t0=clock;           % Start the timer

while kmctime<time
    xi=rand;
    allrates=[rd(:);rsl(:);rsr(:)];
    nonzeroind=find(allrates);
    rates=allrates(nonzeroind);
    normrates=cumsum(rates)./sum(rates);
    evtind(mcstep)=find(normrates>=xi,1,'first');
    location=nonzeroind(evtind(mcstep));
    if location<=numel(rd)
        eventtype=1;
        [ii,jj]=ind2sub(size(rd),location);
    elseif location>numel(rd)&&location<=(numel(rd)+numel(rsl))
        eventtype=2;
        [ii,jj]=ind2sub(size(rsl),location-numel(rd));
    elseif location>(numel(rd)+numel(rsl))&&location<numel(allrates)
        eventtype=3;
        [ii,jj]=ind2sub(size(rsr),location-numel(rd)-numel(rsl));
    end
    rows=size(occp,1); % Mornitor the thickness of the deposit
    rowsrd=size(rd,1);
    rowsrsl=size(rsl,1);
    rowsrsr=size(rsr,1);
    capsz=max(rowsrd,rowsrsl,rowsrsr);
    %% activate the empty cap of occp
    if rows<=capsz
        occp(capsz+1,:)=0;
    end
    switch eventtype
        case 1
            %% An atom is deposited
            occp(ii,jj)=1;  % This site is occupied
            rd(ii,jj)=0;    % No deposition at this site next step
            numdep=numdep+1; % Counter of atoms deposited
            % Update the rd of neighbors
            if issafe(ii+1,pbcind(oddeven(jj)))
                rd(ii+1,pbcind(oddeven(jj)))=rdcu;
```

```
            end
            if issafe(ii+1,pbcind(oddeven(jj-1)))
                rd(ii+1,pbcind(oddeven(jj-1)))=rdcu;
            end
            % Update the surface diffusion rates
            if ii>1
                rsl(ii-1,pbcind(oddeven(jj)))=0;
                rsr(ii-1,pbcind(oddeven(jj)))=0;
                rsl(ii-1,pbcind(oddeven(jj-1)))=0;
                rsr(ii-1,pbcind(oddeven(jj-1)))=0;
            end
            if occp(ii,pbcind(jj-1))==1
                rsl(ii,jj)=0;
                rsr(ii,pbcind(jj-1))=0;
                if occp(ii,pbcind(jj-2))==1
                    rsl(ii,pbcind(jj-1))=0;
                else
                    if  issafe(ii,pbcind(jj-2))&nooverhang(ii,pbcind(jj-
1))
                        rsl(ii,pbcind(jj-1))=sdr(ii,pbcind(jj-1));
                    else
                        rsl(ii,pbcind(jj-1))=0;
                    end
                end
            else
                    if issafe(ii,pbcind(jj-1))&nooverhang(ii,jj)
                        rsl(ii,jj)=sdr(ii,jj);
                    else
                        rsl(ii,jj)=0;
                    end
            end
            if occp(ii,pbcind(jj+1))==1
                rsr(ii,jj)=0;
                rsl(ii,pbcind(jj+1))=0;
                if occp(ii,pbcind(jj+2))==1
                    rsr(ii,pbcind(jj+1))=0;
                else
                    if
issafe(ii,pbcind(jj+2))&nooverhang(ii,pbcind(jj+1))
                        rsr(ii,pbcind(jj+1))=sdr(ii,pbcind(jj+1));
                    else
                        rsr(ii,pbcind(jj+1))=0;
                    end
                end
            else
                if issafe(ii,pbcind(jj+1))&nooverhang(ii,jj)
                    rsr(ii,jj)=sdr(ii,jj);
                else
                    rsr(ii,jj)=0;
                end
            end
            if occp(ii+1,pbcind(oddeven(jj+1)))==1
                if
issafe(ii+1,pbcind(oddeven(jj)))&nooverhang(ii+1,pbcind(oddeven(jj+1)))

rsl(ii+1,pbcind(oddeven(jj+1)))=sdr(ii+1,pbcind(oddeven(jj+1)));
                else
                    rsl(ii+1,pbcind(oddeven(jj+1)))=0;
                end
            end
            if occp(ii+1,pbcind(oddeven(jj-2)))==1
```

```
                if                          issafe(ii+1,pbcind(oddeven(jj-
1)))&nooverhang(ii+1,pbcind(oddeven(jj-2)))
                    rsr(ii+1,pbcind(oddeven(jj-
2)))=sdr(ii+1,pbcind(oddeven(jj-2)));
                else
                    rsr(ii+1,pbcind(oddeven(jj-2)))=0;
                end
            end
        case 2
            %% Surface diffusion to left
            occp(ii,jj)=0;
            occp(ii,pbcind(jj-1))=1;
            rd(ii,pbcind(jj-1))=0;
            %% update the deposition rate at this site and neighbors
            if ii==1
              rd(ii,jj)=rdsub;
            else
              rd(ii,jj)=rdcu;
            end
            rd(ii+1,pbcind(oddeven(jj)))=0;
            rd(ii+1,pbcind(oddeven(jj-1)))=0;
            if issafe(ii+1,pbcind(oddeven(jj-2)))
              rd(ii+1,pbcind(oddeven(jj-2)))=rdcu;
            end
            %% update the surface diffusion rate
            rsl(ii,jj)=0;
            rsr(ii,jj)=0;
            rsr(ii,pbcind(jj-1))=sdr(ii,pbcind(jj-1));
            if occp(ii,pbcind(jj-2))==1
              rsl(ii,pbcind(jj-1))=0;
              rsr(ii,pbcind(jj-2))=0;
              if occp(ii,pbcind(jj-3))==1
                  rsl(ii,pbcind(jj-2))=0;
              else
                  if issafe(ii,pbcind(jj-3))&nooverhang(ii,pbcind(jj-2))
                      rsl(ii,pbcind(jj-2))=sdr(ii,pbcind(jj-2));
                  else
                      rsl(ii,pbcind(jj-2))=0;
                  end
              end
            else
              if issafe(ii,pbcind(jj-2))&nooverhang(ii,pbcind(jj-1))
                  rsl(ii,pbcind(jj-1))=sdr(ii,pbcind(jj-1));
              else
                  rsl(ii,pbcind(jj-1))=0;
              end
            end

            if occp(ii,pbcind(jj+1))==1
              if issafe(ii,jj)&nooverhang(ii,pbcind(jj+1))
                  rsl(ii,pbcind(jj+1))=sdr(ii,pbcind(jj+1));
              else
                  rsl(ii,pbcind(jj+1))=0;
              end
              if occp(ii,pbcind(jj+2))==1
                  rsr(ii,pbcind(jj+1))=0;
              else
                  if issafe(ii,pbcind(jj+2))&nooverhang(ii,pbcind(jj+1))
                      rsr(ii,pbcind(jj+1))=sdr(ii,pbcind(jj+1));
                  else
                      rsr(ii,pbcind(jj+1))=0;
```

```
                end
            end
          end
          if ii>1
            rsl(ii-1,pbcind(oddeven(jj-1)))=0;
            rsr(ii-1,pbcind(oddeven(jj-1)))=0;
            rsl(ii-1,pbcind(oddeven(jj-2)))=0;
            rsr(ii-1,pbcind(oddeven(jj-2)))=0;
            if occp(ii-1,pbcind(oddeven(jj)))==1
                if occp(ii-1,pbcind(oddeven(jj+1)))==0
                    if                                  issafe(ii-
1,pbcind(oddeven(jj+1)))&nooverhang(ii-1,pbcind(oddeven(jj)))
                        rsr(ii-1,pbcind(oddeven(jj)))=sdr(ii-
1,pbcind(oddeven(jj)));
                    else
                        rsr(ii-1,pbcind(oddeven(jj)))=0;
                    end
                end
            end
          end
          if occp(ii+1,pbcind(oddeven(jj+1)))==1
            rsl(ii+1,pbcind(oddeven(jj+1)))=0;
          end
          if occp(ii+1,pbcind(oddeven(jj-3)))==1
            if                    issafe(ii+1,pbcind(oddeven(jj-
2)))&nooverhang(ii+1,pbcind(oddeven(jj-3)))
                rsr(ii+1,pbcind(oddeven(jj-
3)))=sdr(ii+1,pbcind(oddeven(jj-3)));
            else
                rsr(ii+1,pbcind(oddeven(jj-3)))=0;
            end
          end
      case 3
          %% Surface diffusion to right occur
          occp(ii,jj)=0;
          occp(ii,pbcind(jj+1))=1;
          rd(ii,pbcind(jj+1))=0;
          if ii==1
           rd(ii,jj)=rdsub;
          else
           rd(ii,jj)=rdcu;
          end
          rd(ii+1,pbcind(oddeven(jj-1)))=0;
          rd(ii+1,pbcind(oddeven(jj)))=0;
          if issafe(ii+1,pbcind(oddeven(jj+1)))
           rd(ii+1,pbcind(oddeven(jj+1)))=rdcu;
          end
          %%  Update  the  surface  diffusion  rate  of  this  site  and
neighbors
          rsl(ii,jj)=0;
          rsr(ii,jj)=0;
          rsl(ii,pbcind(jj+1))=sdr(ii,pbcind(jj+1));
          if occp(ii,pbcind(jj+2))==1
            rsr(ii,pbcind(jj+1))=0;
            rsl(ii,pbcind(jj+2))=0;
            if occp(ii,pbcind(jj+3))==1
                rsr(ii,pbcind(jj+2))=0;
            else
                if issafe(ii,pbcind(jj+3))&nooverhang(ii,pbcind(jj+2))
                    rsr(ii,pbcind(jj+2))=sdr(ii,pbcind(jj+2));
                else
```

```
                    rsr(ii,pbcind(jj+2))=0;
                end
            end
          else
            if issafe(ii,pbcind(jj+2))&nooverhang(ii,pbcind(jj+1))
                rsr(ii,pbcind(jj+1))=sdr(ii,pbcind(jj+1));
            else
                rsr(ii,pbcind(jj+1))=0;
            end
          end
          if occp(ii,pbcind(jj-1))==1
            if issafe(ii,jj)&nooverhang(ii,pbcind(jj-1))
                rsr(ii,pbcind(jj-1))=sdr(ii,pbcind(jj-1));
            else
                rsr(ii,pbcind(jj-1))=0;
            end
            if occp(ii,pbcind(jj-2))==1
                rsl(ii,pbcind(jj-1))=0;
            else
                if issafe(ii,pbcind(jj-2))&nooverhang(ii,pbcind(jj-1))
                    rsl(ii,pbcind(jj-1))=sdr(ii,pbcind(jj-1));
                else
                    rsl(ii,pbcind(jj-1))=0;
                end
            end
          end
          if ii>1
            rsl(ii-1,pbcind(oddeven(jj)))=0;
            rsr(ii-1,pbcind(oddeven(jj)))=0;
            rsl(ii-1,pbcind(oddeven(jj+1)))=0;
            rsr(ii-1,pbcind(oddeven(jj+1)))=0;
            if occp(ii-1,pbcind(oddeven(jj-1)))==1
                if occp(ii-1,pbcind(oddeven(jj-2)))==0
                    if                    issafe(ii-1,pbcind(oddeven(jj-
2)))&nooverhang(ii-1,pbcind(oddeven(jj-1)))
                        rsl(ii-1,pbcind(oddeven(jj-1)))=sdr(ii-
1,pbcind(oddeven(jj-1)));
                    else
                        rsl(ii-1,pbcind(oddeven(jj-1)))=0;
                    end
                end
            end
          end
          if occp(ii+1,pbcind(oddeven(jj-2)))==1
            rsr(ii+1,pbcind(oddeven(jj-2)))=0;
          end
          if occp(ii+1,pbcind(oddeven(jj+2)))==1
            if
issafe(ii+1,pbcind(oddeven(jj+1)))&nooverhang(ii+1,pbcind(oddeven(jj+2))
)

rsl(ii+1,pbcind(oddeven(jj+2)))=sdr(ii+1,pbcind(oddeven(jj+2)));
            else
                rsl(ii+1,pbcind(oddeven(jj+2)))=0;
            end
          end
    end % end of switch
  %% MC time increment
  kmctime=kmctime-log(xi)/sum(rates);
  %% Data collecting and process monitor
  if kmctime>=timestep(m)
```

```
      history{m}={kmctime occp [ii jj] eventtype rates(evtind(mcstep))};
% Store the simulation results
      lapsedtime=etime(clock,t0);
      percent=100*kmctime/time;
      progress=num2str(percent,3);
      timeleft=elapsedtime*(time-kmctime)/kmctime;
      tleft=num2str(timeleft,6);
      display({clock 'current MC time is:' kmctime})
      display({ progress '%' ' finished; '})
      display({ size(occp,1) 'layers deposited'})
      display({ 'Estimated time remaining:' tleft })
      m=m+1;
  end
  mcstep=mcstep+1;  % MC step counter
end % end of while
%% Save the results
para.temperature={T,'K'};
para.potential={ap,'V'};
para.jump_frequency1={'Cu',wcu,'/s'};
para.jump_frequency2={'Substrate',wsub,'/s'};
para.deposition_rate1={'Cu',kcu,'m^3/mol.s'};
para.deposition_rate2={'Substrate',ksub,'m^3/mol.s'};
para.concentration={con,'mol'};
para.energy_barrier1={'Cu',ebcu,'eV'};
para.energy_barrier2={'Substrate',ebsub,'eV'};
para.equilibrium_potential1={'Cu',eeqcu,'V'};
para.equilibrium_potential2={'Substrate',eeqsub,'V'};
para.charge_transfer1={'Cu',aphcu};
para.charge_transfer2={'Sub',aphsub};
para.lattice_size=ls;
para.preset_time=time;

currenttime=clock;
hhmm=strcat('h',num2str(currenttime(4)),'m',num2str(currenttime(5)));
resultname=strcat(mfilename,'_ls',num2str(ls),'_','t',num2str(time),'-
',date,hhmm);
save(resultname);
%% Report

szoccp=size(occp,1);
display 'computing completed'
display({'Time consumed is' etime(clock,t0)})
display({'Amout of deposits:' numdep/ls 'equivalent atomic layers'})
display({'Thickness of the deposit (layers):' size(occp,1)})
```

NOOVERHANG

```
function f=nooverhang(indi,indj)
%NOOVERHANG check if a site has two nearest neighboring atoms above it.
%Retures true if not and false if yes. INDI and INDJ
%are the site's index
global occp;
rows=size(occp,1);
if indi<rows
    if mod(indi,2)~=0
        f=occp(indi+1,pbcind(indj))==0&occp(indi+1,pbcind(indj-1))==0;
    elseif mod(indi,2)==0
        f=occp(indi+1,pbcind(indj+1))==0&occp(indi+1,pbcind(indj))==0;
    end
elseif indi==rows
    f=ture;
end
```

ISSAFE

```
function f=issafe(indi,indj)
%ISSAFE check if a site has two neighboring atoms below it.
%
global occp;
for k=1:length(indi)
    if indi(k)==1
        f=true;
    elseif indi(k)>1
        if mod(indi,2)~=0
            f=occp(indi(k)-1,pbcind(indj(k)))==1&occp(indi(k)-
1,pbcind(indj(k)-1))==1;
        else
            f=occp(indi(k)-1,pbcind(indj(k)+1))==1&occp(indi(k)-
1,pbcind(indj(k)))==1;
        end
    end
end
```

ODDEVEN

```
function f=oddeven(indj)
% ODDEVEN is used with the function pbcind for applying the period
boundary condition. Because the index of neighbors for
% even row and odd row are different. ODDEVEN make them look same in the
code
global ii
if mod(ii,2)==0
    f=indj+1;
elseif mod(ii,2)~=0
    f=indj;
end
```

PBCIND

```
function f=pbcind(ind)
% PBCIND applys periodic boundary conditions to the x direction
%
global ls
if ind<=0
    f=ind+ls;
elseif ind>0&&ind<=ls
    f=ind;
elseif ind>ls
    f=ind-ls;
end
```

SDR

```
function f=sdr(ii,jj)
% SDR compute the diffusion rate
%
global wsub;
global wcu;
global R;
global T;
global ebsub;
global ebcu;
global kb;
global occp;
nnbs=coordnum(ii,jj);
if ii==1
    f=wsub*exp(-(ebcu*(nnbs-2)+2*ebsub)/(kb*T));
else
    f=wcu*exp(-ebcu*nnbs/(kb*T));
end
```

COORDNUM

```
function f=coordnum(indi,indj)
% coordnum computes the number of neighbors from the input as indi,
indj, the index of the location and occupancy, the status matrice, i.e.
occp
%
global occp
f=0;
if occp(indi,pbcind(indj-1))==1
    f=f+1;
end
if occp(indi,pbcind(indj+1))==1
    f=f+1;
end
if occp(indi+1,pbcind(oe(indj-1,indi)))==1
    f=f+1;
end
if occp(indi+1,pbcind(oe(indj,indi)))==1
    f=f+1;
end
if indi>1
    if occp(indi-1,pbcind(oe(indj,indi)))==1
        f=f+1;
    end
    if occp(indi-1,pbcind(oe(indj-1,indi)))==1
        f=f+1;
    end
elseif indi==1
    f=f+2;
end

function out=oe(jj,indi)
%
%
if mod(indi,2)==0
    out=jj;
else
    out=jj+1;
end
```

Appendix V. POSTPROCESSING CODES FOR THE 2DCS-KMC MODEL

Deposit microstructure is visualized by plotting the pattern of the occupancy matrix. In this model, the column and row indexes of the elements of the occupancy matrix correspond to its X and Y coordinates in the lattice respectively. The function SNAPSHOT computes the X and Y coordinates of all the atoms with the input of the occupancy matrix and the lattice constant. The snapshot of the deposit microstructure is visualized by plotting points at (X,Y).

The microstructre history map is generated by plotting all the snapshots on deposition of a series of amounts of Cu atoms, and mapping color to the deposition amounts. A movie showing the growth history can also be generated by plotting the serial snapshots.

Clusters can be extracted by the following steps:

1) Examine the bottom layer of the occupancy matrix.
2) Search vacant sites of this layer, the atoms between which are the bottom layer of the clusters.
3) Extract the corresponding columns of the occupancy matrix as a sub-matrix for a cluster.

Cluster size is defined as the number of the atoms, which is computed by counting the non-zero sites of the cluster matrix. The size of the cluster matrix corresponds to the dimensions of the cluster, from which the aspect ratio is computed.

SNAPSHOT

```
function y=snapshot(a)
%SNAPSHOT plots the pattern of the input lattice of occupancy a.
%
clf;
cla('reset');
% Set limits for x and y axises
axis([-1 size(a,2)+1 -1 (size(a,1)+1)*sqrt(3)]);
axis('equal');
[numr numc]=size(a);
sz=min(8,500/max(numr,numc));
% Convert the lattice indexes into coordinates for the plotting command
% POINT
if rem(numr,2)~=0
```

```
    [xodd,yodd]=meshgrid(0:(numc-1),0:sqrt(3):(sqrt(3)*(numr-1)/2));
    [xeven,yeven]=meshgrid(0.5:(numc-
0.5),(0.5*sqrt(3)):sqrt(3):(sqrt(3)*(numr-1)*0.5));
    oddoccp=a(1:2:numr,:);
    evenoccp=a(2:2:(numr-1),:);
else
    [xodd,yodd]=meshgrid(0:(numc-1),0:sqrt(3):(sqrt(3)*(numr-2)/2));
    [xeven,yeven]=meshgrid(0.5:(numc-
0.5),(0.5*sqrt(3)):sqrt(3):(sqrt(3)*numr*0.5));
    oddoccp=a(1:2:(numr-1),:);
    evenoccp=a(2:2:numr,:);
end
xxodd=xodd(oddoccp==1);
yyodd=yodd(oddoccp==1);
xxeven=xeven(evenoccp==1);
yyeven=yeven(evenoccp==1);
xxodd=xxodd(:);
xxeven=xxeven(:);
yyodd=yyodd(:);
yyeven=yyeven(:);
xcor=[xxodd;xxeven];
ycor=[yyodd;yyeven];
% plot the converted matrix of the coordinates of all the atoms
y=point(xcor,ycor,'size',sz);
```

CLUSTER

```
function f=cluster(x)
% f=CLUSTER(X) computes and anlyzes the cluters. It outputs a structure
containg the cluster matrices, cluster numbers, cluster hts, widths,
aspect ratios etc
% X is a cell array consisting of the microstructure matrices
latticecon=3.61e-10;

for j=1:length(x) % Loop for the cell array
    mm=x{j}; % mm is the microstructure matrix
    botm=mm(1,:);  % Extract the first layer for subseqent analysis
    %*************************
    % Periodic movement happened
    %************************
    if botm(1)==1&&botm(end)==1
        t=0;
        while t<size(botm,2)&&botm(end-t)==1
            t=t+1;
        end
        mm=circshift(mm',t)';  % Reshape the matrix X to be a non-
periodic matrix
        botm=mm(1,:);
    end
    %**************************
    % Count the clusters
    %**************************
    i=1; % counter of the index of the X
    sn=0; % counter of the index of the cluster SN
    vol=[]; %Defind the volume vector
    width=[];
    ht=[];
    asprat=[];
    while i<=length(botm)
        wid=0; % Define the width of a cluster, initially 0
        while i<=length(botm)&&botm(i)==1
            wid=wid+1;
            i=i+1;
        end
        %---------------------
        % If the first site is not occupied, then skip the following
checks
        %       if occupied, then analyze it,
        %----------------------
        if i>=2
            sn=sn+1; % point to another cluster
            width(sn)=wid;
            tailind(sn)=i-1;    % the index of the last atom in a
cluster
            headind(sn)=tailind(sn)-width(sn)+1;
            clusters{sn}=mm(1:end,headind(sn):tailind(sn));
            [II,JJ]=find(clusters{sn}==1);
            vol(sn)=numel(II);
            ht(sn)=max(II);
            asprat(sn)=ht(sn)/width(sn);
        end
        %---------------------------
        % If vacannt, just move the pointer to the next site
        %--------------------------
```

```
        while i<=length(botm)&&botm(i)==0
            i=i+1;
        end
    end
    %end of the loop for check every site of first layer

    f.clusterMatrix{j}=clusters;         %   cluster matrix, cell array
consisting of sub-matrices of the microstructure matrix
% each sub-matrix corresponds to one cluster
    f.nums(j)=sn;                                              % number of
clusters
    f.density(j)=f.nums(j)/(length(botm)*latticecon); % cluster density,
/m
    f.volume{j}=vol;                                       % cluser size
    f.width{j}=width;                                      % cluster width
    f.height{j}=ht;                                        % the peak of the
cluster
    f.aspectratio{j}=asprat;                   % aspect ratio of clusters
    f.meanvol(j)=mean(vol);
    f.varvol(j)=var(vol);
    f.meanwidth(j)=mean(width);
    f.varwidth(j)=var(width);
    f.meanheight(j)=mean(ht);
    f.varheight(j)=var(ht);
    f.meanaspr(j)=mean(asprat);
    f.varaspr(j)=var(asprat);
end
f.crittime=find(f.nums(2:end)==1, 1 )+1;   % the critical time when all
the clusters merged
```

Appendix VI. SIMULATION CODES FOR THE 2DCSP-KMC MODEL

MAIN SCRIPT

```
%*********************************************************************
%   POLY1_1
%*********************************************************************
clear all
property=input('Descrption about this running: ','s');
name=input('Give the prefix of the name of the result file:','s');
global bxsz % delcare the box size by lattice space global
global a    % lattice space
global dinh % Declare the inhibited distance
global bx   % Declare the BX global
global cellsz %Declare the cellsz global
global corr % Declare the correction coefficience global
global kb   % Declare the boltzman constant global
global T    % Declare the temprature global
global ebme % Declare ebme global
global ebsub %
global wsub
global wme
global rdsub rdme
global err  % Declare the error for compare the distance

corr=0.5;                     % Correction coefficien for computing the
diffusion barrier contributed by strange neighboring atoms
err=-3;
Frd=96485.3415;      % Faraday constant (s.A / mol)
R=8.314472;          %Gas constant (J.K-1.mol-1)
kb=8.617343e-5;      % Boltzmann (eV.k-1)
nn=2;                % electron number, which is 2 for Me ion
NA=6.02e23;          % Avagadro constant
%% Input paramters

kme=input('Deposition rate constant for Me on Me (m^3/mol.s) Kme=
[0.204]');
if isempty(kme)
    kme=0.204;
end
ksub=input('Deposition rate constant for Me on Me (m^3/mol.s) Ksub=
[0.143]');
if isempty(ksub)
    ksub=0.143;
end

wme=input('Jump frequency for Me surface diffusion on Me, (s^-1) Wme=
[1.5e6]');
if isempty(wme)
    wme=1.5e6;
end
wsub=input('Jump frequency for Me surface diffusion on substrate (s^-1)
Wsub= [1.5e6]');
if isempty(wsub)
    wsub=1.5e6;
end
ebme=input('Energy barrier for breaking a Me-Me bond, (eV) Ebme=
[0.13]');
if isempty(ebme)
    ebme=0.13;
```

```
end
ebsub=input('Energy barrier for breaking a Me-substrate bond (eV) Ebsub=
[0.35]');
if isempty(ebsub)
    ebsub=0.35;
end

T=input('Temperature T= [298K]');
if isempty(T)
    T=298;
end
ap=input('Applied electrode potential (V) ap= [-0.13]');
if isempty(ap)
    ap=-0.13;
end
con=input('Me ion concentration (mol) c= [0.5]');
if isempty(con)
    con=0.5;
end
eeqme=input('Equilibrium potential for Me deposition on Me (V) eeqme=
[0]');
if isempty(eeqme)
    eeqme=0;
end
eeqsub=input('Equilibrium potential for Me deposition on substrate (V)
eeqsub= [-0.1]');
if isempty(eeqsub)
    eeqsub=-0.1;
end

target=input('How many EMLs do you want to deposit for this run? [50]');
if isempty(target)
    target=50;
end


dinhcoef=input('What is the inhabitation distance?[0.8]');
if isempty(dinhcoef)
    dinhcoef=0.8;
end

cellsz=input('What is the size of the simulation cell? [50]');
if isempty(cellsz)
    cellsz=50;
end

aphme=0.5;            % charge transfer coefficient for Me deposition on
Me
aphsub=0.5;           % charge transfer coefficient for Me deposition on
substrate

opme=ap-eeqme;       % overpotential for Me on Me
opsub=ap-eeqsub;     % overpotential for Me on sub
a=1;                 % lattice space, a unit value

time=100;                % Define the time when the simulation terminates

dinh=dinhcoef*a; %Inhibited distance
bxsz=4*a;    % Give the box size
```

```
rdme=kme*con*exp(-aphme*nn*Frd*opme/(R*T));        % Deposiiton rate on
metal
rdsub=ksub*con*exp(-aphsub*nn*Frd*opsub/(R*T));  % Deposition rate on
substrate
eml=cellsz*bxsz/a;
%% Parameters for data collection
if target>5
    intedge=[10 1000 target*eml]; % Edges of the regions in which the
step for save result is same
    rstepsz=[10 100]; % the result steps corresponding to the intedge
else
    intedge=[10 target*eml];
    rstepsz=10;
end
rc=1; % results counter

% build all the checkpoints where a result cell element is saved
for i=1:(length(intedge)-1)
    % the vector of checkpoints for each region
    regn{i}=intedge(i):rstepsz(i):(intedge(i+1)-rstepsz(i));
end
rcp=cat(2,regn,intedge(end)); % concatonate all the regions to form the
complete check point lists

%% Initial conditions
kmcclock=0;
t0=clock; %the current time
ic=1; % counter of the intervals
stepinterval=100; % the interval of kmcstep after which the progress is
reported and displayed
gc=0;   % grain counter
% INitial bx.atm
% INitial sub structure and bx.sub
%
% The substrate inital condition can be changed on demand.
xx=0:a:(bxsz*cellsz-a);
xx=pbc(xx+rand*a);
for i=1:cellsz
    bx(1,i).sub=[];
    bx(1,i).site=[];
    bx(1,i).atm=[];
end
for j=1:length(xx)
    [boxi boxj]=xy2bxind(xx(j),0);
    sbc=length(bx(boxi,boxj).sub)+1;
    bx(boxi,boxj).sub(sbc).x=xx(j);
    bx(boxi,boxj).sub(sbc).y=0;
    bx(boxi,boxj).sub(sbc).rate=rdsub;
end


kmcsteps=0;
substeps=0;
depsteps=0;
diffsteps=0;
%% KMC COMPUTATION MAIN CODE
while kmcclock<time&&(substeps+depsteps)<(target*eml)
    %% Event selector
    %------------------------------------------
```

```
    % Build the rate list from atom structure
    subrate=[];
    subind=[];
    atmrate=[];
    atmind=[];
    siterate=[];
    siteind=[];
    [brows bcols]=size(bx);
    m=0; %counter
    for i=1:brows
        for j=1:bcols
            if ~isempty(bx(i,j).atm)
                for l=1:length(bx(i,j).atm)
                    if ~isempty(bx(i,j).atm(l).evt)
                        for k=1:length(bx(i,j).atm(l).evt)
                            if ~isempty(bx(i,j).atm(l).evt(k).rate)
                                m=m+1;
                                atmrate(m)=bx(i,j).atm(l).evt(k).rate;
                                atmind(m,:)=[i j l k];
                            end
                        end
                    end
                end
            end
        end
    end

    n=0; %counter
    for i=1:brows
        for j=1:bcols
            if ~isempty(bx(i,j).site)
                for k=1:length(bx(i,j).site)
                    if ~isempty(bx(i,j).site(k).rate)
                        n=n+1;
                        siterate(n)=bx(i,j).site(k).rate;
                        siteind(n,:)=[i j k];
                    end
                end
            end
        end
    end

    t=0; %Counter
    for i=1:size(bx,2)
        if ~isempty(bx(1,i).sub)
            for j=1:length(bx(1,i).sub)
                if ~isempty(bx(1,i).sub(j).rate)
                    t=t+1;
                    subrate(t)=bx(1,i).sub(j).rate;
                    subind(t,:)=[1 i j];
                end
            end
        end
    end

    % Then build the whole rate list followingly
    rates=[subrate siterate atmrate];
    types=[1.*ones(size(subrate))                2.*ones(size(siterate))
3.*ones(size(atmrate))];
    xi=rand;  %  Generate  a  random  number  for  selection  of  the  events
randomly
```

```
    normrates=cumsum(rates)./sum(rates); % normalize the rate list
    rateind=find(normrates>=xi, 1); % select the rate according to the
random number and rates list
    %-----Retracing the event type
    evttype=types(rateind);
    evtind=rateind-find(types==evttype,1)+1;
    %% Eexecute the selected event and update the database accordingly
    switch evttype
        case 1
            casesub1
            substeps=substeps+1;
        case 2
            casedep1
            depsteps=depsteps+1;
        case 3
            casediff1
            diffsteps=diffsteps+1;
    end

    %% Time increment
    kmcclock=kmcclock-log(xi)/sum(rates);
    clockincrment=-log(xi)/sum(rates);
    kmcsteps=kmcsteps+1;
    %% Mornitoring the processes


    if kmcsteps==stepinterval*ic
        ic=ic+1;
        elapsedtime=etime(clock,t0);
        timecons=s2hms(elapsedtime);

        percent=100*depositamount/(target*eml);
        progress=num2str(percent,3);
        timeleft=elapsedtime*(target*eml-depositamount)/depositamount;
        display (strcat('Time elapsed is: ',timecons))
        display (['KMC clock is: ' num2str(kmcclock) 's'])
        display ([num2str(progress) ' percent finished'])
        display (strcat('Estimated time remaining: ', s2hms(timeleft)))
        display ([num2str(depsteps+substeps) ' atoms deposited'])
        display ([ 'There are ' num2str(gc) ' grains'])
        display ' '
    end
    %% Data collecting
    depositamount=depsteps+substeps;
    if rc<=length(rcp)
        if depositamount==rcp(rc)
            history(rc).bx=bx;
            history(rc).kmcclock=kmcclock;
            history(rc).timespent=etime(clock,t0);
            history(rc).depositamount=depositamount;
            rc=rc+1;
            display  (['data  collected  when  '  num2str(depositamount)  '
atoms has been deposited'])
            display (' ')
        end
    end

end

%% Data collecting
```

```
currenttime=clock;
hhmm=strcat('h',num2str(currenttime(4)),'m',num2str(currenttime(5)));
resultname=strcat(name,'_',mfilename,'_',date,hhmm);
save(resultname);
```

CASESUB1

```
%************************************
% DEPOSITION ON A SUB SITE HAPPENS
%************************************
% NEW STRATEGY
%% Remove the sub site
bxi=1; % box index of the selected subsite
bxj=subind(evtind,2);
inbx=subind(evtind,3); % the index of the sub site in the box
x0=bx(1,bxj).sub(inbx).x;
y0=bx(1,bxj).sub(inbx).y;
bx(1,bxj).sub(inbx)=[]; %get rid of this sub bx.site from the bx.sub
list

%% Add a new atom
%-----------------------------------------------------------
% Add the deposited atom in the box
% Generate a new grain
% Give the values of its fields including .x, .y, .orient, .grain
ac=length(bx(bxi,bxj).atm)+1; % Get the cursor of the atom counter in
the box
bx(bxi,bxj).atm(ac).x=x0; % x cordinate
bx(bxi,bxj).atm(ac).y=y0; % y cordinate of the atom

bx(bxi,bxj).atm(ac).orient=rand*pi/3; %give the atom a random
orientation
gc=gc+1;
bx(bxi,bxj).atm(ac).grain=gc; % this atom's grain ID
bx(bxi,bxj).atm(ac).cn=0;
bx(bxi,bxj).atm(ac).strcn=0;
bx(bxi,bxj).atm(ac).evt.rate=[];
bx(bxi,bxj).atm(ac).evt.dest=[];
%% Update the neighboring sites
updatenbsites(bxi,bxj,ac);
%% Update the inhibited sites
inhibitsite(bxi,bxj,ac);
%% Update the induced sites
induce(bxi,bxj,ac);
%% Update the diffusion events of this deposited atom and its
neighboring atoms within the range of 2a
updatenbatms(bxi,bxj,ac,2*a);
```

CASEDEP1

```
%***********************************
%      DEPOSITION OCCURS
%***********************************
%% Remove the site
bxi=siteind(evtind,1);
bxj=siteind(evtind,2);
inbx=siteind(evtind,3);
x0=bx(bxi,bxj).site(inbx).x;
y0=bx(bxi,bxj).site(inbx).y;
orient0=bx(bxi,bxj).site(inbx).orient;
grain0=bx(bxi,bxj).site(inbx).grain;
cn0=bx(bxi,bxj).site(inbx).cn;
strcn0=bx(bxi,bxj).site(inbx).strcn;
%Get rid of this site
bx(bxi,bxj).site(inbx)=[];
%% Add a new atom
%Replace this site with a new atom
%Add a new atom to the current box
%Give this atom all fields values except .evt.dest and .evt.rate
ac=length(bx(bxi,bxj).atm)+1;
bx(bxi,bxj).atm(ac).x=x0;
bx(bxi,bxj).atm(ac).y=y0;
bx(bxi,bxj).atm(ac).orient=orient0;
bx(bxi,bxj).atm(ac).grain=grain0;
bx(bxi,bxj).atm(ac).cn=cn0;
bx(bxi,bxj).atm(ac).strcn=strcn0;
bx(bxi,bxj).atm(ac).evt.rate=[];
bx(bxi,bxj).atm(ac).evt.dest=[];
%% Update the neighboring site
updatenbsites(bxi,bxj,ac);
%% Remove the inhibited sub sites
inhibitsub(bxi,bxj,ac);
%% update the induced sites
induce(bxi,bxj,ac);
%% Update the ihibited sites
inhibitsite(bxi,bxj,ac);
%% Update the diffusion events of this deposited atom and its neighboring atoms within the range of 2a
updatenbatms(bxi,bxj,ac,2*a);
```

CASEDIFF1

```
%% A DIFFUSION EVENT OCCURS
%-----------------------------------------
%-----------------------------------------
%% Allocate the location and bxind of the diffusion atom and the
destination site
%Get the box index and inbox location of the oringal atom
%Get the index in the EVT field of the original atom
%With these three index, we can index into the individual event in the
BX
biorg=atmind(evtind,1);
bjorg=atmind(evtind,2);
inbxorg=atmind(evtind,3);
whichevt=atmind(evtind,4);
%Allocate the original atom to a variable
%Allocate the destination site to a varaible
%Allocate there coordinates
origatm=bx(biorg,bjorg).atm(inbxorg);
destsite=bx(biorg,bjorg).atm(inbxorg).evt(whichevt).dest;
xorg=origatm.x;
yorg=origatm.y;
xd=destsite.x;
yd=destsite.y;
%Get the box index of the destination site
%Find the inbox location of the destination site by its coordinates,
becuase coordinates of any class are unique
%in this model
%Allocate the coordinates of the destination
[bidest bjdest]=xy2bxind(xd,yd);
inbxdest=find([bx(bidest,bjdest).site.x]==xd&[bx(bidest,bjdest).site.y]=
=yd);
%---------------------------------------------------------
%% Remove an atom from the original box and the site from the
destination box
bx(biorg,bjorg).atm(inbxorg)=[];
bx(bidest,bjdest).site(inbxdest)=[];
%% Add a new atom into the destination box
ac=length(bx(bidest,bjdest).atm)+1;
bx(bidest,bjdest).atm(ac).x=xd;
bx(bidest,bjdest).atm(ac).y=yd;
bx(bidest,bjdest).atm(ac).grain=destsite.grain;
bx(bidest,bjdest).atm(ac).orient=destsite.orient;
dd=da2b(xorg,yorg,xd,yd); %distance between the orignal atom position to
its destination site
if dd<a
    bx(bidest,bjdest).atm(ac).strcn=destsite.strcn-1;
    bx(bidest,bjdest).atm(ac).cn=destsite.cn;
elseif dd==a
    bx(bidest,bjdest).atm(ac).cn=destsite.cn-1;
    bx(bidest,bjdest).atm(ac).strcn=destsite.strcn;
end
bx(bidest,bjdest).atm(ac).evt=[];
%% Add a new site
sc=length(bx(biorg,bjorg).site)+1;
bx(biorg,bjorg).site(sc).x=xorg;
bx(biorg,bjorg).site(sc).y=yorg;
bx(biorg,bjorg).site(sc).orient=origatm.orient;
bx(biorg,bjorg).site(sc).grain=origatm.grain;
if dd<a
    bx(biorg,bjorg).site(sc).strcn=origatm.strcn+1;
```

```
    bx(biorg,bjorg).site(sc).cn=origatm.cn;
elseif dd==a
    bx(biorg,bjorg).site(sc).cn=origatm.cn+1;
    bx(biorg,bjorg).site(sc).strcn=origatm.strcn;
end
if yorg<a
    bx(biorg,bjorg).site(sc).rate=rdsub;
else
    bx(biorg,bjorg).site(sc).rate=rdme;
end
%% Build the nb boxs
[nbatm nbatmind]=buildnbatm(bidest,bjdest);
[nbsite nbsiteind]=buildnbsite(bidest,bjdest);
[nbsub nbsubind]=buildnbsub(bidest,bjdest);

%% Update the inhibited sub sites
inhibitsub(bidest,bjdest,ac)
%% Remove the inhibited sites
inhibitsite(bidest,bjdest,ac);
%% Update the neighboring sites of the destination sites
updatenbsites(bidest,bjdest,ac);
%% Update the neighboring sites of the original atom
[nbsite nbsiteind]=buildnbsite(biorg,bjorg);
d2=da2b([nbsite.x],[nbsite.y],xorg,yorg);
allnbsites=find(d2<=a&d2>=dinh);
%Update the cn and strcn of the neighboring sites
if ~isempty(allnbsites)
    for i=1:length(allnbsites)
        bi=nbsiteind(allnbsites(i),1);
        bj=nbsiteind(allnbsites(i),2);
        itsx=nbsite(allnbsites(i)).x;
        itsy=nbsite(allnbsites(i)).y;
        inbxind=find([bx(bi,bj).site.x]==itsx&[bx(bi,bj).site.y]==itsy);
        if d2(allnbsites(i))<a
            bx(bi,bj).site(inbxind).strcn=bx(bi,bj).site(inbxind).strcn-
1;
        elseif d2(allnbsites(i))==a
            bx(bi,bj).site(inbxind).cn=bx(bi,bj).site(inbxind).cn-1;
        end
        if
bx(bi,bj).site(inbxind).strcn+bx(bi,bj).site(inbxind).cn<2&&itsy>=a
            bx(bi,bj).site(inbxind)=[];
        end
    end
end

%% Add induced sites
induce(bidest,bjdest,ac);
%% Update neighboring atoms within the range of 3a
if ~isempty(nbatm)
    d1=da2b([nbatm.x],[nbatm.y],xd,yd);
    allnbsind=find(d1<=3*a);
    if ~isempty(allnbsind)
        for i=1:length(allnbsind)
            bi=nbatmind(allnbsind(i),1);
            bj=nbatmind(allnbsind(i),2);
            inbxind=nbatmind(allnbsind(i),3);
            itsx=bx(bi,bj).atm(inbxind).x;
            itsy=bx(bi,bj).atm(inbxind).y;
            if d1(allnbsind(i))>=dinh&&d1(allnbsind(i))<a
```

```
bx(bi,bj).atm(inbxind).strcn=bx(bi,bj).atm(inbxind).strcn+1;
            elseif d1(allnbsind(i))==a
                bx(bi,bj).atm(inbxind).cn=bx(bi,bj).atm(inbxind).cn+1;
            end
            d0=da2b(xorg,yorg,itsx,itsy);
            if d0>=dinh&&d0<a&&(itsx~=xd||itsy~=yd)

bx(bi,bj).atm(inbxind).strcn=bx(bi,bj).atm(inbxind).strcn-1;
            elseif d0==a
                bx(bi,bj).atm(inbxind).cn=bx(bi,bj).atm(inbxind).cn-1;
            end
            diffusion(bi,bj,inbxind);
        end
    end
end
```

UPDATENBSITES

```
function f=updatenbsites(bxi,bxj,atmind)
% Update the neighboring sites
%-----------------------------------------------------
% Find the neighboring sites
% Update cn and strcn of all the neighboring sites
global bx dinh a

[nbsite nbsiteind]=buildnbsite(bxi,bxj);
x0=bx(bxi,bxj).atm(atmind).x;
y0=bx(bxi,bxj).atm(atmind).y;
if ~isempty(nbsite)
    d=da2b([nbsite.x],[nbsite.y],x0,y0);
    nbs=find(d<=a&d>=dinh);
    if ~isempty(nbs)
        for i=1:length(nbs)
            bi=nbsiteind(nbs(i),1); %Get the box index of this site
            bj=nbsiteind(nbs(i),2);
            inbxind=nbsiteind(nbs(i),3); %Get the inbox location of this
site
            % Calculate the coordinate number of the sites
            if d(nbs(i))<a&&d(nbs(i))>=dinh

bx(bi,bj).site(inbxind).strcn=bx(bi,bj).site(inbxind).strcn+1;
            elseif d(nbs(i))==a
                bx(bi,bj).site(inbxind).cn=bx(bi,bj).site(inbxind).cn+1;
            end
        end
    end
end
```

DIFFUSION

```
function f=diffusion(bxi,bxj,atmind)
% DIFFUSION updates the fields of the atom indexed by (BXI,BXJ,ATMIND).
The fields includes .dest (destination sites) and
% .rate (diffusion rate)
%
global bx a
bx(bxi,bxj).atm(atmind).evt=[];
x0=bx(bxi,bxj).atm(atmind).x;
y0=bx(bxi,bxj).atm(atmind).y;
cn0=bx(bxi,bxj).atm(atmind).cn;
strcn0=bx(bxi,bxj).atm(atmind).strcn;
[nbsite nbsiteind]=buildnbsite(bxi,bxj);
d2=da2b([nbsite.x],[nbsite.y],x0,y0);
itsnbsites=find(d2<=a);
if ~isempty(itsnbsites)
    for k=1:length(itsnbsites)
        bi=nbsiteind(itsnbsites(k),1);
        bj=nbsiteind(itsnbsites(k),2);
        inbxind=nbsiteind(itsnbsites(k),3);
        cnf=bx(bi,bj).site(inbxind).cn;
        strcnf=bx(bi,bj).site(inbxind).strcn;
        yf=bx(bi,bj).site(inbxind).y;
        if cnf+strcnf>=3||yf<a
            ec=length(bx(bxi,bxj).atm(atmind).evt)+1;

bx(bxi,bxj).atm(atmind).evt(ec).dest=bx(bi,bj).site(inbxind);

bx(bxi,bxj).atm(atmind).evt(ec).rate=diffrate(cn0,strcn0,y0,cnf,strcnf,y
f);
        end
    end
end
```

INDUCE

```
function f=induce(bxi,bxj,atmind)
% INDUCED compute the induced sites
%
% Update the induced sites
% Find up to six potential induced sites
% Check them one by one to see if they are inhibited by other atoms
% Check if will be a stable site for deposition, i.e., if its cn+strcn>2
or if its y coordinate is less than a;
% Add the qualified new induced sites to the BX.SITE
global bx a dinh rdme rdsub cellsz

x0=bx(bxi,bxj).atm(atmind).x;
y0=bx(bxi,bxj).atm(atmind).y;
orient0=bx(bxi,bxj).atm(atmind).orient;
[NBX NBY]=nb(x0, y0,orient0);
for i=1:length(NBX)
    %Get the box index
    %Rebuild the neighbor boxes of the potential site
    %Induce site could be in a box above the current box,so extend the
box size
    [bi,bj]=xy2bxind(NBX(i),NBY(i));
    rows=size(bx,1);
    if bi>rows
        bx(bi,cellsz).site=[];
        bx(bi,cellsz).atm=[];
    end
    [nbatm nbatmind]=buildnbatm(bi,bj);

    if ~isempty(nbatm)
        d1=da2b([nbatm.x],[nbatm.y],NBX(i),NBY(i)); %distance from atoms
to this site
        isinhibited=any(d1<dinh);
    else
        isinhibited=false;
    end

    [nbsite nbsiteind]=buildnbsite(bi,bj);
    if ~isempty(nbsite)
        d2=da2b([nbsite.x],[nbsite.y],NBX(i),NBY(i));%   distance   from
sites to this site
        %Check if it overlaps with existing atoms
        isoverlapped=any(d2==0);
    else
        isoverlapped=false;
    end
    %Check  its  coordinate  number  to  see  it  is  a  stable  site  for
deposition
    itscn=numel(find(d1==a));
    itsstrcn=numel(find(d1>=dinh&d1<a));
    %Exclude it if it is inhibited or overlapped with exisiting sites,
else add it to the bx as a new site
    if (~isinhibited)&&(~isoverlapped)&&(itscn+itsstrcn>=2||NBY(i)<a)
        sc=length(bx(bi,bj).site)+1; %Get the site counter cursor
        bx(bi,bj).site(sc).x=NBX(i);
        bx(bi,bj).site(sc).y=NBY(i);
        if NBY(i)>=a
            bx(bi,bj).site(sc).rate=rdme;
        else
```

```
            bx(bi,bj).site(sc).rate=rdsub;
        end
        bx(bi,bj).site(sc).cn=itscn;
        bx(bi,bj).site(sc).strcn=itsstrcn;
        bx(bi,bj).site(sc).grain=bx(bxi,bxj).atm(atmind).grain;
        bx(bi,bj).site(sc).orient=bx(bxi,bxj).atm(atmind).orient;
    end
end
```

INHIBITSUB

```
function f=inhibitsub(bxi,bxj,atmind)
%
%
global bx dinh err
[nbsub nbsubind]=buildnbsub(bxi,bxj);
x0=bx(bxi,bxj).atm(atmind).x;
y0=bx(bxi,bxj).atm(atmind).y;
if bxi==1
    d3=da2b([nbsub.x],[nbsub.y],x0,y0);
    inhibitedsub=find(d3<dinh);
    %Update the inhibited sub site
    if ~isempty(inhibitedsub)
        for i=1:length(inhibitedsub)
            bi=nbsubind(inhibitedsub(i),1);
            bj=nbsubind(inhibitedsub(i),2);
            itsx=nbsub(inhibitedsub(i)).x;
            itsy=nbsub(inhibitedsub(i)).y;

bx(bi,bj).sub([bx(bi,bj).sub.x]==itsx&[bx(bi,bj).sub.y]==itsy)=[];
        end
    end
end
```

INHIBITSITE

```
function f=inhibitsite(bxi,bxj,atmind)
%
%
% Update the inhibited neighboring sites
% Get rid of those inhibited sites from BX
global bx dinh
[nbsite nbsiteind]=buildnbsite(bxi,bxj);
x0=bx(bxi,bxj).atm(atmind).x;
y0=bx(bxi,bxj).atm(atmind).y;
if ~isempty(nbsite)
    d2=da2b([nbsite.x],[nbsite.y],x0,y0);
    inhibited=find(d2<dinh);
    %Check them one by one, if it was the destination of an atom, then
update that atom's .evt field
    if ~isempty(inhibited)
        for i=1:length(inhibited)
            bi=nbsiteind(inhibited(i),1);
            bj=nbsiteind(inhibited(i),2);
            itsx=nbsite(inhibited(i)).x;
            itsy=nbsite(inhibited(i)).y;

bx(bi,bj).site([bx(bi,bj).site.x]==itsx&[bx(bi,bj).site.y]==itsy)=[];
        end
    end
end
```

BUILDNBATMS

```
function [atm atmind]=buildnbatm(bxi,bxj)
% BUILDNBATM build all the neighbor atoms from the neighboring boxes of
the current box, the input arguement BI is the index
% of this box
%
global bx

atm.x=[];
atm.y=[];
atm.cn=[];
atm.strcn=[];
atm.grain=[];
atm.orient=[];
atm.evt.rate=[];
atm.evt.dest=[];
atmind=[];

[rows cols]=size(bx);
kc=0;%counter
if bxi==1
    if bxi<rows
        boxinds=[bxi pbcs(bxj-1);bxi pbcs(bxj);bxi pbcs(bxj+1);
                 bxi+1,pbcs(bxj-1);bxi+1,pbcs(bxj);bxi+1,pbcs(bxj+1)];
    else
        boxinds=[bxi pbcs(bxj-1);bxi pbcs(bxj);bxi pbcs(bxj+1)];
    end

    for i=1:size(boxinds,1)
        if ~isempty(bx(boxinds(i,1),boxinds(i,2)).atm)
            for j=1:length(bx(boxinds(i,1),boxinds(i,2)).atm)
                if ~isempty(bx(boxinds(i,1),boxinds(i,2)).atm(j))
                    kc=kc+1;
                    atm(kc).x=bx(boxinds(i,1),boxinds(i,2)).atm(j).x;
                    atm(kc).y=bx(boxinds(i,1),boxinds(i,2)).atm(j).y;

atm(kc).orient=bx(boxinds(i,1),boxinds(i,2)).atm(j).orient;

atm(kc).grain=bx(boxinds(i,1),boxinds(i,2)).atm(j).grain;
                    atm(kc).cn=bx(boxinds(i,1),boxinds(i,2)).atm(j).cn;

atm(kc).strcn=bx(boxinds(i,1),boxinds(i,2)).atm(j).strcn;

atm(kc).evt=bx(boxinds(i,1),boxinds(i,2)).atm(j).evt;
                    atmind(kc,:)=[boxinds(i,1) boxinds(i,2) j];
                end
            end
        end
    end
else
    if bxi<rows
        boxinds=[bxi pbcs(bxj-1);bxi pbcs(bxj);bxi pbcs(bxj+1);
                 bxi+1,pbcs(bxj-1);bxi+1,pbcs(bxj);bxi+1,pbcs(bxj+1);
                 bxi-1,pbcs(bxj-1);bxi-1,pbcs(bxj);bxi-1,pbcs(bxj+1)];
    else
        boxinds=[bxi pbcs(bxj-1);bxi pbcs(bxj);bxi pbcs(bxj+1);
                 bxi-1,pbcs(bxj-1);bxi-1,pbcs(bxj);bxi-1,pbcs(bxj+1)];
    end
    for i=1:size(boxinds,1)
```

```
        if ~isempty(bx(boxinds(i,1),boxinds(i,2)).atm)
            for j=1:length(bx(boxinds(i,1),boxinds(i,2)).atm)
                if ~isempty(bx(boxinds(i,1),boxinds(i,2)).atm(j))
                    kc=kc+1;
                    atm(kc).x=bx(boxinds(i,1),boxinds(i,2)).atm(j).x;
                    atm(kc).y=bx(boxinds(i,1),boxinds(i,2)).atm(j).y;

atm(kc).orient=bx(boxinds(i,1),boxinds(i,2)).atm(j).orient;

atm(kc).grain=bx(boxinds(i,1),boxinds(i,2)).atm(j).grain;
                    atm(kc).cn=bx(boxinds(i,1),boxinds(i,2)).atm(j).cn;

atm(kc).strcn=bx(boxinds(i,1),boxinds(i,2)).atm(j).strcn;

atm(kc).evt=bx(boxinds(i,1),boxinds(i,2)).atm(j).evt;
                    atmind(kc,:)=[boxinds(i,1) boxinds(i,2) j];
                end
            end
        end
    end
end
```

BUILDNBSITE

```
function [site siteind]=buildnbsite(bxi,bxj)
%BUILDNBSITE build the site list of all the neighboring boxes to the
current box,  BI is the index of the box. SITE is the
%site list, SITEIND is the corresponding box index and inbox location of
these sites in SITE
%

global bx

site.x=[];
site.y=[];
site.orient=[];
site.grain=[];
site.cn=[];
site.strcn=[];
site.rate=[];
siteind=[];

rows=size(bx,1);
if bxi==1
    if bxi<rows
        boxinds=[bxi pbcs(bxj-1);bxi pbcs(bxj);bxi pbcs(bxj+1);
                 bxi+1,pbcs(bxj-1);bxi+1,pbcs(bxj);bxi+1,pbcs(bxj+1)];
    else
        boxinds=[bxi pbcs(bxj-1);bxi pbcs(bxj);bxi pbcs(bxj+1)];
    end
    kc=0;
    for i=1:size(boxinds,1)
        if ~isempty(bx(boxinds(i,1),boxinds(i,2)).site)
            for j=1:length(bx(boxinds(i,1),boxinds(i,2)).site)
                if ~isempty(bx(boxinds(i,1),boxinds(i,2)).site(j))
                    kc=kc+1;
                    site(kc).x=bx(boxinds(i,1),boxinds(i,2)).site(j).x;
                    site(kc).y=bx(boxinds(i,1),boxinds(i,2)).site(j).y;

site(kc).cn=bx(boxinds(i,1),boxinds(i,2)).site(j).cn;

site(kc).strcn=bx(boxinds(i,1),boxinds(i,2)).site(j).strcn;

site(kc).grain=bx(boxinds(i,1),boxinds(i,2)).site(j).grain;

site(kc).orient=bx(boxinds(i,1),boxinds(i,2)).site(j).orient;

site(kc).rate=bx(boxinds(i,1),boxinds(i,2)).site(j).rate;
                    siteind(kc,:)=[boxinds(i,1) boxinds(i,2) j];
                end
            end
        end
    end
else
    if bxi<rows
        boxinds=[bxi pbcs(bxj-1);bxi pbcs(bxj);bxi pbcs(bxj+1);
                 bxi+1,pbcs(bxj-1);bxi+1,pbcs(bxj);bxi+1,pbcs(bxj+1);
                 bxi-1,pbcs(bxj-1);bxi-1,pbcs(bxj);bxi-1,pbcs(bxj+1)];
    else
        boxinds=[bxi pbcs(bxj-1);bxi pbcs(bxj);bxi pbcs(bxj+1);
                 bxi-1,pbcs(bxj-1);bxi-1,pbcs(bxj);bxi-1,pbcs(bxj+1)];
    end
```

```
    kc=0;
    for i=1:size(boxinds,1)
        if ~isempty(bx(boxinds(i,1),boxinds(i,2)).site)
            for j=1:length(bx(boxinds(i,1),boxinds(i,2)).site)
                if ~isempty(bx(boxinds(i,1),boxinds(i,2)).site(j))
                    kc=kc+1;
                    site(kc).x=bx(boxinds(i,1),boxinds(i,2)).site(j).x;
                    site(kc).y=bx(boxinds(i,1),boxinds(i,2)).site(j).y;

site(kc).cn=bx(boxinds(i,1),boxinds(i,2)).site(j).cn;

site(kc).strcn=bx(boxinds(i,1),boxinds(i,2)).site(j).strcn;

site(kc).grain=bx(boxinds(i,1),boxinds(i,2)).site(j).grain;

site(kc).orient=bx(boxinds(i,1),boxinds(i,2)).site(j).orient;

site(kc).rate=bx(boxinds(i,1),boxinds(i,2)).site(j).rate;
                    siteind(kc,:)=[boxinds(i,1) boxinds(i,2) j];
                end
            end
        end
    end
end
```

BUILDNBSUB

```
function [sub subind]=buildnbsub(bxi,bxj)
%BUILDNBSUB build the sub list of all the neighboring boxes, BI is the
index of the box, SUB is the sub list, SUBIND is the
%corresponding box index and inbox location of these sub site
%
global bx
global cellsz
sub.x=[];
sub.y=[];
sub.rate=[];
subind=[];
kc=0;
if bxi<=2
    boxinds=[1 pbcs(bxj-1);1 pbcs(bxj);1 pbcs(bxj+1)];

    for i=1:3
        if ~isempty(bx(boxinds(i,1),boxinds(i,2)).sub)
            for j=1:length(bx(boxinds(i,1),boxinds(i,2)).sub)
                if ~isempty(bx(boxinds(i,1),boxinds(i,2)).sub(j))
                    kc=kc+1;
                    sub(kc)=bx(boxinds(i,1),boxinds(i,2)).sub(j);
                    subind(kc,:)=[boxinds(i,1),boxinds(i,2) j];
                end
            end
        end
    end
end
```

UPDATENBATMS

```
function f=updatenbatms(bxi,bxj,atmind,range)
% Find the atoms within the range
% Update their cn and strcn if necessary
% Empty their bx.atm.evt
% Re-compute their diffusion event and diffusion rate
global bx a dinh
[nbatm nbatmind]=buildnbatm(bxi,bxj);
x0=bx(bxi,bxj).atm(atmind).x;
y0=bx(bxi,bxj).atm(atmind).y;
if ~isempty(nbatm)
    d1=da2b([nbatm.x],[nbatm.y],x0,y0);
    bx(bxi,bxj).atm(atmind).cn=length(find(d1==a));
    bx(bxi,bxj).atm(atmind).strcn=length(find(d1>=dinh&d1<a));
    allnbsind=find(d1<=range);
    if ~isempty(allnbsind)
        for i=1:length(allnbsind)
            bi=nbatmind(allnbsind(i),1);
            bj=nbatmind(allnbsind(i),2);
            inbxind=nbatmind(allnbsind(i),3);
            if d1(allnbsind(i))>=dinh&&d1(allnbsind(i))<a

bx(bi,bj).atm(inbxind).strcn=bx(bi,bj).atm(inbxind).strcn+1;
            elseif d1(allnbsind(i))==a
                bx(bi,bj).atm(inbxind).cn=bx(bi,bj).atm(inbxind).cn+1;
            end
            diffusion(bi,bj,inbxind)
        end
    end
end
```

NB

```
function [X Y]=nb(x,y,theta)
% NB calculate the coordinates of the neighbouring atoms or sites
%
global a

for i=0:5
    X(i+1)=pbc(x+a*cos(theta+i*(pi/3)));
    Y(i+1)=y+a*sin(theta+i*(pi/3));
end
X(Y<0)=[];
Y(Y<0)=[];
```

PBC

```
function f=pbc(x)
% apply periodic boundary condition to x coordinates
%
global bxsz
global cellsz
totalsize=bxsz*cellsz;
f(x>totalsize)=x(x>totalsize)-totalsize;
f(x>=0&x<=totalsize)=x(x>=0&x<=totalsize);
f(x<0)=x(x<0)+totalsize;
```

PBCS

```
function p=pbcs(n)
% apply the periodic boundary condition to box index
%
%
global cellsz
if n>cellsz
   p=n-cellsz;
elseif (n>=1)&&(n<=cellsz)
   p=n;
elseif n<=0
   p=n+cellsz;
end
```

DA2B

```
function f=da2b(x0,y0,x1,y1)
%  DA2B  calculate  the  distance  between  point/points  (X0,Y0)  and
point/points (X1,Y1);
%
global bxsz cellsz err
% Periodic boundary condition needs to be considered in this function
too
totalsz=bxsz*cellsz;
dx=abs(x0-x1);
dx(dx>=2*bxsz)=abs(dx(dx>=2*bxsz)-totalsz);
f=roundn(sqrt(dx.^2+(y0-y1).^2),err);
```

DIFFRATE

```
function f=diffrate(cn0, strcn0, y0,cnf,strcnf,yf)
% DIFFRATE compute the diffuction rate with the given input arguments
atom postion and the destination
%
global wsub
global wme
global ebme
global ebsub
global corr %correction coeffiecient
global a
global kb
global T

if y0<a
    Emig=cn0*ebme+strcn0*ebme*corr+2*ebsub;
else
    Emig=cn0*ebme+strcn0*ebme*corr;
end
if yf<a
    Ef=cnf*ebme+strcnf*ebme*corr+2*ebsub;
else
    Ef=cnf*ebme+strcnf*ebme*corr;
end
if Ef>=Emig
    E=Emig;
else
    E=2*Emig-Ef;
end
if y0<a
    f=wsub*exp(-E/(kb*T));
else
    f=wme*exp(-E/(kb*T));
end
```

XY2BXIND

```
function [I J]=xy2bxind(x,y)
% XY2BXIND converts the coordinate of input (X,Y) into the index in the
BX structure
global bxsz
I=zeros(size(y));
J=zeros(size(x));
I(rem(y,bxsz)==0)=y((rem(y,bxsz)==0))./bxsz+1;
I(rem(y,bxsz)~=0)=ceil(y((rem(y,bxsz)~=0))./bxsz);

J(rem(x,bxsz)==0)=pbc(x(rem(x,bxsz)==0))./bxsz+1;
J(rem(x,bxsz)~=0)=ceil(pbc(x(rem(x,bxsz)~=0))./bxsz);
```

S2HMS

```
function f=s2hms(x)
%the funtion S2HMS(X) converts the time unit of seconds into the form of
hours, minutes and seconds
%
if x<60
    f=[num2str(x) 's'];
elseif x>=60&&x<3600
    f=strcat(num2str(floor(x/60)),'   min   ',num2str(floor(rem(x,60))),'
s');
elseif x>=3600
    f=strcat(num2str(floor(x/3600)),'                                    h
',num2str(ceil(rem(x,3600)/60)),' min');
end
```

Appendix VII. POSTPROCESSING CODES FOR THE 2DCSP-KMC MODEL

SNAPSHOT

This function visualizes simulated microstructures by plotting all the atoms and mapping their orientation to colors.

```
function f=snapshot(bx)
% SNAPSHOT plot all the atoms
%
m=0; %counter
for i=1:numel(bx)
    if ~isempty(bx(i).atm)
        for j=1:length(bx(i).atm)
            if ~isempty(bx(i).atm(j))
                m=m+1;
                atmx(m)=bx(i).atm(j).x;
                atmy(m)=bx(i).atm(j).y;
                atmorient(m)=bx(i).atm(j).orient;

            end
        end
    end
end
orient=atmorient*180/pi;
scatter(atmx,atmy,3,orient)
gca;
axis equal
axis tight

ym=get(gca,'ylim');
xm=get(gca,'xlim');
set(gca, 'ylim',[ym(1)-3 ym(2)+5]);
set(gca,'xlim',[xm(1)-3,xm(2)+3]);
colorbar
```

GRAINHISTORY

```
%Compute the history of grain growth by inputting all the grain data at
different times of deposition.

savename=input('Please give the name of the file to save the grain
history data:[grainhistorydata]');
if isempty(savename)
    savename='grainhistorydata';
end

range=input('Please give the rang of the history array[1:190]');
if isempty(range)
    range=1:190;
end

threshhold=input('please defind the threshhold grain size [5]');
if isempty(threshhold)
    threshhold=5;
end

for i=range
   grainhist(i)=grains(history(i).bx,threshhold);
   display({num2str(i) 'dtat have been analyzed'})
end
save(savename,'grainhist')
```

GRAINS

```
function f=grains(bxx,threshhold)
% GRAINS compute the grain data from the input bxx
%
global a dinh

display ('The grains are now being analyzed, please wait...')
%% Firstly, a list of all the atoms is build

[atoms atominds]=allatoms(bxx);
%% Sort the atoms into ascending order of their grain IDs
[sortedgrainID originalinds]=sort([atoms.grain]);
sortedatoms=atoms(originalinds);
sortedatominds=atominds(originalinds,:);
% Find the unique grain IDs
% Find the first index of the atom belonging to the grain id in the
sortedatom list
%
[id firstind n]=unique(sortedgrainID,'first');
[id lastind n]=unique(sortedgrainID);

grainsize=lastind-firstind+1; % grain size, a vector
orient=[sortedatoms(firstind).orient]; % grain orientatin, a vector

% f.boundary is a cell vector, each elecments contains a vector of the
index of the boundar atoms in the sortedatoms list
f.atoms=sortedatoms;
f.atominds=sortedatominds;
f.ids=id(grainsize>threshhold);%grain id, f.ids is a vector
f.numgrain=length(f.ids);
f.grainsize=lastind(grainsize>threshhold)-
firstind(grainsize>threshhold)+1;
f.orient=orient(grainsize>threshhold);
f.member=[firstind(grainsize>threshhold)'
lastind(grainsize>threshhold)'];
% index of the atoms in the sortedatoms list, an N*2 matrix, first
column is the first index,
% second column is the last ind

%% Get the ID of neighboring grains and the misorientation
if f.numgrain>=1
    for i=1:f.numgrain
        memberindex=f.member(i,1):f.member(i,2);
        % Identify the grain boundary atoms
        f.boundary{i}=memberindex([sortedatoms(memberindex).strcn]>=1);
        dbatoms=f.atoms(f.boundary{i});
        % Get the box inds of these grainboundary atoms
        dbinds=f.atominds(f.boundary{i},:);
        %% Find strange neighbors and their corresponding grain ids and
orientation
        if ~isempty(f.boundary{i})
            for j=1:length(f.boundary{i})
                x0=dbatoms(j).x;
                y0=dbatoms(j).y;
                bi=dbinds(j,1);
                bj=dbinds(j,2);
                [nbatm nbatmind]=anynbatm(bi,bj,bxx);
                d1=da2b(x0,y0,[nbatm.x],[nbatm.y]);
                nbs=find(d1>=dinh&d1<a);
```

```
                if ~isempty(nbs)
                    for k=1:length(nbs)
                        bxi=nbatmind(nbs(k),1);
                        bxj=nbatmind(nbs(k),2);
                        bxind=nbatmind(nbs(k),3);
                        % neighbor grains
                        g(k).id=bxx(bxi,bxj).atm(bxind).grain;
                        g(k).orient=bxx(bxi,bxj).atm(bxind).orient;
                    end
                     %   Find   the   unique   grain   neighbors   ids   and
corresponding orientations
                    [nbgid{j} first n]=unique([g.id]);
                    nbgorient{j}=[g(first).orient];
                else
                    nbgid={};
                    nbgorient={};
                end

            end

            % Find the unique grain neighbors ID , i.e. eliminate those
repetitious ones caused by different boundary atoms of this
            % grain

            nbgrains=unique(cat(2,nbgid));
            nborientations=unique(cat(2,nbgorient));

            %% output the ID of the neighbor grains and misorienation
            f.nbg{i}=nbgrains;
            f.misorient{i}=abs(nborientations-orient(i));
        else
            f.nbg{i}=[];
            f.misorient{i}=[];
        end
        if ~isempty(f.nbg)
            for j=1:length(f.nbg)
                [f.nbg{j} inds unused]=intersect(f.nbg{j},f.ids);
                f.misorient{j}=f.misorient{j}(inds);
            end
        end
    end
else
    f.boundary={};
    f.nbg={};
    f.misorient={};
end
lightf=rmfield(f,{'atoms' 'atominds'});
f=lightf;
```

EVOMISORIENT

```
function f=evomisorient(graindata,numbin)
% EVOMISORIENT plot the distribution of the misorientation given the
input of the grain data GRAINDATA and how mnay bins
% NUMBINS to use for the historgram plotting
%
k=0;
for i=[10:20:100 101:2:length(graindata)]
    k=k+1;
    [counts(:,k) bins(:,k)]=hist([graindata(i).misorient],numbin);
end
bin=bins(:,1)*60/numbin-30/numbin;
bar3(counts')
axis square
axis tight
set(gca,'XDir','reverse','YDir','Normal','xticklabel',bin);
ylabel('Deposition amount, EML','Rotation',-37);
xlabel('Misorientation, \circ','Rotation',20);
zlabel('Counts')
```